Universidad de Oviedo
Universidá d'Uviéu
University of Oviedo

Programa de Doctorado en Materiales

FOSFATOS DE TITANIO MODIFICADOS: DE MATERIALES LUMINISCENTES A CONTENEDORES DE GASES

TESIS DOCTORAL

Jorge García González

Junio 2018

Universidad de Oviedo
Universidá d'Uviéu
University of Oviedo

Programa de Doctorado en Materiales

FOSFATOS DE TITANIO MODIFICADOS: DE MATERIALES LUMINISCENTES A CONTENEDORES DE GASES

TESIS DOCTORAL

Directores:

María del Camino Trobajo Fernández

Zakariae Amghouz

Vicerrectorado de Organización Académica

Universidad de Oviedo
Universidá d´Uviéu
University of Oviedo

Vicerrectoráu d'Organización Académica
Vice-rectorate for Academic Organization

FOR-MAT-VOA-010-BIS-2

RESUMEN DEL CONTENIDO DE TESIS DOCTORAL

1.- Título de la Tesis	
Español: Fosfatos de titanio modificados: de materiales luminiscentes a contenedores de gases.	Inglés: Modified titanium phosphates: From luminescent materials to gas containers.

2.- Autor	
Nombre: Jorge García González	DNI:
Programa de Doctorado: Materiales	
Órgano responsable: Departamento de Ciencia de los Materiales e Ingeniería Metalúrgica	

RESUMEN (en español)

Los materiales obtenidos en esta investigación, basados en α-fosfato de titanio(IV), $Ti(HPO_4)_2\cdot H_2O$ (α-TiP), como anfitrión, y europio(III) como huésped y fuente de emisión, son sistemas luminóforos que emiten en el rango del naranja-rojo. A partir de α-TiP, se sintetizó un compuesto de intercalación con propilamina, $Ti(HPO_4)_2\cdot 2C_3H_7NH_2\cdot H_2O$ (α-TiPPr), que posteriormente se exfolió en medio acuoso mediante procesos mono-etapa. La inserción de europio(III) tuvo lugar a través de dos vías: (i) intercambio iónico $C_3H_7NH_3^+/[Eu(H_2O)_6]^{3+}$, y (ii) auto-ensamblaje de láminas de fosfato de titanio (cargadas negativamente) y especies catiónicas hidratadas de europio(III), con formación de agregados de nano-placas. Mediante métodos DFT, se modelizó la estructura del compuesto saturado en europio, $[Eu(H_2O)_6]_{2/3}Ti(PO_4)_2\cdot[(H_2O)_6]_{1/3}$ (α-EuTiPPr). Se aplicaron métodos iso-conversionales (diferenciales e integrales) para la adquisición de parámetros cinéticos en procesos de descomposición térmica de algunos de los materiales sintetizados: (i) α-TiP, α-TiPPr, y α-EuTiPPr, (ii) γ-$Ti(PO_4)(NH_4HPO_4)$, (iii) un fosfato-fosfito de amonio-titanio(IV) con estructura tipo pirocloro, y (iv) $Ti_2O(PO_4)_2\cdot 2H_2O$ (ρ-TiP). La monitorización de los procesos de descomposición térmica mediante termo-difracción de rayos X de polvo cristalino, propició la elucidación de la estructura cristalina de nuevas fases: (i) γ-$Ti(PO_4)(NH_4HPO_4)$ y (ii) ρ-$Ti_2O(PO_4)_2$. Se reveló la capacidad del ρ-$Ti_2O(PO_4)_2$ para adsorber nitrógeno a temperaturas de 100-300 ºC. La estructura cristalina de este compuesto está caracterizada por la existencia de canales unidimensionales y dos tipos de átomos de titanio, ambos coordinados por oxígenos, uno de ellos hexa-coordinado y otro en un entorno tetraédrico distorsionado. Las vacancias del titanio tetra-coordinado y las dimensiones moleculares de los canales intra-cristalinos explican la inusual capacidad de este material para retener N_2.

RESUMEN (en Inglés)

The materials obtained in the current research are based on α-titanium(IV) phosphate, $Ti(HPO_4)_2\cdot H_2O$ (α-TiP), as host and europium(III) as guest and emission source. They are phosphors emitting in the orange-red range. From α-TiP, a propylamine intercalation compound, $Ti(HPO_4)_2\cdot 2C_3H_7NH_2\cdot H_2O$ (α-TiPPr), was synthesized and subsequently exfoliated in aqueous medium in a one-step process. Later, the insertion of europium(III) took place through two different routes: (i) $C_3H_7NH_3^+/[Eu(H_2O)_6]^{3+}$ ion-exchange, and (ii) self-assembly of titanium phosphate sheets (negatively charged) and hydrated europium(III) cations with the formation of nano-plate aggregates. The structure of the compound saturated in europium, $[Eu(H_2O)_6]_{2/3}Ti(PO_4)_2\cdot[(H_2O)_6]_{1/3}$ (α-EuTiPPr), was modeled by means of DFT methods. Iso-conversional methods (differential and integral) were applied for the acquisition of kinetic parameters in thermal decomposition processes of some of the synthesized materials: (i) α-TiP, α-TiPPr, and α-EuTiPPr, (ii) γ-$Ti(PO_4)(NH_4HPO_4)$, (iii) a phosphate-phosphite of ammonium-titanium(IV) with pyrochlore-type structure, and (iv) $Ti_2O(PO_4)_2\cdot 2H_2O$ (ρ-TiP). Monitoring the thermal decomposition processes using high-temperature powder X-ray diffraction technique led to the elucidation of the crystalline structure of new phases: (i) γ-$Ti(PO_4)(NH_4HPO_4)$, and (ii) ρ-$Ti_2O(PO_4)_2$. The current investigation shows the ability of ρ-$Ti_2O(PO_4)_2$ to adsorb nitrogen at the 100-300 ºC temperature range. The crystalline structure of this compound reveals the existence of one-dimensional channels, beside two types of titanium atoms both coordinated by

oxygens, one of them being hexa-coordinated and the other in a distorted tetrahedral environment. The vacancies of the tetra-coordinated titanium and the molecular dimensions of the intra-crystalline channels explain the unusual ability of this material to retain N_2 at temperatures above the environment temperature.

Tabla de contenidos

Índices de calidad

De acuerdo con el Reglamento de los Estudios de Doctorado aprobado por el Consejo de Gobierno de la Universidad de Oviedo el 17 de Junio de 2013 (Boletín Oficial del Principado de Asturias Nº 146, de 25-06-2013), para presentar la Tesis Doctoral como Compendio de Publicaciones es necesario incluir en la presente Memoria un informe con el factor de impacto de las publicaciones presentadas, junto con un detalle informativo sobre la calidad de las mismas, basado en el índice de impacto y en la posición que ocupa la revista científica dentro de una determinada categoría. El informe correspondiente a los índices de impacto de las revistas en las que se han publicado, o están en trámite de publicación, los artículos que forman parte de la presente Memoria de Tesis Doctoral se resume en la siguiente Tabla.

Título	**Revista**	**Año**	**Índice de Impacto**	**Área**	**nº de orden / nº total**	**Cuartil**
The ability of a fibrous titanium oxophosphate for nitrogen-adsorption above room temperature	Chemical Communications	2017	6.319	Chemistry, Multidisciplinary	23/166	Q1
α-Titanium phosphate intercalated with propylamine: An alternative pathway for efficient europium(III) uptake into layered tetravalent metal phosphates	Arabian Journal of Chemistry	2017	4.553	Chemistry, Multidisciplinary	31/166	Q1
Morphological study and thermal behaviour of an ammonium-titanium(IV) phosphate with pyrochlore-type structure	Journal of Thermal Analysis and Calorimetry	2016	1.953	Thermodynamics Chemistry, Analytical Chemistry, Physical	20/58 41/76 85/146	Q2 Q3 Q3

Datos obtenidos de *Journal Citations Reports®*

Resumen

La iluminación representa aproximadamente el 19% del consumo mundial de electricidad, lo que hace imprescindible la búsqueda de materiales ecológicos y energéticamente eficientes para este fin, especialmente en el campo de los dispositivos en estado sólido (SSL). Los materiales obtenidos en esta investigación, basados en α-fosfato de titanio(IV), $Ti(HPO_4)_2\cdot H_2O$ (α-TiP), como anfitrión, y europio(III) como huésped y fuente de emisión, son sistemas luminóforos que emiten en el rango del naranja-rojo al ser excitados a 394 nm, por lo que podrán ser empleados en SSL con promoción NUV-LED (rango de excitación: 380-410 nm). A partir de α-TiP, se sintetizó un compuesto de intercalación con propilamina, $Ti(HPO_4)_2\cdot 2C_3H_7NH_2\cdot H_2O$ (α-TiPPr), que posteriormente se exfolió en medio acuoso mediante procesos mono-etapa. La inserción de europio(III) tuvo lugar a través de dos vías: (i) intercambio iónico $C_3H_7NH_3^+/[Eu(H_2O)_6]^{3+}$, y (ii) auto-ensamblaje de láminas de fosfato de titanio (cargadas negativamente) y especies catiónicas hidratadas de europio(III), con formación de agregados de nano-placas. Las muestras se caracterizaron por difracción de rayos X de polvo cristalino (PXRD), microscopia electrónica de barrido y de transmisión (SEM, TEM), microscopia de fuerza atómica (AFM), análisis termo-gravimétrico (TGA) y fotoluminiscencia (PL). Además, mediante métodos DFT, se modelizó la estructura del compuesto saturado en europio, $[Eu(H_2O)_6]_{2/3}Ti(PO_4)_2\cdot[(H_2O)_6]_{1/3}$ (α-EuTiPPr).

El estudio de la cinética de las reacciones en estado sólido persigue conocer el mecanismo de estos procesos químicos, proporcionando además información cuali- y cuantitativa. En esta investigación, se aplicaron métodos iso-conversionales (diferenciales e integrales) para la adquisición de parámetros cinéticos en procesos de descomposición térmica de algunos de los materiales sintetizados: (i) α-TiP, α-TiPPr, y α-EuTiPPr, (ii) γ-$Ti(PO_4)(NH_4HPO_4)$, (iii) un fosfato-fosfito de amonio-titanio(IV) con estructura tipo pirocloro, y (iv) $Ti_2O(PO_4)_2\cdot 2H_2O$ (ρ-TiP). La monitorización de los procesos de descomposición térmica mediante termo-difracción de rayos X de polvo cristalino (HT-PXRD), propició la elucidación de la estructura cristalina de nuevas fases: (i) γ-$Ti(PO_4)(NH_4HPO_4)$ (monoclínica, $P2_1/m$, $a = 5.0725(3)$ Å, $b = 6.3101(3)$ Å, $c = 11.2435(5)$ Å, $\beta = 97.980(3)$º, $Z = 2$), y (ii) ρ-$Ti_2O(PO_4)_2$ (triclínica, P-1, $a = 5.0843(1)$ Å, $b = 8.6121(2)$ Å, $c = 9.6766(2)$ Å, $\alpha = 74.501(2)$º, $\beta = 76.146(2)$º, $\gamma = 74.488(3)$º, $Z = 2$).

El dinitrógeno es la molécula con mayor presencia en la atmósfera terrestre. Su inercia química hace difícil tanto su captura como su reactividad química en la síntesis de compuestos nitrogenados. Esta investigación reveló la capacidad del ρ-$Ti_2O(PO_4)_2$ para adsorber nitrógeno a temperaturas de 100-300 ºC. La estructura cristalina de este compuesto está caracterizada por la existencia de canales unidimensionales y dos tipos de átomos de titanio, ambos coordinados por oxígenos, uno de ellos hexa-coordinado y otro en un entorno tetraédrico distorsionado. Las vacancias del titanio tetra-coordinado y las dimensiones moleculares de los canales intra-cristalinos explican la inusual capacidad de este material para retener N_2.

Abstract

Lighting consumes approximately 19% of electricity globally. This renders the search of ecological and energy efficient materials very important, especially in the field of solid state lighting (SSL) devices. The materials obtained in the current research are based on α-titanium(IV) phosphate, $Ti(HPO_4)_2 \cdot H_2O$ (α-TiP), as host and europium(III) as guest and emission source. They are phosphors emitting in the orange-red range when are excited at 394 nm, so they can be used in SSL with NUV-LED promotion (excitation range: 380-410 nm). From α-TiP, a propylamine intercalation compound, $Ti(HPO_4)_2 \cdot 2C_3H_7NH_2 \cdot H_2O$ (α-TiPPr), was synthesized and subsequently exfoliated in aqueous medium in a one-step process. Later, the insertion of europium(III) took place through two different routes: (i) $C_3H_7NH_3^+/[Eu(H_2O)_6]^{3+}$ ion-exchange, and (ii) self-assembly of titanium phosphate sheets (negatively charged) and hydrated europium(III) cations with the formation of nano-plate aggregates. The samples were characterized by powder X-ray diffraction (PXRD), scanning and transmission electron microscopy (SEM, TEM), atomic force microscopy (AFM), thermo-gravimetric analysis (TGA) and photoluminescence (PL). In addition, the structure of the compound saturated in europium, $[Eu(H_2O)_6]_{2/3}Ti(PO_4)_2 \cdot [(H_2O)_6]_{1/3}$ (α-EuTiPPr), was modeled by means of DFT methods.

The aim of studying of the kinetics of solid state reactions is to explore the mechanism of these chemical processes, providing also qualitative and quantitative information. In this investigation, iso-conversional methods (differential and integral) were applied for the acquisition of kinetic parameters in thermal decomposition processes of some of the synthesized materials: (i) α-TiP, α-TiPPr, and α-EuTiPPr, (ii) γ-$Ti(PO_4)(NH_4HPO_4)$, (iii) a phosphate-phosphite of ammonium-titanium(IV) with pyrochlore-type structure, and (iv) $Ti_2O(PO_4)_2 \cdot 2H_2O$ (ρ-TiP). Monitoring the thermal decomposition processes using high-temperature powder X-ray diffraction (HT-PXRD) technique led to the elucidation of the crystalline structure of new phases: (i) γ-$Ti(PO_4)(NH_4HPO_4)$ (monoclinic, $P2_1/m$, a = 5.0725(3) Å, b = 6.3101(3) Å, c = 11.2435(5) Å, β = 97.980(3)º, Z = 2), and (ii) ρ-$Ti_2O(PO_4)_2$ (triclinic, P-1, a = 5.0843(1) Å, b = 8.6121(2) Å, c = 9.6766(2) Å, α = 74.501(2)º, β = 76.146(2)º, γ = 74.488(3)º, Z = 2).

Dinitrogen is the most abundant molecule in the Earth's atmosphere. Its chemical inertness makes its capture as well as its chemical reactivity in the synthesis of nitrogen compounds difficult. The current investigation shows the ability of ρ-$Ti_2O(PO_4)_2$ to adsorb nitrogen at the 100-300 ºC temperature range. The crystalline structure of this compound reveals the existence of one-dimensional channels, beside two types of titanium atoms both coordinated by oxygens, one of them being hexa-coordinated and the other in a distorted tetrahedral environment. The vacancies of the tetra-coordinated titanium and the molecular dimensions of the intra-crystalline channels explain the unusual ability of this material to retain N_2 at temperatures above the environment temperature.

Abreviaturas

AFM	*Atomic Force Microscopy* (Microscopia de fuerza atómica)
CCT	*Correlated Color Temperature* (Temperatura de color correlacionada)
CIE	*Commission Internationale de l’Éclairage* (Comisión Internacional de Iluminación)
CRI	*Color Rendering Index* (Índice de reproducción cromática)
CVD	*Chemical Vapor Deposition* (Deposición química de vapor)
DFT	*Density Functional Theory* (Teoría del funcional de la densidad)
DSC	*Differential Scanning Calorimetry* (Calorimetría diferencial de barrido)
DTA	*Differential Thermal Analysis* (Análisis térmico diferencial)
ETS	*Engelhard Titano-Silicate* (Silicato de titanio desarrollado por la compañía Engelhard)
FWHM	*Full Width at Half Maximum* (Anchura a media altura)
GIC	*Graphite Intercalation Compounds* (Compuestos de intercalación de grafito)
GO	*Graphite Oxide* (Óxido de grafito)
HMFM	*Huidobro’s Modified Friedman Method* (Método de Friedman modificado por Huidobro)

HT-PXRD	*High-Temperature Powder X-Ray Diffraction* (Termo-difracción de rayos X de polvo cristalino)
ICTAC	*International Confederation for Thermal Analysis and Calorimetry* (Confederación Internacional de Análisis Térmico y Calorimetría)
IR	*Infra-Red* (Infrarrojo)
KAS	*Kissinger-Akahira-Sunose*
LB	*Langmuir-Blodgett*
LbL	*Layer-by-Layer* (Ensamblaje capa a capa)
LDHs	*Layered Double Hydroxides* (Hidróxidos dobles laminares)
LE	*Luminous Efficacy* (Eficiencia luminosa)
LED	*Light Emitting Diode* (Diodo emisor de luz)
MOFs	*Metal-Organic Frameworks* (Red metal-orgánica)
MS	*Mass Spectrometry* (Espectrometría de masas)
NUV	*Near Ultra-Violet* (Ultravioleta cercano)
pcLED	*Phosphor Converted Light Emitting Diode* (Diodo emisor de luz mediante luminóforos)
pcWLED	*Phosphor Converted White Light Emitting Diode* (Diodo emisor de luz blanca mediante luminóforos)
PL	*Photoluminescence* (Foto-luminiscencia)

PSA	*Pressure Swing Adsorption* (Adsorción por inversión de presión)
PXRD	*Powder X-Ray Diffraction* (Difracción de rayos X de polvo cristalino)
QE	*Quantum Efficiency* (Eficiencia cuántica)
RE	*Rare Earth* (Tierras raras, elementos lantánidos)
RGB	*Red, Green, Blue* (Rojo, verde, azul)
RT	*Room Temperature* (Temperatura ambiente)
SEM	*Scanning Electron Microscopy* (Microscopia electrónica de barrido)
SSL	*Solid State Lighting* (Iluminación en estado sólido)
SS-NMR	*Solid-State Nuclear Magnetic Resonance* (Resonancia magnética nuclear en estado sólido)
STP	*Standard Temperature and Pressure* (Temperatura y presión estándar)
TEM	*Transmission Electron Microscopy* (Microscopia electrónica de transmisión)
TGA	*Thermogravimetric Analysis* (Análisis termo-gravimétrico)
UV	*Ultra-Violet* (Ultravioleta)
WLED	*White Light Emitting Diode* (Diodo emisor de luz blanca)

Lista de Figuras

1. Introducción

1.1 Materiales Inorgánicos Luminiscentes

La iluminación representa aproximadamente el 19% del consumo mundial de electricidad, lo que hace imprescindible la búsqueda de dispositivos ecológicos y energéticamente eficientes para este fin [1]. Es ampliamente aceptado que la iluminación de estado sólido (SSL, *solid state lighting*) reemplazará a las tecnologías más antiguas (lámparas incandescentes), que ya han sido eliminadas en los países más desarrollados, y a aquellas que son discutibles desde el punto de vista medioambiental [2]. El descubrimiento a mediados de la década de 1990 de los diodos emisores de luz (LED, *light emitting diodes*) [3,4] condujo al desarrollo de dispositivos que, basados mayoritariamente en materiales inorgánicos, sean capaces de producir luz blanca de manera confiable y eficiente [5]. Las lámparas pcLED (*phosphor converted light emitting diode*) actuales poseen una serie de ventajas importantes en comparación con generaciones anteriores: no contienen materiales altamente tóxicos como el mercurio [6], se encienden instantáneamente, son mecánicamente robustas, tienen una larga vida útil (25000-30000 h), y poseen una elevada eficiencia energética. Aunque inicialmente la luz blanca pudo obtenerse combinando los tres colores primarios, rojo-verde-azul (RGB, *red*, *green*, *blue*), generados por tres LEDs distintos, el empleo de múltiples chips LED genera elevados costes de producción. Por esta razón, actualmente se prefiere usar un solo LED obtenido por combinación de los luminóforos* adecuados.

En la actualidad, en el mercado, se pueden encontrar fácilmente dos familias de LEDs: (i) LEDs azules (que emiten a 450-480 nm) y (ii) LEDs que emiten en el ultravioleta cercano (NUV, *near ultra-violet*) (380-410 nm). A continuación, se describen algunos materiales luminóforos con aplicaciones actuales o potenciales en la generación de luz blanca mediante excitación con LEDs [1,5-14], clasificados en función del color de sus emisiones (Fig. 1): azul (435-500 nm), verde (520-565 nm), amarillo (565-590) y rojo (625-740 nm) [15].

---

*Aunque la palabra luminóforo es de uso relativamente común en ambientes técnicos, no se encuentra recogida en el diccionario de la RAE. En esta Tesis, el término luminóforo se utiliza como equivalente del vocablo inglés *phosphor*. Por analogía con la definición que la RAE proporciona de la palabra cromóforo (dicho de un agrupamiento químico: que causa la coloración de una sustancia), luminóforo podría definirse como “agrupamiento químico que causa emisión de luz al ser estimulado”.

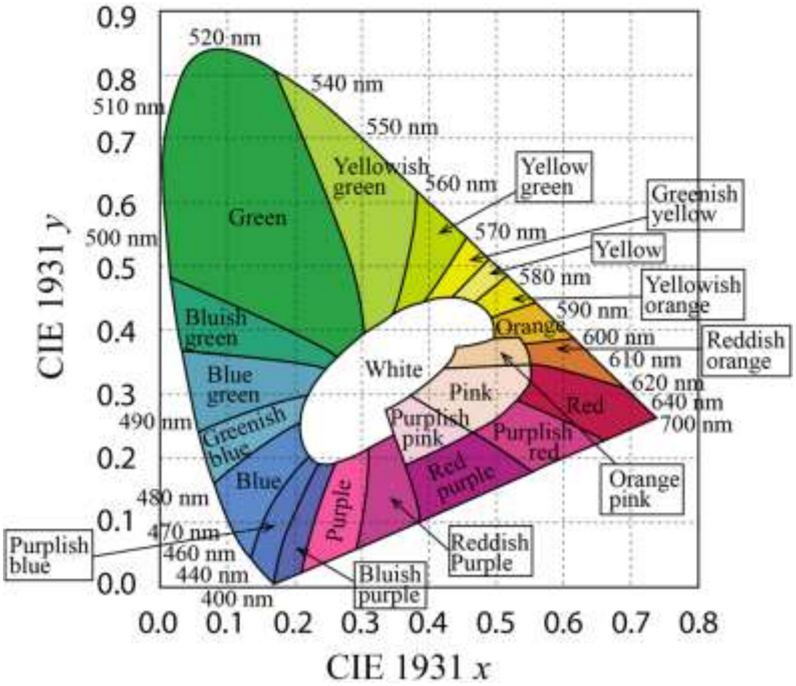

Fig. 1. Regiones aproximadas de color en el diagrama de cromaticidad la *Commission Internationale de l'Éclairage* (CIE) 1931 [16].

Dado que los luminóforos inorgánicos consisten en un material hospedante cristalino dopado con una cantidad relativamente pequeña de iones metálicos de transición o de transición interna, llamados activadores, que convierten luz de una longitud de onda más corta a otra más larga a través de transiciones electrónicas, la descripción de los materiales emisores se realizará, para cada color, en función del tipo de anfitrión (silicatos, fosfatos, aluminatos, boratos, etc.) del catión activador.

1.1.1. Diodos Emisores de Luz Blanca

Dos de los tipos principales de pcWLEDs (*phosphor converted white light emitting diode*) están basados en (i) un chip NUV-LED recubierto con una mezcla de luminóforos RGB (Fig. 2a) y (ii) un chip LED azul recubierto con un luminóforo amarillo (Fig. 2c), mostrándose sus espectros de emisión típicos en las Figuras 2b y 2d, respectivamente. En el pcWLED (Fig. 2c), el luminóforo amarillo puede reemplazarse por una mezcla de luminóforos verde y rojo, con un perfil de emisión similar al representado en la Figura 2b. Dos parámetros son útiles para definir el brillo y el color emitidos por un pcWLED: la eficacia luminosa (LE, *luminous efficacy*) y el índice de reproducción cromática (CRI, *color rendering index*). LE expresa la capacidad de una fuente de luz para producir luz visible, mientras que CRI mide cuantitativamente la capacidad de una fuente de luz para reproducir fielmente los colores de varios objetos en comparación con una fuente de luz ideal (natural). La Figura 2e muestra las coordenadas de la luz visible emitida por los pcWLEDs basados en NUV- y azul-LEDs en el diagrama cromático CIE 1931 (CIE, *Commission Internationale de l'Éclairage*), donde la temperatura de color correlacionada (CCT, *correlated color temperature*) se indica a lo largo del lugar geométrico del cuerpo negro ideal. Cuanto más alto es el CCT, más fría es la percepción de la luz por parte de los humanos. A modo de comparación, las lámparas incandescentes tienen un CRI de 100 (se requiere un valor alto de CRI para una iluminación confortable y de alta calidad).

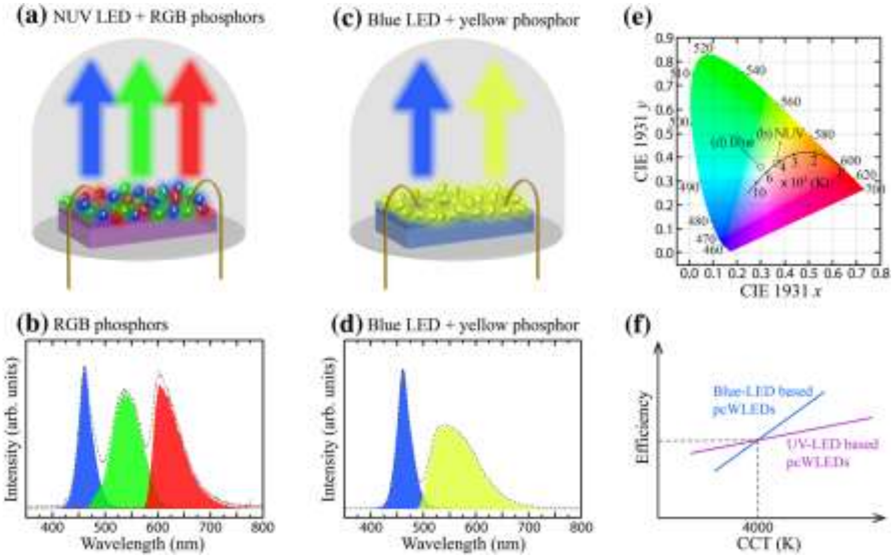

Fig. 2. Representación esquemática de pcWLEDs basados en un NUV-LED y una mezcla de luminóforos RGB (a), y un LED azul combinado con un luminóforo amarillo (c), y sus correspondientes espectros de emisión en (b) y (d). Diagrama cromático CIE 1931 (e) indicando las coordenadas CIE de los espectros de emisión (b) y (d). Comparación esquemática de la eficacia de los dispositivos con respecto a CCT de los pcWLEDs basados en NUV- y azul-LED (f) [7].

Una comparación entre los dos tipos de pcWLEDs (Fig. 2e) muestra que la emisión de luz blanca de los pcWLEDs basados en LEDs azules conteniendo un luminóforo amarillo tiene un CCT más alto (7002 K) que el de los basado en NUV (4521 K), donde los valores de CCT se calculan en términos de las coordenadas cromáticas que se muestran en la Figura 2e [16]. Los valores de CCT revelan que la luz emitida por los pcWLEDs basados en NUV se percibe como una luz más cálida que la de los pcWLEDs basados en el azul-LEDs. Además, los NUV-LEDs funcionan con mayor eficiencia para emisiones de luz blanca más cálida (Fig. 2f). Por contra, son más difíciles de fabricar y, por tanto, más caros. También en destacable que los pcWLEDs que emiten luz blanca cálida se pueden obtener por excitación de luminóforos verdes y rojos mediante LEDs azules, con una alta eficiencia debido a la pequeña diferencia entre las longitudes de onda de excitación y emisión. Por este último motivo, muchas investigaciones se centran en mejorar la tecnología basada en LED azules, especialmente con el objetivo específico de reducir su CCT y aumentar su CRI. Las estrategias para mejorar estas propiedades incluyen, por ejemplo, la adición de componentes rojos altamente eficientes [17]. En la Figura 3 se muestran las coordenadas CIE 1931 de algunos inorgánicos utilizados en dispositivos pcWLED.

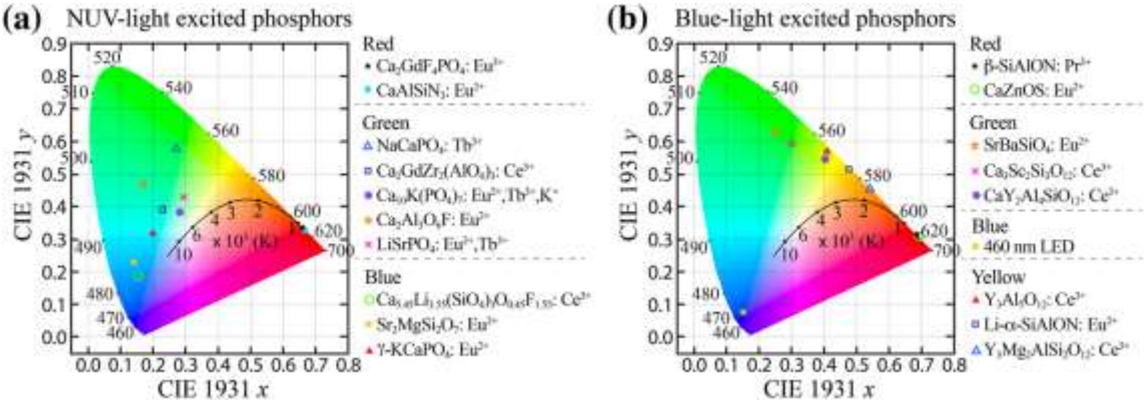

Fig. 3. Diagrama CIE 1931 con coordenadas de luminóforos utilizados en pcWLEDs basados en NUV-LED (a) y azul-LED (b) [1].

1.1.2. Luminóforos Amarillos

Los luminóforos que emiten luz amarilla (con bandas de emisión centradas en 565-590 nm) pueden utilizarse para SSL cuando son excitados por una fuente NUV ($\lambda \approx$ 380-410 nm) o azul ($\lambda \approx$ 450-480 nm). Dado que la luz amarilla se puede obtener combinando luz verde y roja, el papel de los luminóforos verdes y rojos en los pcWLEDs, constituidos por un chip NUV-LED y un luminóforo RGB, puede ser desempeñado por luminóforos amarillos. Éstos, junto a un chip LED azul, si no se precisan CRI elevados, suelen utilizarse para generar luz blanca. Sin embargo, cuando se requiere un CRI alto, es más favorable el uso de luminóforos RGB y chips NUV-LED o RG (rojo y verde) acoplados a una bomba LED azul. Los iones responsables de las radiaciones amarillas son principalmente Ce^{3+} y Eu^{2+}. La luminiscencia de estos cationes es consecuencia de transiciones 5*d*-4*f*, en las que están permitidas las transiciones dipolares eléctricas, por lo que las emisiones son relativamente brillantes, haciéndolos ideales para aplicaciones pcWLED.

Generalmente, los niveles de energía de los iones activos en los luminóforos determinan sus propiedades de excitación y emisión. En los cationes lantánidos (RE, *rare earths*), las transiciones ópticas suelen ocurrir entre los niveles 4*f* y 5*d*. Puesto que los orbitales 5*d* son muy sensibles al entorno del catión metálico, los espectros resultantes varían con la naturaleza del cristal anfitrión, provocando grandes variaciones en las longitudes de onda de emisión/excitación, por lo que la elección del hospedante de la especie activa suele ser un factor determinante.

Las principales matrices hospedantes para la generación de luz amarilla son oxinitruros, silicatos y aluminatos, destacando redes tipo granate a las que se incorporan iones Ce^{3+}, obteniéndose materiales luminiscentes con excelentes características ópticas para la generación de luz blanca, que han sido ampliamente utilizados comercialmente en pcWLEDs.

El material tecnológicamente más importante es el $YAG:Ce^{3+}$ [18], obtenido por sustitución Y/Ce en granates de itrio y aluminio (YAG, *yttrium aluminium garnet*). El hecho de que su rendimiento como luminóforo amarillo acoplado con un chip LED azul sea casi ideal para lámparas LED con un alto CCT, ha ralentizado la búsqueda de nuevos materiales mejorados. A pesar de ello, se han desarrollado algunos otros excelentes luminóforos inorgánicos de emisión amarilla, destacando los basados en oxinitruros, como Ca-α-$SiAlON:Eu^{2+}$ y Li-α-$SiAlON:Eu^{2+}$ [19]. Las coordenadas CIE de Ca-α-$SiAlON:Eu^{2+}$ (0.49, 0.50) y Ca-α-$SiAlON:Eu^{2+}$ (0.48, 0.51), comparadas con las de $YAG:Ce^{3+}$ (0.41, 0.57), revelan que ambos luminóforos tipo oxinitruro son más adecuados para producir luz blanca cálida en pcWLED que el $YAG:Ce^{3+}$. Además, los pcWLEDs que usan Ca-α-$SiAlON:Eu^{2+}$ tienen una mayor estabilidad cromática (es decir, presentan pequeñas variaciones de las coordenadas CIE en el rango de temperatura 25-200 ºC) que los basados en $YAG:Ce^{3+}$. Sin embargo, la absorción y la eficiencia cuántica externa de Li-α-$SiAlON:Eu^{2+}$ son aproximadamente 70 y 40%, respectivamente, valores considerablemente inferiores a los de $YAG:Ce^{3+}$ (90 y 75%) [20]. Otros ejemplos incluyen luminóforos basados en silicatos, tales como $Sr_3SiO_5:Eu^{2+}$ [21] y $Li_2SrSiO_4:Eu^{2+}$ [22]. Finalmente, otras estrategias para desarrollar nuevos luminóforos de mejor rendimiento incluyen el ajuste de las propiedades ópticas del YAG:Ce^{3+} con la adición de un segundo o, incluso, un tercer átomo dopante, en los sitios cristalográficos de Y^{3+} y/o Al^{3+} [23-29].

1.1.3. Luminóforos Azules

Los luminóforos emisores de luz azul podrán ser útiles para SSL si pueden ser excitados por un NUV-LED; es decir, si son capaces de convertir la radiación del rango de 380-410 nm en luz centrada en la región azul (420-500 nm, incluida una parte del violeta) [13]. En la práctica, los únicos iones activadores que han atraído el interés para el desarrollo de luminóforos azules para diodos emisores de luz blanca (WLEDs, *white light emitting diodes*) son Eu^{2+} y Ce^{3+}. Ambos cationes producen bandas de luminiscencia como consecuencia de transiciones $5d$-$4f$ ($4f^{6}5d^{1} \rightarrow 4f^{7}$ y $5d^{1} \rightarrow 4f^{1}$, respectivamente) con tiempos de decaimiento radiativo del orden de 1 μs para el primero [30] y algunas decenas de nanosegundos para el segundo [31]. Las transiciones $5d$-$4f$ están permitidas a través del mecanismo dipolar eléctrico y, por lo tanto, suelen ser muy fuertes. Su eficacia cuántica a temperatura ambiente (RT, *room temperature*) es, en principio, alta, exceptuando los casos en que se produce fotoionización (es decir, salto de un electrón a la banda de conducción) [32,33].

Entre los hospedantes inorgánicos desarrollados para luminóforos LED azules sobresalen las oxosales (fosfatos, silicatos y aluminatos), aunque también se han propuesto y desarrollado con relativo éxito composiciones basadas en nitruros y oxinitruros.

Los fosfatos son, quizá, la clase más importante de luminóforos azules para pcLEDs como consecuencia de combinar métodos de preparación relativamente sencillos con una gran flexibilidad estructural [34-38]. Se han utilizado algunos miembros de la familia de las apatitas como anfitriones de Ce^{3+} y Eu^{2+}, informándose de la síntesis, luminiscencia y propiedades de transferencia de energía del compuesto $Ca_8La_2(PO_4)_6O_2$ activado con Ce^{3+} y Eu^{2+} [38]. Con ambos dopantes se origina fotoluminiscencia azul después de excitación UV, con una emisión de elevada pureza de color y un espectro PL que abarca toda la región UV. Otro anfitrión, Ca_2PO_4Cl, con estructura cristalina tipo spodiosita, dopado con Eu^{2+} [39] presenta un pico de emisión azul intenso a 454 nm tras excitación a 400 nm, con eficiencias cuánticas internas y externas de 85 y 61%, respectivamente. Los ortofosfatos dobles conteniendo un catión alcalino y uno alcalinotérreo también se han estudiado ampliamente. Por ejemplo, $KBaPO_4$:Eu^{2+} [40] emite a 420 nm, casi en el rango del violeta, con una excitación que se extiende a toda la región UV (además, cuando la superficie está recubierta con una capa de SiO_2, el luminóforo muestra una excelente resistencia a la humedad), mientras γ-$KCaPO_4:Eu^{2+}$ [41] se excita en un amplio rango espectral (200-450 nm), abarcando UV y visible, con picos de emisión a 473 nm, lo que resulta en una luminiscencia azul blanquecina. Otro ejemplo de ortofosfato doble es $LiCaPO_4:Eu^{2+}$ [42] en el que, optimizando la concentración del dopante, con una excitación a 395 nm, se obtiene un máximo de luminiscencia azul verdosa a 470 nm con una eficiencia cuántica del 52%. Entre los difosfatos, β-$Ca_2P_2O_7:Eu^{2+}$ [43], por excitación a $\lambda \leq 387$ nm, origina un pico de emisión a 421 nm (más violeta que azul) que se extiende hasta aproximadamente 475 nm en el azul, mientras $KBaBP_2O_8:Eu^{2+}$ [44], tras excitación en una amplia región espectral que se extiende desde 250 a 420 nm, produce un pico de emisión a 445 nm, que se extiende hasta los 600 nm.

Los silicatos constituyen otra importante clase de luminóforos azules, caracterizándose por una excelente estabilidad química y una gran variabilidad composicional, aunque sus procedimientos de síntesis suelen requerir temperaturas más altas que las habituales en la preparación de fosfatos. $Li_2(Sr_{1-3x/2}Ce_x)SiO_4$ ($x = 0.0025$-0.07) [45] produce un pico de emisión azul a 442 nm con un amplio perfil de excitación que cubre la región espectral de 200 a 400 nm, con un enfriamiento térmico débil y eficiencias cuánticas internas y externas del 81 y 66%, respectivamente para una excitación a 358 nm, lo que hace de este luminóforo un material prometedor para aplicaciones SSL. El disilicato $Sr_2MgSi_2O_7:Eu^{2+}$, bien conocido en el campo de la luminiscencia persistente [46], también ha sido investigado como luminóforo azul para pcLEDs [47], mostrando una emisión amplia y asimétrica centrada en 470 nm (excitación a $\lambda \leq 400$ nm), mientras $(Ca_{1-x}Eu_x)MgSi_{2y}O_{6+\delta}$ ($x = 0.001$-0.06, $y = 1.0$-2.0) [48] presenta su intensidad de emisión más alta alrededor de 450 nm en muestras con exceso de silicio. $Ca_{5.45}Li_{3.55}(SiO_4)_3O_{0.45}F_{1.55}:Ce^{3+}$ [49], con los cationes Ce^{3+} ocupando las posiciones estructurales del Ca^{2+}, muestra una amplia banda de emisión asimétrica que alcanza un máximo alrededor de 470 nm, excitándose en un amplio rango de longitudes de onda, con máximos a 256 y 371 nm, mostrando una gran pureza de color y buena estabilidad térmica.

Los aluminatos son otra importante familia de luminóforos. $BaMgAl_{10}O_{17}:Eu^{2+}$ ($BAM:Eu^{2+}$), un material comercial emisor de luz azul en lámparas fluorescentes, también ha sido investigado como luminóforo para pcLEDs [50]. Sus espectros de excitación cubren el rango 280-400 nm, con una emisión amplia, alcanzando un máximo a 440 nm y extendiéndose hasta los 520 nm que, junto a sus coordenadas CIE (0.15, 0.06), hacen de BAM:Eu^{2+} un material adecuado para su uso en SSL. (Mg,Sr)Al_2O_4:Eu^{2+} se ha propuesto como luminóforo azul para WLEDs [51], habiéndose preparado diversos materiales con diferentes relaciones Mg/Sr/Eu, mostrando luminiscencia azul en el rango 400-600 nm (máximo a 460 nm). Cuando el $Sr_3Al_2O_6$ se dopa con Ce^{3+} e iones alcalinos [52] se obtiene un material cuyo espectro de excitación muestra un pico fuerte a 395 nm, originando una amplia banda de emisión hasta 600 nm, con un pico a 460 nm. La adición de Li^+, Na^+, K^+ o Rb^+, cambia ligeramente el perfil de las bandas de excitación, pero no afecta al perfil de emisión. Sin embargo, la intensidad espectral aumenta en presencia de los iones alcalinos (máximo para un 4% de Rb) con tiempos de decaimiento cortos (~20 ns).

A continuación, se citarán algunos otros hospedantes diferentes de fosfatos, silicatos y aluminatos, situando el foco principal sobre los nitruros y oxinitruros. Además, se discutirá brevemente otro catión activador (Ce^{4+}).

Los luminóforos tipos nitruro y oxinitruro han tomado importancia en el campo de SSL debido a su alta eficiencia, estabilidad y fuerte absorción en NUV y las regiones espectrales azules [9]. Como ejemplo, $BaSi_7N_{10}$:Eu^{2+} [53] presenta una fuerte banda de emisión verde-azul centrada en 482-500 nm, con un perfil de excitación en la región 250-400 nm con un máximo a 300 nm. La QE (*quantum efficiency*) externa alcanza el 52% tras la excitación a 300 nm, para la muestra dopada con un 20% de Eu. La fuerte emisión, alta QE y bajo enfriamiento térmico hacen que este material sea adecuado para aplicaciones pcLED. $BaSi_3Al_3O_4N_5$:Eu^{2+} [54] muestra un pico de emisión azul a 470 nm y un amplio espectro de excitación en el NUV. Con un 15% (en moles) del dopante reemplazando al Ba^{2+}, el tiempo de decaimiento de la emisión es superior a 800 ns, con eficiencias cuánticas internas y externas de la luminiscencia del 85 y 79%, respectivamente, cuando se excita a 305 nm. Estos datos hacen de este luminóforo aparentemente superior al material comercial, BAM:Eu^{2+}. El β-SiAlON activado con Ce^{3+} [55] emite luz azul con un máximo a 470-490 nm (pico de excitación a 410 nm). A la concentración óptima del dopante (2%, reemplazando el Si) el enfriamiento térmico es significativamente menor que para YAG:Ce^{3+}, confirmando las buenas propiedades de este material como luminóforo azul. Además, estudios teóricos de varios nitruros y oxinitruros [$LaSi_3N_5$:Ce^{3+} (azul), $La_3Si_6N_{11}$:Ce^{3+} (amarillo), $BaSi_2O_2N_2$:Eu^{2+} (verde azulado), $Ba_3Si_6O_9N_4:Eu^{2+}$ (verde azulado), y $Ba_3Si_6O_{12}N_2:Eu^{2+}$ (verde)] han permitido correlacionar la posición de los niveles 5*d* de los elementos lantánidos (Ce^{3+} y Eu^{2+}) dopantes y, por tanto, su comportamiento como luminóforos, con propiedades dieléctricas cuantitativas que reflejan la polarizabilidad espectroscópica [56], lo que abre un camino hacia el diseño controlado de nuevos materiales con propiedades pre-definidas.

$CaLaGa_3S_6O:Ce^{3+}$ se desarrolló con el fin de obtener un material adecuado para la absorción de la luz emitida por los chips InGaN [57]. Los espectros de luminiscencia de este oxicalcogenuro presentan una emisión de doble pico con máximos a 442 y 478 nm, mientras la excitación está dominada por un pico a 398 nm. La intensidad máxima de emisión se obtiene para la muestra que contiene un 10% de Ce con un tiempo de decaimiento a RT de 16 ns (este valor es relativamente bajo, por lo que la eficiencia cuántica no debería ser muy alta) y unas coordenadas de color (azul) de la luz emitida (0.15, 0.09) adecuadas para su uso como pcLED.

Los cloroboratos $M_2B_5O_9Cl$ (M = Sr, Ca) se utilizaron como anfitriones de Eu^{2+} [58], mostrando su utilidad para el almacenamiento de imágenes de rayos X y como luminóforos azules para SSL.

1.1.4. Luminóforos Verdes

Los luminóforos emisores de luz verde se pueden emplear para SSL ya sea por excitación de un NUV- o un azul-LED con el objetivo de convertir radiación en los rangos 380-410 o 450-480 nm, respectivamente, a luz centrada en la región verde (520-565 nm). En este caso, el arsenal de iones activadores que se puede utilizar para el desarrollo de luminóforos verdes para WLEDs es mayor que para los azules, ya que a Eu^{2+} y Ce^{3+} se suman Tb^{3+} y Mn^{2+}.

Como se comentó previamente, los cationes Eu^{2+} y Ce^{3+} originan bandas de luminiscencia debido a transiciones 5*d*-4*f*. Sin embargo, Tb^{3+} y Mn^{2+} emiten a través de transiciones 4*f*-4*f* y 3*d*-3*d*, respectivamente. Estas transiciones intra-configuracionales están prohibidas por el mecanismo de dipolo eléctrico y, por lo tanto, son débiles. Esto puede crear problemas en el rendimiento de los luminóforos basados en Tb y Mn ya que, en general, las transiciones de excitación disponibles también están prohibidas y son débiles. Por esta razón, en muchos casos, la excitación de Tb^{3+} y Mn^{2+} se produce a través de un proceso de transferencia de energía en el que Eu^{2+} o Ce^{3+} se utilizan como sensibilizadores para los iones activadores. Como en la sección precedente, los anfitriones más comunes son fosfatos, silicatos y aluminatos.

La eulytita, $Sr_3Gd(PO_4)_3$, co-dopada con Ce^{3+} y Eu^{2+} [59] presenta una transferencia de energía de Ce^{3+} a Eu^{2+} con una eficiencia de alrededor del 95% para concentraciones de Eu del 2%, con una emisión verde (518 nm) del Eu^{2+}. El fosfato doble $NaCaPO_4$ dopado con Tb^{3+} ha sido propuesto como luminóforo verde para NUV-LEDs [60]. Con un nivel de dopaje del 5% (Tb) la luminiscencia azul y violeta de $^5D_3$ se extingue por procesos de relajación cruzada [61], estando dominado el espectro de emisión por la banda $^5D_4 \rightarrow {}^7F_5$ en el verde a 547 nm, mientras el espectro de excitación está compuesto por bandas 4*f*-4*f* fuertes (máximo a 370 nm) y bandas 4*f*-5*d* débiles. A priori, este material podría ser útil para pcLEDs, aunque las bandas de excitación probablemente sean demasiado débiles para fines prácticos. En $Ca_{10}K(PO_4)_7$ [62] y $LiSrPO_4$ [63], co-dopados con Eu^{2+} (sensibilizador) y Tb^{3+} (activador), la transferencia Eu^{2+}-Tb^{3+} permite excitar la emisión $^5D_4$ del Tb^{3+} (emisión a 540 nm) de forma eficiente en el UV, justamente en la región donde operan los NUV-LEDs. La transferencia de energía no es completa (la eficiencia es de aproximadamente 66% para $LiSrPO_4$) a causa de la luminiscencia del Eu^{2+} en la región azul. Se construyeron dispositivos pcLEDs acoplando un NUV-LED (398 nm) con los luminóforos en los que se había optimizado la concentración de dopantes. Las coordenadas de color para $Ca_{10}K(PO_4)_7$ (0.28, 0.38) y $LiSrPO_4$ (0.29, 0.43) están ubicadas en la zona verde del diagrama CIE, confirmando que estos materiales son adecuados como luminóforos verdes. El borofosfato $Sr_6BP_5O_{20}:Eu^{2+}$ [64] se utilizó como un luminóforo verde azulado en la fabricación de un WLED. Su espectro de emisión tiene un pico a 475 nm que se extiende hasta 650 nm, mientras que el espectro de excitación muestra máximos a 290 y 365 nm, con un hombro a 390 nm. El tiempo de decaimiento de la emisión está en el rango de l s, típico para el Eu^{2+}. El silicofosfato $Ca_5(PO_4)_2SiO_4$, con estructura tipo silicocarnotita, dopado con Eu^{2+}, emite en el verde [65]. La luminiscencia de este material puede excitarse desde 220 hasta por encima de 400 nm, y se caracteriza por un pico ancho y asimétrico a 530 nm, indicando la existencia de diferentes sitios cristalográficos para el Eu en la estructura del anfitrión. Con un 5% de Eu, se fabricó un pcLED por acoplamiento con un NUV-LED que emite a 380 nm una luz amarillo-verdosa estable.

Es conocido que, en muchos casos, el Eu^{2+} origina emisiones verdes cuando se hospeda en silicatos (además, el Ce^{3+} también produce emisión en el verde como dopante de granates). Como consecuencia, los materiales basados en silicatos son un fértil campo de investigación en la búsqueda de luminóforos verdes para pcLEDs. El $Ca_3Sc_2Si_3O:Ce^{3+}$ [66,67], excitado con un LED azul a 455 nm, emite en el verde (0.30, 0.59). Cuando el $Ba_2MgSi_2O_7:Eu^{2+}$ [68], un luminóforo verde para pcLEDs que presenta un espectro de excitación muy amplio (250-450 nm), es excitado a 395 nm da lugar a una emisión amplia (máximo a 505 nm) que se extiende hasta 650 nm, mostrándose adecuado para la excitación con chips NUV. El $SrBaSiO_4:Eu^{2+}$ [69], aunque su zona de excitación es más restringida, también abarca la región NUV (máximo a 430 nm), originando una emisión relativamente aguda en el verde (máximo a 512 nm). El $Na_3Y_{1-x}Sc_xSi_3O_9:Eu^{2+}$ [70] presenta un rango de excitación muy amplio en el UV, con un espectro de emisión, tras excitación a 365 nm, con una banda ancha a aproximadamente 500 nm y unas coordenadas CIE (0.16, 0.55) que muestran que el luminóforo emite luz verde con alta pureza de color. El aluminosilicato $MAl_2Si_2O_8$ (M = Sr, Ba) co-dopado con Eu^{2+} y Mn^{2+} [71], presenta un comportamiento luminiscente óptimo para contenidos en Eu y Mn del 1 y 10%, respectivamente. La excitación en el UV provoca que el Mn^{2+} emita en el verde-amarillo (picos a 564 y 518 nm para M = Sr y Ba, respectivamente).

El óxido doble $CaSc_2O_4$ dopado con Ce^{3+} [72] presenta un pico de luminiscencia a 515 nm con un hombro a una longitud de onda más larga, como es típico del Ce^{3+}, con un espectro de excitación (máximo a 450 nm) adecuado para la excitación con un LED InGaN azul, con una alta eficiencia cuántica (90% del valor observado para $Ca_3Sc_2Si_3O_{12}:Ce^{3+}$ [66]). En el borato $LiBaBO_3:Tb^{3+}$ [73], por efecto de la especie anfitriona, sólo se observa la emisión desde el nivel $^5D_4$ del Tb^{3+} (544 nm), con un perfil de excitación que comprende dos bandas diferenciadas (242-277 y 368-381 nm, esta última asociada a transiciones 4*f*-4*f* y, por tanto, más débil) y coordenadas CIE de emisión en la región verde (0.25, 0.58). El $SrMoO_4$, dopado con Tb^{3+} y Na^+ (para compensación de carga), ha sido propuesto como luminóforo verde amarillento [74]. Sin embargo, aunque la emisión es fuerte desde $^5D_4$ a 548 nm, los máximos de excitación se encuentran a 488 o 375 nm, correspondiendo con las transiciones 4*f*-4*f* desde el estado fundamental $^7F_6$ a $^5D_4$ y $^5D_3$, respectivamente. A pesar de que la emisión es eficiente, la probabilidad de excitación es débil, por lo que es poco factible que estos materiales puedan encontrar aplicaciones prácticas en pcLEDs. Los espectros de luminiscencia del oxifluoruro $Ca_2Al_3O_6F:Eu^{2+}$ [75] muestran una banda de excitación muy amplia que abarca el intervalo 250-450 nm y un pico de emisión a 502 nm, con una anchura a media altura (FWHM, *full width at half maximum*) de 70 nm. El mismo anfitrión, $Ca_2Al_3O_6F$, co-dopado con Ce^{3+} y Tb^{3+} [76], presenta una transferencia de energía muy eficiente $Ce^{3+} \rightarrow Tb^{3+}$ de forma que la emisión verde del Tb^{3+} ($^5D_4$, 542 nm) se obtiene tras la excitación de las transiciones 4*f*-5*d* permitidas del Ce^{3+} en la región NUV (320-400 nm), con una eficiencia de transferencia de energía muy alta (92% para la muestra que contiene un 5% de Tb). Las coordenadas CIE para esta composición son (0.29, 0.45) señalan a este material como un posible emisor de luz verde para NUV-LEDs (además, en función de la concentración de dopantes, el color emitido puede ser azul, azul verdoso, verde o amarillo verdoso). Algunos fluoruros y oxifluoruros [77] han sido propuestos como materiales adecuados para lámparas LED. Entre ellos, es destacable la familia $(Sr,Ca)_3(Al,Si)O_4(F,O):Ce^{3+}$ (emisores de color amarillo-verdoso). Sus espectros de luminiscencia están dominados por una fuerte emisión alrededor de 540-550 nm, mientras la excitación muestra dos picos anchos en el rango de 250-500 nm. La QE a RT (excitación a 450 nm) es comparable al del granate comercial dopado con Ce^{3+}.

Los nitruros y oxinitruros constituyen una importante familia de luminóforos verdes para SSL [9]. En particular, los SiAlONs son anfitriones ampliamente investigados. Como ejemplo, β-SiAlON:Eu^{2+} ($Eu_xSi_{6-z}Al_zO_zN_{8-z}$; $x = 0.018$, $z = 0.23$) [78] emite en la región verde a 539 nm, mostrando picos de excitación a 300, 358 y 407 nm, siendo un material prometedor para aplicaciones pcLED, mientras α-SiAlON:Yb^{2+} [79] muestra espectros de luminiscencia debidos a transiciones inter-configuracionales $4f^{14} \leftrightarrow 4f^{13}5d^1$ [80] caracterizados por una única banda ancha centrada a 549 nm, mientras los espectros de excitación muestran varios picos anchos en la región UV y azul, en particular uno ubicado a 445 nm, que hace que este luminóforo sea adecuado para la excitación con LED azul. Este material parece potencialmente útil para crear luz blanca en combinación con un luminóforo rojo y un chip LED azul.

El $SrSi_2O_2N_2$ co-dopado con Eu^{2+} y Mn^{2+} [81] emite en verde. Los materiales que sólo contienen Eu muestran una amplia banda de emisión centrada a 530 nm, mientras que la excitación abarca la región UV-visible desde 250 hasta casi 500 nm. La adición de Mn^{2+} provoca la transferencia de energía de este ion a Eu^{2+}, aumentando las vías de excitación en el NUV. Por otro lado, $Ba_3Si_6O_{12}N_2:Eu^{2+}$ [82] presenta espectros de excitación caracterizados por una banda muy amplia en el rango de 200-500 nm, que combina bien con los LED azules y NUV, mientras la emisión se localiza en el verde a 527 nm. Los espectros de luminiscencia de $(Ba,Sr)Y_2Si_2Al_2O_2N_5:Eu^{2+}$ [83] están dominados por una amplia banda de emisión que cambia de 510 a 533 nm cuando aumenta la concentración del dopante, mientras la banda de excitación es ancha con señales características a 291, 354 y 426 nm.

En el sulfuro $Sr_{1-x}Ca_xGa_2S_4:Eu^{2+}$ [84], la excitación a 455 nm produce una amplia banda de emisión simétrica en el rango 500-625 nm, cuyo máximo se desplaza hacia el rojo cuando aumenta el valor de x, posiblemente consecuencia de un campo de ligando más fuerte alrededor del Eu^{2+} cuando el Sr^{2+} es reemplazado por Ca^{2+}.

1.1.5. Luminóforos Rojos

Al igual que en el caso de los luminóforos verdes, los materiales emisores de luz roja podrán emplearse para SSL si son excitados por un NUV- o un azul-LED y, por tanto, deben poder convertir eficientemente la radiación en los rangos 380-410 o 450-480 nm en luz centrada en la región roja (625-740 nm). Hacer esto de una manera eficiente no es una cuestión trivial ya que, en muchos anfitriones, los iones activadores más comunes para pcLEDs (Ce^{3+} y Eu^{2+}) no emiten fuertemente en la región roja. Para lograr una emisión roja eficiente basada en transiciones de excitación y emisión $5d$-$4f$, es necesario contar con materiales hospedantes en los que (i) el centroide de la configuración $4f^{n-1}5d^1$ se desplace a energía bajas (efecto nefelauxético, debido a un aumento de la covalencia) y/o (ii) el campo del ligando sea fuerte, disminuyendo la energía del nivel más bajo (emisor) de la configuración $4f^{\,n-1}5d^1$. Desafortunadamente, como se muestra a continuación, esto ocurre con pocos materiales hospedantes. Una alternativa es el uso de iones activadores que emitan en la región roja aprovechando transiciones intra-configuracionales. Por ejemplo, Eu^{3+} y Mn^{4+} proporcionan luminiscencia a través de transiciones $4f$-$4f$ y $3d$-$3d$, respectivamente que, como se mencionó anteriormente, están prohibidas y, por tanto, son débiles, lo que se aleja de la idealidad en términos del rendimiento del sistema.

Como se procedió anteriormente, se discutirán en primer lugar los anfitriones más tradicionales (fosfatos, silicatos y boratos), considerando después molibdatos, volframatos, niobatos y tantalatos, que constituyen hospedantes relativamente comunes para Eu^{3+}, finalizando con otras composiciones (especialmente, nitruros y oxinitruros).

Aunque es conocido que el Eu^{2+} hospedado en fosfatos muestra bandas de emisión ubicadas en las regiones NUV, azul y verde, los difosfatos $Cs_2CaP_2O_7$ y $Cs_2SrP_2O_7$, dopados con de Eu^{2+} (~1%), se caracterizan por bandas de emisión relativamente agudas centradas a 601 y 567 nm, respectivamente; es decir, en las regiones espectrales naranja y amarilla [85]. Los espectros de excitación en ambos materiales muestran bandas características que se extienden de 300 a 450 nm y de 200 a 300 nm, respectivamente. Los borofosfatos $MBPO_5$ (M = Ba, Sr, Ca) dopados con Bi^{2+} han sido propuestos como luminóforos naranjas y rojos para pcLEDs [86], ya que los espectros de emisión presentan bandas fuertes centradas a 650-660 nm con hombros a longitudes de onda más altas, mientras se detectan amplias bandas de excitación a 350-450 nm (con bandas más débiles a mayor longitud de onda, cerca de 600 nm, y a longitud de onda más baja, cerca de 370 nm). La fuerte absorción en el azul facilita que estos materiales puedan ser útiles como luminóforos rojos adecuados para SSL.

En los materiales $Lu_2CaMg(Si,Ge)_3O_{12}$ dopados con Ce^{3+} [87], este catión da lugar a luminiscencia que se localiza más claramente en el rojo que la emisión de los tradicionales granates basados en Al. Por ejemplo, $(Lu_{0.94}Ce_{0.06})_2CaMgSi_{2.2}Ge_{0.8}O_{12}$ da lugar a una banda ancha con un pico aproximadamente a 600 nm con excitación a 470 nm. En $Ca_3Tb_{2x}Eu_xSi_3O_{12}$ (x = 0-2) [88] la emisión 4*f*-4*f* del Eu^{3+} (un pico agudo a 612 nm) se produce a partir del nivel excitado $^5D_0$, aunque esta emisión eficiente es difícil de excitar debido a la pequeña sección transversal de absorción de la transición 4*f*-4*f* del dopante. Sin embargo, en las composiciones x = 0.02-0.10, la luminiscencia $^5D_0$ puede ser sensibilizada eficientemente por el Tb^{3+}, lo que hace viable un chip NUV para excitar eficientemente las emisiones rojas. Algo semejante sucede para $Sr_3Tb_{0.9}Eu_{0.1}(PO_4)_3$ [89] y $Ba_2Tb(BO_3)_2Cl:Eu$ (donde coexisten Eu^{2+} y Eu^{3+}) [90].

Existe un buen número de artículos en los que se estudian las propiedades luminiscentes de oxosales de metales de transición (en particular, molibdatos, wolframatos, niobatos y tantalatos) contiendo cationes Eu^{3+} [91-107]. En todos ellos, la luminiscencia es debida al nivel de $^5D_0$ de este ion, que tiene un pico agudo localizado a 610-620 nm; es decir, en la región roja pura (de hecho, Y_2O_3 y YVO_4 dopados con Eu^{3+} han sido empleados como luminóforos rojos durante mucho tiempo [108,109]). Además, se ha demostrado que el luminóforo rojo óptimo para un pcLED blanco cálido, con alta eficacia luminosa y CRI alto, debe tener una banda de emisión estrecha entre 615 y 655 nm [4,110]. Estas condiciones las cumple la banda $^5D_0 \rightarrow {}^7F_2$. En principio, NUV y chips azules pueden excitar al Eu^{3+}, aunque sus bandas de absorción (con máximos a 395 y 465 nm) poseen secciones transversales de absorción bajas como consecuencia de ser debidas a transiciones 4*f*-4*f* ($^7F_0 \rightarrow {}^5L_6$ y $^7F_0 \rightarrow {}^5D_2$, respectivamente). Intuitivamente, el rendimiento del luminóforo debería aumentar al hacerlo la concentración de Eu^{3+}, ya que esto debería conducir a un aumento en la población del nivel de emisión y, por lo tanto, a una mayor intensidad de emisión. Sin embargo, este no es el caso, ya que una mayor concentración de iones activadores suele llevar aparejada una disminución de la QE de la emisión como consecuencia de la activación de procesos de transferencia de energía que involucran los estados excitados del Eu^{3+} y a la despoblación de forma no radiante de los niveles de emisión de luz [111]. Por otro lado, los procesos de transferencia de energía entre los iones Eu^{3+} están condicionados por el valor de la distancia interiónica [112]. Si los iones radiantes están separados por aniones voluminosos, se pueden conseguir QE elevadas incluso para huéspedes totalmente concentrados (así, se han obtenido buenos resultados para molibdatos concentrados en Eu^{3+} [91]).

Se ha propuesto el desarrollo de luminósforos rojos para pcLEDs basados en Mn^{4+} en coordinación octaédrica como ion dopante [77] como consecuencia de que el ion Mn^{4+} ($3d^3$), en entorno octaédrico, presenta una transición de espín permitida $^4A_2 \rightarrow {}^4T_2$, de paridad prohibida, que coincide con la excitación en regiones espectrales violeta o azul, y una transición de emisión $^2E \rightarrow {}^4A_2$ con un perfil nítido y un pico alrededor de 632 nm en anfitriones tipo fluoruro [113]. Así, debido a sus intensas (y anchas) bandas de excitación en el azul y agudos picos de emisión en el rojo, se ha sugerido que $K_2SiF_6:Mn^{4+}$ es un material adecuado para ser utilizado en pcWLEDs fabricados con $YAG:Ce^{3+}$ (amarillo) y LEDs azules para obtener una emisión de luz blanca cálida [114]. Un comportamiento semejante se observa en $K_2TiF_6:Mn^{4+}$ [115]. $K_2TiF_6:Mn^{4+}$ y $K_2SiF_6:Mn^{4+}$ muestran valores de QE similares a los granates comerciales dopados con Ce^{3+} [116]. Otros materiales de esta familia (Na_2SnF_6, Cs_2SnF_6, Cs_2SiF_6, Cs_2GeF_6, $KNaSiF_6$), todos ellos dopados con Mn^{4+} [117-120] emiten en la región roja, habiéndose extendido este comportamiento a hospedantes tipo óxido (por ejemplo, $SrGe_{3.495}Mn_{0.005}Si_{0.5}O_9$ [121]).

El $CaSiN_2:Ce^{3+}$ [122] posee un perfil de emisión de banda ancha que se extiende de 550 a 700 nm (máximo a 625 nm), mientras la excitación alcanza un máximo a 535 nm, aunque abarca la región 425-575 nm. La sustitución de Ca por Mg o Sr, y de Si por Al, permite alterar los máximos de emisión/excitación, confirmando el potencial de estos luminóforos en combinación con un LED azul. El nitruro $SrAlSi_4N_7$ ha sido propuesto como anfitrión de Ce^{3+} e Yb^{2+} [123]. El material conteniendo Ce^{3+}, ocupando posiciones cristalográficas del Si, y co-dopado con Li^+ para compensar la carga, se caracteriza por una amplia banda de emisión en el rango 450-700 nm (pico a 500 nm) y un complejo espectro de excitación dominado por bandas anchas centradas en 275 y 425 nm. Por otro lado, $SrAlSi_4N_7:Yb^{2+}$ da lugar a un único pico a 600 nm con excitación en la región 325-500 nm. Estos materiales basados en $SrAlSi_4N_7$ emiten luz amarilla-roja (Ce^{3+}) y roja (Yb^{2+}), habiendo sido propuestos para su uso comercial como pcLEDs. $CaAlSiN_3:Eu^{2+}$ [124,125] puede excitarse de manera efectiva utilizando GaN azul y chips NUV-InGaN-LED y exhibe una amplia banda de emisión que alcanza un máximo a 650 nm. Para intentar resolver el problema de deficiencia de color rojo para algunos tipos de pcWLEDs, se produjo un dispositivo constituido por biláminas de $CaAlSiN_3:Eu^{2+}$ (rojo) y $YAG:Ce^{3+}$ (amarillo) acopladas a un InGaN-LED [126]. $Sr_2Si_5N_8:Eu^{2+}$ [127] puede ser sintetizado en estado sólido, de forma simple y barata, con elevados rendimientos, y propiedades luminiscentes comparables al material preparado por métodos tradicionales. El espectro de excitación presenta una banda fuerte y amplia en el rango 200-600 nm, mientras la banda de emisión se centra en 618 nm bajo excitación a 450 nm. La emisión se vuelve más roja a medida que aumenta la concentración de Eu, aunque el espectro de excitación no se ve afectado significativamente. Tanto en $CaAlSiN_3:Eu^{2+}$ como en $Sr_2Si_5N_8:Eu^{2+}$ la intensidad de emisión es cercana al 90% desde RT hasta 150 ºC, sugiriendo una estabilidad térmica prometedora para el brillo de su luz, por lo que ambos materiales podrían ser útiles en aplicaciones SSL. Cuando el β-SiAlON se activa con Pr^{3+} [128] la excitación se produce a 460 nm (transición 4*f*-4*f*, $^3H_4 \rightarrow {}^3P_2$), mientras el espectro de emisión de la muestra $Si_{5.9}Al_{0.1}O_{0.1}N_{7.9}:Pr_{0.016}$ está dominado por varias bandas agudas en la región 600-660 nm, atribuidas a las transiciones 4*f*-4*f* que se originan en los niveles $^1D_2$ (a $^3H_4$) y $^3P_0$ (a $^3H_6$ y $^3F_2$). A temperaturas superiores a la ambiente, las bandas de emisión de $^3P_0$ se vuelven más débiles, aumentando la intensidad de las $^1D_2$, debido a una relajación no radiativa $^3P_0 \rightarrow {}^1D_2$. Esto hace que la intensidad de emisión aumente hasta 423 K, y luego disminuya ligeramente hasta 573 K. Sin embargo, las coordenadas de color de la emisión solo cambian de (0.69, 0.31) a 298 K a (0.68, 0.31) a 573 K. Así, la elevada estabilidad térmica del β-SiAlON:Pr^{3+}, a pesar de que la sección transversal de absorción es relativamente baja para la excitación, lo convierte en una interesante alternativa para los luminóforos pcLED de emisión roja.

Los calcogenuros $Ca_{1-x}Sr_x(S_ySe_{1-y}):Eu^{2+}$ [129], tras excitación a 460 nm, dependiendo de los valores de x e y, emiten en rangos espectrales rojo, naranja o amarillo. Por otro lado, se ha propuesto el oxisulfuro CaZnOS, dopado con Eu^{2+} como luminóforo rojo con excitación azul [130], mientras los materiales $Ca_{1-x}Eu_xZnOS$, cuando x = 0.04, presentan un comportamiento óptimo en términos de intensidad de emisión (excitación a 400-600 nm, emisión a ~650 nm).

1.2. Coordinación y Reactividad del Dinitrógeno

El nitrógeno molecular (N_2) es el gas más abundante en la atmósfera terrestre pero, tradicionalmente, su baja reactividad ha obstaculizado su uso como precursor de compuestos nitrogenados. Aunque el proceso Haber-Bosch para la producción de amoníaco está activo desde hace más de 100 años, sigue siendo el único que utiliza N_2 como materia prima a escala industrial [131]. Después de todo este tiempo, la ausencia de nuevos procesos competitivos para la transformación de N_2 es un claro testimonio de la dificultad del uso de esta molécula, abundante pero inerte, en un contexto industrial [132,133]. Sin embargo, el interés en el estudio de la forma de activación del dinitrógeno ha seguido floreciendo en la literatura más reciente y, probablemente, uno de los principales estímulos para continuar en esta dirección lo ha proporcionado la notable disparidad en las condiciones de reacción utilizadas para la conversión catalítica del dinitrógeno en amoníaco en la industria, en comparación con las utilizadas por la Naturaleza. Por un lado, el proceso original de Haber y sus posteriores mejoras [134,135] implican el uso de condiciones duras para lograr la transformación catalítica sintética del dinitrógeno. Por otro lado, la enzima nitrogenasa completa la tarea de forma mucho más elegante, en condiciones particularmente suaves, y sin necesidad de aporte de hidrógeno gaseoso [136-138]. La gran diversidad de condiciones de operación, junto a la escasa química del dinitrógeno, proporciona un desafío intelectual y un potente estímulo para intentar comprender los factores que permiten que un centro metálico interactúe con una molécula extremadamente estable como es el N_2.

La coordinación del N_2 con algunos centros metálicos proporciona una manera de superar la inercia intrínseca de la molécula de dinitrógeno, habiéndose descrito la síntesis de un buen número de compuestos nitrogenados a partir de N_2 previamente coordinado. Así, se han desarrollado algunos sistemas moleculares que, en fase homogénea, catalizan la producción de amoníaco a partir de N_2 [139-142]. Aunque estas reacciones no son viables industrialmente, su estudio detallado es crucial para identificar aspectos importantes en el problema de la reducción de N_2, entre los que destaca el entorno de coordinación del dinitrógeno. En este sentido, es interesante recordar que la Naturaleza ha elegido al ligando carburo para situarse en el centro del cofactor (componente no proteico, termoestable y de baja masa molecular, necesario para la acción de una enzima) que provoca la activación de las enzimas nitrogenasas [143-145], en las que el proceso de fijación del N_2 aparentemente transcurre con formación de dihidrógeno y amoníaco, implicando híbridos de hierro como intermediarios [146,147]. La reducción catalítica en condiciones moderadas realizada por la enzima nitrogenasa es el primer paso en una cadena de transformaciones que conduce a la incorporación de átomos de nitrógeno a los sistemas vivos. Estos hechos, indudablemente, impulsan la investigación en la dirección del uso del dinitrógeno como materia prima para la producción de productos químicos básicos (por ejemplo, fertilizantes) [148-149].

La familia, cada vez más numerosa, de complejos de coordinación de N_2 aislables exhibe varios modos de unión que, en algunos casos particulares, facilitan transformaciones catalíticas o estequiométricas de la especie N_2.

La elevada estabilidad de la molécula N_2 (energía de disociación: 945 kJ/mol) y su gran separación HOMO-LUMO (estimada en ~23 eV, con una elevada energía de activación para cualquier proceso químico que involucre a esta molécula) plantean un doble desafío en: (i) controlar las etapas que conducen a la coordinación del N_2 y las posteriores transformaciones químicas elementales (escisión, protonación, transferencia de nitrógeno), y (ii) buscar procesos que permitan la incorporación de nitrógeno a moléculas orgánicas. En este contexto, existen tres direcciones principales en las que se pueden clasificar los desarrollos actuales en este campo: (i) coordinación de dinitrógeno, (ii) escisión de dinitrógeno y transformaciones elementales que involucran nitruros y unidades relacionadas, y (iii) incorporación de dinitrógeno en sustratos orgánicos.

1.2.1. Modos de Enlace del N_2

Una cuestión central, común a áreas de investigación tan diversas como la fijación biológica de nitrógeno, la formación de amoníaco industrial o estudios de modelos de activación en moléculas pequeñas, es la forma en el que la molécula N_2 interactúa con los metales de transición (incluyendo al cofactor FeMo, superficies metálicas heterogéneas, y complejos metálicos discretos) [150].

La molécula de dinitrógeno puede coordinarse con uno o más centros metálicos. La coordinación al centro metálico puede ser lábil o extremadamente robusta, sin que esto implique necesariamente un mayor grado de capacidad de reducción del dinitrógeno. La Figura 4 recoge los modos de coordinación aceptados para el N_2 [151-155], que se han utilizado habitualmente para discutir el grado de activación del N_2 coordinado en función de la longitud del enlace N–N, aunque obviando la mayor parte de las veces la especificidad de su entorno de coordinación. Sin embargo, estudios recientes correlacionan el modo de unión del N_2, y no necesariamente su distancia de enlace, con el grado de activación que es capaz de proporcionar cada material [156-158].

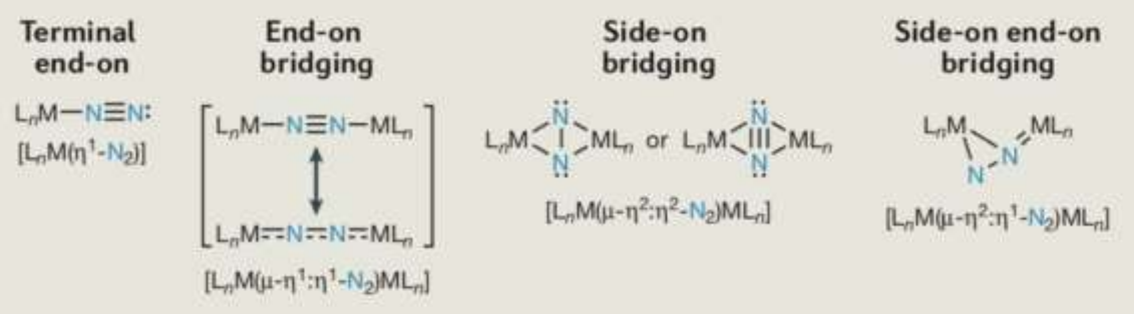

Fig. 4. Modos comunes de coordinación del N_2 a metales de transición [150]. En la notación μ^n-η^m, n es el número de metales unidos a través de la especie N_2 (usualmente, μ^2 se abrevia como μ), mientras m es el número de átomos de la molécula N_2 que interaccionan con un mismo metal.

El descubrimiento del primer modo de enlace del N_2 se remonta a 1965, conocido como terminal (*terminal end-on*) (M–N≡N), habiendo sido descrito en un complejo catiónico de rutenio, $[Ru(NH_3)_5(N_2)]^{2+}$ [159]. Para el N_2, éste es el modo de enlace prevalente [160], seguido de cerca por el modo puente terminal (*end-on bridging*) (M–N≡N–M) [161-163]. El doble puente lateral (*side-on bridging*) es un modo de coordinación del N_2 descrito más recientemente [154,164-166]. El modo de coordinación de puente mixto terminal/lateral (*side-on end-on bridging*) también es poco común [158,167,168].

Probablemente, los complejos de wolframio mononucleares estables sean los materiales de partida más versátiles para la incorporación paso a paso de N_2 en sustratos orgánicos [148,149]. Evidentemente, la coordinación de una molécula a un centro metálico perturbará su estructura electrónica, promoverá su activación, y facilitará posibles transformaciones posteriores por reacción con agentes externos u otros ligandos coordinados. Debido a su naturaleza inerte cuando está aislada, esto es particularmente relevante para la molécula N_2.

1.2.2. Activación del N_2

La elucidación de los requisitos estructurales y electrónicos para la activación de la molécula de dinitrógeno mediante centros metálicos, que permitirá reducir las barreras de energía que facilitarán la ruptura del enlace N≡N y la formación eficiente de productos que contengan nitrógeno a través de reacciones de funcionalización de sus átomos individuales (procesos que, colectivamente, constituyen la fijación de dinitrógeno) sigue siendo un desafío académico importante que, además, si se consiguiese de forma eficiente, tendría un enorme impacto social [169-184].

En el ámbito de los compuestos de coordinación, durante las últimas dos décadas, la química del dinitrógeno ha experimentado un gran progreso en términos de su activación [185-190] y transformación [191-202], estando relativamente bien establecida la forma en que esta molécula extremadamente estable puede escindirse y protonarse [172,203]. Así, la coordinación multimetálica con metales iguales o diferentes proporciona una estrategia viable para la reducción, escisión y transformación del dinitrógeno. La escisión de la especie N_2 en nitruros [204-213] precede a la hidrogenación, que puede transcurrir de tres formas: (i) protonación del nitruro durante la hidrólisis o protonólisis [185,191-201,203], (ii) reacción de formas reducidas de dinitrógeno coordinado con hidrógeno gaseoso [194,214-218], y (iii) ataque de hidruros [205,219-224].

Al intentar la síntesis de nuevas estructuras de fragmentación (sintones) de torio (elemento muy difícil de reducir [225-228]) se obtuvo fortuitamente una unidad Th–NH_2 [229,230]. Los estudios de marcaje isotópico indicaron que el átomo de nitrógeno procedía de la molécula N_2, mientras que el disolvente era la fuente de átomos de hidrógeno. En otras palabras, al canalizar electrones hacia un elemento con escasa tendencia a ser reducido fue posible, no solo disociar el dinitrógeno, sino también provocar que los fragmentos reducidos extraigan átomos de hidrógeno del disolvente. Posteriormente se demostró que otros elementos del bloque *f* presentan un comportamiento semejante [210,231-239].

Usualmente, se acepta que la interacción fuerte entre el dinitrógeno y dos centros metálicos es esencial para la activación de la molécula y su posterior reducción, como sucede en complejos de zirconio [240] y samario [241], con largas distancias N–N para las unidades N_2 en configuración de doble puente lateral (1.548 y 1.525 Å, respectivamente). Sin embargo, existen algunos ejemplos en los que la reactividad se manifiesta en complejos donde la distancia N–N es solamente ligeramente superior a la del N_2 libre. Por ejemplo, en $[(Cp^*{}_2Sm)_2N_2]$ ($Cp^* = \eta^5\text{-}C_5Me_5$) [165], donde N_2 también adopta el modo de unión de doble puente lateral, la distancia N–N es muy corta (1.088 Å), lo que sugiere que el triple enlace permanece casi inalterado como resultado de una débil coordinación con los centros metálicos.

La búsqueda de sistemas capaces de realizar la escisión de dinitrógeno es objeto de gran interés como consecuencia de que los nitruros metálicos son restos reactivos que permiten la transferencia del nitrógeno a sustratos orgánicos. Para ello, es necesario identificar las características de los complejos metálicos que hacen posible la ruptura del triple enlace N≡N. Dado que son necesarios seis electrones para realizar esta transformación de forma estequiométrica, la disociación se puede realizar por dos rutas diferentes: (i) ataque cooperativo de dos o más metales en la misma unidad N_2, y (ii) inmovilización del dinitrógeno entre dos o más metales de transición, seguida del ataque de un reductor externo. Esta última vía es especialmente interesante a consecuencia de la polarización que puede inducirse en el N_2 coordinado [151]. Por ejemplo, algunos complejos de molibdeno y niobio son capaces de realizar la escisión térmica [209], fotoquímica [211] e incluso espontánea [213,242,243] de N_2.

Otra estrategia exitosa para avanzar en este campo ha sido utilizar fragmentos de metales de transición de valencia baja para reducir formalmente el dinitrógeno coordinado formando puentes en complejos dinucleares de fórmula general $[LnM]_2(\mu\text{-}N_2)$ (Fig. 5) [169-171,244]. Las distancias N–N en estos complejos dinucleares, que van desde 1.20 a 1.65 Å, en relación a la de la molécula libre (1.0971 Å) [245], revelan que la extensión de la activación del dinitrógeno depende en gran medida de la naturaleza de los ligandos metálicos enlazados al N_2 y el tipo de puente que adopta la coordinación del dinitrógeno. Por otro lado, $[Na(dme)_3][(LTi)_2(\mu\text{-}NH)(\mu\text{-}N)]$ y $[Na(dme)_3]_4[\{LNa\}_2][(LTi)_2(\mu\text{-}N)_2]\cdot 2dme$ (dme = 1,2-dimetoxietano; L = 2,5-$\{(C_4H_3N)CPh_2\}_2C_4H_2N(Me))$ [176], dos compuestos obtenidos a partir del complejo LTiCl [246], presentan una unidad plana Ti_2N_2 con distancias interatómicas Ti···Ti sustancialmente diferentes entre ambos complejos, mientras que las distancias de enlace Ti–N son bastante similares (Fig. 6).

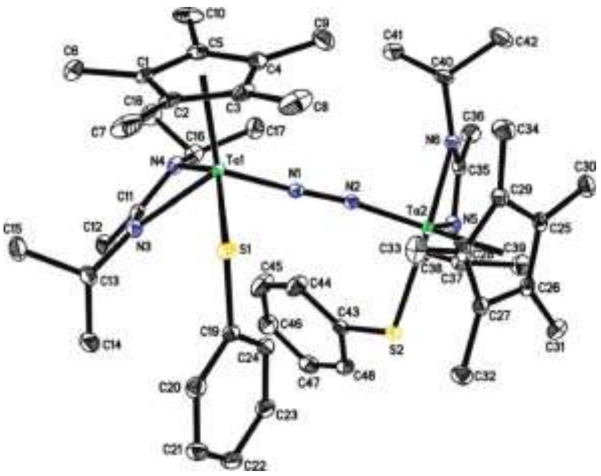

Fig. 5. Estructura molecular de $\{Cp^*Ta[N(^iPr)C(Me)N(^iPr)](SPh)\}_2(\mu\text{-}\eta^1\text{:}\eta^1\text{-}N_2)$. Longitudes de enlace seleccionadas (en Å): Ta1–N1 1.831, Ta2–N2 1.837, N1–N2 1.297 [244].

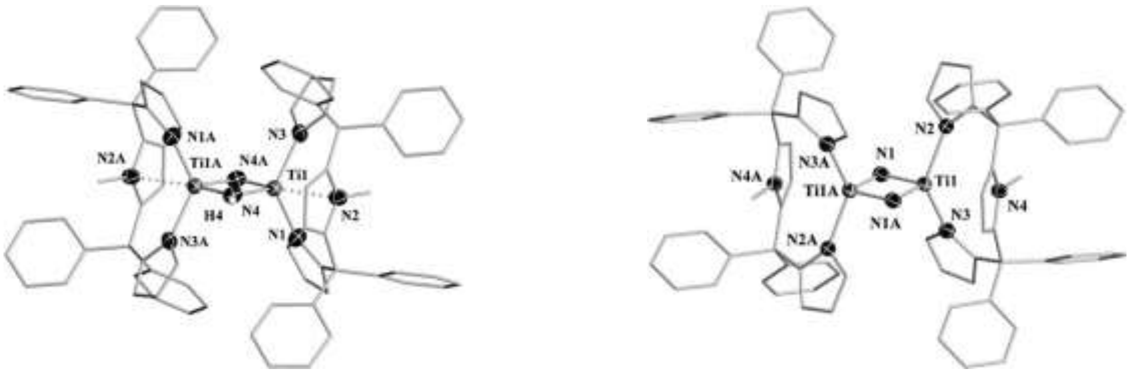

Fig. 6. Estructuras moleculares de $[Na(dme)_3][(LTi)_2(\mu\text{-}NH)(\mu\text{-}N)]$ (**a**, izquierda) y $[Na(dme)_3]_4[\{LNa\}_2][(LTi)_2(\mu\text{-}N)_2]\cdot 2dme$ (**b**, derecha). Longitudes de enlace seleccionadas (en Å) para (**a**) Ti1···Ti1A 2.786, Ti1–N4A 1.837, Ti1–N4 1.878, y (**b**) Ti1···Ti1A 2.642, Ti1–N1 1.812, Ti1–N1A 1.810 [176].

Una nueva estrategia para la fijación de dinitrógeno, incluida su coordinación y posterior reactividad, sería la utilización de materiales microporosos accesibles a la molécula N_2, con centros metálicos intra-cristalinos suficientemente activados para que sobre ellos se produzca quimisorción molecular. En la Figura 7 se presenta la estructura cristalina de un material con esta potencialidad [247], con canales unidimensionales que, en su forma anhidra, poseen átomos de titanio pseudo-tetraédricos demasiado alejados entre sí para que el N_2 interaccione simultáneamente, en configuración de doble puente lateral (véase Fig. 6, donde los átomos metálicos involucrados distan aproximadamente 3 Å), con centros activos de paredes enfrentadas en el canal, pero que se sitúan a una distancia adecuada para que pueda ser posible la coordinación en configuración de doble puente terminal (véase Fig. 5, donde la distancia entre los centros metálicos se encuentra en el rango de los 5 Å).

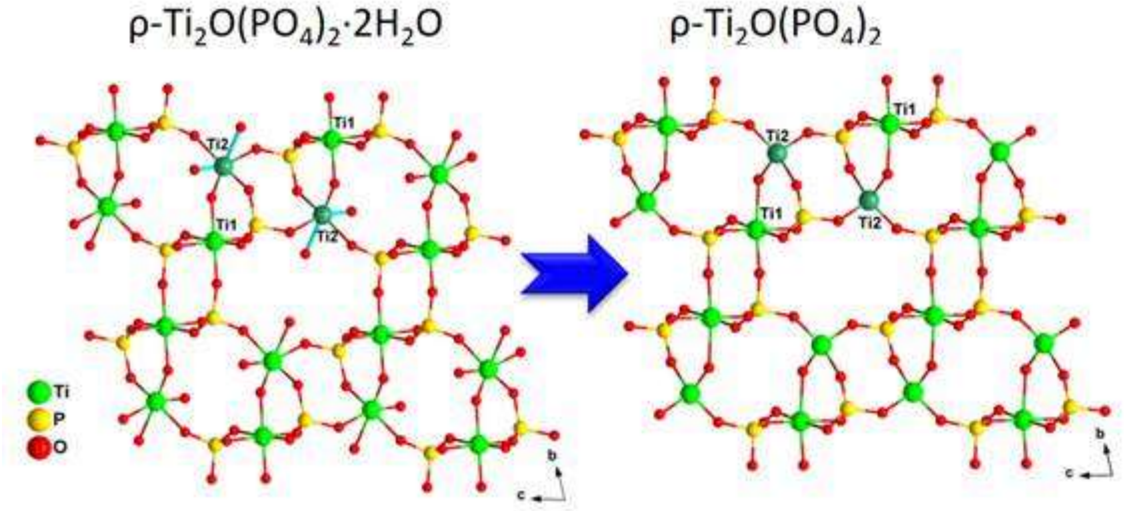

Fig. 7. Estructuras cristalinas de las formas dihidratada y anhidra de un oxofosfato de titanio de morfología fibrosa, con dos tipos de canales unidimensionales extendidos en la dirección del eje *a*. En la forma anhidra, la distancia entre dos átomos de titanio tetra-coordinados (Ti2···Ti2) es corta (4.352 Å) o larga (5.084 Å) en función de que el tipode canal, definido por poliedros $PO_4/TiO_4/TiO_6$ compartiendo vértices, esté constituido por seis u ocho miembros, respectivamente [247].

1.3. Fosfatos Laminares de Metales Tetravalentes

Las variedades amorfas de los fosfatos ácidos de metales tetravalentes se conocen desde hace mucho tiempo, habiendo sido investigadas intensamente entre los años 1955 y 1965, especialmente por su uso potencial como intercambiadores de iones inorgánicos en procesos a altas temperaturas y/o bajo dosis masivas de radiación ionizante [248]. Sin embargo, la historia más actual de estos materiales comenzó en 1964, cuando Clearfield y Stynes cristalizaron por primera vez la variedad α del fosfato de circonio (α-ZrP) mediante reflujo de un gel amorfo en ácido fosfórico [249]. Cuatro años más tarde, en el mismo laboratorio, se obtuvo una segunda fase cristalina, la variedad γ [250]. Ambos compuestos poseen hábito laminar. En el hidrógenofosfato de circonio(IV) monohidratado, $Zr(HPO_4)_2{\cdot}H_2O$ (α-ZrP), cada capa está constituida por un plano de átomos de circonio (Fig. 8), unidos por grupos hidrógenofosfato, situados alternativamente por encima y por debajo del plano definido por los átomos de Zr [251]. Tres átomos de oxígeno del grupo hidrógenofosfato están unidos a tres átomos de Zr diferentes, mientras cada circonio está coordinado octaédricamente por seis oxígenos. Los grupos –OH de cada grupo hidrógenofosfato se orientan perpendicularmente al plano de átomos de Zr, formando enlaces de hidrógeno con las moléculas de agua de cristalización alojadas en la región interlaminar [252], mientras las láminas se mantienen unidas por interacciones tipo van der Waals, generando capas compactas con un espaciado basal de 7.56 Å (Fig. 9).

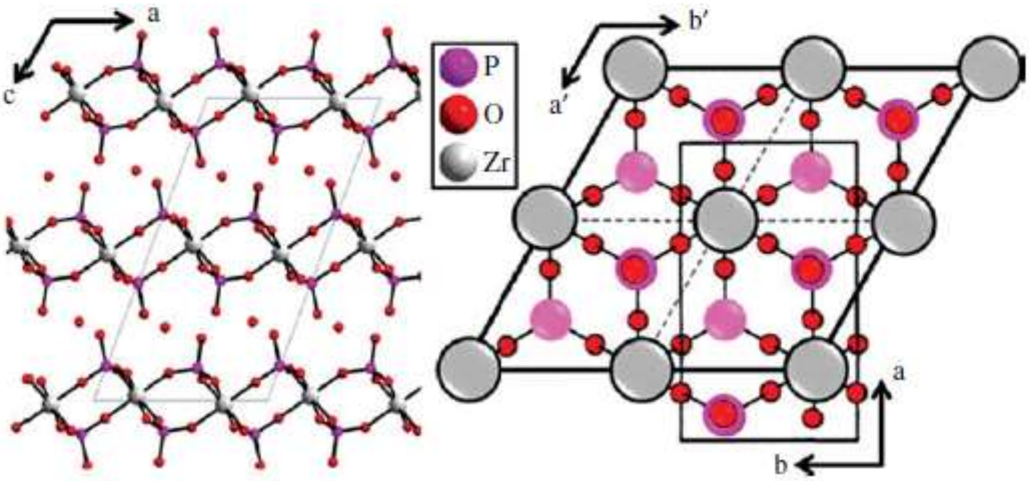

Fig. 8. Representación esquemática de la estructura cristalina del α-ZrP [249].

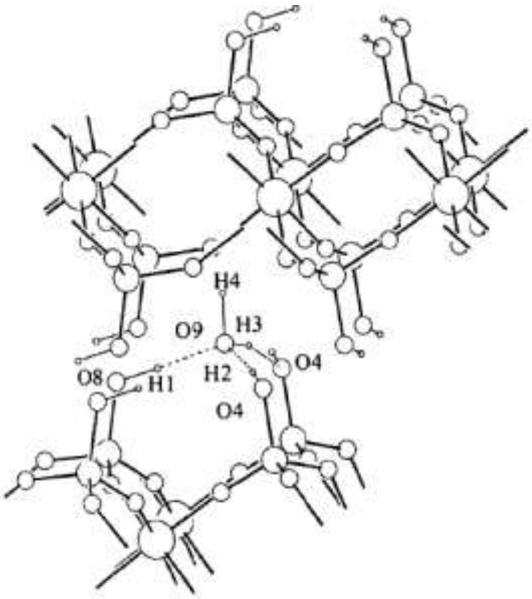

Fig. 9. Detalle de los enlaces de hidrógeno intralaminares en las α-fases [252].

A finales de la década de 1980, se produjo un salto adicional en este campo de trabajo, al descubrirse que el γ-fosfato de circonio, a diferencia del bis(monohidrógeno)fosfato de circonio, debe formularse como un fosfato-dihidrógenofosfato, $Zr(PO_4)(H_2PO_4)\cdot 2H_2O$ [253-255]. Su estructura cristalina [256,257] muestra que los átomos de Zr y los grupos ortofosfato están ubicados casi en el mismo plano. La coordinación octaédrica del Zr se consigue con cuatro átomos de oxígeno del grupo ortofosfato y dos átomos de oxígeno del grupo dihidrógenofosfato. Los dos oxígenos restantes del grupo dihidrógenofosfato se unen a protones y se proyectan hacia el espacio interlaminar. Estos grupos hidroxilo están unidos por enlaces de hidrógeno a las moléculas de agua que, a su vez, interaccionan entre sí mediante enlaces de hidrógeno para formar cadenas en zigzag (Fig. 10) en el espacio interlaminar (d = 12.27 Å).

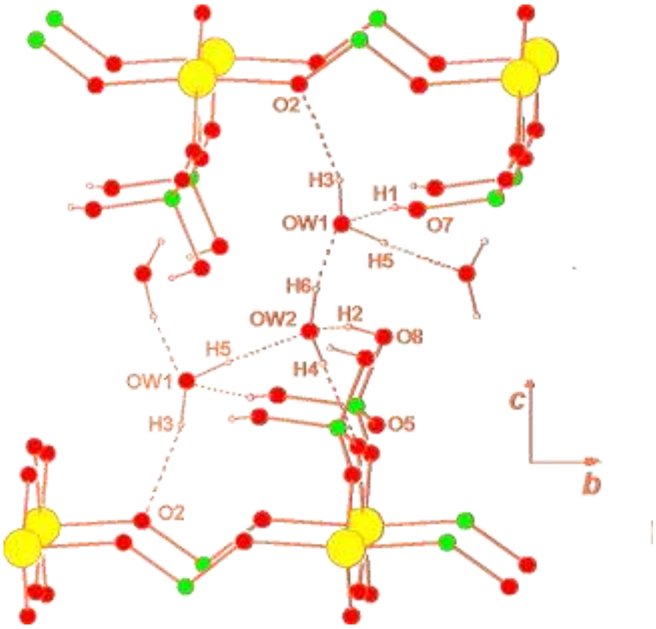

Fig. 10. Representación esquemática de la estructura cristalina del γ-ZrP (Zr: amarillo, P: verde, O: rojo), detallando el entramado interlaminar de enlaces de hidrógeno que conecta las láminas adyacentes a través de moléculas de agua [257].

La descripción de los primeros fosfonatos de metales M^{IV} con estructuras laminares íntimamente relacionadas con las del α-ZrP [258], junto a la posibilidad de relacionar las propiedades de las sales ácidas de metales tetravalentes con su estructura cristalina, así como sus numerosas aplicaciones potenciales en campos como el intercambio iónico, la intercalación, la catálisis y la conductividad iónica, estimularon una gran variedad de investigaciones sobre esta clase de compuestos [259-261].

1.3.1. Síntesis y Propiedades

Además de refluyendo ZrP amorfo en ácido fosfórico, el α-ZrP también se sintetizó a partir de disoluciones que contienen complejos solubles de circonio(IV) y un exceso de ácido fosfórico a una temperatura de ~80 °C [262,263]. Los agentes complejantes más habituales fueron iones fluoruro y oxalato. En estas condiciones, la velocidad de descomposición de los complejos de Zr(IV) es lenta, originándose materiales altamente cristalinos de dimensiones micrométricas (5-10 µm cuando se usa fluoruro y 2-3 µm en presencia de oxalato).

En exceso de ácido fosfórico, el α-ZrP puede obtenerse por precipitación directa de sales solubles de circonio(IV) a temperatura ambiente. Los micro-cristales preparados son muy sensibles a la hidrólisis, transformando por lavado con agua en hidroxofosfatos (amorfos o semi-cristalinos) con relación molar P/Zr inferior a dos [264].

También se preparó una forma derivada del α-ZrP, denominada θ-ZrP, en la que, aumentando considerablemente el contenido en agua en el espaciado basal, se mantiene la disposición estructural de la lámina tipo α. θ-ZrP es una forma quasi-hexahidratada del α-ZrP, con una distancia interlaminar de 10.3-10.4 Å. Aunque esta fase fue observada por primera vez en 1969 [265], no fue hasta el final de la primera década del presente siglo cuando se utilizó sistemáticamente en la intercalación de moléculas voluminosas [266-268].

Más recientemente, se ha desarrollado un nuevo enfoque para la síntesis de estructuras de α-ZrP nanocristalino [269]. Mediante la adición de propionato de circonilo a ácido fosfórico en presencia de alcoholes alifáticos, se obtuvieron nano-placas hexagonales (longitud de cada placa ~40 nm) constituidas por una sucesión de láminas tipo α-ZrP intercaladas por el alcohol utilizado en la síntesis. La eliminación del disolvente (T = 60 ºC) origina materiales con un tamaño de partícula variable (longitud = 90-200 nm, grosor = 20-85 nm) en función de la naturaleza del disolvente. Este procedimiento tiene algunas ventajas: (i) no precisa el uso de altas temperaturas y agentes complejantes, y (ii) la intercalación de moléculas de alcohol, en disposición bimolecular, $Zr(HPO_4)_2{\cdot}2ROH$, provoca el aumento de la distancia interlaminar desde los 7.56 Å, característicos del α-ZrP, hasta valores de 14.4 Å, 16.1 Å, o 18.6 Å, cuando ROH = etanol, propanol, o butanol, respectivamente. Esta ampliación del espaciado basal facilitará la intercalación de especies huésped y los procesos de intercambio iónico de especies catiónicas voluminosas. Estos materiales nanométricos poseen una reactividad inusual, ya que sufren una transición de fase a 120 ºC (Fig. 11), no observada en α-ZrP microcristalino, en la que se genera una nueva fase tridimensional (τ'-ZrP), de fórmula $Zr(HPO_4)_2$, constituida por nano-partículas cúbicas, con simetría cristalina tetragonal (en lugar de monoclínica, característica del α-ZrP) y cadenas empaquetadas de anillos de ocho miembros conectando átomos de Zr mediante grupos HPO_4 puente [270].

Los procedimientos de preparación de α-fosfatos laminares (o de sus arseniatos análogos) con otros metales tetravalentes son en gran parte variantes de los utilizados para sintetizar α-ZrP [271,272], siendo destacable que, aunque hasta la fecha no se conocen los α-fosfatos laminares de metales tetravalentes de grandes dimensiones, tales como Ce^{IV} y Th^{IV}, aunque se haya sintetizado un buen número de fosfatos de estos metales en el ámbito de la tecnología nuclear [273-281], la familia de los fosfatos laminares de metales tetravalentes de los grupos 4 y 14 de la Tabla Periódica, α-$M(HPO_4)_2\cdot H_2O$ (M = Ti, Zr, Hf, Ge, Sn, Pb) y γ-$M(PO_4)(H_2PO_4)\cdot 2H_2O$ (M = Ti, Zr, Hf), ha sido objeto de interés continuo en el último medio siglo [252,255,257,282-286].

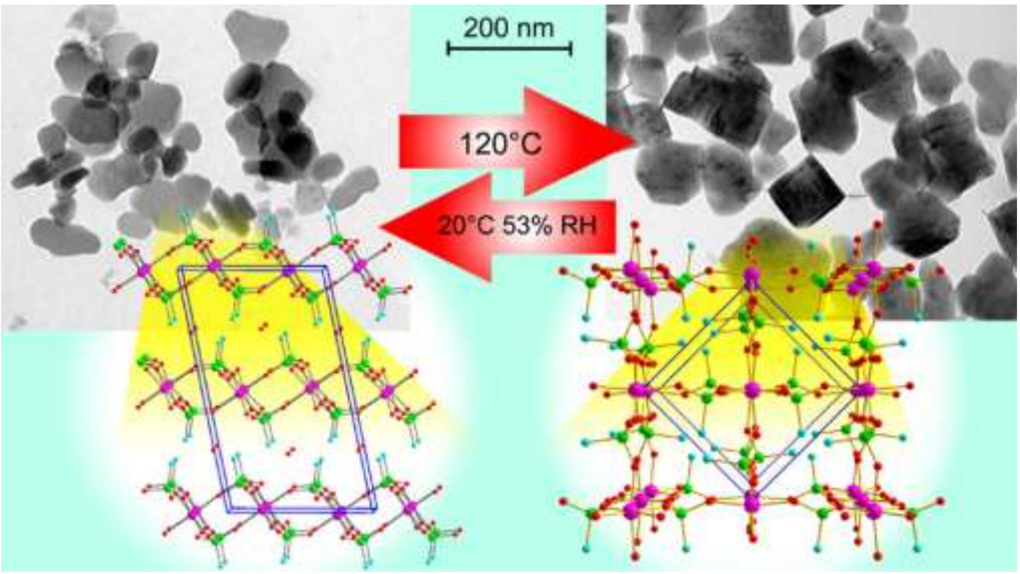

Fig. 11. Morfología y representación esquemática de las estructuras cristalinas de α-ZrP (izquierda) y τ'-ZrP (derecha). La fase α-ZrP transforma térmicamente en τ'-ZrP, mientras τ'-ZrP se convierte en α-ZrP a temperatura ambiente en presencia de vapor de agua [270].

Las variedades α y γ de los fosfatos laminares de metales tetravalentes son intercambiadores de iones inorgánicos que exhiben buena estabilidad térmica y química [259]. El intercambio iónico tiene lugar por difusión de los cationes desde la parte externa del cristal hacia el interior de la lámina, definiéndose un frente de reacción que, avanzando con el tiempo, delimita dos fases cristalinas diferenciadas. Es decir, el proceso tiene lugar con una transición de fase discontinua y, de acuerdo con la regla de las fases, cada etapa se produce a una composición constante de la disolución. A pH ácido, sólo un número limitado de cationes (Li^+, Na^+, Ag^+, Tl^+, Cu^+, Ca^{2+}) pueden sustituir a los protones del α-ZrP con una cinética adecuada. Cationes monovalentes o divalentes de mayor tamaño (NH_4^+, Rb^+, Cs^+, Ba^{2+}) o cationes divalentes y trivalentes altamente hidratados (Mg^{2+}, Cu^{2+}, Cr^{3+}) reemplazan los protones del α-ZrP a temperatura ambiente a velocidades lentas, debido a la alta energía de activación requerida para la expansión de la región interlaminar [260,287-289]. Los compuestos tipo γ muestran menores impedimentos estéricos para la difusión de cationes grandes, siendo especialmente reseñable su afinidad por cationes Cs^+ [290-293].

La química de intercalación del $Zr(HPO_4)_2{\cdot}H_2O$ está dominada por la presencia en la región interlaminar de grupos ácidos tipo Brønsted [294,295]. En consecuencia, las especies con tendencia a ser protonadas son los huéspedes preferidos, habiéndose conseguido la intercalación de grandes moléculas neutras como ciclodextrinas [296] o porfirinas [297] mediante la síntesis previa de compuestos de intercalación con aminas. Además, con procedimientos especiales, también ha sido posible insertar huéspedes con una fuerza básica muy baja, como alcanoles, glicoles, cetonas y amidas [298] y otras muchas especies voluminosas con aplicación en el campo de la liberación controlada de fármacos [299]. Cuando la intercalación es completa, en fases tipo α, las *n*-alquilmonoaminas dan lugar a compuestos que contienen dos moles de amina por mol de metal tetravalente, formando una bicapa de cadenas alquílicas extendidas en la región interlaminar [260,300]. En el caso de las fases γ, la bicapa se forma con proporciones inferiores de amina (1.0-1.3 moles por mol de M^{IV}) [301-305] (Fig. 12). Las alquildiaminas forman una mono-capa de cadenas alquílicas extendidas, con sus grupos $–NH_2$ terminales interaccionando con grupos –POH de láminas enfrentadas [306,307]. Los alcanoles y glicoles adoptan una disposición similar a la de alquilmonoaminas y diaminas, respectivamente [298].

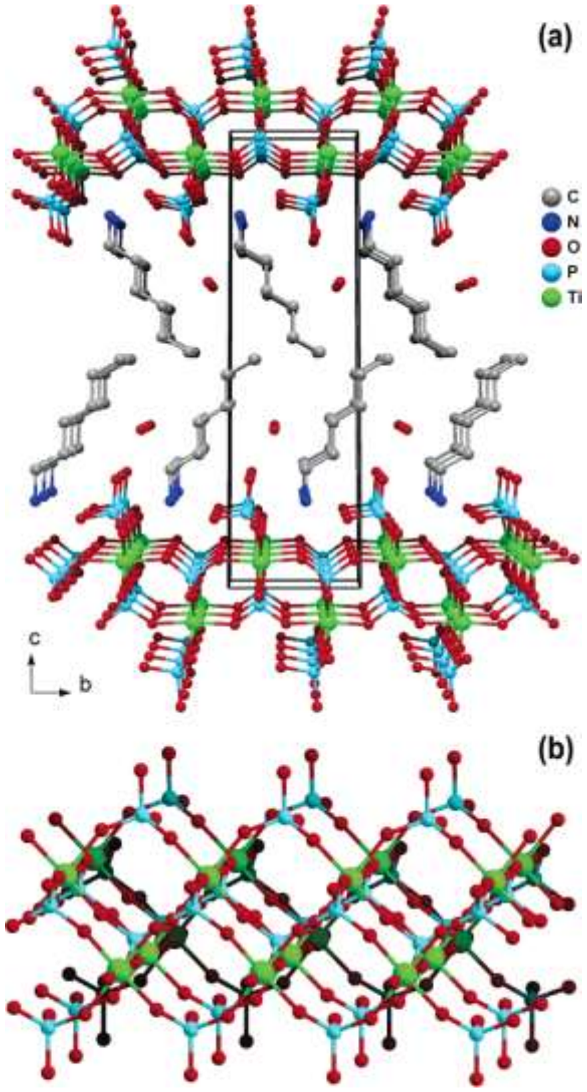

Fig. 12. Representación de la estructura cristalina de un compuesto de intercalación *n*-hexilamina/γ-TiP, $(C_6H_{13}NH_3)[Ti(HPO_4)(PO_4)]\cdot H_2O$ (a), y perspectiva de la capa aniónica bidimensional, $[Ti(HPO_4)(PO_4)]$ (b) [305].

1.3.2. Procesos de Exfoliación

Una propiedad interesante de muchos compuestos laminares es su capacidad para hincharse al insertar agua u otros disolventes entre sus capas. En algunos casos, el grado de hinchamiento puede ser tan grande que los cristales laminares acaban desintegrándose en láminas individuales. Usualmente, la eliminación del disolvente produce la re-agregación de las laminillas para formar películas o membranas delgadas. El α-ZrP y sus formas salinas no se hinchan espontáneamente en agua. Sin embargo, en presencia de disoluciones acuosas de determinadas aminas (especialmente, propil- y butilamina), este compuesto y otros congéneres de la misma familia, exfolian para producir dispersiones coloidales de capas únicas o paquetes constituidos por unas pocas láminas. Cuando la dispersión coloidal del compuesto intercalado se trata con un ácido mineral, puede obtenerse una suspensión de laminillas del fosfato laminar polihidratado, a partir del cual pueden prepararse membranas del material correspondiente [308], que posteriormente puede ser manipulado, mediante hidrólisis controlada de los grupos fosfatos [309], para llevar a cabo reacciones de intercambio topotáctico [63-66], u obtener materiales pilareados por inserción de, por ejemplo, polioxocationes de aluminio o cromo [310-317].

La historia más reciente de las nano-láminas o láminas exfoliadas se inicia en la década de 1950, cuando se observó que los minerales arcillosos tipo esmectita se dispersaban eficazmente en agua, produciendo suspensiones coloidales como consecuencia de su des-laminación espontánea [318-321]. Desde la década de 1970, se ha logrado la exfoliación de una amplia gama de compuestos inorgánicos con estructura en capas, incluidos calcogenuros metálicos, [322-324], fosfatos y fosfonatos metálicos [308,325] y óxidos metálicos laminares [326-335], introduciendo cationes y/o disolventes en su espacio interlaminar. A diferencia de las arcillas esmectíticas, con una baja densidad de carga en su espaciado basal y, como consecuencia, con una interacción débil entre sus laminillas, estos nuevos compuestos estratificados tienen una mayor densidad de carga y requieren modificaciones químicas en su espacio interlaminar para promover artificialmente el proceso de exfoliación [329-335].

El espesor de los cristales resultantes en forma de placas (*sheet-like*) se encuentra en el rango de las dimensiones moleculares (usualmente, alrededor de 1 nm), mientras que la dimensión lateral suele ser micrométrica. El término *nano-sheets* (nano-placas) fue definido y utilizado por primera vez en 1996 en un estudio detallado sobre la exfoliación de óxidos de titanio [330]. Recientemente, el gran interés suscitado por los nuevos desarrollos en nanociencia y nanotecnología ha propiciado la aparición de nanomateriales bidimensionales (*leaf-like*) consecuencia de crecimientos anisotrópicos espontáneos, a los que algunos autores se refieren como *nano-sheets* [336], a pesar de que sus espesores suelen estar muy lejos de ser mono-laminares.

La familia de materiales constituidos por nano-placas ha crecido de forma constante en los últimos años [337]. Además de los óxidos metálicos laminares mencionados anteriormente, útiles como intercambiadores catiónicos, también se han realizado extensas investigaciones sobre la exfoliación de hidróxidos dobles laminares (LDHs, *layered double hydroxides*) con capacidad de intercambio aniónico [338-341], incluyendo la incorporación de metales de transición [342-344] y de transición interna [345-349]. Posteriormente, la irrupción del grafeno ha provocado una fiebre de investigación sin precedentes debido a sus notables propiedades electrónicas [350,351]. El grafeno se produjo inicialmente en 2004 mediante escisión micromecánica de grafito [352]. En comparación con las nanoláminas semiconductoras o aislantes de óxidos e hidróxidos, una buena parte de la fascinación que provoca este material radica en su capacidad para conducir electrones. Su red casi perfecta de átomos de carbono permite que los electrones fluyan a través de él a velocidades ultrarrápidas, lo que permite su uso como banco de pruebas relativamente simple para estudios mecano-cuánticos [353-355]. Posteriormente, entre otros procedimientos, se ha sintetizado grafeno por deposición química de vapores (CVD, *chemical vapor deposition*) en diversos sustratos metálicos, por pirolisis de aerosoles, o por síntesis solvotermal [356,357]. En particular, un método químico para la producción de grafeno en cantidades relativamente grandes, que tiene su origen en investigaciones realizadas en los años 1950-1960 sobre oxidación de grafito en presencia de ácidos fuertes u oxidantes para producir suspensiones coloidales acuosas [358-362], se basa en la exfoliación química de derivados del grafito, como el óxido de grafito (GO, *graphite oxide*) y compuestos de intercalación de grafito (GIC, *graphite intercalation compounds*), que posteriormente se reducen para formar grafeno (es decir, GO reducido) [363,364]. El nitruro de boro laminar (BN, *boron nitride*), estructuralmente análogo al grafito, aunque aislante eléctrico, también puede exfoliarse en nano-hojas ultrafinas, con unas pocas capas atómicas de espesor [365,366].

Como se muestra esquemáticamente en la Figura 13, se pueden sintetizar nano-placas de materiales inorgánicos a partir del compuesto laminar precursor utilizando una disolución exfoliante, con el fin de lograr un alto grado de hinchamiento y, consecuentemente, el debilitamiento de la interacción interlaminar [367]. En general, el proceso de exfoliación depende de la composición y las propiedades químicas de las láminas del material, así como de las fuerzas de interacción que mantienen su disposición apilada. Los factores intrínsecos a considerar serían la composición química de la capa, su densidad de carga, y las especies iónicas que se localizan en el espacio interlaminar, mientras que las propiedades del disolvente usado es un factor extrínseco determinante en el resultado final. Eligiendo adecuadamente las condiciones de operación, se podrá lograr una fase altamente expandida, cuya exfoliación en nano-placas podrá favorecerse con ayuda mecánica (por ejemplo, agitación o uso de ultrasonidos).

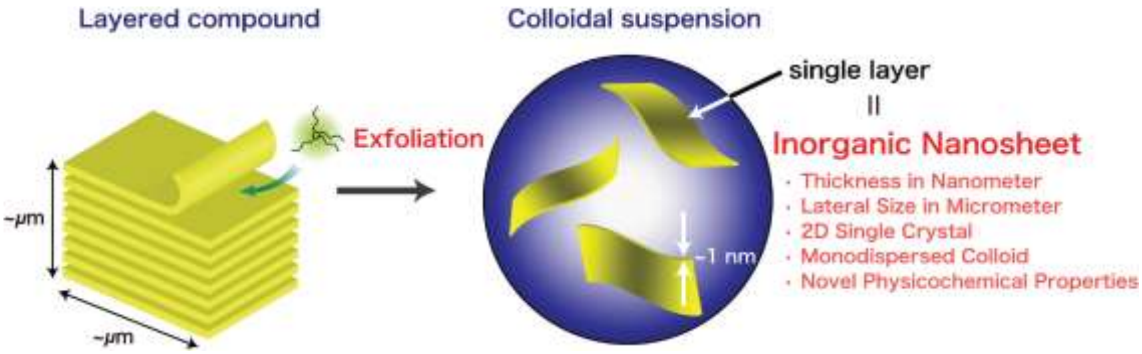

Fig. 13. Esquema ilustrando la exfoliación de un compuesto estratificado en nano-placas coloidales [367].

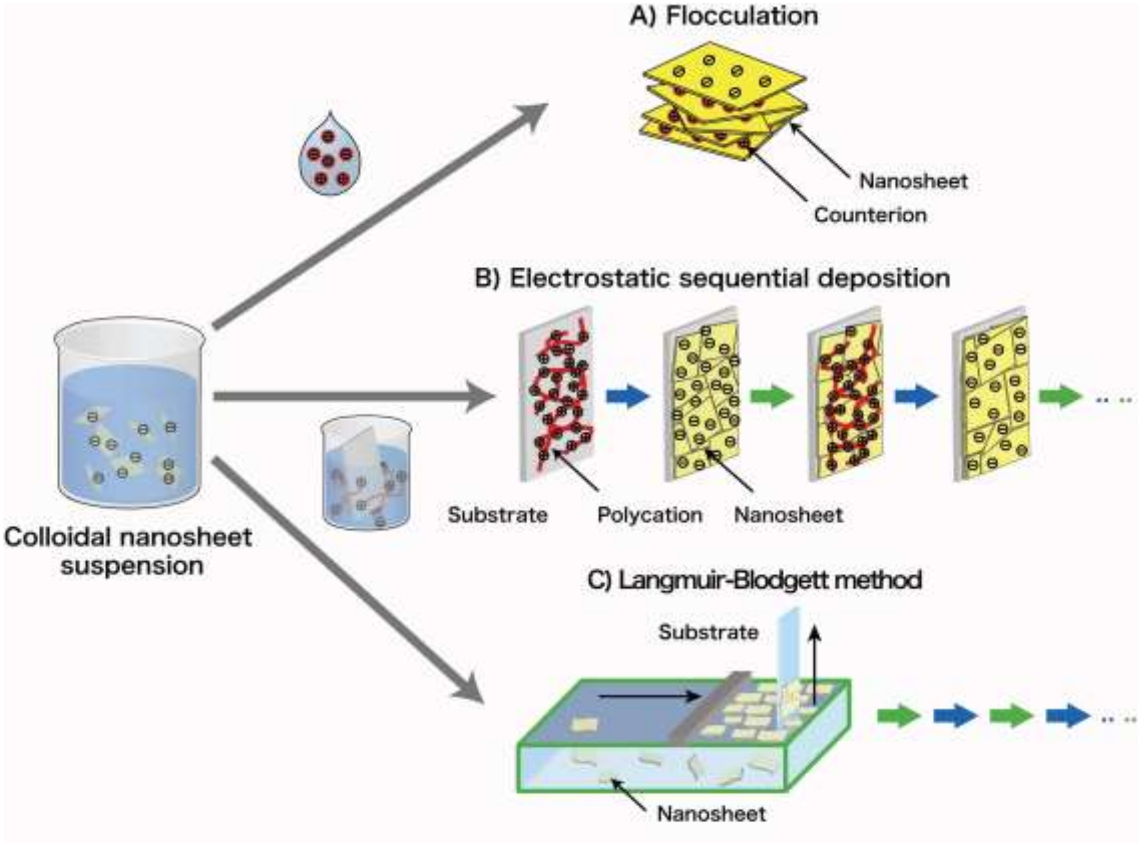

Fig. 14. Esquema ilustrando procesos de ensamblaje de nano-placas: floculación (A), adsorción secuencial electrostática (B), y método LB (C) [367].

Las nano-placas dispersas en una suspensión coloidal se pueden emplear como bloques de construcción para generar materiales funcionales [368-374]. En la Figura 14 se ilustran esquemáticamente los procesos de ensamblaje típicos de nano-placas, floculación y ensamblaje capa a capa (LbL, *layer-by-layer*), que suelen emplearse para preparar materiales micro- y mesoporosos o nano-composites [367]. Por otro lado, la adsorción secuencial electrostática y la deposición LB (*Langmuir-Blodgett*) suelen usarse para diseñar y construir nano-películas multicapa y nano-arquitecturas núcleo-carcasa (*core-shell*) sobre superficies planas o curvas, respectivamente. En la deposición secuencial electrostática y en el método LB, en principio, puede controlarse el proceso de construcción en pasos de ~1 nm de grosor, con mejores resultados que los obtenidos por técnicas convencionales como el recubrimiento por rotación (*spin-coating*) o inmersión (*dip-coating*), y la deposición electroforética. Las nano-arquitecturas y las nano-películas fabricadas de este modo son atractivas para aplicaciones electrónicas, magneto-ópticas, catalíticas y fotosintéticas, en función de las propiedades únicas de las nano-placas y sus posibles interacciones con las especies pre-diseñadas hospedadas entre ellas.

Aunque, inicialmente, la deposición secuencial electrostática se desarrolló para fabricar películas poliméricas, posteriormente se extendió a la preparación de una variada gama de materiales, que van desde proteínas [375] hasta α-fosfato de circonio [376,377]. Mediante este método, se puede construir una película multicapa sumergiendo alternativamente el sustrato en la suspensión coloidal de nano-placas y una disolución acuosa que contenga los electrólitos adecuados, siguiendo una secuencia LbL [378-382]. Poli-cationes como PDDA (*poly(diallyldimethylammonium chloride*), PEI (*polyethylenimine*) o iones tipo Keggin (Al_{13}), entre otros complejos catiónicos, se utilizan para compensar la carga de nano-placas cargadas negativamente, mientras que aniones tales como PSS (*poly(styrene 4-sulfonate*) se usan a menudo para las cargadas positivamente. En el método LB, siguiendo un proceso LbL, la deposición de monocapas sobre un sustrato plano se realiza mediante inmersión vertical. Aunque esta técnica se usó inicialmente para sistemas orgánicos, posteriormente se ha extendido a una gran variedad de nano-materiales inorgánicos [383-391].

2. Objetivos

Las preguntas más relevantes que nos planteamos al inicio de esta investigación, que conformaron nuestros objetivos, fueron:

(i) ¿Seremos capaces de obtener nuevas fases de composición, estructura y/o morfología diferentes a las descritas en la literatura?

(ii) ¿Cuáles serán las propiedades de los nuevos materiales?

(iii) ¿Podremos establecer relaciones composición-textura-morfología-estructura-propiedades?

(iv) ¿Podremos prever la existencia y abordar la síntesis de nuevas fases con propiedades predeterminadas?

(v) ¿Seremos capaces de alcanzar elucidaciones estructurales de las nuevas fases?

(vi) ¿Seremos capaces de realizar predicciones cinéticas en procesos de descomposición térmica?

(vii) ¿Podremos preparar nuevos luminóforos basados en fosfato de titanio?

Después de presentar y discutir los resultados alcanzados en el desarrollo de esta Tesis Doctoral, en nuestra opinión, estamos en condiciones de dar respuesta afirmativa a todas y cada una de las preguntas anteriores e, incluso, gracias a la serendipia, contestar otras cuestiones interesantes, que no alcanzamos siquiera a plantearnos al comenzar este proceso.

3. Resultados y Discusión

3.1. Materiales Luminiscentes

En 2014, Ortiz-Oliveros *et al.* [392] publicaron la síntesis, la caracterización físico-química y la evaluación preliminar del α-fosfato de titanio (α-TiP) en la retención de Eu^{3+} en medio acuoso, invocando que la analogía química entre el Eu^{3+} y otros metales trivalentes de elementos lantánidos y actínidos (como Np, Am, Cm y Pu, elementos radiactivos habituales en desechos radiactivos al finalizar el ciclo de uso de combustibles nucleares) hace del europio un banco de pruebas eficiente para la evaluación del comportamiento químico de esta familia de metales. Los autores concluyeron que el proceso de retención del Eu^{3+} puede tener lugar tanto en la superficie como en las cavidades internas del sólido en dos etapas diferenciadas: (i) difusión y (ii) quimisorción. Sin embargo, en los Artículos I y S1 de esta Tesis, hemos demostrado que el proceso de retención se encuentra limitado a la superficie del α-TiP, ya que el espacio interlaminar del material resulta inaccesible a las especies catiónicas de Eu(III) cuando se usa como sorbente su forma protonada. Sin embargo, es posible la difusión en las cavidades intra-cristalinas cuando el espaciado basal se ha expandido previamente (por ejemplo, intercalando propilamina).

En el Artículo I, se describió la síntesis y caracterización del α-TiP y su producto de intercalación con propilamina, $Ti(HPO_4)_2{\cdot}2C_3H_7NH_2{\cdot}H_2O$ (α-TiPPr). Posteriormente, se investigó la capacidad de ambos materiales en la retención de europio(III) en disoluciones acuosas de nitrato de europio(III) a diferentes concentraciones hasta alcanzar el equilibrio. Todas las muestras se caracterizaron por difracción de rayos X de polvo cristalino (PXRD), microscopia electrónica de barrido y de transmisión (SEM, TEM), análisis termogravimétrico (TGA) y fotoluminiscencia (PL). Los resultados mostraron que la adsorción de Eu^{3+} se limita a la superficie cuando se usa α-TiP como sorbente. Sin embargo, la capacidad de retención de Eu^{3+} aumenta considerablemente cuando se utiliza α-TiPPr, como resultado de un proceso de intercambio iónico que, afectando al espacio interlaminar, involucra cationes propilamonio, $C_3H_7NH_3^+$, y especies hexahidratadas de europio(III), $[Eu(H_2O)_6]^{3+}$, con la formación de α-$[Eu(H_2O)_6]_{2/3}Ti(PO_4)_2{\cdot}[(H_2O)_6]_{1/3}$ como producto final, cuya estructura cristalina se modelizó mediante métodos DFT.

Los resultados descritos en el Artículo I discrepan apreciablemente de las conclusiones vertidas por Ortíz-Oliveros *et al.* [392], probablemente a consecuencia de que estos autores proponen al α-TiP como barrera química de los cationes Eu^{3+}, basándose en el hecho de que los fosfatos de titanio y circonio, y otros fosfatos isoestructurales de metales tetravalentes, α-$M(HPO_4)_2 \cdot H_2O$ (M = Zr, Ti, Sn, etc.), ya habían sido utilizados con éxito en la recuperación de uranio, plutonio y productos de fisión por Zhuravlev *et al.* [393] y Mrad *et al.* [394]. Sin embargo, en ninguno de los casos invocados se utilizaron fases cristalinas de fosfatos de metales tetravalentes. Por el contrario, en el primero de ellos [393] se emplearon muestras amorfas de fosfatos de titanio y circonio (además, ambos materiales fueron modificados con iones Al^{3+} o Fe^{3+} durante el proceso de gelificación), mientras que en el segundo [394] se usó un fosfato de circonio semicristalino donde, además, se demostró que la adsorción estaba limitada a la superficie del material.

En el Artículo S1, el compuesto de intercalación α-TiPPr se exfolió en medio acuoso mediante un proceso mono-etapa. Posteriormente, las nano-placas obtenidas se funcionalizaron utilizando disoluciones acuosas de nitrato de europio(III). Los nuevos materiales se caracterizaron por PXRD, SEM, TEM, AFM (microscopia de fuerza atómica) y espectroscopia PL. La captación de europio(III) tiene lugar a través de dos vías distintas: (i) mediante un proceso de intercambio iónico $C_3H_7NH_3^+/[Eu(H_2O)_6]^{3+}$, previamente descrito en el Artículo I, y (ii) por auto-ensamblaje de láminas de fosfato de titanio (cargadas negativamente) y especies catiónicas hidratadas de Eu(III), con formación de agregados de nano-placas.

En el Artículo I, los espectros de emisión de las muestras obtenidas por interacción de disoluciones de nitrato de europio(III) con α-TiP ($\lambda_{excitación}$ = 394 nm, $^7F_0 \rightarrow {}^5L_6$) se deben a transiciones $^5D_0 \rightarrow {}^7F_J$ (J = 0-4), detectadas a longitudes de onda de 580 nm ($^5D_0 \rightarrow {}^7F_0$), 592 nm ($^5D_0 \rightarrow {}^7F_1$), 616 nm ($^5D_0 \rightarrow {}^7F_2$), 650 nm ($^5D_0 \rightarrow {}^7F_3$), y 689-697 nm ($^5D_0 \rightarrow {}^7F_4$), atribuibles a la presencia de nano-fibras de $EuPO_4 \cdot H_2O$ (fase secundaria originada como consecuencia de la hidrólisis parcial del α-TiP en el medio acuoso usado para la síntesis). Cuando se estudian muestras obtenidas a partir de α-TiPPr, los espectros de emisión también registran las cinco líneas debidas a transiciones $^5D_0 \rightarrow {}^7F_J$ (J = 0-4). En este caso, la emisión de más alta energía ($^5D_0 \rightarrow {}^7F_0$) es ancha, indicando que el Eu^{3+} se encuentra en un entorno de simetría C_n, C_{nv} o C_s, mientras que la elevada intensidad de la línea $^5D_0 \rightarrow {}^7F_2$ es coherente con una posición no centro-simétrica [395].

En el Artículo S1, se produjeron materiales exfoliados en los que las nano-partículas que los constituyen presentan espesores de 0.8-50 nm (longitud lateral = 100-600 nm). Sus espectros de emisión vuelven a corresponder con los típicos del Eu^{3+}, con un aumento en la intensidad relativa de las transiciones $^5D_0 \rightarrow {}^7F_{0-4}$ cuando lo hace la concentración de europio en fase sólida. La intensidad de la emisión $^5D_0 \rightarrow {}^7F_4$ (λ = 697 nm) decae exponencialmente con el tiempo. El mejor ajuste de los datos experimentales se obtiene con una función bi-exponencial, $I(t) = A_1 \exp(-t/\tau_1) + A_2 \exp(-t/\tau_2)$ (donde $I(t)$ es la intensidad de la radiación luminiscente, t es el tiempo transcurrido desde la excitación, A_1 and A_2 son constantes, y τ_1 and τ_2 son los tiempos de decaimiento). Ambos valores, τ_1 y τ_2, aumentan ligeramente cuando lo hace el contenido de europio en fase sólida (τ_1 = 0.16-0.26 ms, τ_2 = 0.51-0.65 ms), revelando que la progresiva extinción de la luminiscencia debe asociarse a dos tipos diferentes de decaimiento radiativo, diferenciando entre los cationes Eu(III) adsorbidos en la superficie de las nano-placas (principal contribuyente del componente más rápido) y los que se encuentran formando parte del espacio interlaminar.

En resumen, se ha demostrado que, cuando se utiliza α-TiP como sorbente, el proceso de captación de cationes europio(III) se limita a su superficie, siendo el espacio interlaminar inaccesible a los cationes hexahidratados, $[Eu(H_2O)_6]^{3+}$. Sin embargo, la retención de Eu(III) aumenta considerablemente en presencia de α-TiPPr como consecuencia de la existencia de procesos de intercambio iónico en un espacio interlaminar expandido, que implica la participación de cationes $C_3H_7NH_3^+$ y especies $[Eu(H_2O)_6]^{3+}$, con la formación de $\alpha\text{-}[Eu(H_2O)_6]_{2/3}Ti(PO_4)_2\cdot[(H_2O)_6]_{1/3}$ como producto final. Además, pueden obtenerse nano-placas derivadas de α-TiP a partir de partículas hexagonales de α-TiPPr, que pueden ser funcionalizadas con europio(III) mediante reacción sólido-líquido en medio acuoso, obteniéndose materiales con dos tipos de morfología: grandes placas apiladas y nano-placas agregadas. En este trabajo, todos los materiales que contienen europio son sistemas luminóforos que emiten principalmente en el rango naranja-rojo cuando son excitados a 394 nm, por lo que podrán ser empleados en SSL con excitación NUV-LED (rango de excitación = 380-410 nm).

Artículo I

“α-Titanium phosphate intercalated with propylamine: An alternative pathway for efficient europium(III) uptake into layered tetravalent metal phosphates”

Arabian Journal of Chemistry
Vol. 10
Pág. 885–894
Año 2017
DOI: 10.1016/j.arabjc.2016.07.013
Índice de Impacto: 4.553

Arabian Journal of Chemistry (2017) **10**, 885–894

King Saud University

Arabian Journal of Chemistry

www.ksu.edu.sa
www.sciencedirect.com

ORIGINAL ARTICLE

α-Titanium phosphate intercalated with propylamine: An alternative pathway for efficient europium(III) uptake into layered tetravalent metal phosphates

Jorge García-Glez [a], Camino Trobajo [a], Sergei A. Khainakov [b], Zakariae Amghouz [b,*]

[a] *Department of Organic and Inorganic Chemistry, University of Oviedo-CINN, 33006 Oviedo, Spain*
[b] *Scientific and Technical Services, University of Oviedo-CINN, 33006 Oviedo, Spain*

Received 8 April 2016; revised 21 July 2016; accepted 23 July 2016
Available online 30 July 2016

KEYWORDS

Titanium phosphate;
Propylamine;
Europium;
Intercalation;
Sorption;
Ion-exchange

Abstract α-$Ti(HPO_4)_2 \cdot H_2O$ (α-TiP) and its propylamine intercalation product, $Ti(HPO_4)_2 \cdot 2C_3H_7NH_2 \cdot H_2O$ (α-TiPPr), have been synthesized and characterized. Later, their sorption capacity for europium(III) was investigated, and this purpose was accomplished by treating α-TiP and α-TiPPr with europium(III) nitrate solutions at different concentrations until the equilibrium is reached. All samples were characterized, among others, by powder X-ray diffraction (PXRD), scanning and transmission electron microscopies (SEM, TEM, STEM-EDX, SAED), thermogravimetric analysis (TGA), and photoluminescence (PL) measurements. The results show that the Eu^{3+} uptake is limited to surface when α-TiP is used as sorbent. Nevertheless, the Eu-retention is considerably enhanced with α-TiPPr as a consequence of an ion-exchange process into the interlayer space of the layered titanium phosphate (involving propylammonium cations, $C_3H_7NH_3^+$, and hexahydrate europium(III) species, $[Eu(H_2O)_6]^{3+}$), and the crystal structure of a hypothetical final product, α-$[Eu(H_2O)_6]_{2/3}Ti(PO_4)_2 \cdot [(H_2O)_6]_{1/3}$, has been proposed by using DFT calculations.

1. Introduction

Recently, Ortiz-Oliveros et al. (2014) have published the synthesis, physical-chemical characterization and preliminary evaluation of α-$Ti(HPO_4)_2 \cdot H_2O$ (α-TiP) sorption of Eu^{3+}, which is often considered as a chemical analogue for trivalent heavy metals, lanthanides and also actinides (such as Np, Am, Cm and Pu, radionuclides found in high-level radioactive waste produced during the nuclear fuel cycle). The authors concluded that the retention process for Eu^{3+} can take place on the surface and in the cavities of the solid in two stages: (a) diffusion into the cavities of the material and (b) chemisorption. In this work, we will show that the uptake process is, in fact, limited to the surface of

---

* Corresponding author.
E-mail address: amghouz.uo@uniovi.es (Z. Amghouz).

Peer review under responsibility of King Saud University.

Production and hosting by Elsevier

http://dx.doi.org/10.1016/j.arabjc.2016.07.013

the α-titanium phosphate (the interlayer space is inaccessible to the europium species when the α-TiP hydrogen form is used as sorbent), while the diffusion into internal cavities is only possible when basal spacing is previously expanded (e.g., intercalated by propylamine).

Ortiz-Oliveros et al. (2014) addressed, among other things, the evaluation of Eu^{3+} sorption capacity by crystalline α-TiP, based on the fact that the titanium and zirconium phosphates, and other isomorphic tetravalent metal phosphates α-$M(HPO_4)_2 \cdot H_2O$ (M = Zr, Ti, Sn, etc.) have been successfully used in the recovery of uranium, plutonium and fission products (Zhuravlev et al., 2002; Mrad et al., 2011). However, Zhuravlev et al. (2002) relied on the use of amorphous samples of titanium and zirconium phosphates (modified with Al^{3+} or Fe^{3+} ions during the gelation process), whereas Mrad et al. (2011) carried out their work using semi-crystalline $Zr(HPO_4)_2 \cdot H_2O$ (where an adsorption occurs on the surface, and an ion-exchange mechanism is not fully confirmed).

Metal salts of phosphoric acid have been known for over a century. Because of their extraordinary properties, a great variety of potential and realized uses have been invoked. Among the many uses in addition to both ion-exchange and intercalation-chemistry are catalysis, polymer composites, proton conduction, drug delivery and many others, such as energy storage, sensors and biosensors, flame retardants, and antibiomaterials (Clearfield and Diaz, 2015). Titanium phosphate can be prepared either as gel or in intermediate stages of crystallinity, but also in several crystalline forms including γ-$Ti(PO_4)(H_2PO_4) \cdot 2H_2O$ (γ-TiP) and α-TiP (Salvadó et al., 1996; García-Granda et al., 2010), being known that the main factors affecting the ion-exchange behavior of tetravalent metal phosphates are their structures and the degree of crystallinity (Llavona et al., 1989). α- and γ-TiP are layered compounds with flexible two-dimensional structures that, although they have ion-exchange properties, display low affinity toward both transition and inner transition metal ions (Álvarez et al., 1987; Trobajo et al., 1991). The synthesis of ion-exchange phases with polyvalent cations is possible by means of an indirect route. In the first stage, the reaction between the inorganic solid acid (α- or γ-TiP) and the vapor of an organic base (e.g., *n*-alkylamine), produced an essentially non-porous intercalation compound (Menéndez et al., 1993; Espina et al., 1998a, 1998b), usually with strong preferential orientation effects and thermal disorder of the alkyl chains (Mafra et al., 2005, 2008). In a second step, the intercalation compound reacts with an aqueous solution of the desired metal salt, and the substitution of intercalated organic cation by the inorganic metal cation takes place (Trobajo et al., 1991; Alfonso et al., 2005).

In this paper, α-TiP intercalated with propylamine (α-TiPPr) has been selected to investigate its sorption of Eu(III) by means of PXRD, SEM, TEM, TGA and PL. Moreover, the structural modeling of a hypothetical full ion-exchange phase, $[Eu(H_2O)_6]_{2/3}Ti(PO_4)_2 \cdot [(H_2O)_6]_{1/3}$, has been also proposed on the basis of DFT calculations.

2. Materials and methods

2.1. Synthesis of sorbents

All chemicals used were of reagent grade. MilliQ water was used throughout the experiments. α-TiP was obtained by the method described by Alberti et al. (1967) using 10 M H_3PO_4 and reflux times of 50 h. Propylamine intercalation compound, α-$Ti(HPO_4)_2 \cdot 2C_3H_7NH_2 \cdot H_2O$ (α-TiPPr), was obtained by placing α-TiP in an atmosphere saturated with propylamine vapor during 6 days at room temperature (Menéndez et al., 1990).

2.2. Sorption experiments

In bath, the α-TiP (or α-TiPPr) was equilibrated with europium nitrate solutions ($T = 25.0 \pm 0.1$ °C, $t = 72$ h, solution/solid ratio = 20 mL/1 g). The prepared samples were designated as **TiP_x** (or **TiPPr_x**), where **x** indicates the molar concentration europium nitrate solution in the starting solutions, $[Eu^{3+}]_i$.

2.3. Characterization procedures

In residual solutions, the phosphorous and titanium contents were determined with a SpectraSpectrometer DCP-AEC. The powder X-ray diffraction (PXRD) patterns were recorded on Xpert Panalytical diffractometer with Cu Kα radiation ($\lambda = 1.5418$ Å). The samples were gently ground in an agate mortar in order to minimize the preferred orientation. A Mettler-Toledo thermogravimetric (TG) equipment (TGA/SDTA851°) was used for the thermal analyses in oxygen dynamic atmosphere (50 mL/min) at a heating rate of 10 °C/min. In TG test, a Pfeiffer Vacuum ThermoStar™ GSD301T mass spectrometer was used to determine the evacuated vapors. Micrographs and X-ray microanalysis (SEM/EDX) were recorded with a JEOL JSM-6100 electron microscope operating at 20 kV coupled with an INCA Energy-200 energy dispersive X-ray microanalysis system (EDX) with Oxford PentaFET ultrathin window detector. The TEM studies were performed on a JEOL JEM-2100F field emission transmission electron microscope operated at an accelerating voltage of 200 kV and equipped with an ultra-high resolution pole-piece that provided a point-resolution better than 0.19 nm. Fine powder of the sample was dispersed in ethanol, sonicated and sprayed on a carbon coated copper grid, and then allowed to air-dry. Photoluminescence studies in air at RT were performed using a standard spectrofluorometer from Edinburgh Instruments model FLSP920, having a 450 W Xe lamp as the excitation source. The sample was placed between two quartz plates placed at 45° from the incident beam and the detector.

2.4. Structural modeling

The structural modeling of the material with the idealized formula $[Eu(H_2O)_6]_{2/3}Ti(PO_4)_2 \cdot [(H_2O)_6]_{1/3}$ has been performed according to the following steps. In the first stage, the bond lengths and angles of free H_2O and $Eu(H_2O)_6^{3+}$ species were optimized by DFT methods (GGA approximation and BLYP functional) by using the DMOL3 module implemented in BIOVIA Materials Studio (B.M.S., 2015). The results of the optimization are shown in Fig. S1. In the second step, the interlayer distance between the sheets of the starting structure α-$Ti(HPO_4)_2 \cdot H_2O$ was expanded up to 12.0 Å (according to PXRD data) and then water molecules and hydrogenous atoms of HPO_4 groups were removed. Later, H_2O molecules and $Eu(H_2O)_6^{3+}$ cations were placed between the sheets, and subsequently, the supercell 1 × 3 × 1 of the expanded structure was built in order to keep fixed the idealized composition $[Eu(H_2O)_6]_{2/3}Ti(PO_4)_2 \cdot [(H_2O)_6]_{1/3}$. The position optimization of H_2O molecules, $Eu(H_2O)_6^{3+}$ cations and the sheets as rigid bodies were performed by means of molecular mechanics methods with the Forcite module (Universal force field) implemented in Biovia Materials Studio (B.M.S., 2015). In the final stage, the optimization was performed, leaving all atoms free for structure relaxation, by DFT methods (GGA approximation, PBE functional) using CASTEP module.

3. Results and discussion

PXRD analysis shows the both **TiP_10^{-4}** and **TiP_0.1** samples are highly crystalline and their patterns are identical, as seen in Fig. 1, with the first characteristic peak at $2\theta = 11.65°$ ($d_{002} = 7.58$ Å) corresponding to the interlayer distance of α-TiP. TEM images in Figs. 2a and b and 3a and b show that both samples maintain the typical platelet-like pseudo-hexagonal morphologies (length: 0.2–0.8 µm; thickness: 10–30 nm) similar to other metal phosphates (Manickam et al., 2004). However, in the case of **TiP_0.1**, an additional phase with nanorod-like morphology (thickness of *ca.* 10 nm) has been formed (for instance Fig. 3b and c). This phase was undetectable by PXRD as a consequence of its low content, poor crystallinity and nano crystallite size. In addition, the selected area electron diffraction (SAED) pattern of these nanorods found in **TiP_0.1** (Fig. 3d) has been indexed as standard hexagonal $EuPO_4$ H_2O phase ($P3_12_1$, $a = 6.91$ Å, $b = 6.34$ Å; ICSD PDF4: 20-1044). In contrast, the only identified phase in the case of **TiP_10^{-4}** was α-TiP, as confirmed by SAED patterns in Fig. 2c and d. Furthermore, the chemical composition of $EuPO_4$ nanorods was confirmed by EDX analysis, revealing that both α-TiP and $EuPO_4$ phases are clearly distinguishable by EDX elemental mapping (see Fig. 4) in the case of **TiP_0.1**, while the only detectable element in the case of **TiP_10^{-4}** was Ti, P and O as seen in Fig. S2. In order to investigate the photoluminescence properties of **TiP_10^{-4}** and **TiP_0.1**, the emission spectra were obtained with $\lambda_{ex} = 394$ nm as shown in Fig. 5. The emission spectrum of **TiP_10^{-4}** does not show any transition line due to the sorption of Eu^{3+}. In contrast, the **TiP_0.1** spectrum shows the typical emission transitions of Eu^{3+}, which are attributed to $^5D_0 \rightarrow {}^7F_J$ ($J = 0$–4) transitions at, i.e. 580 nm ($^5D_0 \rightarrow {}^7F_0$), 592 nm ($^5D_0 \rightarrow {}^7F_1$), 616 nm ($^5D_0 \rightarrow {}^7F_2$), 650 nm

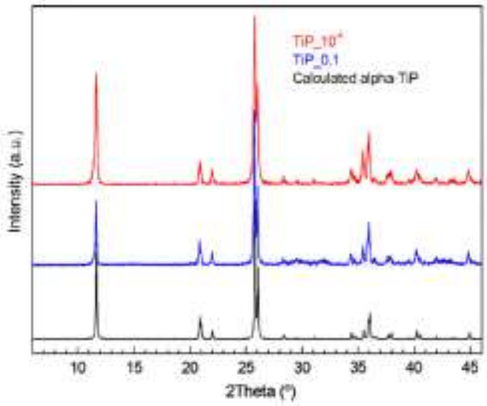

Figure 1 PXRD patterns of the samples **TiP_10^{-4}** (red) and **TiP_0.1** (blue), and calculated for α-TiP (black).

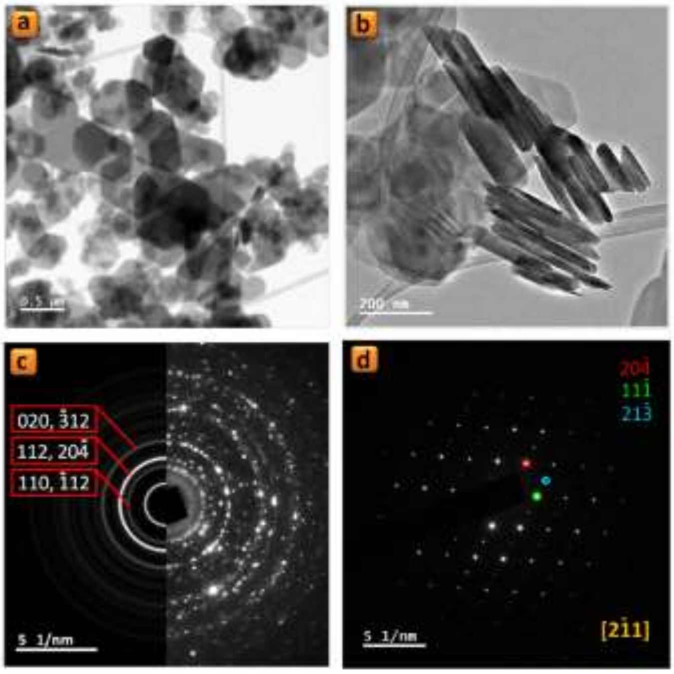

Figure 2 (a and b) TEM images, (c) selected area electron diffraction (SAED) patterns (left: simulated, right: experimental), and (d) nanobeam electron diffraction (NBD) pattern along [2–11] zone axis for a single particle of **TiP_10^{-4}** sample.

($^5D_0 \rightarrow {}^7F_3$), and 689 and 697 nm ($^5D_0 \rightarrow {}^7F_4$), with the most intense peak corresponding to the $^5D_0 \rightarrow {}^7F_2$ transition. These transition lines correspond basically to the $EuPO_4 \cdot H_2O$ nanorod phase. The observed low-intensity $^5D_0 \rightarrow {}^7F_0$ line is expected for Eu^{3+} in a site with C_n, C_{nv} and C_s symmetry. The high relative intensity of the hypersensitive $^5D_0 \rightarrow {}^7F_2$ transition is in accord with the Eu^{3+} local site symmetry (C_s), which is determined based on the crystal structure of hexagonal $EuPO_4 \cdot H2O$ phase. Moreover, the $^5D_0 \rightarrow {}^7F_4$ transition is less intense than the $^5D_0 \rightarrow {}^7F_2$ transition but much more intense than the $^5D_0 \rightarrow {}^7F_1$ transition, and the same remarks have been made with Eu^{3+} in an asymmetric site with Cs symmetry in the case of $LaBO_3{:}Eu^{3+}$ with an orthorhombic aragonite structure (Binnemans, 2015).

From all the above data, we can conclude that the Eu^{3+} sorption process takes place only on the surface of α-TiP rather than in its interlayer space, because of the following summarized observations: (i) at high $[Eu^{3+}]_i$ no change in the interlayer distance of α-TiP has been observed by PXRD, and (ii) Eu^{3+} was undetectable by EDX analysis or by PL emission spectra at low $[Eu^{3+}]_i$.

In this context, α-TiP intercalated with propylamine (**TiPPr**) was selected as a potential material for efficient europium(III) uptake into layered tetravalent metal phosphates. For this purpose, **TiPPr** was treated with europium nitrate solutions at different concentrations until the equilibrium is reached. PXRD patterns of **TiPPr_10**$^{-4}$ to **TiPPr_0.1** (Fig. 6) show a structural order in the direction perpendicular to the plane of the sheet. In the range 0.0001–0.0625 M, the interlayer distance of the sheets remains substantially constant (16.0 Å), which is slightly lower than that of the starting material (16.9 Å, α-TiPPr) (Menéndez et al., 1990) as a consequence of a partial evacuation of the amine occupying the interlayered space. However, a new diffraction peak at $2\theta = 7.3°$ corresponding to *d*-spacing of 12.0 Å appears when the concentration is increased to 0.0750 M, which became the only observed peak when the $[Eu^{3+}]_i$ is raised to 0.1000 M. Moreover, the carbon content of the resulting solids (Table 1) continuously decreases with increasing concentration of europium nitrate in the starting solutions, in agreement with the results of STEM-EDS elemental mapping (Fig. S3), which obviously indicates the removal of the amine increases as the ionic strength of the solution increases. As a result, the behavior **TiPPr_x** can be divided into four different zones (red-blue-green-black), as illustrated in Table 1 and Fig. 6, depending on the concentration of Eu^{3+} in the initial solutions.

In the zone of low concentrations (red zone), the material consists of slightly wrinkled thin films (Figs. 7a–c and 8a–c) with lateral dimensions varying from about 0.1 µm to 1 µm and thicknesses of *ca.* 6.0 nm measured by atomic force microscopy. These thin films maintain a long-range order in the direction of the crystallographic *c*-axis as revealed by PXRD studies (Fig. 6), while a certain order is still maintained in *ab* plane as illustrated by the SAED pattern (see inset in

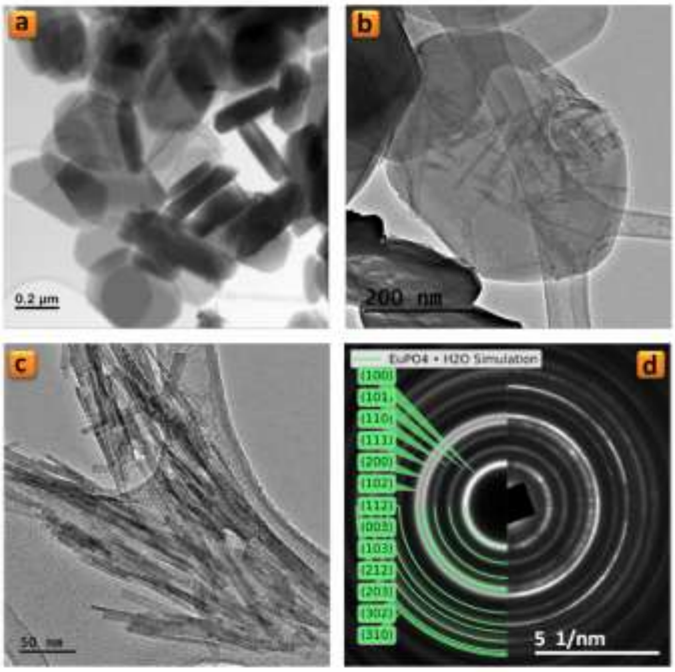

Figure 3 (a–c) TEM images of **TiP_0.1** sample and (d) selected area electron diffraction (SAED) patterns (left: simulated, right: experimental) corresponding to the image (c).

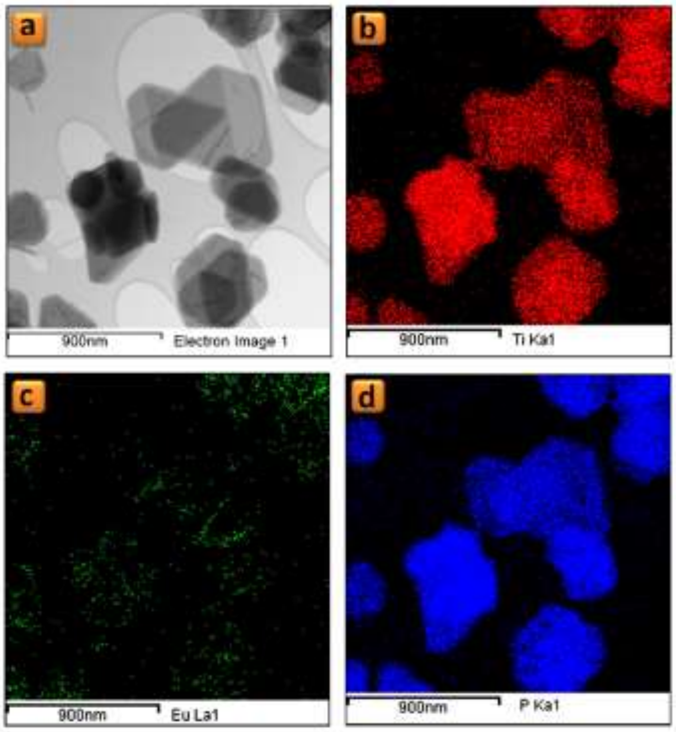

Figure 4 Elemental mapping for **TiP_0.1** sample: (a) Bright field-STEM images, (b) Ti-Kα_1 map, (c) Eu-Lα_1 map and (d) P-Kα_1 map.

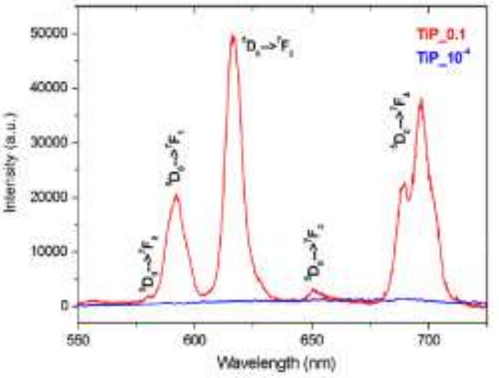

Figure 5 Emission spectra of the samples **TiP_0.1** (red) and **TiP_10^{-4}** (blue) obtained up excitation at 394 nm.

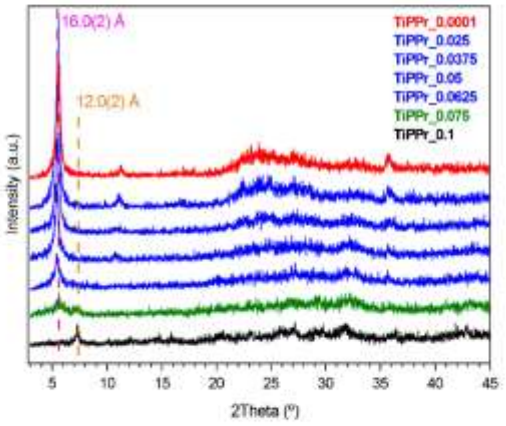

Figure 6 PXRD patterns of the **TiPPr_x** samples.

Fig. 8a–c). Moreover, the propylamine content decreases in this red zone (see Table 1 and Fig. 6) compared to the starting material **TiPPr** with interlayer distance 16.9 Å (Menéndez et al., 1990). However, the presence of Eu^{3+} in these films was undetectable by STEM-EDS elemental mapping as shown in Fig. 9a and b, in agreement with the emission spectrum (for instance **TiPPr_10^{-4}** spectrum in Fig. 10) which does not show any transition line due to the sorption and/or intercalation of Eu^{3+}.

In the region of intermediate concentrations (blue zone), the layers are stacked in the direction perpendicular to the

Table 1 Experimental data for samples obtained when α-TiPPr was equilibrated with europium(III) nitrate solutions of several concentrations ($[Eu^{3+}]_i$): Carbon content (C), total weight loss at 1000 °C in air atmosphere (Δm) obtained by TG-analysis, and phosphorus (P) and titanium (Ti) contents in a non-centrifugal fraction expressed as concentration (mg/L) and percentage (%) of the total content in the starting material.

Sample	$[Eu^{3+}]_i$ (mol/L)	C (%)	Δm (%)	P (mg/L)	Ti (mg/L)	P (%)	Ti (%)
TiPPr_10^{-4}	0.0001	13.4	33.8	6254	4374	76	69
TiPPr_10^{-3}	0.001	13.4	37.4	5489	3903	67	61
TiPPr_10^{-2}	0.01	12.7	34.7	4595	3119	56	49
TiPPr_0.025	0.025	11.9	36.1	1401	734	17	11
TiPPr_0.0375	0.0375	9.9	32.7	761	273	9	4
TiPPr_0.05	0.05	8.3	29.8	409	< 1	5	< 1
TiPPr_0.0625	0.0625	5.8	26.6	177	< 1	2	< 1
TiPPr_0.075	0.075	4.9	25.7	82	< 1	1	< 1
TiPPr_0.1	0.1	2.5	25.0	24	< 1	< 1	< 1

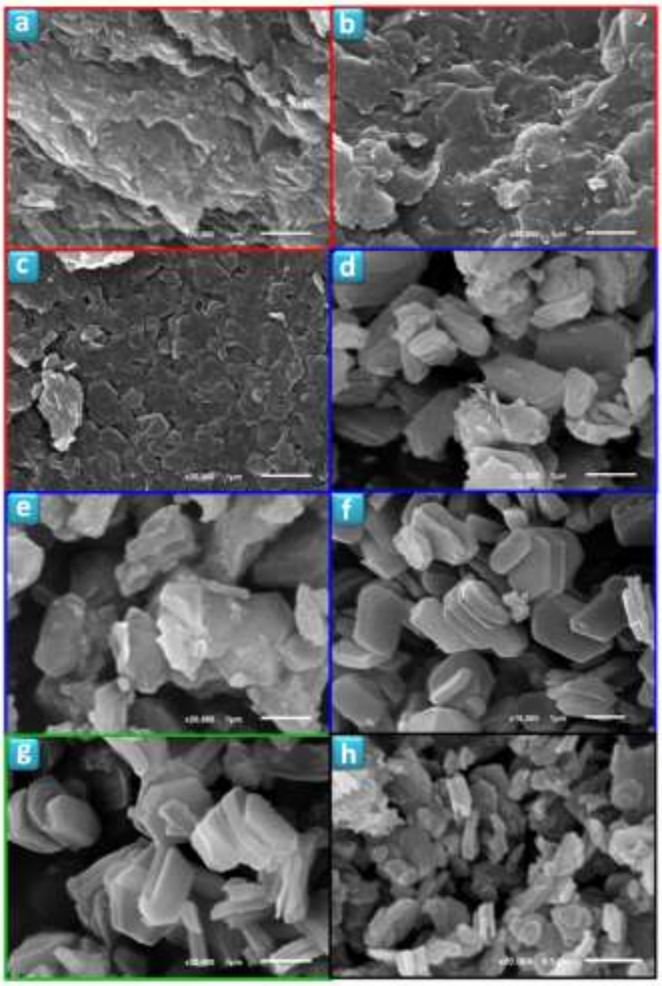

Figure 7 SEM images of **TiPPr_x** samples (**x** = 10^{-4} (a), 10^{-3} (b), 0.01 (c), 0.025 (d), 0.0375 (e), 0.0625 (f), 0.075 (g) and 0.1 (h)).

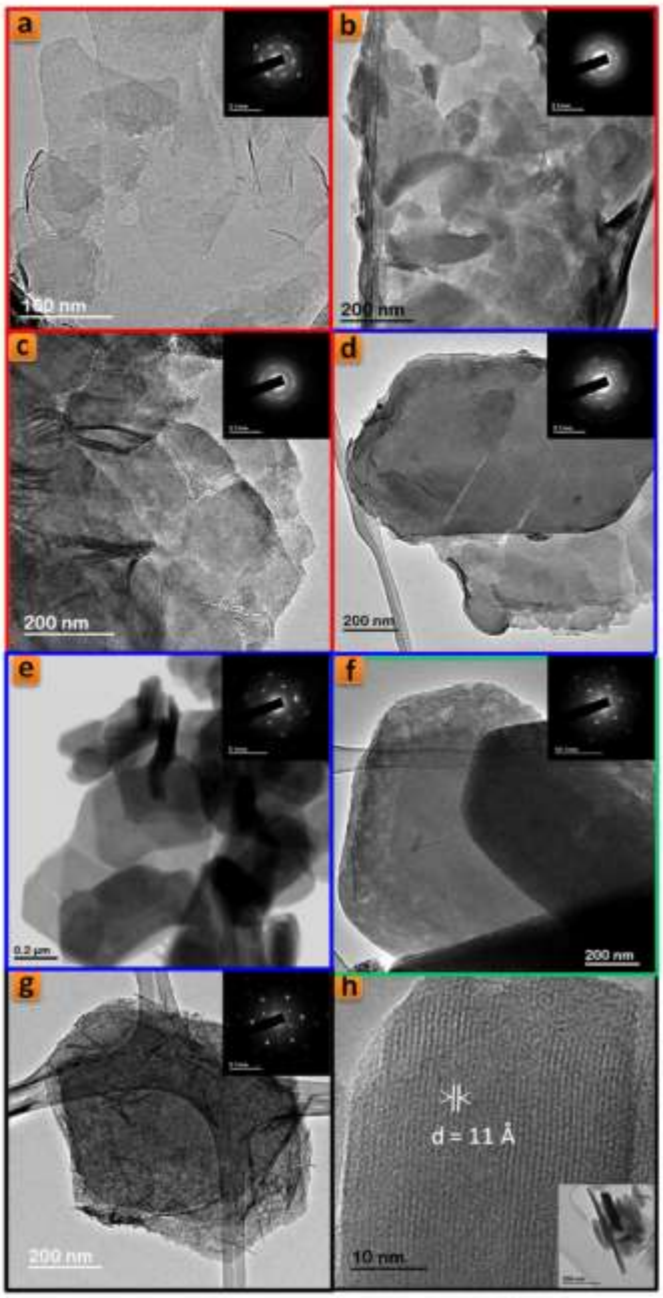

Figure 8 TEM images of **TiPPr_x** samples ($\mathbf{x} = 10^{-4}$ (a), 10^{-3} (b), 0.01 (c), 0.025 (d), 0.05 (e), 0.075 (f) and 0.1 (g and h)).

plane of the titanium phosphate sheet, where the interlayer distance is slightly lower than in the starting material **TiPPr**, but it is essentially constant (16.0 Å) as shown in Fig. 6, while the pseudo-hexagonal morphologies are preserved (Figs. 7d–f and 8d and e). The amine content gradually decreases (reflected in the decrease in carbon content, see Table 1); thus,

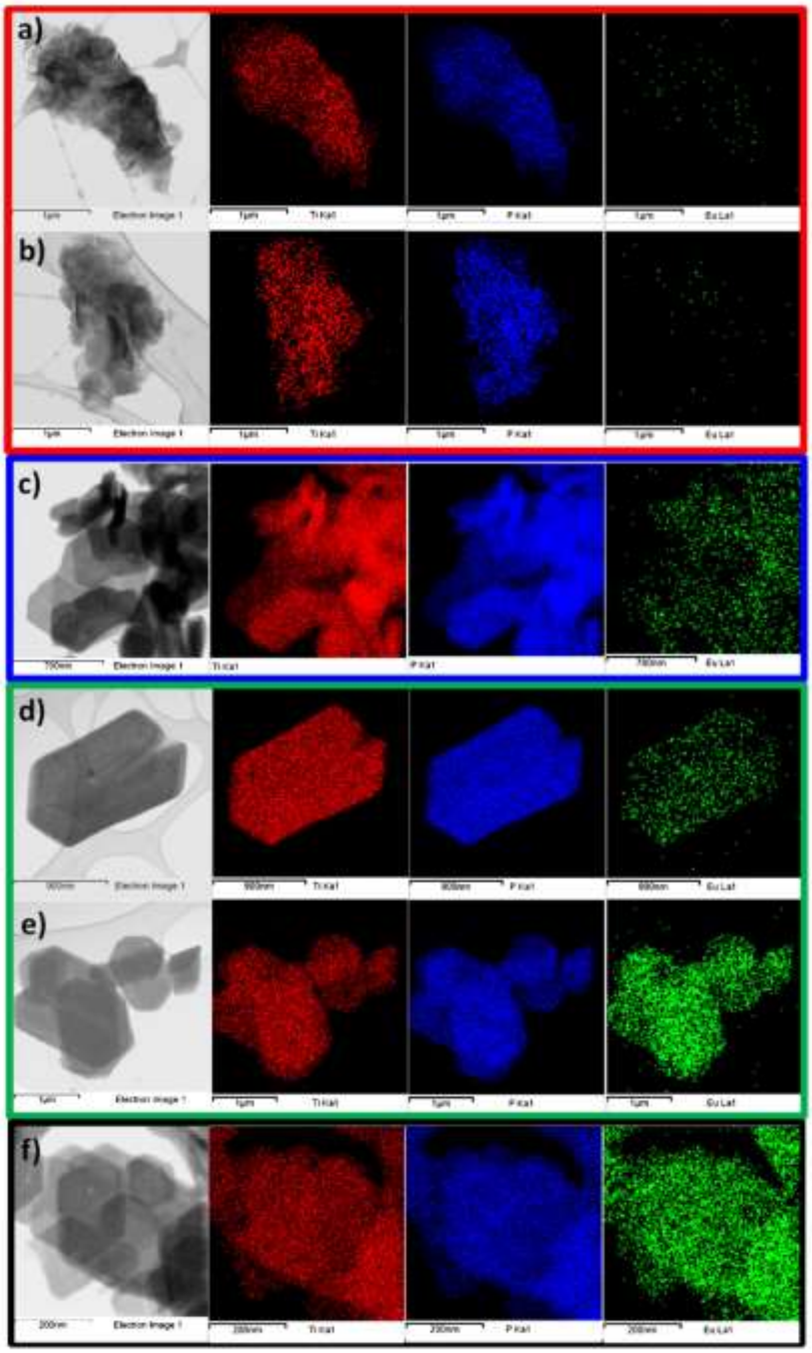

Figure 9 STEM-EDS elemental mapping of **TiPPr_x** samples (**x** = 10^{-4} (a), 10^{-3} (b), 0.05 (c), 0.075 (d and e) and 0.1 (f)); Ti-Kα_1 (red), P-Kα_1 (blue) and Eu-Lα_1 (green) elemental maps.

the Eu-content increases in the solid phase as confirmed by EDX mapping (Fig. 9c) and by the presence of $^5D_0 \rightarrow {}^7F_J$ ($J = 0$–4) transition peaks in the emission spectrum of **TiPPr_0.05** (Fig. 10). Assuming that an ion-exchange process is taking place between the propylammonium cations, $C_3H_7NH_3^+$, and the hexahydrate species of europium, $[Eu(H_2O)_6]^{3+}$, the following tentative formula, $(C_3H_7NH_3)_{2-3y}[Eu(H_2O)_6]_y Ti(PO_4)_2 \cdot [(H_2O)_6]_{y/2}$, has been proposed for the resulting materials. This process proceeds *via* the formation of solid solutions, where $C_3H_7NH_3^+$ species act as pillars adopting a bilayer structure with the tilt angle of the alkyl chain of *ca.* 50° relative to the plane of the titanium phosphate sheet, and occupying a fraction of the pseudo-zeolitic cavities of the titanium phosphate, while the rest of the cavities would be occupied by $[Eu(H_2O)_6]^{3+}$ species. The calculated total mass loss decreases from 36.65% ($y = 0.15$) to 26.69% ($y = 0.55$), in a good agreement with experimental data: 36.1–26.6% obtained from TGA data (see Table 1).

At higher concentration (zones shown in green and black), the particles maintain their pseudo-hexagonal morphologies (Fig. 7g and h and 8f and g), and besides the presence of an interlayer distance of 16.0 Å in the case of **TiPPr_0.075**, the appearance of a new phase with *d*-spacing of 12.0 Å is also observed (Fig. 6), which is the only one that remains in the black zone (**TiPPr_0.1**). HRTEM (Fig. 8h) shows a *d*-spacing of *ca.* 11.0 Å, close to the value obtained by PXRD, and this difference is due to the instantaneous dehydration followed by a fast amorphization of the particles under the electron beam irradiation. In this latter zone, the low carbon content suggests that almost all the alkylammonium cations have been involved in the ion-exchange process, thus leading to the formation of a material with the idealized formula $[Eu(H_2O)_6]_{2/3}Ti(PO_4)_2 \cdot [(H_2O)_6]_{1/3}$, where $[Eu(H_2O)_6]^{3+}$ occupying 2/3 of the pseudo-zeolitic cavities so as to counteract the negatively charged titanium phosphate layer. The rest of the pseudo-zeolitic cavities (1/3 of the total) will be occupied by water molecules. Based on this expected formula, the calculated mass loss of 24.15% is in good accordance with the experimental mass loss of 25.0%. Moreover, STEM-EDS elemental mapping of **TiPPr_0.075** (Fig. 9d and e) and **TiPPr_0.1** (Fig. 9f), corresponding to the green and black zones, respectively, shows a significant increase in Eu-content compared to the blue zone, and it is noteworthy that in the case of green zone there are particles with low and high Eu-content (Fig. 9d and e), which could be related to the presence of two phases with different basal spacing (16.0 Å and 12.0 Å), as revealed by PXRD analysis (Fig. 6). On the other hand, the emission spectrum of **TiPPr_0.1** (Fig. 10) still shows the expected $^5D_0 \rightarrow {}^7F_J$ ($J = 0$–4) transition peaks but with a decrease in their relative intensities compared to the spectrum of the blue zone, which is probably associated with the absence of propylamine and high degree of hydration leading to emission quenching. The emission spectra of samples **TiPPr_0.05** and **TiPPr_0.1** show the five possible luminescence bands expected in the registered spectral region. The number of lines observed for the $^5D_0 \rightarrow {}^7F_J$ ($J = 0$–4) transitions in the luminescence spectrum allows determining the site symmetry of the Eu^{3+} ion (Binnemans, 2015). The highest energy $^5D_0 \rightarrow {}^7F_0$ line is very weak, in agreement with Judd–Ofelt theory (the transition should only be expected to be observed for Eu^{3+} in a site with C_n, C_{nv} or C_s symmetry). The very intense hypersensitive transition $^5D_0 \rightarrow {}^7F_2$ indicates that the Eu^{3+} is not at a site with a center of symmetry. In addition, the transition $^5D_0 \rightarrow {}^7F_3$ has very weak intensity since they are forbidden by the selection rule of ΔJ for electric dipole transitions.

The colloidal suspensions (non-centrifugal phases) of **TiPPr_10^{-4}** to **TiPPr_0.1** have been analyzed by ICP-MS. The results (Table 1) show that the concentrations of both P and Ti decrease with increasing $[Eu^{3+}]_i$. In the red zone (low concentrations), about three quarters of the starting material **TiPPr** are found in the liquid phase, mainly in the form of nanometric colloidal TiP monolayers, although a portion of this % is dissolved due to the partial hydrolysis of the starting material. While in the blue zone (intermediate concentrations), the amount of the nanometric colloidal TiP suspension decreases drastically with increasing $[Eu^{3+}]_i$, which is reflected in the decrease in P and Ti content in the liquid phase. The fact that the percentage of P in solution is higher than Ti, in both the red and blue zones, indicates the existence of hydrolysis processes of the titanium phosphate, which may give rise to

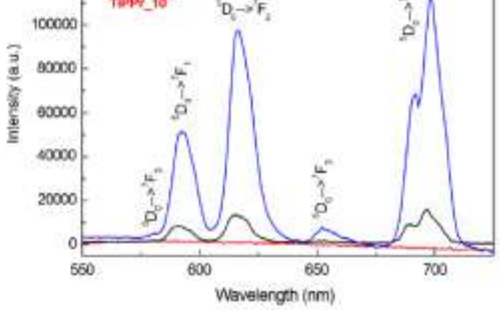

Figure 10 Emission spectra of **TiPPr_10^{-4}** (red), **TiPPr_0.05** (blue) and **TiPPr_0.1** (black), obtained up excitation at 394 nm.

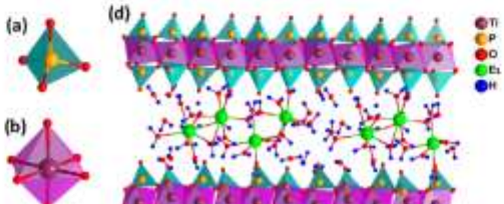

Figure 11 Perspective view of the coordination environment of P (a), Ti (b), Eu (c) and the projection of the structural model of $[Eu(H_2O)_6]_{2/3}Ti(PO_4)_2 \cdot [(H_2O)_6]_{1/3}$ along the *a*-axis (d).

the formation of aqueous phosphate species and precipitation of titanium dioxide gels. Finally, in the green zone, and especially in the black one, high $[Eu^{3+}]_i$ causes the liquid phase to be substantially free of P and Ti. However, in the solid phase, and beside the hypothetical ion-exchange phase $[Eu(H_2O)_6]_{2/3}Ti(PO_4)_2{\cdot}[(H_2O)_6]_{1/3}$, it shall be present variable amounts of $EuPO_4{\cdot}H_2O$ (for instance, see nanorods in Fig. 8g) and $TiO_2{\cdot}nH_2O$ (not observed by TEM), coexisting with a residual phase containing propylamine (Fig. S3d).

The final structural model proposed by using DFT calculations for the material with the idealized formula $[Eu(H_2O)_6]_{2/3}Ti(PO_4)_2{\cdot}[(H_2O)_6]_{1/3}$ is shown in Fig. 11. Its structure consists of PO_4 tetrahedral (Fig. 11a) and TiO_6 octahedral (Fig. 11b) units connected through their vertices, giving rise to 2D-dimensional inorganic sheets, which are still closely related to those of the α-TiP. The hexahydrate species of europium, $[Eu(H_2O)_6]^{3+}$ (Fig. 11c), and non-coordinated H_2O molecules occupy the interlamellar space, with the average Eu–O bond distance and Eu–Eu distance between adjacent $[Eu(H_2O)_6]^{3+}$ cations of 2.58 Å and 4.91 Å, respectively.

4. Conclusions

In summary, we have shown that when α-TiP is used as sorbent the Eu^{3+} uptake process is limited to its surface, being the interlayer space inaccessible to the hexahydrate $[Eu(H_2O)_6]^{3+}$ cations. However, the Eu^{3+} uptake is considerably improved with α-TiPPr as a consequence of an ion-exchange process into the expanded interlayer space, involving $C_3H_7NH_3^+$ cations and $[Eu(H_2O)_6]^{3+}$ species, with the formation of α-$[Eu(H_2O)_6]_{2/3}Ti(PO_4)_2{\cdot}[(H_2O)_6]_{1/3}$ as final product.

Acknowledgments

Financial support from Spanish *Ministerio de Economía y Competitividad* (MAT2013-40950-R) and *Gobierno del Principado de Asturias* (GRUPIN14-060), and FEDER funding is acknowledged.

Appendix A. Supplementary material

Supplementary data associated with this article can be found, in the online version, at http://dx.doi.org/10.1016/j.arabjc.2016.07.013.

References

Alberti, G., Cardini-Galli, P., Costantino, U., Torracca, E., 1967. Crystalline insoluble salts of polybasic metals. I. Ion-exchange properties of crystalline titanium phosphate. J. Inorg. Nucl. Chem. 29, 571.

Alfonso, B.F., Trobajo, C., Salvadó, M.A., Pertierra, P., García-Granda, S., Rodríguez-Fernández, J., Blanco, J.A., García, J.R., 2005. Synthesis and characterization of α-titanium phosphate/propylamine intercalation compounds containing transition-metal ions. Z. Anorg. Allg. Chem. 631, 2174.

Álvarez, C., Llavona, R., García, J.R., Suárez, M., Rodríguez, J., 1987. Lamellar inorganic ion-exchangers. Proton-copper(II) ion-exchange in γ-titanium bis(hydrogenphosphate). J. Chem. Soc., Dalton Trans., 2045.

B.M.S., 2015. <http://accelrys.com/products/collaborative-science/biovia-materials-studio/>.

Binnemans, K., 2015. Interpretation of europium(III) spectra. Coord. Chem. Rev. 295, 1.

Clearfield, A., Díaz, A., 2015. Zirconium phosphate nanoparticles and their extraordinary properties. In: Brunet, E., Colón, J.L., Clearfield, A. (Eds.), Tailored Organic–Inorganic Materials. John Wiley & Sons Inc, Hoboken, New Jersey.

Espina, A., García, J.R., Guil, J.M., Jáimez, E., Parra, J.B., Rodríguez, J., 1998a. Calorimetric study of amine adsorption on α- and γ-titanium phosphate. J. Phys. Chem. B 102, 1713.

Espina, A., Jáimez, E., Khainakov, S.A., Trobajo, C., García, J.R., Rodríguez, J., 1998b. Synthesis of new n-alkylamines intercalation compounds with α-titanium phosphate. Process selectivity and structural and morphological characterization. Chem. Mater. 10, 2490.

García-Granda, S., Khainakov, S.A., Espina, A., García, J.R., Castro, G.R., Rocha, J., Mafra, L., 2010. Revisiting the thermal decomposition of layered γ-titanium phosphate and structural elucidation of its intermediate phases. Inorg. Chem. 49, 2630.

Llavona, R., Suárez, M., García, J.R., Rodríguez, J., 1989. Lamellar inorganic ion-exchangers. Alkali-metal ion exchange on α- and γ-titanium phosphate. Inorg. Chem. 28, 2863.

Mafra, L., Paz, F.A.A., Rocha, J., Espina, A., Khainakov, A., García, J.R., Fernández, C., 2005. Structural characterization of layered γ-titanium phosphate $(C_6H_{13}NH_3)[Ti(HPO_4)(PO_4)]{\cdot}H_2O$. Chem. Mater. 17, 6287.

Mafra, L., Rocha, J., Fernández, C., Castro, G.R., García-Granda, S., Espina, A., Khainakov, S.A., García, J.R., 2008. Characterization of layered γ-titanium phosphate $(C_2H_5NH_3)[Ti(H_{1.5}PO_4)(PO_4)]_2{\cdot}H_2O$ intercalate: a combined NMR, synchrotron XRD, and DFT calculations study. Chem. Mater. 20, 3944.

Manickam, M., Minato, K., Takata, M., 2004. Synthesis and electrochemical properties of $TiNb(PO_4)_3$ cathode materials for lithium secondary batteries. J. Electroanal. Chem. 562, 1.

Menéndez, A., Bárcena, M., Jáimez, E., García, J.R., Rodríguez, J., 1993. Intercalation of n-alkylamines by γ-titanium phosphate. Synthesis of new materials by thermal treatment of the intercalation compounds. Chem. Mater. 8, 1078.

Menéndez, F., Espina, A., Trobajo, C., Rodríguez, J., 1990. Intercalation of n-alkylamines by lamellar materials of the α-zirconium phosphate type. Mater. Res. Bull. 25, 1531.

Mrad, O., Abdul-Hadi, A., Arsan, H., 2011. Preparation and characterization of three different phases of zirconium phosphate: study of sorption of ^{234}Th, ^{238}U, ^{134}Cs. J. Radioanal. Nucl. Chem. 287, 177.

Ortiz-Oliveros, H.B., Flores-Espinosa, R.M., Ordóñez-Regil, E., Fernández- Valverde, S.M., 2014. Synthesis of α-$Ti(HPO_4)_2{\cdot}H_2O$ and sorption of Eu (III). Chem. Eng. J. 236, 398.

Salvadó, M.A., Pertierra, P., García-Granda, S., García, J.R., Rodríguez, J., Fernández-Díaz, M.T., 1996. Neutron powder diffraction study of α-$Ti(HPO_4)_2{\cdot}H_2O$ and [alpha]-$Hf(HPO_4)_2{\cdot}H_2O$; H-atom positions. Erratum. Acta Cryst. B52, 896.

Trobajo, C., Suárez, M., Rodríguez, J., 1991. Quantitative extraction of uranium(VI) in aqueous solutions with n-alkylamine intercalates of γ-titanium phosphate. J. Radioanal. Nucl. Chem. 149, 67.

Zhuravlev, I., Zakutevsky, O., Psareva, T., Kanibolotsky, V., Strelko, V., Taffet, M., Gallios, G., 2002. Uranium sorption on amorphous titanium and zirconium phosphates modified by Al^{3+} or Fe^{3+} ions. J. Radioanal. Nucl. Chem. 254, 85.

α-Titanium phosphate intercalated with propylamine: An alternative pathway for efficient europium(III) uptake into layered tetravalent metal phosphates

Jorge García-Glez[a], Camino Trobajo[a], Sergei A. Khainakov[b], Zakariae Amghouz[b,*]

[a]*Department of Organic and Inorganic Chemistry, and* [b]*Scientific and Technical Services, University of Oviedo-CINN, 33006 Oviedo, Spain*

**Corresponding author E-mail address: amghouz.uo@uniovi.es*

Electronic Supporting Information

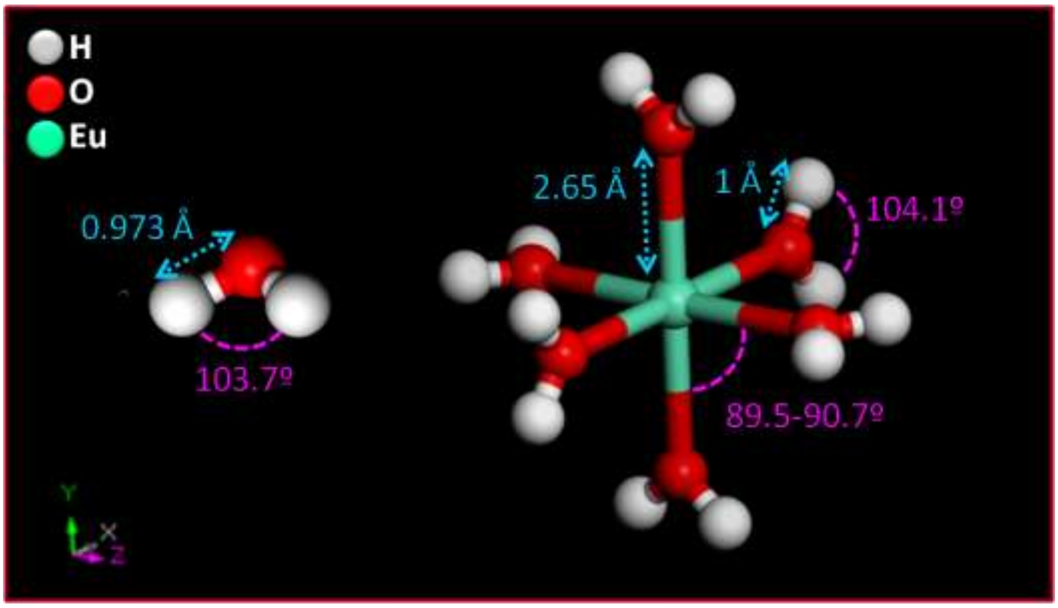

Figure S1. The optimization results by DFT methods of bond lengths and angles for free H_2O molecule and $Eu(H_2O)_6^{3+}$ cation.

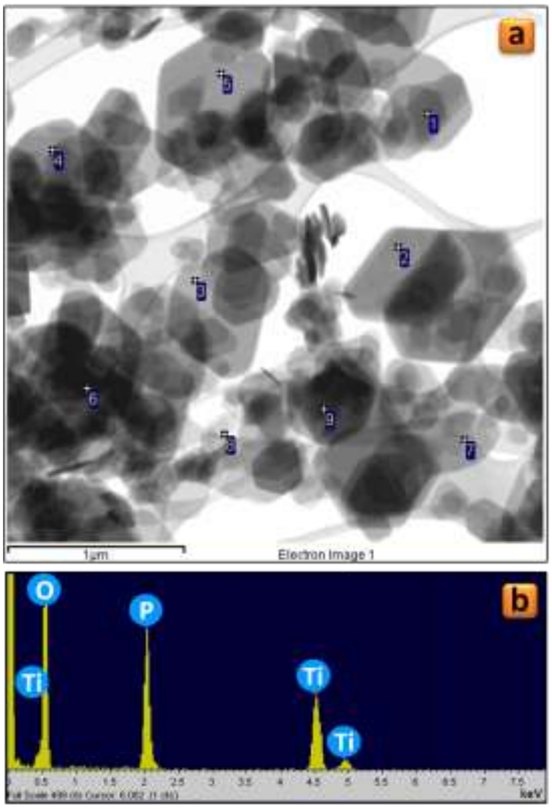

Figure S2. BF-STEM image (a) and a typical EDX spectrum (b) for **TiP_10^{-4}** sample.

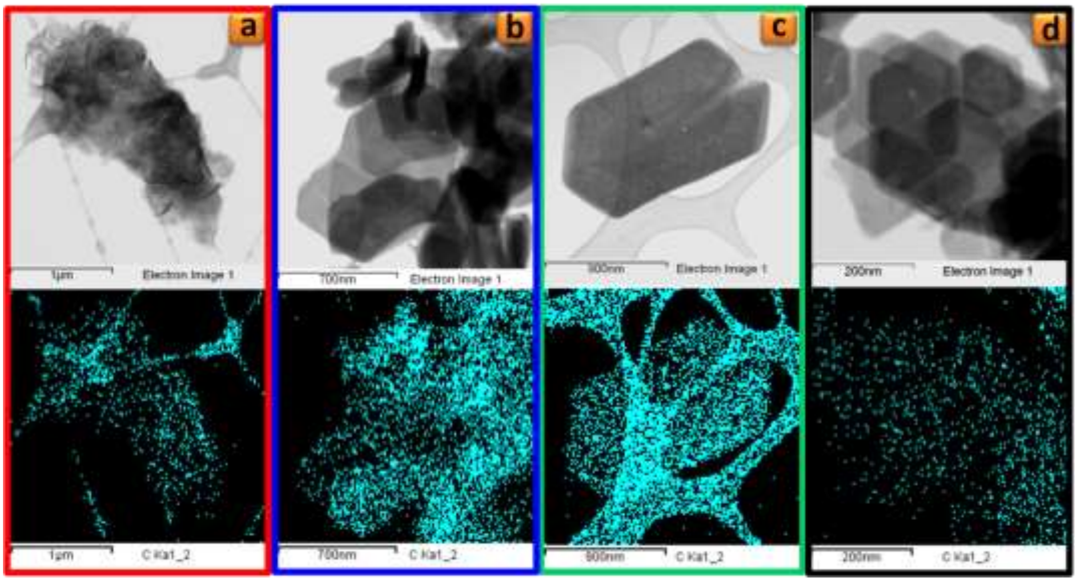

Figure S3. STEM-EDS elemental mapping of **TiPPr_10^{-4}** (a), **TiPPr_0.05** (b), **TiPPr_0.075** (c) and **TiPPr_0.1** (d) samples, where the C-Kα_{1-2} map is shown in cyan color.

3.2. Evolución Térmica de los Materiales

El estudio de la cinética de las reacciones en estado sólido persigue conocer el mecanismo de estos procesos químicos, así como permitir el acceso a parámetros relacionados con ellos, proporcionando información cuali- y cuantitativa sobre transformaciones de fase, procesos de cristalización o descomposición térmica de materiales, entre otros [396]. Con este fin, habitualmente se utilizan datos experimentales obtenidos a partir de los análisis termo-gravimétricos (TGAs), para cuyo tratamiento matemático es esencial tener en consideración las recomendaciones del Comité Cinético de la Confederación Internacional de Análisis Térmico y Calorimetría (ICTAC, *International Confederation for Thermal Analysis and Calorimetry*) [397], uno de cuyos objetivos es ayudar a un no experto a realizar el análisis de manera eficiente, e interpretar adecuadamente los resultados obtenidos. De acuerdo con la ICTAC, el primer paso que debe realizar un usuario de estas técnicas es obtener datos cinéticos de calidad a, al menos, tres velocidades de calentamiento diferentes. El segundo paso será aplicar un método iso-conversional para el tratamiento de dichos datos. La obtención de la dependencia de la energía de activación (E) con el grado de conversión (α) es suficiente para realizar predicciones cinéticas por lo que, si éste es el único objetivo del análisis cinético, no serán necesarios más cálculos. Sin embargo, se pueden utilizar modelos de ajuste para analizar la dependencia de E con α y evaluar los parámetros de la ecuación de velocidad, por lo que la obtención del triplete (A, E, $f(\alpha)$) será el tercer paso a alcanzar en los cálculos cinéticos. Finalmente, como cuarto paso, se recomienda validar los parámetros cinéticos calculados, con el fin de demostrar que se pueden reproducir satisfactoriamente las curvas cinéticas experimentales a partir de las que se calcularon dichos parámetros, aunque una validación más rigurosa consistirá en probar si los parámetros cinéticos calculados pueden usarse para predecir una curva experimental no incluida en los cálculos que condujeron a su obtención.

Una reacción de descomposición simple, estimulada térmicamente, sigue el esquema $Re \rightarrow P + S$ donde Re es el reactivo, P el producto sólido y S el vapor evacuado en el proceso. El progreso de la reacción viene dado por el grado de conversión, $\alpha(t) = (m_0 - m(t)) / (m_0 - m_f)$, donde $m(t)$ es la masa de Re en el tiempo t, y m_0 y m_f son las masas inicial y final, respectivamente. Estas reacciones son comúnmente descritas por la Ecuación (1), donde α es el grado conversión, t el tiempo, T la temperatura, A el factor de Arrhenius, E la energía de activación, R la constante universal de los gases y $f(\alpha)$ el modelo de reacción. Aunque los mecanismos en las reacciones en estado sólido suelen ser complejos e implicar varias etapas de reacción, la Ecuación (1) representa un modelo simple que puede utilizarse para realizar una aproximación a la cinética del proceso [397-399].

$$\frac{\mathrm{d}\alpha}{\mathrm{d}t} = A \exp\left(-\frac{E}{RT}\right) f(\alpha) \tag{1}$$

A lo largo de las últimas décadas, se han desarrollado varios métodos para estimar los parámetros cinéticos de reacciones en fase sólida, resultando los más confiables aquellos que utilizan formalismos iso-conversionales (el principio de iso-conversión establece que, para un valor determinado del grado de conversión, α, la velocidad de reacción solamente depende de la temperatura). Los datos experimentales se obtienen utilizando diferentes programas de calefacción, generalmente a velocidades de calentamiento (β) constantes, $T = T_0 + \beta_i t$, que posteriormente son tratados para obtener la energía de activación del proceso para cada grado de conversión (α).

El método diferencial de Friedman (Ec. (2)) [400] es consecuencia de tomar logaritmos en la Ecuación (1), donde $T_{\alpha,i}$ representa la temperatura a la que se alcanza α en un programa de calentamiento *i*. Así, representando $\ln\left(\left(\frac{\mathrm{d}\alpha}{\mathrm{d}t}\right)_{\alpha,i}\right)$ frente a $1/T_{\alpha,i}$, se puede estimar el valor de E_α.

$$\ln\left(\left(\frac{\mathrm{d}\alpha}{\mathrm{d}t}\right)_{\alpha,i}\right) = \ln(Af(\alpha)) - \frac{E}{RT_{\alpha,i}} \tag{2}$$

El método de Friedman resulta muy sensible al ruido experimental, en particular cuando se aplica a datos procedentes de análisis termo-gravimétricos. Intentando atemperar este inconveniente, recientemente, Huidobro *et al.* [401] han propuesto una modificación de dicho método (HMFM, *Huidobro's Modified Friedman Method*) donde, dado un valor α, se define un conjunto de cuatro valores incrementales adicionales: $\alpha_j = \alpha$, $\alpha_{j-2} = \alpha - 2\Delta\alpha$, $\alpha_{j-1} = \alpha - \Delta\alpha$, $\alpha_{j+1} = \alpha + \Delta\alpha$, $\alpha_{j+2} = \alpha + 2\Delta\alpha$. Para cada uno de ellos, considerando un número limitado de programas de calentamiento a velocidad constante, la Ecuación (2) transforma en la (3).

$$\ln\left(\frac{\mathrm{d}\alpha(t_{k,i})}{\mathrm{d}t}\right) = \ln(A\, f(\alpha_k)) - \frac{E}{\mathrm{R}T_{k,i}} \tag{3}$$

Asumiendo despreciables las variaciones en la energía de activación en el intervalo $[\alpha_{j-2}, \alpha_{j+2}]$, para cada valor de k, la Ecuación (3) define cinco rectas diferentes con la misma pendiente, $m = -E/R$, de manera que se puede calcular el valor de dicha pendiente ajustando simultáneamente los datos experimentales para todos los puntos, en lugar de para un sólo valor de α.

Como sugiere su nombre, los métodos iso-conversionales integrales son consecuencia de integrar la Ecuación (1), originando la Ecuación (4), donde $g(\alpha) = \int_0^{\alpha} [1/(Af(\alpha))]\,\mathrm{d}\alpha$.

$$g(\alpha) = \int_{t_0}^{t_\alpha} \exp\left(-\frac{E}{RT}\right) \mathrm{dt} \tag{4}$$

La parte derecha de la Ecuación (4) se conoce como integral de temperatura, y no tiene solución analítica. Por esta razón, se han propuesto varias aproximaciones para su cálculo, dando lugar a diferentes métodos iso-conversionales integrales. Aunque algunos de ellos son muy populares [402], muchos han sido criticados debido a la inconsistencia de su formulación, particularmente cuando la energía de activación cambia con el grado de conversión [403,404]. En este ámbito, el método lineal propuesto por Vyazovkin [403,405] es uno de los procedimientos más precisos descritos para el análisis cinético de procesos de descomposición térmica. Para un pequeño incremento de la conversión, $\Delta\alpha$, asumiendo que A es constante durante el intervalo $[\alpha - \Delta\alpha, \alpha]$, la integración de la Ecuación (1) respecto a t conduce a la Ecuación (5), donde $J(E_\alpha) = \int_{t_{\alpha-\Delta\alpha}}^{t_\alpha} \exp(-E_\alpha/RT)\ dt$. Entonces, para un valor dado de α y valores de i comprendidos entre 1 y n, la función $J_{\alpha,i}$ debe ser idéntica. Para obtener E_α, Vyazovkin propone la minimización de la función descrita por la Ecuación (6), usando integración numérica para evaluar $J(E_\alpha)$.

$$\int_{\alpha-\Delta\alpha}^{\alpha} \frac{1}{Af(\alpha)} \mathrm{d}\alpha = J(E_\alpha) \tag{5}$$

$$\Phi(E_\alpha) = \sum_{i=1}^{n} \sum_{j \neq i}^{n} \frac{J_i(E_\alpha)}{J_j(E_\alpha)} \tag{6}$$

En el Artículo S2 se demostró que, aprovechando sus propiedades de intercalación e intercambio iónico, pueden realizarse con éxito modificaciones químicas en el α-TiP. En conexión con el Artículo I, se describió que la morfología de las partículas de las formas intercaladas y de intercambio iónico (α-TiPPr y α-EuTiPPr, respectivamente) es similar a la del compuesto precursor (α-TiP). Sin embargo, tanto el análisis térmico como la resonancia magnética nuclear en estado sólido (SS-NMR, *Solid-State Nuclear Magnetic Resonance*) detectaron diferencias estructurales entre los tres materiales. Además, se estimó la energía de activación aparente para las etapas de descomposición termo-oxidativa observadas en los experimentos TG para todos ellos, demostrándose una excelente concordancia entre los resultados obtenidos por los métodos diferencial e integral aplicados a todos los sistemas en estudio.

En el Artículo S3, se describió la preparación de la sal amónica del γ-fosfato de titanio por tratamiento hidrotermal de la fase π-$Ti_2O(PO_4)\cdot 2H_2O$ (π-TiP), en presencia de urea y ácido fosfórico. A partir de datos de PXRD, se determinó su estructura cristalina. γ-$Ti(PO_4)(NH_4HPO_4)$ presenta simetría monoclínica (grupo espacial $P2_1/m$, a = 5.0725(3) Å, b = 6.3101(3) Å, c = 11.2435(5) Å, β = 97.980(3)º, Z = 2), definida por láminas de γ-fosfato de titanio cargadas negativamente, localizándose tanto los átomos de titanio como uno de los dos tipos de grupos fosfato en el plano de la lámina (*ab*). La totalidad de los átomos de oxígeno de estos grupos fosfato participan en la esfera de coordinación del titanio. La segunda clase de grupos fosfato se ubica en los bordes de las láminas, uniendo dos átomos de titanio vecinos, en la dirección *a*, mediante dos de sus átomos de oxígeno. Los dos oxígenos restantes se orientan hacia el espacio interlaminar, relacionados mediante enlaces de hidrógeno con los cationes amonio, que contrarrestan la carga negativa de la lámina, interaccionando cada catión amonio con cuatro oxígenos pertenecientes a cuatro grupos hidroxilo de fosfatos diferentes. La transformación térmica del γ-$Ti(PO_4)(NH_4HPO_4)$ en TiP_2O_7 se monitorizó mediante TGA, calorimetría diferencial de barrido (DSC, *Differential Scanning Calorimetry*), espectrometría de masas (MS, *Mass Spectrometry*) y termo-difracción de rayos X de polvo cristalino (HT-PXRD, *High-Temperature Powder X-Ray Diffraction*). γ-$Ti(PO_4)(NH_4HPO_4)$ es estable por debajo de 450 K, transformándose a partir de esa temperatura en un nuevo polimorfo, γ'-$Ti(PO_4)(NH_4HPO_4)$, que comienza a descomponer por encima de 570 K, obteniéndose difosfato de titanio como producto final, con la formación previa de dos compuestos intermedios pseudo-laminares, $Ti(PO_4)(NH_4HP_2O_7)_{0.5}$ y $Ti(PO_4)(H_2P_2O_7)_{0.5}$. Para todo el intervalo del proceso, se determinó la energía de activación en función del grado de conversión, aplicando el método isoconversional de Kissinger-Akahira-Sunose (KAS) a datos termogravimétricos.

En el Artículo II, en condiciones hidrotermales, se obtuvo un fosfato doble de amonio-titanio(IV) policristalino con estructura tipo pirocloro, formulado previamente como $(NH_4)_{0.79}(P_{1.14}Ti_{0.86})O_{3.93}(OH)_{2.07}$ [406]. El material se caracterizó por HT-PXRD, microscopia electrónica (SEM y TEM) y análisis térmico (TG/DTA-MS). La muestra está constituida por partículas quasi-esféricas (diámetro ~25 nm) que, en medios acuosos, tienden a auto-ensamblarse para originar fibras poli-cristalinas. Los análisis termogravimétricos demostraron diferencias significativas cuando la descomposición térmica se produce en atmósfera inerte (N_2) u oxidante (O_2), revelando la presencia en el material de una fracción significativa de P(III), concluyendo que la muestra es de hecho un material de valencia mixta (fosfato-fosfito). Además, se determinó la energía de activación del proceso de descomposición térmica en función del grado de conversión aplicando el método de iso-conversional de Vyazovkin a datos termogravimétricos.

En el artículo S4, se preparó un oxofosfato de titanio(IV) fibroso, ρ-$Ti_2O(PO_4)_2 \cdot 2H_2O$ (ρ-TiP), un polimorfo del compuesto de partida (π-TiP) utilizado para la preparación de la nueva fase laminar descrita en el Artículo S3 (γ-$Ti(PO_4)(NH_4HPO_4)$), cuya síntesis había sido reportada previamente por nuestro grupo [407]. La muestra fresca (ρ-TiP) se trató térmicamente en atmósfera de aire 673 K durante 24 h y, posteriormente, se almacenó en el laboratorio a temperatura ambiente durante diferentes periodos de tiempo. Después de 1 día, 2 meses y 1 año, las muestras se caracterizaron por PXRD, SEM, ^{31}P SS-NMR y análisis térmico, observándose que el material fresco y los activados térmicamente (y estos entre sí) presentan comportamientos térmicos diferenciados, siendo la descomposición térmica de algunos de estos materiales un proceso complejo consecuencia de su capacidad para adsorber gases (N_2) a temperaturas superiores a la ambiente. En muestras activadas térmicamente, la ganancia de masa aparente y la pérdida de masa total cambian en función del tiempo de almacenamiento. El hecho de que ambos parámetros sean inversamente proporcionales indica que la rehidratación del material inhibe su capacidad para retener gases. Además, para la muestra de ρ-TiP, se obtuvo la energía de activación del proceso de descomposición térmica como una función del grado de conversión utilizando el método diferencial HMFM y el procedimiento integral de Vyazovkin. Nuevamente, ambas aproximaciones proporcionan resultados similares, lográndose un excelente acuerdo entre las curvas α–T reconstruidas y las experimentales, a pesar de tratarse de un proceso complejo, que incluye procesos solapados de desorción/adsorción.

Artículo II

“Morphological study and thermal behaviour of an ammonium-titanium(IV) phosphate with pyrochlore-type structure”

Journal of Thermal Analysis and Calorimetry

Vol. 125

Pág. 1087–1093

Año 2016

DOI: 10.1007/s10973-016-5585-5

Índice de Impacto: 1.953

J Therm Anal Calorim (2016) 125:1087–1093
DOI 10.1007/s10973-016-5585-5

Morphological study and thermal behaviour of an ammonium-titanium(IV) phosphate with pyrochlore-type structure

Jorge García-Glez[1] · **Belén F. Alfonso**[2] · **José A. Huidobro**[3] · **Zakariae Amghouz**[4] · **Camino Trobajo**[1]

Received: 14 October 2015 / Accepted: 21 May 2016 / Published online: 14 June 2016

Abstract Polycrystalline ammonium-titanium(IV) phosphate with pyrochlore-type structure has been obtained under hydrothermal conditions and characterised by powder X-ray thermodiffractometry (HT-pXRD), electron microscopy (SEM and TEM) and thermal analysis (TG/SDTA–MS). Moreover, the activation energy of thermal decomposition has been calculated as a function of the extent of conversion applying the Vyazovkin isoconversional method to the thermogravimetric data. The sample is constituted by nearly spherical plate-like particles (diameter ca. 25 nm) which in an aqueous medium are prone to auto-assembling to originate polycrystalline fibres. Thermogravimetric analysis showed significant differences between the thermal decomposition behaviour in inert (N_2) and oxidiser (O_2) atmospheres (e.g. the total mass loss), revealing the presence of a fraction of P(III) which oxidises to P(V) when the N_2 atmosphere is replaced at 823 K by O_2 atmosphere.

Keywords Titanium phosphate · Pyrochlore · Morphology · Thermal decomposition · Kinetic analysis

Introduction

Pyrochlore is an end member of a solid-solution series between itself and the mineral microlite, (Ca, Na)$_2$(Nb, Ta)$_2$O$_6$(O, OH, F). Both minerals have similar structures and properties, but microlite is the tantalum-rich end member, whereas pyrochlore is the niobium-rich end member of this series. The generally lighter pyrochlore is found in a rather unusual igneous rock called carbonatite and also in alkali pegmatites called nepheline syenites [1]. Pyrochlore-type minerals allow the structural inclusion of many different elements and frequently appear associated to phosphorus minerals. The pyrochlore group is basically composed of three minerals (pyrochlore, betafite and microlite) and other respective subgroup members [2]. All have the general formula $A_{2-x}B_2O_6(O, OH, F)\cdot nH_2O$, where *A* may belong to a long list of metal ions: lead, iron, calcium, potassium, bismuth, sodium, barium, cerium, caesium, tin, strontium, thorium, uranium, yttrium, zirconium and/or antimony, while *B* represents an octahedral site in the structure and can be any of the following metal ions: niobium, tungsten, tin, tantalum and/or titanium. In the course of our systematic research, the hydrothermal synthesis has been used to synthesise new materials exhibiting promising ion-exchange properties [3–10], such as ammonium-titanium(IV) phosphate, $(NH_4)_{0.79}(P_{1.14}Ti_{0.86})O_{3.93}(OH)_{2.07}$, with a pyrochlore-type structure [11]. Its framework is made up of MO_6 ($M = P, Ti$) octahedra connected by vertices, where *M* atoms occupy the 16*c* site, the 8*b* site is partially occupied by NH_4^+, the 16*d* site remains unoccupied, and OH^- are located at the 48*f* site. In this contribution, we report the morphological characterisation of this compound and its thermal decomposition data.

✉ Camino Trobajo
ctf@uniovi.es

[1] Departamento de Química Orgánica e Inorgánica, Universidad de Oviedo-CINN, 33006 Oviedo, Spain

[2] Departamento de Física, Universidad de Oviedo-CINN, 33006 Oviedo, Spain

[3] Departamento de Matemáticas, Universidad de Oviedo-CINN, 33006 Oviedo, Spain

[4] Servicios Científico-Técnicos, Universidad de Oviedo-CINN, 33006 Oviedo, Spain

Experimental and methodology

Sample preparation and analytical procedures

Hydrothermal synthesis was carried out in a stainless steel (100 mL) Teflon-lined vessel under autogenous pressure. $(NH_2)_2CO$ (solid), H_3PO_3 (solid), H_2O_2 (33 vol%) and $TiCl_4$ (4 M) were mixed in the molar ratio 3:1:8:0.6:100 ($TiCl_4/H_3PO_3/(NH_2)_2CO/H_2O_2/H_2O$). The autoclave was sealed and heated at 453 K for 5 days. The solid obtained was filtered off, washed with an excess of the distilled water, and dried in air at room temperature, as previously reported [11]. The phosphorus and titanium contents of the solids were determined by inductively coupled plasma mass spectrometry (ICP-MS) analysis (Finnigan, Element model) after dissolving a weighed amount in HF(aq). Microanalytical data (C, H and N) were determined by an Elementar Model Vario MACRO elemental analyser. Elemental analysis (mass%): P 18.7, Ti 21.8, N 5.9, H 2.6 (calculated for $(NH_4)_{0.79}(P_{1.14}Ti_{0.86})O_{3.93}(OH)_{2.07}$: P 18.68, Ti 21.78, N 5.85, H 2.79).

Powder diffraction studies

Room temperature powder X-ray diffraction patterns were collected on an X'Pert PRO MPD X-ray diffractometer with PIXcel detector, operating in the Bragg–Brentano ($\theta/2\theta$) geometry, using CuK_α radiation ($\lambda = 1.5418$ Å). For the powder X-ray thermodiffraction studies in air and vacuum, the sample was placed in an Anton Paar HTK 1200 N oven chamber, on a PANalytical XPERT PRO diffractometer, using CuK_α radiation, equipped with PIXcel linear detector with 255 channels. Each powder pattern was recorded in the 10°–60° range (2θ) with a step of 0.013° and a counting time of 0.424 s channel^{-1}. Temperature intervals of 50 K, from room temperature up to 773 K, and 100 K from 773 K up to 1173 K were chosen. The temperature ramp between two consecutive temperatures was 10 K min^{-1}.

Electron microscopy studies

SEM images were obtained by using JEOL 6610VL scanning electron microscope operating at 20 kV and equipped with an X-Max Silicon Drift Detector for EDX analysis. TEM images and selected area electron diffraction (SAED) pattern were collected on a JEOL JEM-2100F field emission transmission electron microscope operated at an accelerating voltage of 200 kV and equipped with an ultra-high-resolution pole piece that provided a point resolution better than 0.19 nm. It is also equipped with STEM control unit (Gatan), EDX detector (Oxford Instruments, 80 mm^2 X-Max Silicon Drift Detector), CCD camera (14-bit Gatan Orius SC600), and bright-field (BF) and HAADF detectors (JEOL). Fine powder of the sample was dispersed in ethanol, sonified and sprayed on a carbon-coated copper grid, and then allowed to air-dry. Finally, SOLARUS 950 Advanced Plasma Cleaning System was used before observation.

Thermal analysis

A Mettler-Toledo TGA/SDTA851^e was used for the thermal analyses in dynamic nitrogen atmosphere (50 mL min^{-1}) at a heating rate of 10 K min^{-1}. In all cases, ca. 15 mg of powder sample was thermally treated, and blank runs were performed. A Pfeiffer Vacuum ThermoStar™ GSD301T mass spectrometer was used to determine the evacuated vapours. The masses 15 (NH_3) and 18 (H_2O) were tested by using a detector C-SEM, operating at 1200 V, with a time constant of 1 s.

Determination of kinetic parameters

The kinetics of a solid-state reaction, in conditions far from equilibrium, can be described by the general equation

$$\frac{d\alpha}{dt} = A\exp(-E/RT)f(\alpha) \tag{1}$$

where $f(\alpha)$ is the reaction model, α is the extent of conversion, which is determined experimentally as a fraction of the total mass loss in the process, T is the temperature, t is the time, A is the pre-exponential factor, E is the activation energy, and R is the gas constant. The dependence of the temperature is assumed given by the Arrhenius equation [12]. For a non-isothermal process with a constant heating rate, $T = T_0 + \beta t$, Eq. (1) can be written as

$$\frac{d\alpha}{dT} = \frac{A}{\beta}\exp(-E/RT)f(\alpha) \tag{2}$$

In this research, we study the thermal decomposition of $(NH_4)_{0.79}(P_{1.14}Ti_{0.86})O_{3.93}(OH)_{2.07}$ combining several experimental techniques: thermogravimetric analysis (associated with mass spectrometry) and powder X-ray thermodiffraction measurements. An isoconversional method is used to perform the kinetics analysis because it allows estimating the activation energy as a function of the extent of conversion, without the need to specify either the reaction model or the pre-exponential factor. The basic assumption of isoconversional methods is that the reaction rate for a constant extent of conversion depends only on temperature [13]. An important number of mathematical methods have been developed to evaluate solid-state kinetics and get the kinetic parameters from thermal experimental data: differential and integral methods. The differential methods are very sensitive to experimental noise and tend to be numerically unstable partially because the rate is computed by numerical differentiation [14, 15]. The integral methods may lead to important errors in the activation energy values due to fact that some approximations are used for estimation of the temperature integral and their intrinsic inconsistency when the activation energy changes with α [13, 16, 17]. In any case, the physical meaning of the obtained results should be treated with care [17, 18].

In the kinetic study, we use the nonlinear method proposed by Vyazovkin [19, 20], which is included in the family of incremental integral methods. These methods were developed assuming that activation energy is constant in a small interval. The activation energy is obtained by minimisation of the function

$$\Phi(E_\alpha) = \sum_{i=1}^{n} \sum_{j \neq i}^{n} \frac{J_i(E_\alpha)}{J_j(E_\alpha)} \tag{3}$$

where

$$J_i(E_\alpha) = \int_{t_{\alpha i}-\Delta\alpha}^{t_{\alpha,i}} \exp\left(-\frac{E_\alpha}{RT_{\alpha i}}\right) \mathrm{d}t \tag{4}$$

Four different heating rates were used ($\beta = 5$, 10, 15 and 20 K min^{-1}) for the thermal treatment of a certain amount (ca. 15 mg) of title compound in a nitrogen dynamic atmosphere (50 mL min^{-1}).

Results and discussion

For $(NH_4)_{0.79}(P_{1.14}Ti_{0.86})O_{3.93}(OH)_{2.07}$, the SEM micrograph (Fig. 1a) shows small homogeneous spherical particles of ca. 0.1 µm of diameter that, in aqueous suspension, are prone to auto-assembling to originate polycrystalline fibres (Fig. 1b). Transmission electron microscopy (TEM) images displayed in Fig. 2a, b show the presence of small primary particles with nearly spherical plate-like shapes and average size of 25 nm comparable to the mean crystallite diameter obtained from PXRD data (22 ± 4 nm). Selected area electron diffraction (SAED) pattern (Fig. 2c) shows the polycrystalline nature of the sample, and all the rings have been indexed as cubic structure [$a = 9.9551(9)$ Å, space group: Fd-3m] [11] described for $(NH_4)_{0.79}(P_{1.14}Ti_{0.86})O_{3.93}(OH)_{2.07}$, with interplanar spaces of 5.7, 3.0 and 2.8 Å corresponding, respectively, to (111), (311) and (222) atomic planes. SAED and PXRD (Fig. 3) patterns are found to agree that the (111) plane showed the most intense reflection.

Experimental data previously reported [11] for the thermal decomposition (in N_2 atmosphere) of $(NH_4)_{0.79}(P_{1.14}Ti_{0.86})O_{3.93}(OH)_{2.07}$ indicate that the final product is a mixture of two crystalline phases: TiP_2O_7 and $(TiO)_2P_2O_7$. In this work, the thermal transformation was monitored by powder X-ray thermodiffraction (in air and vacuum) from room temperature to 1173 K (Fig. 3). The starting phase is stable up to 523 and 473 K in air and vacuum, respectively. The variations of the unit cell parameters from room temperature to 523 K in air (473 K in vacuum) are illustrated in Fig. 4. In air, a slight contraction of the cell parameter of ca. 0.5 % has been observed from room temperature to 473 K, while at 523 K, it markedly decreased by ~6 %. Under vacuum, the cell parameter at 298 K decreased by ~0.5 % compared to air, then it is slightly decreased by ~0.2 % up to 423 K, and finally it decreased by ~5 % at 473 K. In air, higher temperatures provoke the decomposition of this compound and the formation of an amorphous material, which at 1073 K crystallises to TiP_2O_7 (JCPDS PDF #052-1469) [21]. However, under vacuum condition, a complex mixture of TiP_2O_7 (JCPDS PDF #052-1469) [21], $Ti_4P_6O_{23}$ (JCPDS PDF #039-0004) [22] and TiO_2 (JCPDS PDF #01-076-1936) [23] phases crystallises at 873 K, where TiO_2 phases evolved to anatase-TiO_2 (JCPDS PDF #01-071-1169) [24] at 1173 K.

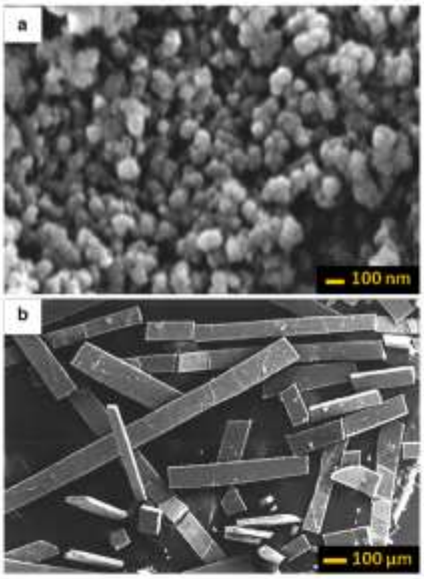

Fig. 1 (Colour online). SEM images, small homogeneous spherical particles (**a**) and polycrystalline fibres (**b**)

The TG/DTG/SDTA curves of $(NH_4)_{0.79}(P_{1.14}Ti_{0.86})O_{3.93}(OH)_{2.07}$ under N_2 atmosphere, depicted in Fig. 5a, show a total mass loss of 21.6 % (cal. 20.74 %) up to 1273 K. The DTG curve shows two minima at ca. 378 and

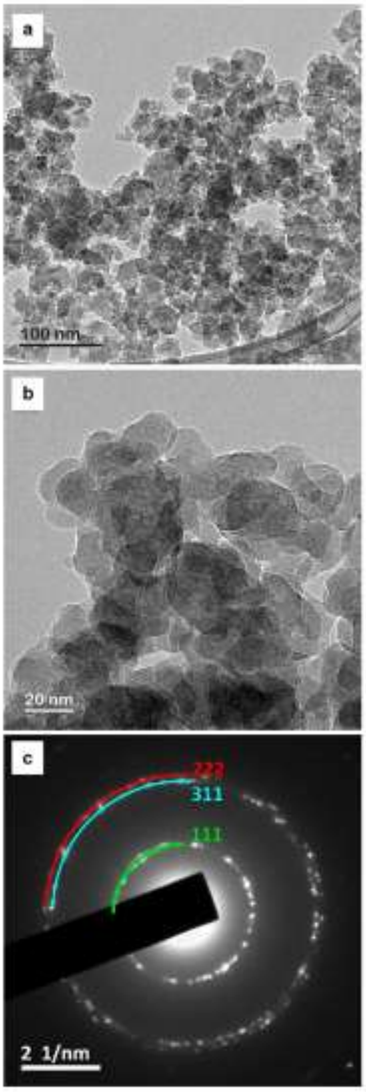

Fig. 2 (Colour online). TEM images (**a**, **b**) and SAED pattern (**c**)

633 K, indicating two consecutives decomposition processes and associated with two endothermic bands in the SDTA curve, while at ca. 1073 K, an additional exothermic peak is observed, which is due to crystallisation of the amorphous material produced by thermal decomposition of the starting material, in good agreement with HT-pXRD studies. In the range 850–1273 K, the TG curve shows a small but noticeable mass gain (ca. 0.4 %), which is

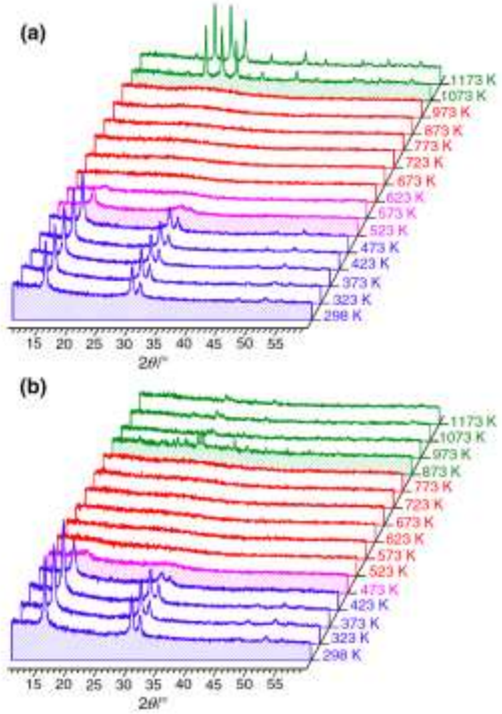

Fig. 3 (Colour online). Powder X-ray thermodiffraction patterns of the sample recorded in air (**a**) and vacuum (**b**) heating up from 298 to 1173 K. Colour code corresponding to the structural change. *Blue* $(NH_4)_{0.79}(P_{1.14}Ti_{0.86})O_{3.93}(OH)_{2.07}$, *pink* begging of $(NH_4)_{0.79}(P_{1.14}Ti_{0.86})O_{3.93}(OH)_{2.07}$ amorphisation, *red* the complete amorphisation of $(NH_4)_{0.79}(P_{1.14}Ti_{0.86})O_{3.93}(OH)_{2.07}$, *green* transformation to TiP_2O_7, $Ti_4P_6O_{23}$ and TiO_2 phases

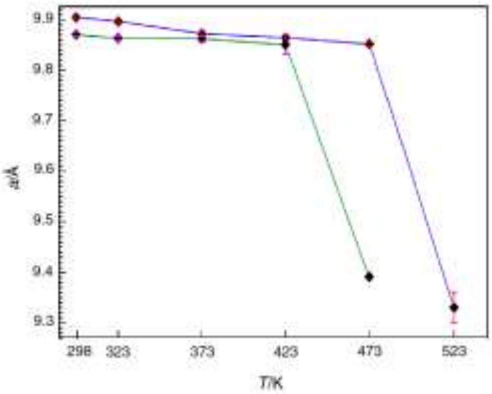

Fig. 4 (Colour online). Variation of the *a*-axis lattice parameter versus temperature, air (*blue*) and vacuum (*green*) conditions

probably due to the oxidation processes caused by O_2 traces in the N_2 atmosphere. The associated mass spectrometric analysis shown in Fig. 5b is in good agreement with the TG/DTG/SDTA curves. The MS signal related to water (*m/z* 18, H_2O) has two maxima, where the first one tends to be smaller than the second. However, the MS signal associated to ammonia (*m/z* 15, NH_3) has only one maximum, which coincides with the second maximum of *m/z* 18 signal. This behaviour indicates that a fraction of the dehydroxylation process occurs before the ammonium cation decomposition. The first evacuation process appears in the range of 353–533 K with the loss of ca. 7.2 % of H_2O. Later, in the interval 533–823 K, the evacuation of NH_3 and the rest of H_2O (ca. 14.4 %) takes place. Finally, after treatment up to 1273 K, a mixture of two crystalline phases was obtained, TiP_2O_7 and $(TiO)_2P_2O_7$. The difference between the final decomposition products obtained in the case of HT-pXRD (under air or vacuum) and TG (in N_2 atmosphere) experiments could be assigned to the atmosphere used in each case. Nevertheless, the thermogravimetric analysis showed significant differences between the thermal behaviour in inert (N_2) and oxidiser (O_2) atmospheres (Fig. 6), where the total mass loss were 21.6 and 20.3 %, respectively. The lower total mass loss observed in the case of O_2 atmosphere compared to N_2 atmosphere, which could not be negligible, made us to carry out another TG experiment in N_2 atmosphere which was replaced at 825 K by O_2 atmosphere (Fig. 6). Given the fact that the material has the white colour, the presence of detectable titanium(III) species should be discarded, so this very sensitive thermal experiment has revealed the presence of a fraction of P(III) [which in O_2 atmosphere oxidises to P(V)] unnoticed by other sophisticated characterisation techniques.

Figure 7 shows the conversion curves for the thermal decomposition of $(NH_4)_{0.79}(P_{1.14}Ti_{0.86})O_{3.93}(OH)_{2.07}$ at four different heating rates ($\beta = 5, 10, 15$ and $20\ K\ min^{-1}$) in inert atmosphere as a function of temperature. As can be observed, the heating rate does not affect the mass loss, although it has an effect on the shape of the conversion curves which moves to higher temperatures as the heating rate increases. Application of the Vyazovkin method leads to the calculation of the activation energy as a function of the extent of conversion (Fig. 8). As can be deduced, the activation energy increases rapidly (from ca. 65 to 115 kJ mol^{-1}) until the conversion is ca. 0.4. In this stage, desorption of approximately 50 % of H_2O takes place.

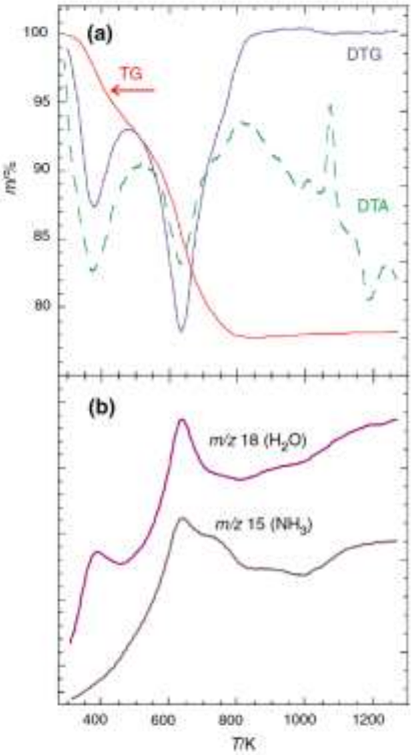

Fig. 5 (Colour online). TG (*red*), DTG (*blue*) and DTA (*green*) curves of $(NH_4)_{0.79}(P_{1.14}Ti_{0.86})O_{3.93}(OH)_{2.07}$ obtained at 10 K min^{-1} heating rate in N_2 atmosphere (**a**). MS signals of evacuated vapours on the TG experiment: *m/z* 15 (NH_3) and *m/z* 18 (H_2O) (**b**)

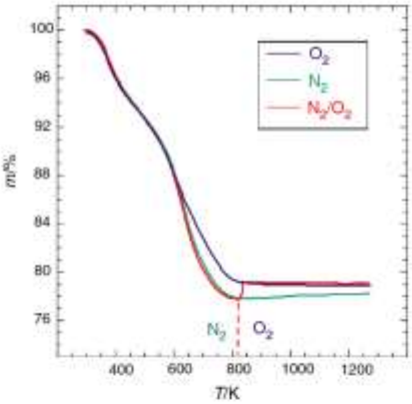

Fig. 6 (Colour online). TG curves of $(NH_4)_{0.79}(P_{1.14}Ti_{0.86})O_{3.93}(OH)_{2.07}$ obtained at 10 K min^{-1} heating rate; *red* TG curve obtained in O_2 atmosphere; *blue* TG curve obtained in N_2 atmosphere; *green* TG curve obtained in N_2 atmosphere up to 823 K and in O_2 atmosphere higher than 823 K

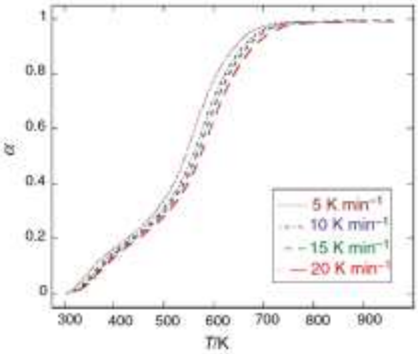

Fig. 7 (Colour online). Thermal decomposition of $(NH_4)_{0.79}(P_{1.14}$-$Ti_{0.86})O_{3.93}(OH)_{2.07}$: conversion curves in N_2 atmosphere as a function of temperature at different heating rates

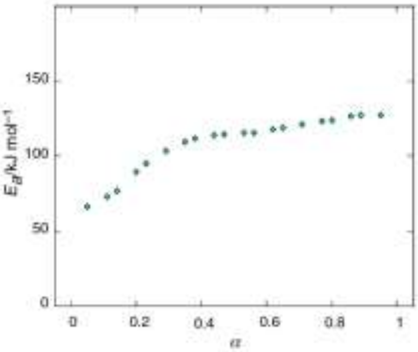

Fig. 8 (Colour online). Thermal decomposition of $(NH_4)_{0.79}(P_{1.14}$-$Ti_{0.86})O_{3.93}(OH)_{2.07}$: activation energy in N_2 atmosphere versus extent of conversion

Later, E_α increases slightly from ca. 115 to 125 kJ mol^{-1} (0.9 of conversion), which corresponds to the evacuation of NH_3 and the remaining H_2O.

In order to test the results, we have compared the experimental data and the reconstructed α–T curves obtained from the computed kinetic parameters for the same heating rates used in the laboratory. These curves have been reconstructed following the idea of Wu et al. [25]. So, Eq. (2) has been written in the form

$$\beta \frac{d\alpha}{dT} = Af(\alpha)\exp(-E/RT) \tag{5}$$

In this case, instead of applying the Friedman method as in [25], since the activation energy has already been computed, the following problem is considered: find c_α such that

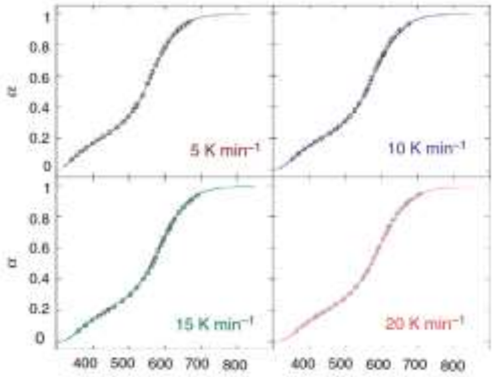

Fig. 9 (Colour online). Calculated (*lines*) and experimental (*open circles*) α–T curves for $(NH_4)_{0.79}(P_{1.14}Ti_{0.86})O_{3.93}(OH)_{2.07}$

$$\beta_i\left(\frac{d\alpha(T_{\alpha,i})}{dT}\right) = c_\alpha \exp\left(-\frac{E_\alpha}{RT_{\alpha,i}}\right), \quad i = 1, \ldots, n \tag{6}$$

This means that the points $(\exp(-\frac{E_\alpha}{RT_{\alpha,i}}), \beta_i(\frac{d\alpha(T_{\alpha,i})}{dT}))$ lie on a straight line passing through the origin, and then, its slope $c_\alpha = Af(\alpha)$ can be obtained by the least-squares fitting method. Then, after knowing E_α and the product $Af(\alpha)$, for a particular heating rate β_i, differential equation (2) can be solved and the α–T curve solution can be plotted. Figure 9 shows a good agreement between the calculated and experimental α–T curves.

Conclusions

The ammonium-titanium(IV) phosphate, previously formulated as $(NH_4)_{0.79}(P_{1.14}Ti_{0.86})O_{3.93}(OH)_{2.07}$, has pyrochlore-type structure, which is built up of MO_6 (M = P, Ti) octahedra connected by vertices. However, the new thermal analysis data reported in this work indicate that this material is in fact a mixed valence compound [an ammonium-titanium(IV) phosphate–phosphite]. Further structural studies are now being conducted in order to re-establish the chemical formula and the structural features of this interesting pyrochlore-type compound.

Acknowledgements This work is supported by "Ministerio de Economía y Competitividad" (MAT2013-40950-R, MAT2011-27573-C04-02), "Gobierno del Principado de Asturias" (GRUPIN14-060) and FEDER.

References

1. Deer WA, Howie RA, Zussman J. An introduction to the rock forming minerals. Hong Kong: Longman; 1992.
2. Hogarth DD. Classification and nomenclature of the pyrochlore group. Am Minerol. 1977;62:403–10.
3. Salvadó MA, Pertierra P, García-Granda S, García JR, Fernández-García MT, Dooryhee E. Crystal structure, including H-atom positions, of $Ti_2O(PO_4)_2(H_2O)_2$ determined from synchrotron X-ray and neutron powder data. Eur J Solid State Inorg Chem. 1997;34:1237–47.
4. Jaimez E, Bortun AI, Khainakov SA, Voitko II, García JR, Rodríguez J. Hydrothermal preparation of the mixed titanium (IV) phosphate-phenylphosphonates and characterization of their properties. J Mater Res. 1998;13:323–8.
5. Clearfield A, Bortun AI, Bortun LN, García JR. Direct hydrothermal synthesis of zirconium phosphate and zirconium arsenate with a novel basic layered structure in alkaline media. Inorg Chem Commun. 1998;1:206–8.
6. Khainakov SA, Bortun AI, Bortun LN, Clearfield A, Trobajo C, García JR. Hydrothermal synthesis and characterization of alkali metal titanium silicates. J Mater Chem. 1999;9:269–72.
7. Bortun AI, Bortun LN, Khainakov SA, Clearfield A, Trobajo C, García JR. Hydrothermal synthesis and ion exchange properties of the novel framework sodium and potassium niobium silicates. Solvent Extr Ion Exch. 1999;17:649–75.
8. Puziy AM, García JR. Synthesis, characterization and ion exchange properties of the framework sodium titanium germanate $Na_3H(TiO)_3(GeO)(GeO_4)_3 \cdot 7H_2O$. J Radioanal Nucl Chem. 1999;240:851–7.
9. Salvadó MA, Pertierra P, García-Granda S, Espina A, Trobajo C, García JR. Hydrothermal synthesis and structure of Fe(NH3)2PO4: a novel monophosphate. Inorg Chem. 1999;38:5944–7.
10. Trobajo C, Espina A, Jaimez E, Khainakov SA, García JR. Hydrothermal synthesis of iron(III) phosphates in the presence of urea. J Chem Soc Dalton Trans. 2000;5:787–90.
11. García-Granda S, Salvadó MA, Pertierra P, Bortun AI, Khainakov SA, Trobajo C, Espina A, García JR. Hydrothermal synthesis and characterization of an ammonium titanium(IV) phosphate with pyrochlore-type structure. Inorg Chem Commun. 2001;4:555–7.
12. Galwey AK, Brown ME. A theoretical justification for the application of the Arrhenius equation to kinetics of solid state reactions (mainly ionic crystals). Proc R Soc Lond A. 1995;450:501–12.
13. Vyazovkin S. Model-free kinetics. Staying free of multiplying entities without necessity. J Therm Anal Calorim. 2006;83:45–51.
14. Ortega A. A simple and precise linear integral method for isoconversional data. Thermochim Acta. 2008;474:81–6.
15. Vyazovkin S, Burnham AK, Criado JM, Pérez-Maqueda LA, Popescu C, Sbirrazzuoli N. ICTAC Kinetics Committee recommendations for performing kinetic computations on thermal analysis data. Thermochim Acta. 2011;520:1–19.
16. Simon P, Thomas P, Dubaj T, Cibulkova Z, Peller A, Veverka M. The mathematical incorrectness of the integral isoconversional methods in case of variable activation energy and the consequences. J Therm Anal Calorim. 2014;115:853–9.
17. Simon P. Isoconversional methods. Fundamentals, meaning and application. J Therm Anal Calorim. 2004;76:123–32.
18. Maciejewski M. Computational aspects of kinetic analysis. Part B: The ICTAC Kinetics Project—the decomposition kinetics of calcium carbonate revisited, or some tips on survival in the kinetic minefield. Thermochim Acta. 2000;355:145–54.
19. Vyazovkin S. Evaluation of activation energy of thermally stimulated solid-state reactions under arbitrary variation of temperature. J Comput Chem. 1997;18:393–402.
20. Vyazovkin S. Modification of the integral isoconversional method to account for variation in the activation energy. J Comput Chem. 2001;22:178–83.
21. Anderson A, Norby P. Structural aspects of the dehydration and dehydroxylation of γ-titanium phosphate, γ-$Ti(PO_4)(H_2PO_4)$-$2H_2O$. Inorg Chem. 1998;37:4313–20.
22. Ono A. Preparation and properties of $NH_4Ti_2P_3O_{12}$ in the pseudobinary system $NH_4H_2PO_4TiO_2$. J Solid State Chem. 1985;56:260–2.
23. Meagher EP, Lager GA. Polyhedral thermal expansion in the TiO_2 polymorphs; refinement of the crystal structures of rutile and brookite at high temperature. Can Mineral. 1979;17:77–85.
24. Horn M, Schwerdtfeger CF, Meagher EP. Refinement of the structure of anatase at several temperatures. Z Kristallogr Kristallgeom Kristallphys Kristallchem. 1972;136:273–81.
25. Wu W, Cai J, Liu R. Isoconversional kinetic analysis of distributed activation energy model processes for pyrolysis of solid fuels. Ind Eng Chem Res. 2013;52:14376–83.

3.3. Adsorción de Nitrógeno

El nitrógeno es la molécula con mayor presencia en la atmósfera terrestre, por lo que es común encontrarlo como impureza no deseada en corrientes de gases industriales. La captura de este gas o la posibilidad de realizar separaciones selectivas respecto a otros gases resulta de gran interés para multitud de sectores, lo que hace imprescindible el desarrollo de materiales y tecnologías, de bajo coste, capaces de alcanzar ese propósito.

El gas natural, combustible fósil compuesto principalmente de metano, es una fuente de energía limpia y barata. Sin embargo, muchas de sus reservas contienen cantidades elevadas de nitrógeno, haciendo imprescindible su eliminación para alcanzar la calidad requerida en tubería, que debe ser inferior al 4% (en volumen) de N_2 [408]. Aunque, actualmente, la eliminación del nitrógeno en corrientes de metano se consigue por destilación criogénica, el elevado coste económico de la operación hace entrever el uso de procesos de adsorción y tecnologías de membrana como una alternativa económica y energéticamente eficiente para la captura selectiva de N_2.

La adsorción por inversión de presión (PSA, *Pressure Swing Adsorption*) es una tecnología potencialmente interesante para la separación N_2/CH_4. Sin embargo, su escalado a nivel industrial es difícil debido a la falta de un sorbente que posea alta selectividad hacia el nitrógeno. En el equilibrio, para todos los sorbentes conocidos, incluyendo el carbón activo, las zeolitas y los tamices moleculares (gel de sílice, alúmina), la selectividad favorece al metano. En consecuencia, se han buscado sorbentes adecuados para su separación cinética (basada en diferencias en difusividad en los microporos de un material cristalino). Así, el silicato de titanio micro-poroso ETS-4 (ETS, *Engelhard TitanoSilicate*) es capaz de efectuar eficientemente la separación cinética nitrógeno/metano, especialmente cuando se utiliza su forma deshidratada [409], mientras que el uso de zeolitas [410,411] o el diseño de redes metal-orgánicas (MOFs, *Metal-Organic Frameworks*) conteniendo sitios metálicos insaturados, capaces de interaccionar con el N_2, proporciona una relativamente nueva y prometedora ruta para su separación selectiva [412]. Además de en corrientes de metano, la eliminación de nitrógeno es un gran reto para otras muchas aplicaciones relacionadas con el campo de la energía, el medioambiente, la medicina o, incluso, la industria del acero [413].

Por otro lado, el amoníaco es uno de los compuestos de mayor importancia a nivel global ya que se utiliza en grandes cantidades como fuente de fertilizantes nitrogenados y materia prima de numerosos compuestos, tanto orgánicos (aminas, sulfanilamidas) como inorgánicos (ácido nítrico, sales de amonio) [414]. El proceso Haber-Bosch produce aproximadamente 160 millones de toneladas métricas de amoníaco por año, en condiciones muy drásticas de presión (200-500 atm) y temperatura (500-600 ºC) y en presencia de catalizadores de $Fe_3O_4/K_2O/Al_2O_3$ [414,415]. En estas operaciones, que consumen anualmente el 1-2% del suministro de energía primaria mundial [416], el paso determinante para controlar la cinética de la síntesis del amoníaco es la ruptura del enlace N–N. Actualmente, los metales de transición (como Fe o Ru) son indispensables para promover la escisión del enlace N–N [417,418], al igual que la presencia de especies donantes de electrones [419]. Cuando una molécula de N_2 interacciona con un metal de transición, lo hace proporcionándole electrones a través de sus orbitales de enlace y aceptando, por donación posterior, electrones en sus orbitales pi anti-enlazantes. Este último proceso, reforzado por la presencia de especies nucleófilas, coadyuva al debilitamiento del enlace N–N, promoviendo la disociación de la molécula de N_2 [420,421]. A pesar del excelente conocimiento teórico de esta reacción, es extremadamente difícil producir un catalizador eficiente para facilitar su transcurso y que, además, posea la estabilidad química y térmica adecuada para su operatividad industrial [422,423].

La palabra serendipia (*serendipity*) fue acuñada por Horace Walpole en una carta a su amigo sir Horace Mann en 1754 [424]. Walpole quedó impresionado por un relato sobre las aventuras de “Los tres príncipes de Serendip” (Serendip es un antiguo nombre para Ceilán, actual Sri Lanka), los cuales estaban siempre haciendo descubrimientos, por accidente y sagacidad, de cosas que no se habían planteado previamente. Aunque Walpole usó el término para describir alguno de sus propios descubrimientos accidentales, la serendipia (hallazgo valioso que se produce de manera accidental o casual) ha sido, desde Arquímedes hasta Pasteur, pasando por Newton o Wöhler, el motor de arranque de muchos descubrimientos científicos relevantes.

En el desarrollo de esta Tesis, la serendipia hizo su aparición en el verano de 2015, cuando nos encontrábamos evaluando sistemáticamente el comportamiento térmico de diferentes fosfatos de titanio, que pretendíamos utilizar como anfitriones de cationes europio(III), que serían insertados por reacción sólido-sólido, utilizando como fuente de europio(III) una de sus sales nitrato a temperaturas ligeramente inferiores a su punto de fusión, siguiendo un procedimiento análogo al previamente descrito por nuestro grupo para la incorporación de cationes alcalinos a oxofosfatos de titanio (π- y ρ-TiP) [425,426].

Las curvas TG del ρ-TiP muestran una pérdida de masa total (% en peso) del 11.8 a 1273 K (calculado para $Ti_2O(PO_4)_2{\cdot}2H_2O$: 10.66%), con una primera etapa relacionada con la evacuación de agua de imbibición (~0.9%), produciéndose a partir de 400 K la pérdida de agua coordinada, obteniéndose $Ti_2O(PO_4)_2$ como producto final de la deshidratación, previamente a su evolución hacia fases de mayor densidad a temperaturas más elevadas.

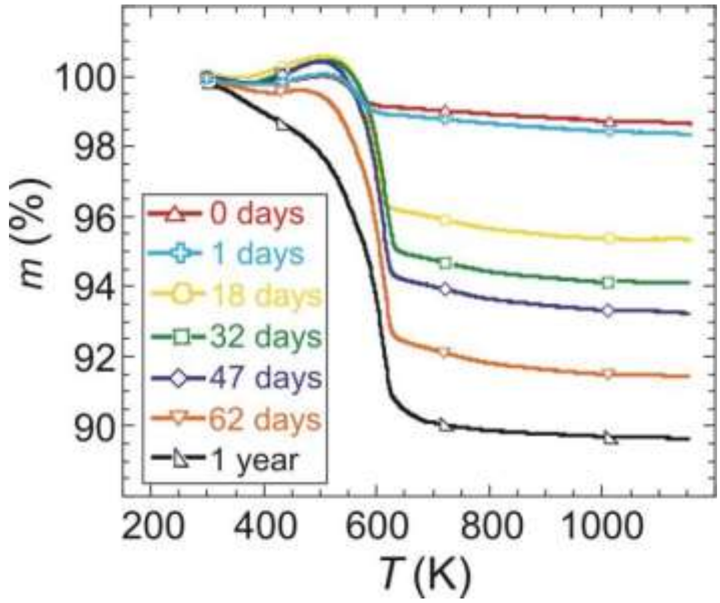

Fig. 15. Curvas TG para ρ-TiP, previamente tratado a 673 K, en función del tiempo de almacenamiento (atmósfera de laboratorio y temperatura ambiente).

Nuestra sorpresa apareció al observar la curva TG de la muestra ρ-TiP inmediatamente después de haber sido tratada (en aire) a 673 K (Fig. 15). Aunque la pérdida de masa total alcanza un valor de 1.6%, lo que indica una rápida adsorción de agua en la superficie del material, entre 400 y 550 K se observa una ganancia apreciable de masa, que alcanza su máximo (~0.2%) a ~500 K. Después de 24 horas de almacenamiento en aire a temperatura ambiente, el comportamiento térmico del material no se alteraba apreciablemente. Sin embargo, transcurridas varias semanas, el material mostraba una mayor ganancia de masa (~0.6%), mientras que la pérdida total aumentaba. Después de 2 meses, la pérdida de masa total fue del 8.4% y apenas se observó ganancia de masa (<0.05%). Finalmente, después de 1 año, la pérdida total de masa alcanzó el 10.3% y la curva TG fue la esperada para la fase ρ-TiP libre de agua fisisorbida. En las condiciones experimentales utilizadas, la alternativa más plausible para explicar la ganancia de masa observada a temperaturas superiores al ambiente (400-550 K) es la capacidad de nuestro material para retener nitrógeno (atmósfera en la que se fueron realizados todos los experimentos termo-gravimétricos).

En el Artículo III, se describió cómo el ρ-TiP, $Ti_2O(PO_4)_2 \cdot 2H_2O$, por efecto de la temperatura, se transforma en $Ti_2O(PO_4)_2$, un nuevo material fibroso. La estructura cristalina del compuesto anhidro se resolvió *ab initio* usando datos de PXRD. Su estructura, de simetría triclínica (P-1, a = 5.0843(1) Å, b = 8.6121(2) Å, c = 9.6766(2) Å, α = 74.501(2)º, β = 76.146(2)º, γ = 74.488(3)º, Z = 2), contiene dos tipos de canales unidimensionales paralelos al eje a y también dos tipos de átomos de titanio (Ti1 y Ti2) conectados por un puente oxo no lineal. Mientras el Ti1 está hexa-coordinado por átomos de oxígeno, el Ti2 se encuentra en un entorno tetraédrico distorsionado. Las isotermas de adsorción-desorción de gases a 77 K (N_2 e H_2) sugieren que este material es esencialmente no poroso (área superficial específica: 13 m^2/g). Sin embargo, como se muestra en la Figura 16, a temperaturas de 200-300 ºC, el $Ti_2O(PO_4)_2$ capta nitrógeno de forma reversible en cantidades no desdeñables (0.35 cm^3/g, STP).

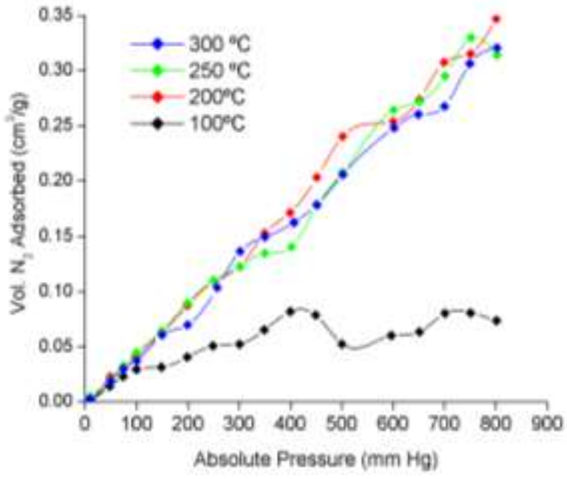

Fig. 16. Capacidad del $Ti_2O(PO_4)_2$ para retener N_2 a temperaturas elevadas.

En nuestro laboratorio, previamente al desarrollo de esta Tesis, se describió la síntesis y caracterización de algunos fosfatos metálicos interesantes [427,428]. Entre ellos, se encuentra el único sólido tridimensional ($Fe(NH_3)_2PO_4$) en el que, hasta ahora, se ha descrito la existencia de enlaces Fe–NH_3 [429]. La estructura de este material, constituida por octaedros FeO_4N_2 y tetraedros PO_4 compartiendo vértices, con las moléculas NH_3 orientadas hacia canales unidimensionales, está estrechamente relacionada con la de algunos minerales de hierro (por ejemplo, dos polimorfos, estrengita y fosfosiderita, del $FePO_4 \cdot 2H_2O$ [430]), y no muy alejada de la descrita para el ρ-TiP. En nuestra opinión, la capacidad de la fase anhidra del ρ-TiP para adsorber nitrógeno por encima de temperatura ambiente debe considerarse la punta del iceberg que indica el camino hacia la fabricación de una nueva familia de materiales adsorbentes útiles en la separación de gases e, incluso, en el diseño de catalizadores para la síntesis de amoníaco.

Artículo III

"The ability of a fibrous titanium oxophosphate for nitrogen-adsorption above room temperature"

Chemical Communications
Vol. 53
Pág. 2249–2251
Año 2017
DOI: 10.1039/c6cc07518e
Índice de Impacto: 6.319

ChemComm

COMMUNICATION

View Article Online
View Journal | View Issue

Cite this: Chem. Commun., 2017, 53, 2249

Received 14th September 2016, Accepted 24th January 2017

DOI: 10.1039/c6cc07518e

rsc.li/chemcomm

The ability of a fibrous titanium oxophosphate for nitrogen-adsorption above room temperature†

Jorge García-Glez,[a] Zakariae Amghouz,‡*[b] Iván da Silva,[c] Conchi O. Ania,[d] José B. Parra,[d] Camino Trobajo[a] and Santiago García-Granda[a]

$Ti_2O(PO_4)_2{\cdot}2H_2O$ (1), a three-dimensional titanium oxophosphate, thermally transforms to $Ti_2O(PO_4)_2$ (2), a fibrous novel compound. The crystal structure of 2 was solved *ab initio* using powder X-ray diffraction data (triclinic, $P\bar{1}$, a = 5.0843(1) Å, b = 8.6121(2) Å, c = 9.6766(2) Å, α = 74.501(2)°, β = 76.146(2)°, γ = 74.488(3)°, Z = 2). Compound 2, containing both 4- and 6-fold coordinated titanium atoms, shows measurable thermally activated nitrogen-adsorption. To our knowledge, the process described here constitutes the first example of nitrogen-fixation by an inorganic material at above-ambient temperature.

The Haber–Bosch process produces roughly 160 million metric tons of ammonia per year under very drastic conditions of pressure (200–500 atm) and temperature (500–600 °C) in the presence of catalysts containing $Fe_3O_4/K_2O/Al_2O_3$.[1,2] In this process, which consumes 1–2% of the annual primary energy supply of the world,[3] the rate-determining step of ammonia synthesis is the cleavage of the N–N bond. Actually, transition metals (such as Fe or Ru) are indispensable for the promotion of N–N bond cleavage,[4,5] as are electron donors that provide electrons to the transition metals.[6] A N_2 molecule is fixed to form a bond with a transition metal by donating electrons from its bonding orbitals and accepting electrons to its antibonding p-orbitals (back donation). Effectively, this back donation is enhanced by electron donors, which further weakens the N–N bond and results in the cleavage of N_2.[7,8] Electron donation from appropriate promoters is therefore key to enhance the efficiency of ammonia synthesis. However, in general, it is extremely difficult to produce a material with a low work function as well as chemical and thermal stability.[9,10]

In the past few years, a great variety of metal phosphates have been synthesized and characterized. These compounds exhibit a wide range of fascinating structures with different dimensionalities that include one-dimensional chain or ladder structures, two-dimensional layers and three-dimensional structures possessing channels of different sizes.[11] By the end of the last century, two $Ti_2O(PO_4)_2{\cdot}2H_2O$ polymorphs (ρ-TiP and π-TiP), among other open-framework inorganic materials,[12] were prepared hydrothermally,[13] and the crystal structure of the ρ-polymorph was solved *ab initio* from both neutron and synchrotron X-ray powder diffraction data.[14] The topology of fibrous ρ-TiP consists of a Ti/P/O framework enclosing two different linear channels parallel to the direction of fiber growth, both containing water molecules coordinated to only one of two octahedral-coordinated independent titanium atoms. Although it is known that the thermal decomposition of ρ-TiP occurs in two partially overlapping steps, giving $Ti_2O(PO_4)_2$ as the final product, the crystal structure of the anhydrous compound is unknown so far.

In this paper, we describe the crystal features in the thermal transformation of compound **1** to its anhydrous phase (compound **2**), where the hydrated titanium coordination changed from octahedral to distorted tetrahedral, and how this structural change provokes a measurable thermally activated nitrogen-adsorption.

Initially, the thermal transformation of compound **1** to **2** under vacuum was monitored by X-ray powder diffraction (see the ESI†). Fig. S1 (ESI†) shows the evolution of powder diffraction patterns from room temperature up to 400 °C. The starting phase **1** is stable up to 175 °C; above this temperature, the phase transition into compound **2** takes place and it is almost complete at 225 °C, as there is only a slight intensity contribution from compound **1**. At 275 °C no trace of compound **1** is found and no other phase transition is seen up to 400 °C. Compound **2** remains stable after cooling down from 400 °C to room temperature, indicating that dehydration is an irreversible process.

---

[a] *Departments of Organic and Inorganic Chemistry and Physical and Analytical Chemistry, University of Oviedo-CINN, 33006 Oviedo, Spain*

[b] *Scientific and Technical Services, University of Oviedo, 33006 Oviedo, Spain. E-mail: amghouz.uo@uniovi.es*

[c] *ISIS Facility, Rutherford Appleton Laboratory, Chilton, Oxfordshire OX11 0QX, UK*

[d] *ADPOR Group, Instituto Nacional del Carbón (INCAR, CSIC), 33011 Oviedo, Spain*

† Electronic supplementary information (ESI) available: Synthesis, experimental procedures, details on the crystal structure of **2**, and cif file of **2**. CCDC 1496186. For ESI and crystallographic data in CIF or other electronic format see DOI: 10.1039/c6cc07518e

‡ Current address: Department of Materials Science and Metallurgical Engineering, University of Oviedo, Campus Universitario, 33203 Gijón, Spain.

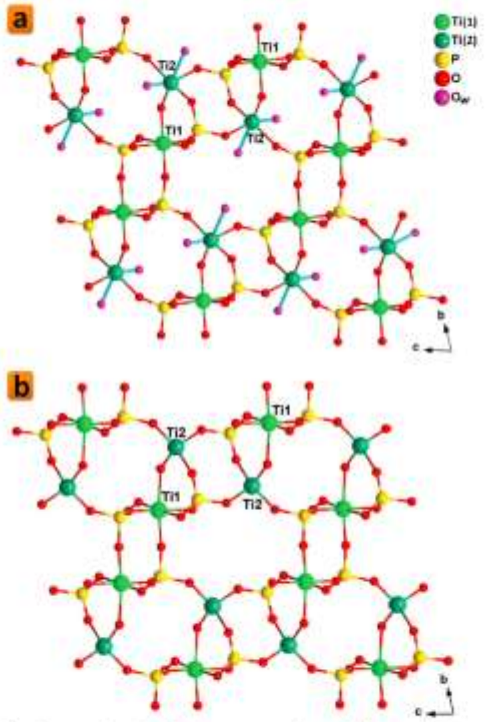

Fig. 1 A perspective view showing a comparison of the coordination and geometry around the titanium atoms (compounds **1** (a) and **2** (b)).

The crystal structure of compound **1** is already known.[14] The unit cell is triclinic (space group $P\bar{1}$, with $a = 5.1147(2)$ Å, $b = 8.8258(4)$ Å, $c = 9.6627(4)$ Å, $\alpha = 73.323(3)°$, $\beta = 86.173(3)°$, $\gamma = 86.330(3)°$, $Z = 2$). The perspective view of the crystal structure of compound **1** (Fig. 1a) shows that there are two types of one-dimensional channels running parallel to the *a*-axis, one small and the other larger, created by the connectivity of the TiO_6 octahedra and PO_4 tetrahedra. There are two independent titanium atoms (Ti1 and Ti2) octahedrally coordinated, bridged by an oxygen atom and the remaining coordination sites are completed by phosphate and water oxygen atoms. PO_4 groups and the $Ti1O_6$ octahedron are almost regular, whereas the $Ti2O_6$ octahedron environment shows a significant distortion due to the presence of two coordinated water molecules in the *cis* position with an Ow10-Ti-Ow11 angle of 78.1°.

The crystal structure of the novel anhydrous compound **2** was solved *ab initio* using powder X-ray diffraction data (triclinic, $P\bar{1}$, $a = 5.0843(1)$ Å, $b = 8.6121(2)$ Å, $c = 9.6766(2)$ Å, $\alpha = 74.501(2)°$, $\beta = 76.146(2)°$, $\gamma = 74.488(3)°$, $Z = 2$) (see ESI,† Fig. S2 and Table S1). The perspective view of the crystal structure of compound **2** is shown in Fig. 1b. Although the structure of compound **2** also consists of a 3D-framework of tetrahedra and octahedra linked only by vertex-sharing, it has similar features to the structure of compound **1**, such as the two types of one-dimensional channels running parallel to the *a*-axis and also two independent titanium atoms (Ti1 and Ti2) connected by a non-linear oxo-bridge. However, in this case, the Ti2 coordination environment changed from a fairly distorted Ti_2O_6 octahedron to a slightly regular Ti_2O_4 tetrahedron, which is due to the irreversible dehydration process induced by thermal treatment above 175 °C.

Compound **2** was studied by TEM and the representative results are illustrated in Fig. 2. The particles of compound **2** have a fibrous morphology with variable lengths, widths and thicknesses/depths (Fig. 2a). The HRTEM images of the fiber rods (**1**) and (**2**), represented in Fig. 2c and d show that the favorable growth direction of these fibers is along the *a*-axis, being characterized by the exposed {010} facet. These results are in accordance with the selected area electron diffraction (SAED) pattern of an individual crystal rod, depicted in Fig. 2b, which shows the highly crystalline nature of the fibers aligned along the [010] zone-axis.

The gas adsorption measurements revealed that the sample is rather non-porous (see further details in the ESI,† Fig. S3 and Table S2, showing reversible isotherms and a low accessibility for both N_2 and H_2 at 77 K), with a BET surface area of 13 $m^2\,g^{-1}$ and a total pore volume of 0.03 $cm^3\,g^{-1}$. The use of hydrogen as a gas probe for the textural characterization was based on its lower kinetic diameter compared to N_2 (*i.e.*, 2.6 Å and 3.6 Å, respectively). Thus, the extremely low adsorption of H_2 confirmed the non-porous character of compound **2**, demonstrating that the channels (after elimination of water molecules) are not accessible to either of these gases due to the size effect (not temperature).[15–18] Such size constrictions are independent of the

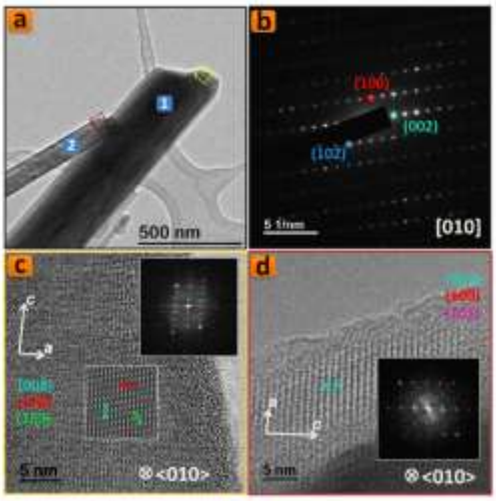

Fig. 2 (a) TEM image of compound **2**. (b) SAED pattern of a single crystal rod (1), and (c and d) HRTEM images of the fiber rods (1) and (2); (c and d) correspond to magnification of the zones highlighted by the yellow and brown squares in (a); insets of (c and d) show their FFT patterns and the processed HRTEM image of the zone highlighted by the dashed white line in (c).

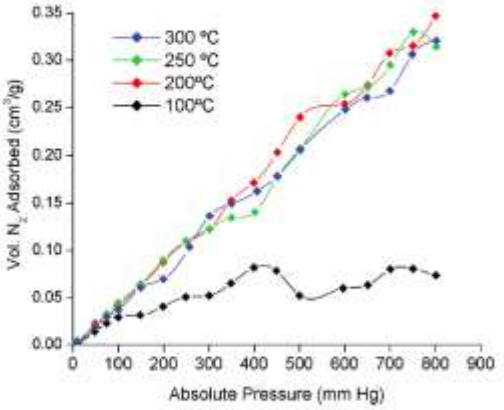

Fig. 3 N_2 uptake of compound **2** at above-ambient temperature.

temperature of the adsorption, thus demonstrating that the amount of N_2 adsorbed at 300 °C is located on the external surface of the material, as it cannot access the internal surface. Furthermore, the S_{BET}-value of the material is also sufficiently high to support the amount of nitrogen adsorbed at high temperature, supporting these observations.

Interestingly, compound **2** showed a non-negligible reversible nitrogen uptake at temperatures well above ambient conditions, as shown in Fig. 3. Furthermore, the adsorption capacity gradually increases with temperature, reaching 0.35 $cm^3\ g^{-1}$ (STP) between 100–300 °C at atmospheric pressure. An increase in the amount adsorbed with temperature is clearly seen from 100 °C to 200 °C, evidencing the occurrence of a chemisorption process. Above 200 °C and up to 300 °C, the behavior becomes similar, indicating that the chemisorption process has reached a plateau (constant adsorption value), that could be likely attributed to the saturation of the chemisoption sites (*i.e.*, completion of the monolayer).

The thermal stability of **2** was confirmed by PXRD, with no significant changes in the cell parameters, thus implying that the pore volume and surface area remain unchanged with temperature. Consequently, compound **2** undergoes a thermally activated fixation of nitrogen that would depend on the affinity of the solid/guest rather than on the molecular size of the gas. At high pressures, a similar effect has been reported for amine-impregnated porous montmorillonite and other amorphous nanoclays.[19] Considering the lack of structural changes upon N_2 loading (as confirmed by the powder-XRD pattern acquired at 300 °C) and the above-mentioned textural features, this behavior has to be attributed to specific interactions between the adsorbate and the surface of **2**. Indeed, the thermal activation of **1** leads to the elimination of water molecules, leaving open acidic sites at the external surface that would interact with nitrogen molecules, resulting in a higher uptake (channels are too small to be accessible to N_2). N_2 interaction with these active sites through the presence of the quadrupole moment of N_2 molecules would be more favorable in the acidic environment at higher temperature.[20] On the other hand, the increased nitrogen uptake at high temperatures might also be attributed to dissociative adsorption of the gas in acidic sites of compound **2**, as the high temperature would allow the energetic barrier of the N_2-dissociation process to be overcome.

In our Lab,[21,22] several interesting metal phosphates were previously synthesized including, to the best of our knowledge, the unique three-dimensional $Fe(NH_3)_2PO_4$ solid containing Fe–NH_3 bonds.[23] Its topology is related to the ρ-TiP-type structure and consists of a network of FeO_4N_2 octahedra and PO_4 tetrahedra linked by vertex sharing. In our opinion, the ability of the ρ-TiP anhydrous phase to adsorb nitrogen above room temperature may be considered the iceberg-tip that indicates the way towards the manufacturing of a new family of catalysts for the synthesis of ammonia at moderate temperatures and atmospheric pressure.

This work was financially supported by Spanish MINECO (MAT2013-40950-R, MAT2016-78155-C2-1-R) and *Gobierno del Principado de Asturias* (GRUPIN14-060), and FEDER. We would like to acknowledge the *Servicio Integrado de Difracción de Rayos X (SIDIX)*, from the University of La Laguna (Spain), for the powder diffraction measurements.

References

1 H. Liu, *Ammonia Synthesis Catalysts*, Chemical Industries Press & World Scientific, Singapore, 2013.
2 M. Kitano, Y. Inoue, Y. Yamazaki, F. Hayashi, S. Kanbara, S. Matsuishi, T. Yokoyama, S.-W. Kim, M. Hara and H. Hosono, *Nat. Chem.*, 2012, **4**, 934.
3 N. Gruber and J. N. Galloway, *Nature*, 2008, **451**, 293.
4 N. D. Spencer, R. C. Schoonmaker and G. A. Somorjai, *Nature*, 1981, **294**, 643.
5 C. J. H. Jacobsen, S. Dahl, B. S. Clausen, S. Bahn, A. Logadottir and J. K. Nørskov, *J. Am. Chem. Soc.*, 2001, **123**, 8404.
6 H. Bielawa, O. Hinrichsen, A. Birkner and M. Muhler, *Angew. Chem., Int. Ed.*, 2001, **40**, 1061.
7 T. W. Hansen, J. B. Wagner, P. L. Hansen, S. Dahl, H. Topsøe and C. J. H. Jacobsen, *Science*, 2001, **294**, 1508.
8 G. Ertl, *Angew. Chem., Int. Ed.*, 2008, **47**, 3524.
9 D. V. Yandulov and R. R. Schrock, *Science*, 2001, **301**, 76.
10 K. Arashiba, Y. Miyake and Y. Nishibayashi, *Nat. Chem.*, 2011, **3**, 120.
11 Z. Amghouz, B. Ramajo, S. A. Khainakov, I. da Silva, G. R. Castro, J. R. Garcia and S. Garcia-Granda, *Chem. Commun.*, 2014, **50**, 6729, and references therein.
12 A. K. Cheetham, G. Férey and T. Loiseau, *Angew. Chem., Int. Ed.*, 1999, **38**, 3268.
13 I. Bortun, S. A. Khainakov, L. N. Bortun, D. M. Poojary, J. Rodriguez, J. R. Garcia and A. Clearfield, *Chem. Mater.*, 1997, **9**, 1805.
14 M. A. Salvadó, P. Pertierra, S. Garcia-Granda, J. R. García, M. T. Fernández-Díaz and E. Dooryhee, *Eur. J. Solid State Inorg. Chem.*, 1997, **34**, 1237.
15 A. M. Arkharov, B. P. Bering, I. A. Kalinnikova and V. V. Serpinskii, *Russ. Chem. Bull.*, 1972, **21**, 1389.
16 J. D. Eagan and R. B. Anderson, *J. Colloid Interface Sci.*, 1975, **50**, 419.
17 A. Martin-Calvo, J. B. Parra, C. O. Ania and S. Calero, *J. Phys. Chem. C*, 2014, **118**, 25460.
18 J. Silvestre-Albero, A. Silvestre-Albero, F. Rodriguez-Reinoso and M. Thommes, *Carbon*, 2012, **50**, 3128.
19 M. Atilhan, S. Atilhan, R. Ullah, B. Anaya, T. Cagin, C. T. Yavuz and S. Aparicio, *J. Chem. Eng. Data*, 1999, **47**, 647.
20 E. Garcia-Pérez, J. B. Parra, C. O. Ania, A. Garcia-Sánchez, J. M. van Baten, R. Krishna, D. Dubbeldam and S. Calero, *Adsorption*, 2007, **13**, 469.
21 S. Garcia-Granda, S. A. Khainakov, A. Espina, J. R. García, G. R. Castro, J. Rocha and L. Mafra, *Inorg. Chem.*, 2010, **49**, 2630, and references therein.
22 B. F. Alfonso, C. Piqué, C. Trobajo, J. R. García, E. Kampert, U. Zeitler, J. Rodriguez-Fernández, M. T. Fernández-Díaz and J. A. Blanco, *Phys. Rev. B: Condens. Matter Mater. Phys.*, 2010, **82**, 144431, and references therein.
23 M. A. Salvadó, P. Pertierra, S. Garcia-Granda, A. Espina, C. Trabajo and J. R. Garcia, *Inorg. Chem.*, 1999, **38**, 5944.

Electronic Supplementary Information

The ability of a fibrous titanium oxophosphate for nitrogen-adsorption above room temperature

Jorge García-Glez,[a] Zakariae Amghouz,[b,c*] Iván da Silva,[d] Conchi O. Ania,[e]
José B. Parra,[e] Camino Trobajo[a], and Santiago García-Granda[a]

[a] Departments of Organic and Inorganic Chemistry and Physical and Analytical Chemistry, University of Oviedo-CINN, 33006 Oviedo (Spain).
[b] Scientific and Technical Services, University of Oviedo, 33006 Oviedo (Spain).
[c] Current address: Department of Materials Science and Metallurgical Engineering, University of Oviedo, Campus Universitario, 33203 Gijón (Spain).
[d] ISIS Facility, Rutherford Appleton Laboratory, Chilton, Oxfordshire OX11 0QX (UK).
[e] ADPOR Group, *Instituto Nacional del Carbón* (INCAR, CSIC), 33011 Oviedo (Spain).
*****E-mail: amghouz.uo@uniovi.es

1. Synthesis

All chemicals used were of reagent grade and were employed without further purification. Hydrothermal synthesis of $Ti_2O(PO_4)_2{\cdot}2H_2O$ (**1**) was carried out in a Teflon-lined stainless steel vessel (100 mL) under autogenous pressure. Details about its preparation procedure are previously reported (I. Bortun, S. A. Khainakov, L. N. Bortun, D. M. Poojary, J. Rodríguez, J. R. García, A. Clearfield, *Chem. Mater.*, **1997**, 9, 1805).

2. Powder thermodiffraction studies.

Thermal evolution of $Ti_2O(PO_4)_2 \cdot 2H_2O$ (**1**) to $Ti_2O(PO_4)_2$ (**2**) in vacuum was monitored by X-ray powder diffraction. The sample was placed in an Anton Paar HTK 1200N oven-chamber on a Panalytical X'Pert Pro diffractometer. Each powder pattern was recorded in the 10 - 40° range (2θ) at intervals of *ca.* 50 °C up to 400 °C and cooling down to RT. The measurements were done in continuous mode with an effective step and a counting time of 0.013° and 1 s/step, respectively. The temperature ramp between two consecutive temperatures was 5 °C/min.

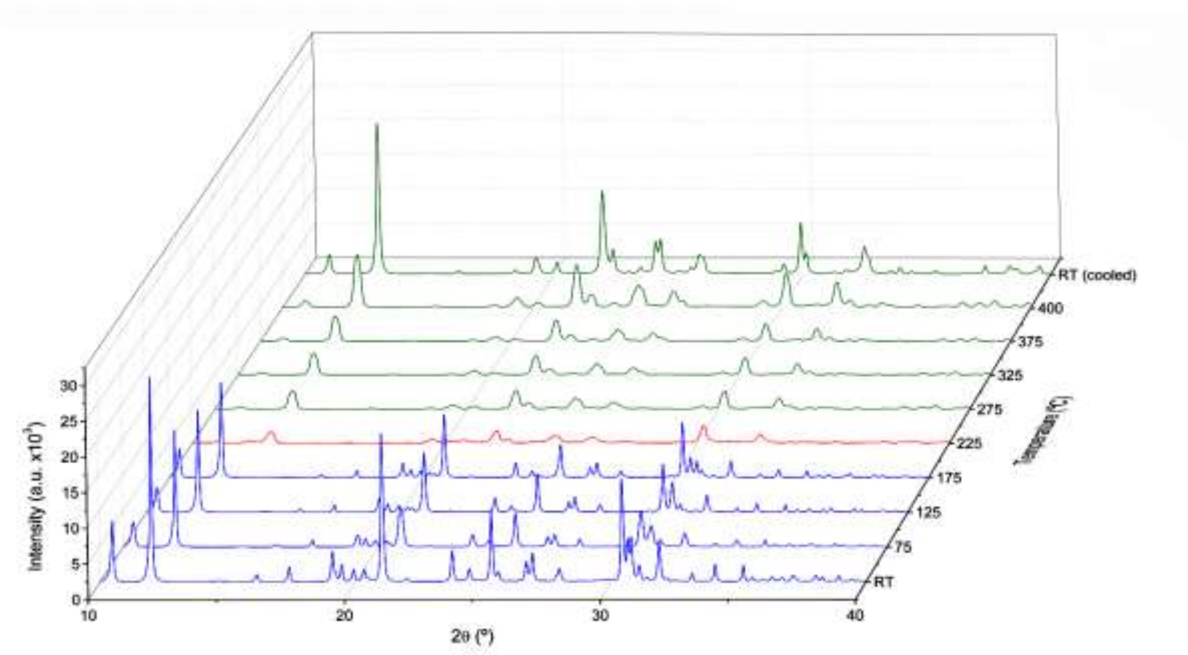

Figure S1. X-ray thermodiffractograms recorded in vacuum, heating up from RT to 400 ºC and cooling down to RT. Colour code corresponding to the structural changes. Blue: compound **1**, red: phase transition of **1** into compound **2**, green: compound **2**.

3. Structural data for $Ti_2O(PO_4)_2$ (2)

The X-ray powder diffraction pattern was recorded in vacuum using a Panalytical X'Pert Pro diffractometer with CuKα_1 radiation (1.540596 Å). The sample was finely powdered in an agate mortar. Room-temperature data was collected over the angular 2θ range 5 – 120° in continuous mode, with an effective step and a counting time of 0.013° and 2 s/step, respectively. The structure of compound **2** was solved *ab initio* by using EXPO2014 program (A. Altomare, C. Cuocci, C. Giacovazzo, A. Moliterni, R. Rizzi, N. Corriero, A. Falcicchio. *J. Appl. Cryst*. 2013, **46**, 1231-1235) and refined using Rietveld method with Topas Academic 5 program (http://www.topas-academic.net/). The refinement cycles were carried out with Topas on the free atom coordinates, without using constraints for Ti-O and P-O bonds or O-P-O angles. The final Rietveld plot is given in Figure S2. Crystallographic parameters are summarized in Table S1.

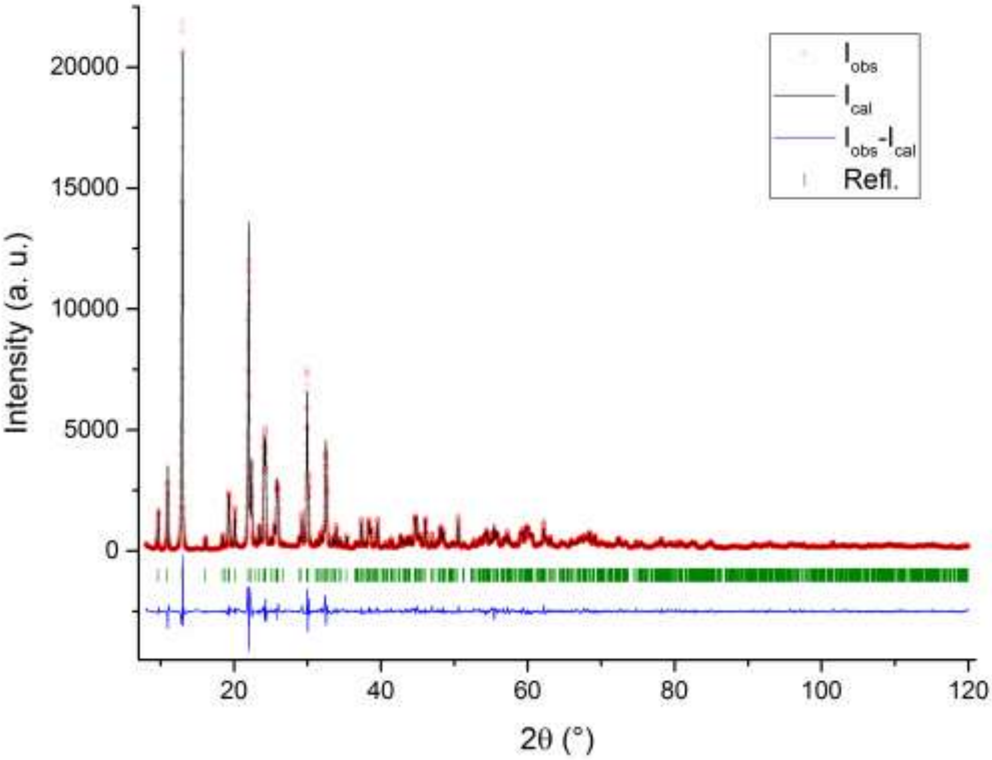

Figure S2. Final Rietveld refinement plot for $Ti_2O(PO_4)_2$ (**2**), showing the experimental (red circles), calculated (black line) and difference profiles (blue line); green marks indicate reflection positions.

Table S1. Crystallographic data and Rietveld refinement summary for compound $Ti_2O(PO_4)_2$ (**2**).

CCDC nos.	1496186
Formula	$Ti_2O(PO_4)_2$
Formula weight (g/mol)	301.68
Crystal system	Triclinic
Space group	*P* -1
a (Å)	5.0843(1)
b (Å)	8.6121(2)
c (Å)	9.6766(2)
α ***(°)***	74.501(2)
β ***(°)***	76.146(2)
γ ***(°)***	74.488(3)
V ***(Å^3)***	386.93(2)
Z	2
Rp (%)	8.91
Rwp (%)	11.57
R_B ***(%)***	2.65
GoF	2.32

4. TEM studies.

Transmission electron microscopy (TEM) studies were performed on a JEOL JEM-2100F microscope operated at an accelerating voltage of 200 kV, equipped with a field emission gun (FEG) and an ultra-high resolution pole-piece that provided a point-resolution better than 0.19 nm. The samples for TEM were dispersed in ethanol, sonicated and sprayed on a carbon-coated copper grid and then allowed to air-dry, finally, *Gatan SOLARUS 950* was used before observation.

5. Gas Adsorption experiments.

High resolution N_2 adsorption–desorption isotherms (between 10^{-6} and 1 bar) were measured using a volumetric analyzer (ASAP 2020 HD, Micromeritics) equipped with a turbo molecular drag vacuum pump and three pressure transducers (ca. 0.1, 10, 1000 mmHg, uncertainty within 0.15% of reading), allowing high sensitivity in the low pressure range. The samples were previously outgassed under a dynamic vacuum (ca. 10^{-5} mbar) at 673 K (1K min^{-1}) for 12 hours to remove moisture. The isotherms were measured at 77 K for textural characterization and above ambient temperature (between 373-573 K) for the evaluation of the nitrogen uptake. The warm and cold free-space correction measurements were performed by using ultrahigh purity He gas (grade 5.0, 99.999% purity). The temperature of the isotherms was controlled using a liquid nitrogen bath (77 K) and an air-assisted oven (373-573 K). Ultrahigh purity N_2 (99.992%) was supplied by Air Products. The Brunauer-Emmett-Teller (BET) theory was used to calculate the specific surface area from the N_2 adsorption isotherms at 77 K (see Figure S3 and Table S2).

The gas adsorption of the studied sample (i.e., non-porous material) at such high temperatures (ca. 100-300 ºC) is quite low, which makes the accurate experimental measurement of the adsorption a delicate and time-consuming process. In order to guarantee the accuracy of the recorded data, all the adsorption isotherms were performed in triplicate. Most importantly, the corrections of the dead volume (free space) of the tubes were performed at each temperature using the helium density of the sample (measured by helium pycnometry), the volume of the empty tube and the mass of the sample, to correct the measurements of the gas adsorbed by the sample at each temperature (measurements of the free space were also recorded in triplicate). This protocol allows us to assure the accuracy of the experimental data.

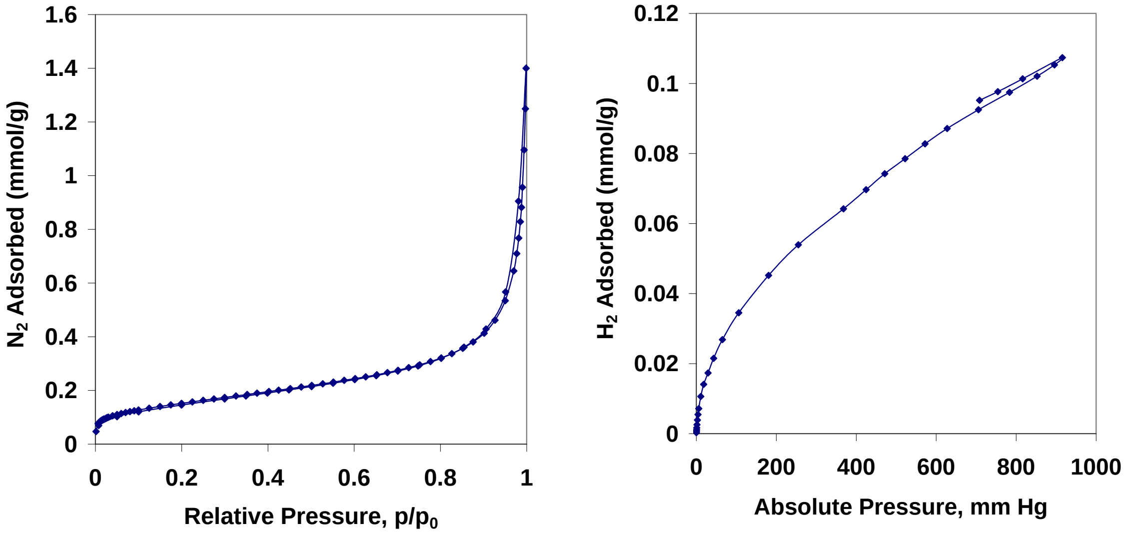

Figure S3. High resolution N_2 (left) and H_2 (right) adsorption-desorption isotherms at 77 K for compound **2**.

Table S2. Main textural parameters obtained from the equilibrium nitrogen adsorption isotherm at 77 K.

He density $[cm^3g^{-1}]$	**S_{BET} $[m^2g^{-1}]$**	**$V_{TOTAL\ PORES}$ ^{A} $[cm^3\ g^{-1}]$**	**Wo N_2 ^{B} $[cm^3\ g^{-1}]$**
2.59	13	0.032	0.003
^{A} Total pore volume evaluated at 77 K at $p/p_0 \sim 0.99$.			
^{B} Micropore volume evaluated form the Dubinin-Radushkevich equation			

4. Referencias

1. Y.-C. Lin, M. Karlsson, M. Bettinelli, Top. Curr. Chem., 374, 21, 2016.
2. European Commission (2011), Green Paper Lighting the Future: Accelerating the Deployment of Innovative Lighting Technologies. http://ec.europa.eu/newsroom/dae/document.cfm?doc_id=1127.
3. S. Nakamura, T. Mukai, M. Senoh, Appl. Phys. Lett., 64, 1687, 1994.
4. S. Pimputkar, J.S. Speck, S.P.DenBaars, S. Nakamura, Nat. Photonics 3, 180, 2009.
5. N.C. George, K.A. Denault, R. Seshadri, Annu. Rev. Mater. Res. 43, 481, 2013.
6. T. Jüstel, H. Nikol, C. Ronda, Angew. Chem. Int. Ed., 37, 3084, 1998.
7. C.C. Lin, R.-S. Liu, J. Phys. Chem. Lett., 2, 1268, 2011.
8. H.A. Höppe, Angew. Chem. Int. Ed., 48, 3572, 2009.
9. R.-J. Xie, N. Hirosaki, Sci. Technol. Adv. Mater., 8, 588, 2007.
10. P.F. Smet, A.B. Parmentier, D. Poelman, J. Electrochem. Soc., 158, R37, 2011.
11. L. Chen, C.-C. Lin, C.-W. Yeh, R.-S. Liu, Materials, 3, 2172, 2010.
12. L.S. Rohwer, A.M. Srivastava, Electrochem. Soc. Interface, 12, 36, 2003.
13. J. McKittrick, M.E. Hannah, A. Piquette, J.K. Han, J.I. Choi, M. Anc, M. Galvez, H. Lugauer, J.B. Talbot, K.C. Mishra, ECS J. Solid State Sci. Technol., 2, R3119, 2013.
14. S. Ye, F. Xiao, Y.X. Pan, Y.Y. Ma, Q.Y. Zhang, Mater. Sci. Eng., 71, 1, 2010.
15. http://hyperphysics.phy-astr.gsu.edu/hbase/vision/specol.html.
16. http://hyperphysics.phy-astr.gsu.edu/hbase/vision/cie.html.
17. C.S. McCamy, Color Res. Appl., 17, 142, 1992.
18. R.-J. Xie, N. Hirosaki, M. Mitomo, K. Takahashi, K. Sakuma, Appl. Phys. Lett., 88, 101104, 2006.
19. R.-J. Xie, N. Hirosaki, K. Sakuma, Y. Yamamoto, M. Mitomo, Appl. Phys. Lett., 84, 5404, 2004.
20. T.Y. Seong, J. Han, H. Amano, H. Morkoc, Nitride Based Light Emitting Diodes and Applications, Springer Science and Business Media, 2014.
21. J.K. Park, C.H. Kim, S.H. Park, H.D. Park, S.Y. Choi, Appl. Phys. Lett., 84, 1647, 2004.
22. M.P. Saradhi, U.V. Varadaraju, Chem. Mater., 18, 5267, 2006.
23. A. Katelnikovas, T. Bareika, P.Vitta, Jüstel, H. Winkler, A. Kareiva, Zukauskas, G. Tamulaitis, Opt. Mater., 32, 1261, 2010.
24. J.L. Wu, G. Gundiah, A.K. Cheetham, Chem. Phys. Lett., 441, 250, 2007.
25. T.Y. Tien, E.F. Gibbons, R.G. DeLosh, P.J. Zacmanidis, D.E. Smith, H.L. Stadler, J. Electrochem. Soc., 120, 278, 1973.
26. C.-C. Chiang, M.-S. Tsai, M.-H. Hon, J. Electrochem. Soc., 155, B517, 2008.
27. Q. Shao, Y. Dong, J. Jiang, C. Liang, J. He, J. Lumin., 131, 1013, 2011.
28. Y. Kanke, A. Navrotsky, J. Solid State Chem., 141, 424, 1998.
29. A. Kalaji, P.J. Saines, N.C. George, A.K. Cheetham, Chem. Phys. Lett., 586, 91, 2013.
30. M. Yamaga, Y. Masui, S. Sakuta, N. Kodama, K. Kaminaga, Phys. Rev. B, 71, 205102, 2005.
31. T. Senden, F.T. Rabouw, A. Meijerink, ACS Nano 9, 1801, 2015.
32. M. Raukas, S.A. Basun, W. Schaik, W.M. Yen, U. Happek, Appl. Phys. Lett., 69, 3300, 1996.
33. U. Happek, S.A. Basun, J. Choi, J.K. Krebs, M. Raukas, J. Alloys Compd., 303, 198, 2000.
34. P. Dorenbos, J. Lumin., 104, 239, 2003.
35. P. Dorenbos, J. Phys. Condens. Matter., 15, 4797, 2003.
36. P. Dorenbos, Phys. Rev. B, 64, 125117, 2001.
37. P. Dorenbos, Phys. Rev. B, 65, 235110, 2002.
38. M. Shang, G. Li, D. Geng, D. Yang, X. Kang, Y. Zhang, H. Lian, J. Lin, J. Phys. Chem. C, 116, 10222, 2012.
39. Y.-C. Chiu, W.-R. Liu, C.-K. Chang, C.-C. Liao, Y.-T. Yeh, S.-M. Jang, T.-M. Chen, J. Mater. Chem., 20, 1755, 2010.
40. W.B. Im, H.S. Yoo, S. Vaidyanathan, K.H. Kwon, H.J. Park, Y.-I. Kim, D.Y. Jeon, Mater. Chem. Phys., 115, 161, 2009.
41. D.K. Yim, I.-S. Cho, C.W. Lee, J.H. Noh, H.S. Roh, K.S. Hong, Opt. Mater. 33, 1036, 2011.
42. X. Zhang, F. Mo, L. Zhou, M. Gong, J. Alloys Compd., 575, 314, 2013.
43. N. Ta, D. Chen, J. Alloys Compd., 484, 514, 2009.
44. J. Sun, G. Shen, X. Wang, D. Shen, Mater. Lett., 93, 169, 2013.
45. L. Liu, R.-J. Xie, N. Hirosaki, Y. Li, T. Takeda, C.-N. Zhang, J. Li, X. Sun, J. Am. Ceram. Soc., 93, 2018, 2010.
46. J. Hölsä, M. Kirm, T. Laamanen, M. Lastusaari, J. Niittykoski, P. Novák, J. Lumin. 129, 1560, 2009.
47. X. Zhang, X. Tang, J. Zhang, H. Wang, J. Shi, M. Gong, Powder Technol., 204, 263, 2010.
48. K.Y. Jung, J.H. Kim, Y.C. Kang, J. Lumin. 129, 615, 2009.

49. J. Zhou, Z. Xia, M. Yang, K. Shen, J. Mater. Chem., 22, 21935, 2012.
50. Z.L. Wang, K.W. Cheah, H.L. Tam, M.L. Gong, J. Alloys Compd., 482, 437, 2009.
51. S. Cui, H. Jiao, G. Li, M. Su, J. Electrochem. Soc., 157, J88, 2010.
52. G. Li, Y. Lai, T. Cui, H. Yu, D. Liu, S. Gan, Mater. Chem. Phys., 124, 1094, 2010.
53. H.-L. Li, R.-J. Xie, G.-H. Zhou, N. Hirosaki, Z. Sun, J. Electrochem. Soc., 157, J251, 2010.
54. J.-Y. Tang, W.-J. Xie, K. Huang, L.-Y. Hao, X. Xu, R.-J. Xie R-J (2011) Electrochem. Solid-State Lett., 14, J47, 2011.
55. J.H. Ryu, H.S. Won, Y.-G. Park, S.H. Kim, W.Y. Song, H. Suzuki, C.-B. Yoon, D.H. Kim, W.J. Park, C. Yoon, Electrochem. Solid-State Lett. 13, H30, 2010.
56. M. Mikami, N. Kijima, Opt. Mater., 33, 145, 2010.
57. R. Yu, J. Wang, M. Zhang, J. Zhang, H. Yuan, Q. Su, Chem. Phys. Lett., 453, 197, 2008.
58. C. Guo, Y. Xu, X. Ding, M. Li, J. Yu, Z. Ren, J. Bai, J. Alloys Compd., 509, L38, 2011.
59. J. Sun, J. Zeng, Y. Sun, H. Du, J. Alloys Compd., 540, 81, 2012.
60. B.V. Ratnam, M. Jayasimhadri, G.B. Kumar, K. Jang, S.S. Kim, Y.I. Lee, J.M. Lim, D.S. Shin, T.K. Song, J. Alloys Compd., 564, 100, 2013.
61. D.J. Robbins, B. Cockayne, B. Lent, J.L. Glasper, Solid State Commun., 20, 673, 1976.
62. J. Wang, Z. Zhang, M. Zhang, Q. Zhang, Q. Su, J. Tang, J. Alloys Compd., 488, 582, 2009.
63. Y. Chen, J. Wang, X. Zhang, G. Zhang, M. Gong, Q. Su, Sens. Actuators, B148, 259, 2010.
64. M. Zhang, J. Wang, W. Ding, Q. Zhang, Q. Su, Appl. Phys. B, 86, 647, 2007.
65. H.-S. Roh, S. Hur, H.J. Song, I.J. Park, D.K. Yim, D.-W. Kim, K.S. Hong, Mater. Lett., 70, 37, 2012.
66. Y. Shimomura, T. Honma, M. Shigeiwa, T. Akai, K. Okamoto, N. Kijima, J. Electrochem. Soc., 154,J35, 2007.
67. Y. Liu, W. Zhuang, Y. Hu, W. Gao, J. Hao, J. Alloys Compd., 504, 488, 2010.
68. X. Zhang, J. Zhang, R. Wang, M. Gong, J. Am. Ceram. Soc., 93, 1368, 2010.
69. X. Zhang, X. Tang, J. Zhang, M. Gong, J. Lumin. 130, 2288, 2010.
70. Z. Xia, J. Zhou, Z. Mao, J. Mater. Chem. C, 1, 5917, 2013.
71. S. Ye, Z.-S. Liu, X.-T. Wang, J.-G. Wang, L.-X. Wang, X.-P. Jing, J. Lumin., 129, 50, 2009.
72. Y. Shimomura, T. Kurushima, N. Kijima, J. Electrochem. Soc., 154, J234, 2007.
73. P. Li, L. Pang, Z. Wang, Z. Yang, Q. Guo, X. Li, J. Alloys Compd., 478, 813, 2009.
74. X. Li, Z. Yang, L. Guan, Q. Guo, Mater. Lett., 63, 1096, 2009.
75. Z. Xia, R.-S. Liu, K.-W. Huang, V. Drozd, J. Mater. Chem., 22, 15183, 2012.
76. Z. Xia, R.-S. Liu, J. Phys. Chem. C, 116, 15604, 2012.
77. A.A. Setlur, E.V. Radkov, C.S. Henderson, J.-H. Her, A.M. Srivastava, N. Karkada, M.S. Kishore, N.P. Kumar, D. Aesram, A. Deshpande, B. Kolodin, L.S. Grigorov, U. Happek, Chem. Mater. 22, 4076, 2010.
78. J. Ryu, H. Won, Y.-G. Park, S. Kim, W. Song, H. Suzuki, C. Yoon, Appl. Phys. A, 95, 747, 2009.
79. R.-J. Xie, N. Hirosaki, M. Mitomo, K. Uheda, T. Suehiro, X. Xu, Y. Yamamoto, T. Sekiguchi, J. Phys. Chem. B, 109, 9490, 2005.
80. S. Lizzo, E.P. Klein, N. Nagelvoort, R. Erens, A. Meijerink, G. Blasse, J. Phys. Chem. Solids, 58, 963, 1997.
81. X. Song, R. Fu, S. Agathopoulos, H. He, X. Zhao, J. Zeng, Mater. Sci. Eng. B, 164, 12, 2009.
82. J. Tang, J. Chen, L. Hao, X. Xu, W. Xie, Q. Li, J. Lumin., 131, 1101, 2011.
83. W.-R. Liu, C.-W. Yeh, C.-H. Huang, C.C. Lin, Y.-C. Chiu, Y.-T. Yeh, R.-S. Liu, J. Mater. Chem., 21, 3740, 2011.
84. Y.R. Do, K.-Y. Ko, S.-H. Na, Y.-D. Huh, J. Electrochem. Soc., 153, H142, 2006.
85. A.M. Srivastava, H.A. Comanzo, S. Camardello, S.B. Chaney, M. Aycibin, U. Happek, J. Lumin., 129, 919, 2009.
86. M. Peng, N. Da, S. Krolikowski, A. Stiegelschmitt, L. Wondraczek, Opt. Express, 17, 21169, 2009.
87. A.A. Setlur, W.J. Heward, Y. Gao, A.M. Srivastava, R.G. Chandran, M.V. Shankar, Chem. Mater., 18, 3314, 2006.
88. I. Carrasco, K. Bartosiewicz, M. Nikl, F. Piccinelli, M. Bettinelli, Opt. Mater., 48, 252, 2015.
89. Z. Xia, J. Zhuang, L. Liao, Inorg. Chem., 51, 7202, 2012.
90. M. Bettinelli, A. Speghini, F. Piccinelli, J. Ueda, S. Tanabe, Opt. Mater. 33, 119, 2010.
91. A. Katelnikovas, J. Plewa, S. Sakirzanovas, D. Dutczak, D. Enseling, F. Baur, H. Winkler, A. Kareiva, T. Justel, J. Mater. Chem., 22, 22126, 2012.
92. P.S. Dutta, A. Khanna, ECS J. Solid State Sci. Technol. 2, R3153, 2013.
93. Y.-C. Chang, C.-H. Liang, S.-A. Yan, Y.-S. Chang, J. Phys. Chem. C, 114, 3645, 2010.
94. T. Kim, S. Kang, J. Lumin., 122-123, 964, 2007.
95. Z. Wang, H. Liang, L. Zhou, H. Wu, M. Gong, Q. Su, Chem. Phys. Lett., 412, 313, 2005.
96. Y. Hu, W. Zhuang, H. Ye, D. Wang, S. Zhang, X. Huang, J. Alloys Compd., 390, 226, 2005.

97. H. Jin, H. Wu, L. Tian, J. Lumin., 132, 1188, 2012.
98. L. Yi, X. He, L. Zhou, F. Gong, R. Wang, J. Sun, J. Lumin., 130, 1113, 2010.
99. J. Liao, H. You, D. Zhou, H.-R. Wen, R. Hong, Opt. Mater., 34, 1468, 2012.
100. X.-X. Wang, Y.-L. Xian, G. Wang, J.-X. Shi, Q. Su, M.-L. Gong, Opt. Mater., 30, 521, 2007.
101. Z. Ci, Y. Wang, J. Zhang, Y. Sun, Phys. B, 403, 670, 2008.
102. M. Thomas, P.P. Rao, M. Deepa, M.R. Chandran, P. Koshy, J. Solid State Chem., 182, 203, 2009.
103. Z. Ju, R. Wei, X. Gao, W. Liu, C. Pang, Opt. Mater. 33, 909, 2011.
104. F.-B. Cao, J. Lumin. 132, 641, 2012.
105. S. Neeraj, N. Kijima, A.K. Cheetham, Chem. Phys. Lett., 387, 2, 2004.
106. F.-B. Cao, Y.-W. Tian, Y.-J. Chen, L.-J. Xiao, Q. Wu, J. Lumin., 129, 585, 2009.
107. M. Nyman, M.A. Rodríguez, L.E. Shea-Rohwer, J.E. Martin, P.P.Provencio, J. Am. Chem Soc., 131, 11652, 2009.
108. R.G. Pappalardo, R.B. Hunt, J. Electrochem. Soc., 132, 721, 1985.
109. H.N. Hersh, H. Forest, J. Lumin., 1–2, 862, 1970.
110. A. Zukauskas, M.S. Shur, R. Gaska, Introduction to Solid-State Lighting, Wiley, 2002.
111. D.L. Dexter, J.H. Schulman, J. Chem. Phys., 22, 1063, 1954.
112. B. Di Bartolo, Energy Transfer Processes in Condensed Matter, Springer, 1984.
113. A.G. Paulusz, J. Electrochem. Soc., 120, 942, 1973.
114. L. Lv, X. Jiang, S. Huang, X. Chen, Y. Pan, J. Mater. Chem. C, 2, 3879, 2014.
115. T. Han, T. Lang, J. Wang, M. Tu, L. Peng, RSC Adv., 5, 100054, 2015.
116. N. Narendran, Y. Gu, J.P. Freyssinier-Nova, Y. Zhu, Phys. Status Solidi A, 202, R60, 2005.
117. Y. Arai, S. Adachi, J. Lumin., 131, 2652, 2011.
118. Y. Arai, S. Adachi, J. Electrochem. Soc., 158, J179, 2011.
119. S. Adachi, H. Abe, R. Kasa, T. Arai, J. Electrochem. Soc., 159, J34, 2011.
120. R. Kasa, S. Adachi, J. Electrochem. Soc., 159, J89, 2012.
121. R. Suzuki, Y. Takahashi, K. Iwasaki, N. Terakado, T. Fujiwara, Appl. Phys. Express, 8, 072603, 2015.
122. R.L. Toquin, A.K. Cheetham, Chem. Phys. Lett., 423, 352, 2006.
123. Z. Zhang, O.M. ten Kate, A.C.A. Delsing, Z. Man, R. Xie, Y. Shen, M.J.H. Stevens, P.H.L. Notten, P. Dorenbos, J. Zhao, H.T. Hintzen, J. Mater. Chem. C, 1, 7856, 2013.
124. K. Uheda, N. Hirosaki, H. Yamamoto, Phys. Status Solidi A, 203, 2712, 2006.
125. J. Wang, H. Zhang, B. Lei, Z. Xia, H. Dong, Y. Liu, M. Zheng, Y. Xiao, J. Mater. Chem. C, 3, 4445, 2015.
126. Z. Lin, H. Lin, J. Xu, F. Huang, H. Chen, B. Wang, Y. Wang, J. Alloys Compd., 649, 661, 2015.
127. R.-J. Xie, N. Hirosaki, T. Suehiro, F.-F. Xu, M. Mitomo, Chem. Mater., 18, 5578, 2006.
128. T.-C. Liu, B.-M. Cheng, S.-F. Hu, R.-S. Liu, Chem. Mater., 23, 3698, 2011.
129. M. Nazarov, C. Yoon, J. Solid State Chem., 179, 2529, 2006.
130. T.-W. Kuo, W.-R. Liu, T.-M. Chen, Opt. Express 18, 8187, 2010.
131. M. Appl, Ammonia, Wiley-VCH, 1999.
132. N. Khoenkhoen, B. de Bruin, J.N.H. Reek, W.I. Dzik, Eur. J. Inorg. Chem., 567, 2015.
133. M.D. Fryzuk, Chem. Commun., 49, 4866, 2013.
134. G. Ertl, Catalytic Ammonia Synthesis, Ed. J.R. Jennings, Plenum, 1991.
135. R. Schlogl, Angew. Chem. Int. Ed., 42, 2004, 2003.
136. J. Kim, D.C. Rees, Science, 257, 1677, 1992.
137. O. Einsle, F.A. Tezcan, S.L.A. Andrade, B. Schmid, M. Yoshida, J.B. Howard, D.C. Rees, Science, 297, 1696, 2002.
138. D. Sellmann, J. Sutter, Acc. Chem. Res., 30, 460, 1997.
139. Y. Tanabe, Y. Nishibayashi, Chem. Rec., 16, 1549, 2016.
140. Y. Nishibayashi, C. R. Chim., 18, 776, 2015.
141. Y. Nishibayashi, Inorg. Chem., 54, 9234, 2015.
142. R.R. Schrock, Angew. Chem. Int. Ed., 47, 5512, 2008.
143. T. Spatzal, K.A. Pérez, O. Einsle, J.B. Howard, B. James B., D.C. Rees, C. Douglas, Science 334, 940, 2011.
144. O. Einsle, J. Biol. Inorg. Chem., 19, 737, 2014.
145. K.M. Lancaster, M. Roemelt, P. Ettenhuber, Y.L. Hu, M.W. Ribbe, F. Neese, U. Bergmann, S.K. DeBeer, Science, 334, 974, 2011.
146. B.M. Hoffman, D. Lukoyanov, Z.-Y. Yang, D.R. Dean, L.C. Seefeldt, Chem. Rev., 114, 4041, 2014.
147. P.E.M. Siegbahn, J. Am. Chem. Soc., 138, 10485, 2016.
148. M. Hidai, Coord. Chem. Rev., 185, 99, 1999.
149. M. Hidai, Y. Mizobe, Pure Appl. Chem., 73, 261, 2001.

150. R.J. Burford, M.D. Fryzuk, Nature Rev. Chem., 1, 0026, 2017.
151. S. Gambarotta, J. Scott, Angew. Chem. Int. Ed., 43, 5298, 2004.
152. B.A. MacKay, M.D. Fryzuk, Chem. Rev., 104, 385, 2004.
153. F. Studt, F. Tuczek, J. Comput. Chem., 27, 1278, 2006.
154. P.J. Chirik, Dalton Trans., 16, 2007.
155. H.-P. Jia, E.A. Quadrelli, Chem. Soc. Rev., 43, 547, 2014.
156. S.P. Semproni, P.J. Chirik, Eur. J. Inorg. Chem., 3907, 2013.
157. T.M. Figg, P.L. Holland, T.R. Cundari, Inorg. Chem., 51, 7546, 2012.
158. D.M. Fryzuk, Acc. Chem. Res., 42, 127, 2009.
159. A.D. Allen, C.V. Senoff, Chem. Commun., 621, 1965.
160. G.J. Leigh, Acc. Chem. Res., 25, 177, 1992.
161. D.F. Harrison, E. Weissberger, H. Taube, Science, 159, 320, 1968.
162. J. Chatt, J.R. Dilworth, G.J. Leigh, R.L. Richards, J. Chem. Soc. D, 955, 1970.
163. M.D. Fryzuk, T.S. Haddad, M. Mylvaganam, D.H. McConville, S.J. Rettig, J. Am. Chem. Soc., 115, 2782, 1993.
164. E.A. MacLachlan, M.D. Fryzuk, Organometallics, 25, 1530, 2006.
165. W.J. Evans, T.A. Ulibarri, J.W. Ziller, J. Am. Chem. Soc., 110, 6877, 1988.
166. D.V. Fomitchev, K.A. Bagley, P. Coppens, J. Am. Chem. Soc., 122, 532, 2000.
167. L.J. Murray, W.W. Weare, J. Shearer, A.D. Mitchell, K.A. Abboud, J. Am. Chem. Soc., 136, 13502, 2014.
168. D. Pun, E. Lobkovsky, P.J. Chirik, J. Am. Chem. Soc., 130, 6047, 2008.
169. M.D. Fryzuk, S.A. Johnson, Coord. Chem. Rev., 379, 2000.
170. M.P. Shaver, M.D. Fryzuk, Adv. Synth. Catal., 345, 1061, 2003.
171. Y. Ohki, M.D. Fryzuk, Angew. Chem., Int. Ed., 46, 3180, 2007.
172. D.V. Yandulov, R.R. Schrock, Science, 306, 76, 2003.
173. R.R. Schrock, Acc. Chem. Res., 38, 955, 2005.
174. J.A. Pool, E. Lobkovsky, P.J. Chirik, Nature, 427, 527, 2004.
175. D. Pun, C.A. Bradley, E. Lobkovsky, I. Keresztes, P.J. Chirik, J. Am. Chem. Soc., 130, 14046, 2008.
176. G.B. Nikiforov, I. Vidyaratne, S. Gambarotta, I. Korobkov, Angew. Chem., Int. Ed., 48, 7415, 2009.
177. K. Komori, H. Oshita, Y. Mizobe, M.J. Hidai, J. Am. Chem. Soc., 111, 1939, 1989.
178. M. Kol, R.R. Schrock, R. Kempe, W.M. Davis, J. Am. Chem. Soc., 116, 4382, 1994.
179. M.D. Fryzuk, B.A. MacKay, B.O. Patrick, J. Am. Chem. Soc., 125, 3234, 2003.
180. B.A. MacKay, R.F. Munha, M.D. Fryzuk, J. Am. Chem. Soc., 128, 9472, 2006.
181. H. Tanaka, A. Sasada, T. Kouno, M. Yuki, Y. Miyake, H. Nakanishi, Y. Nishibayashi, K. Yoshizawa, J. Am. Chem. Soc., 133, 3498, 2011.
182. F. Akagi, T. Matsuo, H. Kawaguchi, Angew. Chem., Int. Ed., 46, 8778, 2007.
183. D.J. Knoblock, E. Lobkovsky, P.J. Chirik, Nat. Chem., 2, 30, 2010.
184. M. Hirotsu, P.P. Fontaine, P.Y. Zavalij, L.R. Sita, J. Am. Chem. Soc., 129, 12690, 2007.
185. R.R. Schrock, Chem. Commun., 2389 , 2003.
186. M.D. Fyzuk, Mod. Coord. Chem., 187, 2002.
187. M. Hidai, Y. Mizobe, Chem. Rev., 95, 1115, 1995.
188. J.C. Peters, M. P. Mehn, Bio-organometallic Approaches to Nitrogen Fixation Chemistry, in Activation of Small Molecules (Ed.: W. B. Tolman), Wiley-VCH, 2006, pp. 81-119.
189. J. Chatt, J.R. Dilworth, R.L. Richards, Chem. Rev., 78, 589, 1978.
190. M. Hidai, Y. Mizobe, Met. Ions Biol. Syst., 39, 121 2002.
191. H. Tanaka, H. Mori, H. Seino, M. Hidai, Y. Mizobe, K. Yoshizawa, J. Am. Chem. Soc., 130, 9037 2008.
192. D.J. Knobloch, H.E. Toomey, P.J. Chirik, J. Am. Chem. Soc., 130, 4248, 2008.
193. M. Yuki, Y. Miyake, Y. Nishibayashi, Organometallics, 27, 3947, 2008.
194. M. Hirotsu, P.P. Fontaine, A. Epshteyn, P.Y. Zavalij, L.R. Sita, J. Am. Chem. Soc., 129, 9284, 2007.
195. E.A. MacLachlan, F.M. Hess, B.O. Patrick, M.D. Fryzuk, J. Am. Chem. Soc., 129, 10895, 2007,
196. S.C. Bart, A.C. Bowman, E. Lobkovsky, P.J. Chirik, J. Paul, J. Am. Chem. Soc., 129, 7212, 2007.
197. W.H. Bernskoetter, E. Lobkovsky, P.J. Chirik, Angew. Chem. Int. Ed., 46, 2858, 2007.
198. W.H. Bernskoetter, E. Lobkovsky, P.J. Chirik, Angew. Chem. Int. Ed., 46, 2858, 2007.
199. F. Studt, F. Tuczek, Angew. Chem. Int. Ed., 44, 5639, 2005.
200. F. Studt, B.A. MacKay, S.A. Johnson, B.O. Patrick, M.D. Fryzuk, F. Tuczek, Chem. Eur. J., 11, 604, 2005.
201. W.H. Bernskoetter, J.A. Pool, E. Lobkovsky, P.J. Chirik, J. Am. Chem. Soc., 127, 7901, 2005.
202. J.A. Pool, W.H. Bernskoetter, P. J. Chirik, J. Am. Chem. Soc., 126, 14326, 2004.
203. D.V. Yandulov, R. R. Schrock, Inorg. Chem., , 44, 1103, 2005.

204. J.J. Curley, T.R. Cook, S.Y. Reece, P. Müller, C.C. Cummins, J. Am. Chem. Soc., 130, 9394, 2008.
205. I. Vidyaratne, J. Scott, S. Gambarotta, P.H.M. Budzelaar, Inorg. Chem., 46, 7040, 2007.
206. I. Vidyaratne, P. Crewdson, E. Lefebvre, S. Gambarotta, Inorg. Chem., 46, 8836, 2007.
207. J.S. Figueroa, C.C. Cummins, Dalton Trans., 2161, 2006.
208. F. Studt , V.M.E. Lamarche, G.K.B. Clentsmith, F.G.N. Cloke, F. Tuczek, Dalton Trans., 1052, 2005.
209. M.D. Fryzuk, C.M. Kozak, M.R. Bowdridge, B.O. Patrick, S.J. Rettig, J. Am. Chem. Soc., 124, 8389, 2002.
210. I. Korobkov, S. Gambarotta, G.P.A. Yap, Angew. Chem. Int. Ed., 41, 3433, 2002.
211. E. Solari, C. Da Silva, B. Iacono, J. Hesschenbrouck, C. Rizzoli, R. Scopelliti, C. Floriani, Angew. Chem. Int. Ed., 40, 3907, 2001.
212. A. Caselli, E. Solari, R. Scopelliti, C. Floriani, N. Re, C. Rizzoli, A. Chiesi-Villa, J. Am. Chem. Soc., 122, 3652 2000.
213. C.E. Laplaza, C.C. Cummins, Science, 268, 861, 1995.
214. M.D. Fryzuk, J.B. Love, S.J. Rettig, Science, 275, 1445, 1997.
215. Y. Nishibayashi, S. Iwai, M. Hidai, Science, 279, 540, 1998.
216. P. Chen, Z.T. Xiong, J.Z. Luo, J.Y. Lin, K.L. Tan, Nature, 420, 302, 2002.
217. W.H. Bernskoetter, E. Lobkovsky, P.J. Chirik, J. Am. Chem. Soc., 127, 14051, 2005.
218. W.H. Bernskoetter, A.V. Olmos, E. Lobkovsky, P.J. Chirik, Organometallics, 25, 1021, 2006.
219. P. Avenier, M. Taoufik, A. Lesage, X. Solans-Monfort, A. Baudouin, A. de Mallmann, L. Veyre, J.-M. Basset, O. Eisenstein, L. Emsley, E.A. Quadrelli, Science, 317, 1056, 2007.
220. J. Li, S. Li, Angew. Chem. Int. Ed., 47, 8040, 2008.
221. J.M. Smith, R.J. Lachicotte, P.L. Holland, J. Am. Chem. Soc., 125, 15752, 2003
222. M.D. Fryzuk, S.A. Johnson, B.O. Patrick, A. Albinati, S.A. Mason, T.F. Koetzle, J. Am. Chem. Soc., 123, 3960, 2001.
223. J.M. deWolf, R. Blaauw, A. Meetsma, J.H. Teuben, R. Gyepes, V. Varga, K. Mach, N. Veldman, A. L. Spek, Organometallics, 15, 4977, 1996.
224. P. J. Chirik, L.M. Henling, J.E. Bercaw, Organometallics, 20, 534, 2001.
225. J.S. Parry, G.F.N. Cloke, S.J. Cole, M.B. Hursthouse, J. Am. Chem. Soc., 121, 6867, 1999.
226. B. Kanellakopulos, E. Dornberger, F. Baumgaertner, Inorg. Nucl. Chem. Lett., 10, 155, 1974.
227. P.C. Blake, M.F. Lappert, J.L. Atwood, H. Zhang, J. Chem. Soc. Chem. Commun., 15, 1148, 1986.
228. M.R. Spirlet, J. Rebizant, J. Goffart, Acta Crystallogr. B, 38, 2400, 1982.
229. I. Korobkov, S. Gambarotta, G.P.A. Yap, Angew. Chem. Int. Ed., 42, 814, 2003.
230. I. Korobkov, S. Gambarotta, G.P.A. Yap, Angew. Chem. Int. Ed., 42, 4958, 2003.
231. P. Roussel, P. Scott, J. Am. Chem. Soc., 120, 1070, 1998.
232. D.J. Mindiola, Y.C. Tsai, R. Hara, Q. Chen, K. Meyer, C.C. Cummins, Chem. Commun., 125, 2001.
233. F.G.N. Cloke, P.B. Hitchcock, J. Am. Chem. Soc., 124, 9352, 2002.
234. W.J. Evans, S.A. Kozimor, J.W. Ziller, J. Am. Chem. Soc., 125, 14264, 2003.
235. I. Castro-Rodríguez, H. Nakai, P. Gantzel, L.N. Zakharov, A.L. Rheingold, K. Meyer, J. Am. Chem. Soc., 125, 15734, 2003.
236. O.T. Summerscales, G.F.N. Cloke, P.B. Hitchcock, J.C. Green, N. Hazari, Science, 311, 829, 2006.
237. I. Castro-Rodríguez, H. Nakai, L. N. Zakharov, A. L. Rheingold, K. Meyer, Science, 305, 1757, 2004.
238. P.L. Diaconescu, P.L. Arnold, T.A. Baker, D.J. Mindiola, C.C. Cummins, J. Am. Chem. Soc., 122, 6108, 2000.
239. W.J. Evans, S.A. Kozimor, J.W. Ziller, N. Kaltsoyannis, J. Am. Chem. Soc., 126, 14533, 2004.
240. M.D. Fryzuk, T.S. Haddad, S.J. Rettig, J. Am. Chem. Soc., 112, 8185, 1990.
241. J. Jubb, S. Gambarotta, J. Am. Chem. Soc., 116, 4477, 1994.
242. C.C. Cummins, Chem. Commun., 1777, 1998.
243. H. Kawaguchi, T. Matsuo, Angew. Chem. Int. Ed., 41, 2792, 2002.
244. B.L. Yonke, A.J. Keane, P.Y. Zavalij, L.R. Sita, Organometallics, 31, 345, 2012.
245. P.G. Wilkinson, N.B. Houk, J. Chem. Phys., 24, 528, 1956.
246. G.B. Nikiforov, P. Crewdson, S. Gambarotta, I. Korobkov, P.H.M. Budzelaar, Organometallics, 26, 48 2007.
247. J. García-Glez, Z. Amghouz, I. da Silva, C.O. Ania, J.B. Parra, C. Trobajo, S. García-Granda, Chem. Commun., 53, 2249, 2017.
248. C.B. Amphlett, Inorganic Ion Exchangers, Elsevier, 1964.
249. A. Clearfield, J.A. Stynes, J. Inorg. Nucl. Chem., 26, 117, 1964.
250. A. Clearfield, R.H. Blessing, J.A. Stynes, J. Inorg. Nucl. Chem., 30, 2249, 1968.

251. A. Clearfield, U. Costantino, in Comprehensive Supramolecular Chemistry (Eds. G. Alberti, T. Bein) Pergamon, Vol. 7, Chap. 4, 1996.
252. M.A. Salvadó, P. Pertierra, S. García-Granda, J.R. García, J. Rodríguez, M.T. Fernández-Díaz, *Acta Cryst.* B, 52, 896, 1996.
253. N.J. Clayden, J. Chem. Soc. Dalton Trans., 1877, 1987.
254. G. Alberti, M.G. Bernasconi, M. Casciola, React. Polym., 11, 245, 1989.
255. A. Christensen, E.K. Andersen, I.G.K. Andersen, G. Alberti, N. Nielsen, M.S. Lehmann, Acta Chem. Scand., 44, 865, 1990.
256. D.M. Poojary, B. Shpeizer, A. Clearfield, J. Chem. Soc. Dalton Trans., 111, 1995.
257. M.A. Salvadó, P. Pertierra, S. García-Granda, L.M. Barcina, R. Llavona, J. Rodríguez, Z. Krist., 216, 326, 2001.
258. G. Alberti, U. Costantino, S. Allulli, N. Tomassini, J. Inorg. Nucl. Chem., 40, 1113, 1978.
259. G. Alberti, Acc. Chem. Res., 11, 163, 1978.
260. G. Alberti, U. Costantino, in Inclusion Compounds. Vol. 5: Inorganic and Physical Aspects of Inclusion (Eds. J.L. Atwood, J.E.D. Davies, D.D. MacNicol), Oxford University Press, pp. 136-173, 1991.
261. M. Pica, Catalysts, 7, 190, 2017.
262. G. Alberti, E. Torracca, J. Inorg. Nucl. Chem., 30, 317, 1968.
263. D. Capitani, M. Casciola, A. Donnadio, R. Vivani, Inorg. Chem., 49, 9409, 2010.
264. C. Trobajo, S.A. Khainakov, A. Espina, J.R. García, Chem. Mater., 12, 1787, 2000.
265. A. Clearfield, W.L. Duax, A.S. Medina, G.D. Smith, J.R. Thomas, J. Phys. Chem., 73, 3424, 1969.
266. E.J. Rivera, C. Figueroa, J.L. Colon, L. Grove, W.B. Connick, Inorg. Chem., 46, 8569, 2007.
267. M.B. Santiago, G.A. Daniel, A. David, B. Casanas, G. Hernández, A.R. Guadalupe, J.L. Colon, Electroanal., 22, 1097, 2010.
268. A.A. Marti, J.L. Colon, Inorg. Chem., 49, 7298, 2010.
269. M. Pica, A. Donnadio, D. Capitani, R. Vivani, E. Troni, M. Casciola, Inorg. Chem., 50, 11623, 2011.
270. M. Pica, R. Vivani, A. Donnadio, E. Troni, S. Fop, M. Casciola, Inorg. Chem., 54, 9146, 2015.
271. A. Clearfield, in Inorganic Ion Exchange Materials (Ed: A. Clearfield), CRC Press, pp. 1-74, 1982.
272. G. Alberti, in Inorganic Ion Exchange Materials (Ed: A. Clearfield), CRC Press, pp. 75-109, 1982.
273. G. Alberti, U. Costantino, F. DiGregorio, P. Galli, E. Torracca, J. Inorg. Nucl. Chem., 30, 295, 1968.
274. G. Alberti, U. Costantino, J. Chromatogr., 50, 482, 1970.
275. M.A. Salvadó, P. Pertierra, C. Trobajo, J.R. García, J Am. Chem. Soc., 129, 10970, 2007.
276. M.A. Salvadó, P. Pertierra, A.I. Bortun, C. Trobajo, J.R. García, Inorg. Chem., 44, 3512, 2005.
277. M.A. Salvadó, P. Pertierra, G.R. Castro, C. Trobajo, J.R. García, Inorg. Chem., 47, 1246, 2008.
278. M.A. Salvadó, P. Pertierra, A.I. Bortun, C. Trobajo, J.R. García, Inorg. Chem., 47, 7207, 2008.
279. A.I. Orlova, V.Yu.Volgutov, G.R. Castro, S. García-Granda, S.A. Khainakov, J.R. García, Inorg. Chem., 48, 9046, 2009.
280. J. García-Glez, B.F. Alfonso, J.A. Huidobro, S.A. Khainakov, G.R. Castro, C. Trobajo, J. Thermal. Anal. Calorim., 118, 759, 2014.
281. I. Iglesias, B.F. Alfonso, Z. Amghouz, C. Trobajo, J.R. García, J.A. Huidobro, Ceram. Int., 43, 10776, 2017.
282. U. Costantino, A. Gasperoni, J. Chromatogr., 51, 289, 1970.
283. A. LaGinestra, P. Galli, M.L. Berardelli, M.A. Massucci, J. Chem. Soc. Dalton Trans., 521, 1984.
284. R. Llavona, M. Suárez, J.R. García, J. Rodríguez, Inorg. Chem., 28, 2863, 1989.
285. I. Nakai, K. Imai, T. Kawashima, K.Ohsumi, F. Irumi, I. Tomita, Anal. Sci., 6, 689, 1990.
286. S. Bruque, M.A.G. Aranda, E.R. Losilla, P. Olivera-Pastor, P. Maireles-Torres, Inorg Chem., 34, 893, 1995.
287. G. Alberti, in Inorganic Ion Exchangers and Adsorbents for Chemical Processing in the Nuclear Fuel Cycle, IAEA-TECDOC-337, IAEA, Vienna, pp. 195-211, 1985.
288. G. Alberti, in Recent Developments in Ion Exchange (Eds: P. A. Williams, M. J. Hudson), Elsevier Applied Science, pp. 233-248, 1987.
289. A. Clearfield, in Tailored Organic-Inorganic Materials (Eds. E. Brunet, J.L. Colon, A. Clearfield), Wiley, pp. 1-44, 2015.
290. R. Llavona, M. Suárez, J.R. García, J. Rodríguez, Anal. Chem., 58, 547, 1986.
291. C. Álvarez, R. Llavona, J.R. García, M. Suárez, J. Rodríguez, Inorg. Chem., 26, 1045, 1987.
292. C. Álvarez, R. Llavona, J.R. García, M. Suárez, J. Rodríguez, J. Chem. Soc. Dalton Trans., 2045, 1987.
293. E. González, R. Llavona, J.R. García, J. Rodríguez, J. Chem. Soc. Dalton Trans., 829, 1989.
294. U. Costantino, in Inorganic Ion Exchange Materials (Ed. A. Clearfield), CRC Press, pp. 111-132, 1982.

295. G. Alberti, U. Costantino, in Intercalation Chemistry (Eds. M.S . Whittingham, A.J. Jacobson), Academic Press, pp. 147-180, 1982.
296. T. Kijima, Y. Matsui, Nature, 322, 533, 1986.
297. R.M. Kim, J.E. Pillion, D.A. Burwell, J.T. Groves, M.E. Thompson, Inorg. Chem., 21, 4509, 1993.
298. U. Costantino, J. Chem. Soc. Dalton Trans., 402, 1979.
299. J.L. Colon, in Tailored Organic-Inorganic Materials (Eds. E. Brunet, J.L. Colon, A. Clearfield), Wiley, pp. 395-438, 2015.
300. F. Menéndez, A. Espina, C. Trobajo, J. Rodríguez, Mater. Res. Bull., 25, 1531, 1990.
301. U. Costantino, J. Inorg. Nucl. Chem., 43, 3329, 1981.
302. A. Menéndez, M. Bárcena, E. Jáimez, J.R. García, J. Rodríguez, Chem. Mater., 5, 1078, 1993.
303. A. Espina, J.R. García, J.M. Guil, E. Jáimez, J.B. Parra, J. Rodríguez, J. Phys. Chem. B, 102, 1713, 1998.
304. A. Espina, E. Jáimez, S.A. Khainakov, C. Trobajo, J.R. García, J. Rodriguez, Chem. Mater., 10, 2490, 1998.
305. L. Mafra, F.A.A. Paz, J. Rocha, A. Espina, S.A. Khainakov, J.R. García, C. Fernández, Chem. Mater., 17, 6287, 2005.
306. U. Costantino, M. Casciola, L. Di Croce, F. Marmottini, J. Incl. Phenom., 6, 291, 1988.
307. A. Espina, E. Jáimez, S.A. Khainakov, C. Trobajo, J.R. García, J. Rodríguez, Eur. J. Solid State Inorg. Chem., 34, 959, 1997.
308. G. Alberti, M. Casciola, U. Costantino, J. Colloid Interface Sci., 107, 256, 1985.
309. G. Alberti, F. Marmottini, J. Colloid Interface Sci., 157, 513, 1993.
310. G. Alberti, U. Costantino, R. Vivani, R.K. Biswas, React. Polym., 17, 245, 1992.
311. G. Alberti, M. Casciola, R.K. Biswas, Inorg. Chim. Acta, 201, 207, 1992.
312. G. Alberti, R. Vivani, R.K. Biswas, S. Murcia-Mascarós, React. Polym., 19, 1, 1993.
313. G. Alberti, M. Casciola, R. Vivani, R.K Biswas, Inorg. Chem., 32, 4600, 1993.
314. G. Alberti, S. Murcia-Mascarós, R. Vivani, Mater. Chem. Phys., 35, 187, 1993.
315. D.J. Jones, J.M. Leloup, D. Yi, J. Rozière, Solid State Ionics, 61, 117, 1993.
316. A. Espina, J.B. Parra, J.R. García, J.A. Pajares, J. Rodríguez, Mater. Chem. Phys., 35, 250, 1993.
317. P. Olivera-Pastor, J. Maza-Rodríguez, P. Maireles-Torres, E. Rodríguez-Castellón, A. Jiménez-López, J. Mater. Chem., 4, 179, 1994.
318. G.F. Walker, Nature, 187, 312, 1960.
319. R.E. Grim, Clay Mineralogy, McGraw-Hill, 1968.
320. P.H. Nadeau, Appl. Clay Sci., 2, 83, 1987.
321. A.J. Jacobson, Mater. Sci. Forum, 152-153, 1, 1994.
322. A. Lerf, R. Schöllhorn, Inorg. Chem., 16, 2950, 1977.
323. P. Joensen, R.F. Frindt , S.R. Morrison, Mater. Res. Bull., 21, 457, 1986.
324. L.F. Nazar, A.J. Jacobson, Chem. Commun., 570, 1986.
325. N. Yamamoto, T. Okuhara, T. Nakato, J. Mater. Chem., 11, 1858, 2001.
326. H. Rebbah, M.M. Borel, B. Raveau, Mater. Res. Bull., 15, 317, 1980.
327. H. Rebbah, J. Pannetier, B. Raveau, J. Solid State Chem., 41, 57, 1982.
328. L.F. Nazar, S.W. Liblong, X.T. Yin, J. Am. Chem. Soc., 113, 5889, 1991.
329. M.M.J. Treacy, S.B. Rice, A.J. Jacobson, J.T. Lewandowski , Chem. Mater., 2, 279, 1990.
330. T. Sasaki, M. Watanabe, H. Hashizume, H. Yamada, H. Nakazawa, J. Am. Chem. Soc., 118, 8329, 1996.
331. T. Sasaki, M. Watanabe, J. Am. Chem. Soc., 120, 4682, 1998.
332. M. Fang, C.H. Kim, T.E. Mallouk, Chem. Mater., 11, 1519, 1999.
333. R.E. Schaak, T.E. Mallouk, Chem. Mater., 12, 2513, 2000.
334. R.E. Schaak, T.E. Mallouk, Chem. Mater., 14, 1455, 2002.
335. J.-Y. Kim, I. Chung, J.-H. Choy, G.-S. Park, Chem. Mater., 13, 2759, 2001.
336. Z.R. Dai, Z.W. Pan, Z.L. Wang, J. Phys. Chem. B, 106, 902, 2002.
337. V. Nicolosi, M. Chhowalla, M.G. Kanatzidis, M.S. Strano, J.N. Coleman, Science, 340, 1420, 2013.
338. M. Adachi-Pagano, C. Forano, J.P. Besse, Chem. Commun., 91, 2000.
339. F. Leroux, M. Adachi-Pagano, M. Intissar, S. Chauvière, C. Forano, J.P. Besse, J. Mater. Chem., 11, 105, 2001.
340. T. Hibino, W. Jones, J. Mater. Chem., 11, 1321, 2001.
341. T. Hibino, Chem. Mater., 16, 5482, 2004.
342. L. Li, R. Ma, Y. Ebina, N. Iyi, T. Sasaki, Chem. Mater., 17, 4386, 2005.
343. Z. Liu, R. Ma, M. Osada, N. Iyi, Y. Ebina, K. Takada, T. Sasaki, J. Am. Chem. Soc., 128, 4872, 2006.
344. Z. Liu, R. Ma, Y. Ebina, N. Iyi, K. Takada, T. Sasaki, Langmuir, 23, 861, 2007.

345. J.M. Haschke, Inorg. Chem., 13, 1812, 1974.
346. L.J. McIntyre, L.K. Jackson, A.M. Fogg, Chem. Mater., 20, 335, 2008.
347. F. Geng, H. Xin, Y. Matsushita, R. Ma, M. Tanaka, F. Izumi, N. Iyi, T. Sasaki, Chem.-Eur. J., 14, 9255, 2008.
348. L. Hu, R. Ma, T.C. Ozawa, T. Sasaki, Chem. Asian J., 5, 248, 2010.
349. Y.S. Yoon, B.-I. Lee, K.S. Lee, G.H. Im, S.-H. Byeon, J. H. Lee, I. S. Lee, Adv. Funct. Mater. , 19, 3375, 2009.
350. R.F. Service, Science, 324, 875, 2009.
351. A.K. Geim, Science, 324, 1530, 2009.
352. K.S. Novoselov, A.K. Geim, S.V. Morozov, D. Jiang, Y. Zhang, S.V. Dubonos, I.V. Grigorieva, A.A. Firsov, Science, 306, 666, 2004.
353. X. Du, I. Skachko, F. Duerr, A. Luican, E.Y. Andrei, Nature, 462, 192, 2009.
354. K.I. Bolotin, F. Ghahari, M.D. Shulman, H.L. Stormer, P. Kim, Nature, 462, 196, 2009.
355. Y.-M. Lin, K.A. Jenkins, A. Valdés-García, J.P. Small, D.B. Farmer, P. Avouris, Nano Lett., 9, 422, 2009.
356. X. Li, W. Cai, J. An, S. Kim, J. Nah, D. Yang, R. Piner, A. Velamakanni, I. Jung, E. Tutuc, S.K. Banerjee, L. Colombo, R.S. Ruoff , Science, 324, 1312, 2009.
357. M. Choucair, P. Thordarson, J.A. Stride, Nat. Nanotechnol., 4, 30, 2009.
358. H. Thiele, Kolloid-Z., 111, 15, 1948.
359. W. Hummers, R. Offeman, J. Am. Chem. Soc., 80, 1339, 1958.
360. R.C. Croft, Quart. Rev. Chem. Soc., 14, 1, 1960.
361. W. Scholz, H.P. Boehm, Z. Anorg. Allg. Chem., 369, 327, 1969.
362. N.I. Kovtyukhova, P.J. Ollivier, B.R. Martin, T.E. Mallouk, S.A. Chizhik, E.V. Buzaneva, A.D. Gorchinskiy, Chem. Mater., 1 , 771, 1999.
363. S. Park, R.S. Ruoff, Nat. Nanotechnol., 4, 217, 2009.
364. G. Eda, M. Chhowalla, Adv. Mater., 22, 2392, 2010.
365. D. Pacilé, J.C. Meyer, Ç.Ö. Girit, A. Zettl, Appl. Phys. Lett., 92, 133107, 2008.
366. C. Zhi, Y. Bando, C. Tang, H. Kuwahara, D. Golberg, Adv. Mater., 21, 2889, 2009.
367. R. Ma, T. Sasaki, Adv. Mater., 22, 5082, 2010.
368. T. Sasaki, S. Nakano, S. Yamauchi, M. Watanabe, Chem. Mater., 9, 602, 1997.
369. M. Iida, T. Sasaki, M. Watanabe, Chem. Mater., 10, 3780, 1998.
370. R. Abe, K. Shinohara, A. Tanaka, M. Hara, J.N. Kondo, K. Domen, Chem. Mater., 10, 329, 1998.
371. T. Yui, Y. Mori, T. Tsuchino, T. Itoh, T. Hattori, Y. Fukushima, K. Takagi, Chem. Mater., 17, 206, 2005.
372. W. Sugimoto, O. Terabayashi, Y. Murakami, Y. Takasu, J. Mater. Chem., 12, 3814, 2002.
373. K. Okamoto, T. Sasaki, T. Fujita, N. Iyi, J. Mater. Chem., 16, 1608, 2006.
374. K.-H. Lee, B.-I . Lee, J.-H. You, S.-H. Byeon, Chem. Commun., 1461, 2010.
375. G. Decher, Science, 277, 1232, 1997.
376. E.R. Kleinfeld, G.S. Ferguson, Science, 265, 370, 1994.
377. S.W. Keller, H.-N. Kim, T. E. Mallouk, J. Am. Chem. Soc., 116, 8817, 1994.
378. M. Fang, C.H. Kim, G.B. Saupe, H.-N. Kim, C.C. Waraksa, T. Miwa, A. Fujishima, T.E. Mallouk, Chem. Mater., 11, 1526, 1999.
379. T. Sasaki, Y. Ebina, M. Watanabe, G. Decher, Chem. Commun., 2163, 2000.
380. T. Sasaki, Y. Ebina, T. Tanaka, M. Harada, M. Watanabe, G. Decher, Chem. Mater., 13, 4661, 2001.
381. L.Z. Wang, Y. Omomo, N. Sakai, K. Fukuda, I. Nakai, Y. Ebina, K. Takada, M. Watanabe, T. Sasaki, Chem. Mater., 15, 2873, 2003.
382. J. Huang, R. Ma, Y. Ebina, K. Fukuda, K. Takada, T. Sasaki, Chem. Mater., 22, 2582, 2010.
383. S. Acharya, J.P. Hill, K. Ariga, Adv. Mater., 21, 2959, 2009.
384. H. Lee, L.J. Kepley, H.-G. Hong, T.E. Mallouk, J. Am. Chem. Soc., 110, 618, 1988.
385. T. Yamaki, K. Asai, Langmuir, 17, 2564, 2001.
386. S. Takahashi, R. Tanaka, N. Wakabayashi, M. Taniguchi, Yamagishi, Langmuir, 19, 6122, 2003.
387. Y. Umemura, E. Shinohara, A. Koura, T. Nishioka, T. Sasaki, Langmuir, 22, 3870, 2006.
388. M. Muramatsu, K. Akatsuka, Y. Ebina, K. Wang, T. Sasaki, T. Ishida, K. Miyake, M. Haga, Langmuir, 21, 6590, 2005.
389. K. Akatsuka, M. Haga, Y. Ebina, M. Osada, K. Fukuda, T. Sasaki, ACS Nano, 3, 1097, 2009.
390. B.-W. Li, M. Osad, T.C. Ozawa, R. Ma, K. Akatsuka, Y. Ebina, H. Funakubo, S. Ueda, K. Kobayashi, T. Sasaki, Jpn. J. Appl. Phys., 48, 09KA15, 2009.
391. M. Osada, K. Akatsuka, Y. Ebina, H. Funakubo, K. Ono, K. Takada, T. Sasaki, ACS Nano, 4, 5225, 2010.

392. H.B. Ortiz-Oliveros, R.M. Flores-Espinosa, E. Ordóñez-Regil, S.M. Fernández-Valverde, Chem. Eng. J., 236, 398, 2014.
393. I. Zhuravlev, O. Zakutevsky, T. Psareva, V. Kanibolotsky, V. Strelko, M. Taffet, G. Gallios, J. Radioanal Nucl. Chem., 254, 85, 2002.
394. O. Mrad, A. Abdul-Hadi, H. Arsan, J. Radioanal Nucl. Chem., 287, 177, 2011.
395. K. Binnemans, Coord. Chem. Rev., 295, 1, 2015.
396. J.A. Huidobro, I. Iglesias, B.F. Alfonso, C. Trobajo, J.R. García, in Computational Mathematics, Numerical Analysis and Applications, SEMA SIMAI Springer Series, pp. 229-233, 2017.
397. S. Vyazovkin, A.K. Burnham, J.M. Criado, L.A. Pérez-Maqueda, C. Popescu, N. Sbirrazzuoli, Thermochim. Acta, 520, 1, 2011.
398. P. Simon, P.S. Thomas, J. Okuliar, A.S. Ray, J. Therm. Anal. Calorim., 72, 867, 2003.
399. N. Sbirrazzuoli, L. Vincent, A. Mija, N. Guigo, Chemometr. Intell. Lab., 96, 219, 2009.
400. H. Friedman, J. Polymer. Sci. C, 6, 183, 1964.
401. J.A. Huidobro, I. Iglesias, B.F. Alfonso, A. Espina, C. Trobajo, J.R. García, Chemometr. Intell. Lab., 151, 146, 2016.
402. Z. Ma, D. Chen, J. Gu, B. Bao, Q. Zhang, Energy Conv. Manag., 89, 251, 2015.
403. S. Vyazovkin, J. Comput. Chem., 22, 178, 2001.
404. P. Simon, P. Thomas, T. Dubaj, Z. Cibulkova, A. Peller, M. Veverka, J. Therm. Anal. Calorim., 115, 853, 2014.
405. S. Vyazovkin, J. Comput. Chem., 18, 393, 1997.
406. S. García-Granda, M.A. Salvadó, P. Pertierra, A.I. Bortun, S.A. Khainakov, C. Trobajo, A. Espina, J.R. García, Inorg. Chem. Commun., 4, 555, 2001.
407. A.I. Bortun, S.A. Khainakov, L.N. Bortun, D.M. Poojary, J. Rodríguez, J.R. García, A. Clearfield, Chem. Mater.,9, 1805, 1997.
408. S. Cavenati, C.A. Grande, Chem. Eng. Sci., 61, 3893, 2006.
409. B. Majumdar, Ind. Eng. Chem. Res., 50, 3021, 2011.
410. H. Habgood, Canadian J. Chem, 36, 1384, 1958.
411. A. Jayaraman, A.J. Hernández-Maldonado, Chem. Eng. Sci., 59, 2407, 2004.
412. J. Yoon, H. Chang, Nature Mater., 16, 526, 2017.
413. H. Ghanbaria, F. Pettersson, , Chem. Eng. Res. Des., 102, 322, 2015.
414. H. Liu, Ammonia Synthesis Catalysts, Chemical Industries Press & World Scientific, 2013.
415. M. Kitano, Y. Inoue, Y. Yamazaki, F. Hayashi, S. Kanbara, S. Matsuishi, T. Yokoyama, S.-W. Kim, M. Hara, H. Hosono, Nature Chem., 4, 934, 2012.
416. N. Gruber, J.N.; Galloway, Nature, 451, 293, 2008.
417. N.D. Spencer, R.C. Schoonmaker, G.A. Somorjai, Nature, 294, 643, 1981.
418. C.J.H. Jacobsen, S. Dahl, B.S. Clausen, S. Bahn, A. Logadottir, J.K. Nørskov, J. Am. Chem. Soc., 123, 8404, 2001.
419. H. Bielawa, O. Hinrichsen, A. Birkner, M. Muhler, Angew. Chem. Int. Ed., 40, 1061, 2001.
420. T.W. Hansen, J.B. Wagner, P.L. Hansen, S. Dahl, H. Topsøe, C. J.H. Jacobsen, Science, 294, 1508, 2001.
421. G. Ertl (Nobel Lecture), Angew. Chem. Int. Ed., 2008, 47, 3524.
422. D.V. Yandulov, R.R. Schrock, Science, 301, 76, 2001.
423. K. Arashiba, Y. Miyake, Y. Nishibayashi, Nature Chem., 3, 120, 2011.
424. R.M. Roberts, Serendipia, Alianza Editorial, 2010.
425. A. Espina, C. Trobajo, S.A. Khainakov, J.R. García, Mater. Res. Bull., 36, 2531, 2001.
426. A. Espina, C. Trobajo, S.A. Khainakov, J.R. García, M.A. Salvadó, P. Pertierra, S. García-Granda, Mater. Res. Bull., 37, 1381, 2002.
427. S. García-Granda, S.A. Khainakov, A. Espina, J.R. García, G.R. Castro, J. Rocha, L. Mafra, Inorg. Chem., 49, 2630, 2010 (and references therein).
428. B.F. Alfonso, C. Piqué, C. Trobajo, J.R. García, E. Kampert, U. Zeitler, J. Rodríguez-Fernández, M.T. Fernández-Díaz, J.A. Blanco, Phys. Rev. B, 82, 144431, 2010 (and references therein).
429. M.A. Salvadó, P. Pertierra, S. García-Granda, A. Espina, C. Trabajo, J.R. García, Inorg. Chem., 38, 5944, 1999.
430. P.B. Moore, Am. Mineral., 51, 168, 1966.

5. Conclusiones

5.1. Conclusiones

1. Se sintetizó y caracterizó tanto el $Ti(HPO_4)_2 \cdot H_2O$ (α-TiP) como su producto de intercalación con propilamina, $Ti(HPO_4)_2 \cdot 2C_3H_7NH_2 \cdot H_2O$ (α-TiPPr).
2. Se demostró que, en el α-TiP, la captación de cationes europio(III) en medio acuoso está limitada a la superficie del material.
3. La inserción de europio(III) en α-TiPPr se llevó a cabo mediante: (i) procesos de intercambio iónico $C_3H_7NH_3^+/[Eu(H_2O)_6]^{3+}$, y (ii) auto-ensamblaje de láminas de fosfato de titanio (cargadas negativamente) y especies catiónicas hidratadas de Eu^{3+}, con formación de nano-placas.
4. Se sintetizaron nano-placas de fosfatos dobles de europio(III)-titanio(IV) de espesor variable (0.8-50 nm).
5. Se caracterizó la fase saturada en europio, α-$[Eu(H_2O)_6]_{2/3}Ti(PO_4)_2 \cdot [(H_2O)_6]_{1/3}$ (α-EuTiPPr), modelizando su estructura cristalina mediante métodos DFT.
6. Los nuevos fosfatos dobles de europio(III)-titanio(IV) emiten en el rango del naranja-rojo cuando son excitados a 394 nm, como resultado de transiciones $^5D_0 \rightarrow {}^7F_J$ (J = 0-4) en niveles electrónicos de los cationes Eu^{3+}.
7. La velocidad de decaimiento radiativo en los fosfatos dobles de europio(III)-titanio(IV) depende de la localización de los cationes Eu^{3+} en el material, siendo más rápida para cationes adsorbidos en la superficie de las nano-placas que para los que ocupan el espacio interlaminar.
8. Se obtuvo una sal amónica del γ-fosfato de titanio, γ-$Ti(PO_4)(NH_4HPO_4)$ (γ-NH_4TiP) por tratamiento hidrotermal de la fase π-$Ti_2O(PO_4) \cdot 2H_2O$ (π-TiP) en presencia de urea y ácido fosfórico.
9. γ-NH_4TiP posee simetría monoclínica (grupo espacial $P2_1/m$, a = 5.0725(3) Å, b = 6.3101(3) Å, c = 11.2435(5) Å, β = 97.980(3)º, Z = 2) y una estructura cristalina bidimensional definida por láminas de γ-fosfato de titanio cargadas negativamente y cationes amonio ocupando el espacio interlaminar.
10. En la descomposición térmica del γ-NH_4TiP, se detectaron dos nuevos compuestos pseudo-laminares, $Ti(PO_4)(NH_4HP_2O_7)_{0.5}$ y $Ti(PO_4)(H_2P_2O_7)_{0.5}$.

11. El fosfato doble de amonio-titanio(IV) policristalino con estructura tipo pirocloro, formulado previamente como $(NH_4)_{0.79}(P_{1.14}Ti_{0.86})O_{3.93}(OH)_{2.07}$ (pc-NH_4TiP), se demostró que es un compuesto de valencia mixta P(III)-P(V).

12. El tratamiento térmico del ρ-$Ti_2O(PO_4)_2\cdot 2H_2O$ (ρ-TiP) conduce a un compuesto anhidro, $Ti_2O(PO_4)_2$ (ρ-TiP-dh).

13. ρ-TiP-dh posee simetría triclínica (grupo espacial *P*-1, a = 5.0843(1) Å, b = 8.6121(2) Å, c = 9.6766(2) Å, α = 74.501(2)º, β = 76.146(2)º, γ = 74.488(3)º, Z = 2) y una estructura cristalina tri-dimensional caracterizada por la presencia de dos tipos de canales unidimensionales paralelos al eje *a*. Presenta dos átomos de titanio (Ti1 y Ti2), química y cristalográficamente inequivalentes, coordinados por átomos de oxígeno y conectados por un puente oxo no lineal. Ti1 posee coordinación octaédrica ligeramente distorsionada. Ti2 se encuentra en un entorno pseudo-tetraédrico.

14. La rehidratación de ρ-TiP-dh es un proceso lento que, saturando las vacantes de coordinación del Ti2, tarda meses en completarse en condiciones ambientales.

15. El ρ-TiP, un material esencialmente no poroso (área superficial específica: 13 m^2/g), que puede ser activado térmicamente y utilizado como contenedor de gases.

16. ρ-TiP-dh, en el intervalo de temperaturas 200-300 ºC, capta nitrógeno de forma reversible en cantidades no desdeñables (0.35 cm^3/g, STP).

17. Se aplicaron métodos iso-conversionales (diferenciales e integrales) para la adquisición de parámetros cinéticos en procesos de descomposición térmica de los nuevos materiales.

18. Se determinaron los valores de energía de activación aparente en la descomposición térmica de α-TiP, α-TiPPr, α-EuTiPPr, γ-NH_4TiP, pc-NH_4TiP, y ρ-TiP.

5.2. Conclusions

1. $Ti(HPO_4)_2{\cdot}H_2O$ (α-TiP), and its propylamine intercalation product, $Ti(HPO_4)_2{\cdot}2C_3H_7NH_2{\cdot}H_2O$ (α-TiPPr), were synthesized and characterized.
2. It was shown that for α-TiP, in aqueous media, the europium(III) uptake takes place on the material's surface.
3. In α-TiPPr, the europium(III) insertion was carried out by: (i) $C_3H_7NH_3^+/[Eu(H_2O)_6]^{3+}$ ion-exchange, and (ii) self-assembly of titanium phosphate sheets (negatively charged) and hydrated Eu^{3+} species, with formation of nano-plates.
4. Europium(III)-titanium(IV) phosphate nano-plates with variable thickness (0.8-50 nm) were synthesized.
5. The α-$[Eu(H_2O)_6]_{2/3}Ti(PO_4)_2{\cdot}[(H_2O)_6]_{1/3}$ (α-EuTiPPr) europium saturated phase was characterized, and its crystalline structure was modeled by DFT methods.
6. As a result of transitions $^5D_0 \rightarrow {}^7F_J$ (J = 0-4) on the Eu^{3+} electronic levels, the new europium(III)-titanium(IV) phosphates emit in the orange-red range when are excited at 394 nm.
7. In the new europium(III)-titanium(IV) phosphates, the radiative decay is a function of the Eu^{3+} location, being faster for cations adsorbed on the surface of the nano-plates than for those occupying the interlaminar space.
8. A new ammonium-titanium phosphate, γ-$Ti(PO_4)(NH_4HPO_4)$ (γ-NH_4TiP), was obtained by hydrothermal treatment of π-$Ti_2O(PO_4){\cdot}2H_2O$ (π-TiP) in presence of urea and phosphoric acid.
9. γ-NH_4TiP is monoclinic ($P2_1/m$, a = 5.0725(3) Å, b = 6.3101(3) Å, c = 11.2435(5) Å, β = 97.980(3)°, Z = 2). Its two-dimensional crystalline structure is defined by negatively charged titanium-phosphate sheets and ammonium cations occupying the interlayered space.
10. By thermal decomposition of γ-NH_4TiP, two new pseudo-layered compounds, $Ti(PO_4)(NH_4HP_2O_7)_{0.5}$ and $Ti(PO_4)(H_2P_2O_7)_{0.5}$, were detected.

11. The polycrystalline ammonium-titanium(IV) phosphate with pyrochlore-type structure, previously formulated as $(NH_4)_{0.79}(P_{1.14}Ti_{0.86})O_{3.93}(OH)_{2.07}$ (pc-NH_4TiP), reveals a P(III)-P(V) mixed valence compound.

12. By thermal decomposition of $Ti_2O(PO_4)_2 \cdot 2H_2O$ (ρ-TiP) a new anhydrous fibrous compound, $Ti_2O(PO_4)_2$ (ρ-TiP-dh), is detected.

13. ρ-TiP-dh is triclinic (P-1, a = 5.0843(1) Å, b = 8.6121(2) Å, c = 9.6766(2) Å, α = 74.501(2)º, β = 76.146(2)º, γ = 74.488(3)º, Z = 2). Its three-dimensional crystalline structure presents two different one-dimensional channels, both parallel to the a-axis, and two atoms of titanium (Ti1 and Ti2) chemically and crystallographically inequivalents, both coordinated by oxygen atoms and connected by a non-linear oxo-bridge. Ti1 has a slightly distorted octahedral coordination and Ti2 is found into a pseudo-tetrahedral environment.

14. ρ-TiP-dh rehydration is a slow process (it needs months to be completed under environmental conditions) saturating the Ti2 coordination vacancies.

15. ρ-TiP, an essentially non-porous material (specific surface area: 13 m^2/g), after thermal activation transforms into a framework with high potential as a gas container.

16. ρ-TiP-dh, in the 200-300 ºC temperature range, retains nitrogen reversibly in non-negligible amount (0.35 cm^3/g, STP).

17. Iso-conversional methods (differential and integral) were applied for the acquisition of kinetic parameters in the thermal decomposition processes of some of the new materials.

18. The values of the apparent activation energy for the thermal decomposition of α-TiP, α-TiPPr, α-EuTiPPr, γ-NH_4TiP, pc-NH_4TiP and ρ-TiP were obtained.

6. Información Suplementaria

Artículo S1

“Exfoliation and europium(III)-functionalization of α-titanium phosphate *via* propylamine intercalation: From multilayer assemblies to single nanosheets”

Materials Science and Engineering B

En trámite de publicación

Índice de Impacto: 2.552

Elsevier Editorial System(tm) for Materials Science and Engineering B

Manuscript Draft

Manuscript Number:

Title: Exfoliation and europium(III)-functionalization of α-titanium phosphate via propylamine intercalation: From multilayer assemblies to single nanosheets

Article Type: Research paper

Keywords: Titanium phosphate; Propylamine; Exfoliation; Europium; Luminescence

Corresponding Author: Professor Zakariae Amghouz, PhD

Corresponding Author's Institution: University of Oviedo

First Author: Jorge García-Glez, PhD student

Order of Authors: Jorge García-Glez, PhD student; Camino Trobajo, PhD, Profesor; Alaa Adawy, PhD; Zakariae Amghouz, PhD

Research Data Related to this Submission

Title: Data for: Exfoliation and europium(III)-functionalization of a-titanium phosphate via propylamine intercalation: From multilayer assemblies to single nanosheets
Repository: Mendeley Data
https://data.mendeley.com/datasets/b8zzyyyc8f/draft?a=66431176-2201-4ea7-ac35-981b787d7bda

Graphical Abstract (for review)

Graphical Abstract

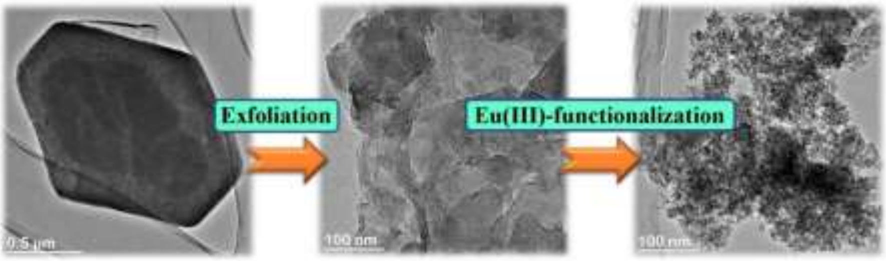

HIGHLIGHTS

- α-TiPPr has been exfoliated *via* a single-stage approach in aqueous medium
- α-TiPPr nanosheets were functionalized with Eu(III)
- Eu(III) uptake takes place *via* two distinct pathways
- These two pathways are attributed to the degree of exfoliation of α-TiPPr
- Functionalization of α-TiPPr nanosheets leads to two different morphologies

Exfoliation and europium(III)-functionalization of α-titanium phosphate *via* propylamine intercalation: From multilayer assemblies to single nanosheets[§]

Jorge García-Glez[a], Camino Trobajo[a], Alaa Adawy[b] and Zakariae Amghouz[c*]

[a] Department of Organic and Inorganic Chemistry, and [b] Scientific and Technical Services, University of Oviedo-CINN, 33006 Oviedo, Spain

[c] Department of Materials Science and Metallurgical Engineering, University of Oviedo, Campus Universitario, 33203 Gijón, Spain

**Corresponding author E-mail address:* amghouz.uo@uniovi.es

[§] *Dedicated to Prof. Abraham Clearfield, a luminary in the field of materials science for more than 60 years, on his 90th birthday.*

Abstract

Layered α-titanium phosphate intercalated with propylamine, $Ti(HPO_4)_2 \cdot 2C_3H_7NH_2 \cdot H_2O$ (α-TiPPr), has been synthesized by solid-vapour reaction and then exfoliated *via* a single-stage approach based on overnight stirring in aqueous medium. The obtained nanosheets were then functionalized using solid-liquid reaction with europium(III) nitrate aqueous solutions. The obtained materials were characterized by powder X-ray diffraction (PXRD), scanning electron microscopy (SEM), transmission electron microscopy (TEM, SAED, STEM-EDX), atomic force microscopy (AFM) and photoluminescence spectroscopy (PL). The europium(III) uptake takes place *via* two distinct pathways, the first is the previously reported $C_3H_7NH_3^+/[Eu(H_2O)_6]^{3+}$ ion-exchange process into the titanium-phosphate interlayer space of the multilayered α-TiPPr. The second pathway is the self-assembly of single-sheets which is provoked by electrostatic interactions between the negatively charged titanium-phosphate sheets and the Eu(III)-aqueous cations, leading to the formation of layered ultra-nanoparticles.

Keywords: Titanium phosphate; Propylamine; Exfoliation; Europium; Luminescence

1. Introduction

Although metal salts of phosphoric acid have been known for over a century, research on layered metal phosphates only began in the end of 1950's after some of these salts have been utilized as cation exchangers in radioactive waste streams [1]. In the beginning, tetravalent metal phosphates were only available as amorphous gels owing to their low solubility. In 1964, Clearfield and Stynes [2] prepared the first crystalline compound, α-$Zr(HPO_4)_2 \cdot H_2O$ (α-ZrP), which made their layered structure [3] and chemical reactivity [4] clearly understood. Later, the γ-layered compound, γ-$Zr(PO_4)(H_2PO_4) \cdot 2H_2O$ (γ-ZrP), was also reported by Clearfield et al. [5]. Not only can titanium phosphate be prepared as a gel or in intermediate stages of crystallinity, but also in several crystalline forms including α- and γ-TiP [6,7]. These layered tetravalent metal phosphates, with strong bonds in two dimensions and weak bonds in the third one, usually undergo two kinds of chemical reactions. The first one is the intercalation reactions that occur with the retention of the two-dimensional bonding, where the interlayer spacing could be expanded enough to accept the guest molecules [8-10]. In this case, the material remains crystalline or semi-crystalline, because of the attractive interactions between the guest and the sheets of the host [11-13]. The other type of reaction is the exfoliation, which can be considered an extreme case of intercalation. In this case, the forces between the sheets are weakly attractive or even repulsive, resulting in easily separable (nano)sheets by the effect of solvent molecules [14].

Two-dimensional (2D) nanosheets possessing atomic or molecular thickness and infinite planar dimensions are the thinnest known functional nanomaterials. These 2D nanosheets, derived from the layered parent materials *via* exfoliation processes, have recently gained increasing attention because of their outstanding functionalities and ability to serve as a building blocks [15,16]. Exfoliated nanosheets have been realized by implementing graphite oxide [17,18], transition metal dichalcogenides (e.g. MoS_2 and $MoSe_2$) [19,20], layered double hydroxides (LDHs, e.g. M(II)-Al-CO_3 where M = Zn, Ni, Co, Fe) [21,22], and metal oxides ($Ca_2Nb_3O_{10}^-$, $Ti_4O_9^{2-}$, $MnO_2^{-0.45}$) [23-25]. In principle, these materials undergo exfoliation in solvents to form colloidal dispersions of single layer nanosheets. Under specific conditions, they can form dimers and higher aggregates of individual sheets. Interestingly, these lamellar colloids can be re-stacked to make the parent solid or its intercalation compounds, and this feature has prompted their use as precursors, for nanocomposites and layered self-assembled hybrids.

Nowadays, exfoliation of layered tetravalent metal phosphate (e.g. α-ZrP, γ-ZrP and α-TiP) has also received considerable attention [26-28], especially their ability to reassemble with functional guest molecules [29-32]. This implies the possibility of combining α-TiP nanosheets and cationic species to further explore the plausible novel functionalities of these layered tetravalent metal phosphates. We have recently reported that when α-TiP is used as Eu^{3+}-sorbent in aqueous media, the material's surface is responsible only for the uptake [33-34], while the interlayer space is solely accessible to the europium species when the basal spacing is already expanded and an amine-intercalation product, $Ti(HPO_4)_2\cdot 2C_3H_7NH_2\cdot H_2O$ (α-TiPPr), is used as a starting material [34]. Under these operating conditions, a complex process takes place that includes partial hydrolysis of the titanium phosphate with the precipitation of crystalline europium phosphates and titanium dioxide gels together with the transformation of α-TiPPr to $\alpha\text{-}[Eu(H_2O)_6]_{2/3}Ti(PO_4)_2\cdot[(H_2O)_6]_{1/3}$ *via* an ion-exchange mechanism. In the present work, the exfoliation of α-TiP intercalated with propylamine (α-

TiPPr) and its Eu(III)-functionalization is proposed as an efficient procedure for the synthesis of luminescent layered ultra-nanoparticles.

2. Materials and methods

2.1. *Experimental procedures*

n-propylamine (98%) and europium(III) nitrate pentahydrate (99.9%) were purchased from Sigma-Aldrich and used as received. The starting material, α-TiPPr, was obtained by placing α-TiP in an atmosphere saturated with propylamine vapor for 6 days at room temperature [35]. In a bath, four equal samples, each constituted 0.3 g of α-TiPPr were equilibrated by adding 6 mL of 10^{-4} M europium nitrate solution ($T = 25.0 \pm 0.1$ °C, $t = 72$ h, solution/solid ratio = 20 mL/g) to provoke the material's exfoliation as previously described [34]. By *in situ* addition of different amounts of MilliQ water and 0.25 M europium(III) nitrate solution (pH 3.94) to a total volume of 8.4 mL, four samples **Eu_*x*** (*x* indicates the total volume added, in mL, of europium nitrate solution) were prepared. **Eu_0** was taken as the reference sample that was prepared by adding a total volume of 2.4 mL of MilliQ water in three successive portions of 0.8 mL separated by 1 h of stirring. The mixture was then stirred for 24 h before being centrifuged. In a similar procedure, **Eu_0.8** was obtained by adding two portions of 0.8 mL MilliQ water followed by 0.8 mL of europium nitrate solution. For **Eu_1.6**, one portion of 0.8 mL MilliQ water followed by two portions of 0.8 mL europium nitrate solution were added. Finally, **Eu_2.4** has been obtained after adding three successive portions (0.8 mL each) of europium nitrate solution. The elemental analysis results on carbon are summarized in Table S1 (see Electronic Supporting Information, ESI).

2.1. *Characterization procedures*

The powder X-ray diffraction (PXRD) patterns were recorded on X´pert Panalytical diffractometer with Cu-Kα radiation (λ = 1.5418 Å). The samples were gently ground in an agate mortar in order to minimize the preferred orientation. A Mettler-Toledo equipment (TGA/SDTA851^e) were used for the thermal analyses in oxygen dynamic atmosphere (50 mL/min) at a heating rate of 10 ºC/min. In TG test, a Pfeiffer Vacuum ThermoStar^{TM} GSD301T mass spectrometer was used to determine the evacuated vapours. Micrographs and X-ray microanalysis (SEM/EDX) were recorded with a JEOL JSM-6100 electron microscope operating at 20 kV coupled with an X-Max SDD 80 mm^2 energy dispersive X-ray spectroscopy (EDS) detector from Oxford instruments. The TEM studies were performed on a JEOL JEM-2100F field emission transmission electron microscope operated at an accelerating voltage of 200 kV and equipped with an ultra-high resolution pole-piece that provided a point-resolution better than 0.19 nm. Fine powder of the sample was dispersed in ethanol, sonified and sprayed on a carbon coated copper grid, and then allowed to air-dry. The Atomic force microscopy (AFM) images were obtained with a NanotecTM AFM. The Photoluminescence studies at RT were obtained using a standard spectrofluorometer Edinburgh Instruments FLSP920, having a 450W Xe lamp as the excitation source. The sample was placed between two quartz plates placed at 45° from the incident beam and the detector.

3. Results and discussion

The powder XRD patterns of **Eu_*x*** samples are shown in Fig. 1. The structural ordering in the direction perpendicular to the plane of the sheet is still observable in the case of the exfoliated α-TiPPr (**Eu_0**), with the first characteristic peak at $2\theta = 5.5°$ and *d*-spacing of 16.0 Å which correspond to the interlayered distance in the starting structure of the layered α-TiPPr. However, we observed that for **Eu_0.8** to **Eu_2.4** the structural ordering decreased substantially with the increase in the concentration of europium in the contact solutions.

The morphology of **Eu_*x*** samples were characterized by SEM and the results are presented in Fig. 2. The pristine α-TiPPr exhibits hexagonal shaped plates (Fig. S1, ESI), indicative of high crystallinity. After the exfoliation of α-TiPPr (**Eu_0**), the shaped hexagonal plates disappeared, and the nanosheets are tightly stacked and slightly wrinkled (Fig. 2a). After europium species was grafted onto α-TiPPr nanosheets, aggregate-like nanoparticles along with roughly layered morphologies could be observed (Fig. 2b-d). However, no obvious different observations can be seen between **Eu_0.8** to **Eu_2.4**, and the sizes of these aggregates are still too small to be visualized and estimated directly from the SEM images (Fig. 2b-d). Overall, these results are highly consistent with the PXRD analysis (Fig. 1).

As mentioned above, the pristine α-TiPPr was exfoliated *via* overnight stirring to produce α-TiPPr sheets (**Eu_0**). TEM analyses were performed for the as-prepared α-TiPPr sheets (**Eu_0**) and for all the solids **Eu_0.8**, **Eu_1.6** and **Eu_2.4** treated with Eu(III), and the observations are shown in Fig. 3. Figs. 3a-c show a general view of **Eu_0**, clearly illustrating that the crystalline α-TiPPr could be fully exfoliated into individual nanosheets by the process implemented here. From the TEM data of **Eu_0.8**, **Eu_1.6** and **Eu_2.4** presented in Fig. 3d-l, it is obvious that there are two type of easily distinguishable morphologies: (1) the stacked α-TiPPr sheets, which are probably uniformly decorated and/or intercalated by Eu(III) species; (2) the aggregated nanosheets, which tend to pile up into larger particles at increasing Eu(III) concentrations.

The chemical composition of these morphologies was inspected by EDX analysis in the Bright-Field Scanning Transmission Electron Microscopy (BF-STEM) mode (including line-scan and mapping analyses); the results are illustrated in Fig. 4 and Figs. S2-S6 in ESI. These results reveal that both α-TiPPr sheets and the nano-aggregates contain Eu(III) species, and that the Eu(III) content increases in the stacked α-TiPPr sheets as the starting Eu(III) concentration increases, indicating that the immobilization/sorption of Eu(III) species is successful. The EDX elemental mapping of carbon (Fig. 4 and Figs. S2,S4,S6 in ESI) shows that these large stacked α-TiPPr sheets is still intercalated with the propylamine. In addition, their propylamine content decreases as the starting Eu(III) concentration increases, in agreement with the results of elemental analysis on carbon, as shown in Table S1. These two observations suggest that the Eu(III) retention is a consequence of an ion-exchange process into the interlayer space of the layered titanium phosphate, that involves propylammonium cations and europium(III) species. The second observed morphology, nano-aggregates, are most probably formed by the self-assembly of single α-TiPPr nanosheets that takes place after they retain Eu(III) species on their both sides, because of the electrostatic interaction between these negatively charged α-TiPPr sheets and Eu(III) species. Therefore, we can conclude that the mechanism of Eu retention may be initially caused by the degree of exfoliation of the α-TiPPr hexagonal plates.

To confirm the above hypothesis about the exfoliation degree of the α-TiPPr hexagonal plates, an AFM study was performed for **Eu_0** solid, and the results are illustrated in the Fig. 5 and Fig. S7 in ESI. The results reveal that the exfoliation leads to variations in both size (*ca.* 100 nm to 600 nm - agreeing with TEM results) and thickness (*ca.* 8 Å up to 50 nm) of the sheets. As per AFM data, the measured thickness for the particles with the size between *ca.* 100-170 nm, *ca.* 200 nm to 300 nm and larger than 350 nm were ranging from *ca.* 0.8 to 12 nm, *ca.* 10-20 nm, and *ca.* 30 nm to 50 nm, respectively.

To investigate the photoluminescence properties of **Eu_*x*** samples, the emission spectra were obtained under $\lambda_{ex} = 394$ nm (direct intra $4f^6$ excitation, $^7F_0 \rightarrow {}^5L_6$), as shown in Fig. 6. The emission spectrum of **Eu_0**, as expected, does not show any transition line due to absence of the Eu^{3+} sorption. Whereas, **Eu_0.8**, **Eu_1.6** and **Eu_2.4** spectra show the typical emission transitions of Eu^{3+} [36-41], which are attributed to $^5D_0 \rightarrow {}^7F_J$ (J = 1-4) transitions at 591 nm ($^5D_0 \rightarrow {}^7F_1$), 616 nm ($^5D_0 \rightarrow {}^7F_2$), 650 nm ($^5D_0 \rightarrow {}^7F_3$), and 689 and 697 nm ($^5D_0 \rightarrow {}^7F_4$), with the most intense peak corresponding to $^5D_0 \rightarrow {}^7F_4$ transition. The emission spectra show an increase in the relative intensities of $^5D_0 \rightarrow {}^7F_{0\text{-}4}$ transition peaks as the starting Eu(III) concentration increases. This indicates that the Eu-content increases in solid phase accordingly.

It is well known that the intensity of the hypersensitive $^5D_0 \rightarrow {}^7F_2$ transition is strongly dependent on the local symmetry of the Eu^{3+} cation and the nature of the ligands surrounding it. Whereas, the intensity of the $^5D_0 \rightarrow {}^7F_4$ transition is influenced not only by the symmetry factors, but also by the nature of the host matrix (chemical composition, electronegativity, the radius of the rare earth elements and of other trivalent cations) [42]. It has been observed that the luminescence spectra of the Eu-containing compounds with Eu^{3+} local site symmetry D_{4d} are often dominated by the $^5D_0 \rightarrow {}^7F_4$ transition. In the absence of a center of inversion, the $^5D_0 \rightarrow {}^7F_4$ transition intensity is, in most cases, as intense as the $^5D_0 \rightarrow {}^7F_2$ one [43]. Since the Eu^{3+} cation is expected to be hydrated ($[Eu(H_2O)n]^{3+}$ species where n = 6-9), the abnormally dominant emission at ca. 700 nm ($^5D_0 \rightarrow {}^7F_4$) with intensity comparable to $^5D_0 \rightarrow {}^7F_2$ transition at 616 nm could be attributed to the presence of eight-coordinate species $[Eu(H_2O)_8]^{3+}$ with a square antiprism geometry (D_{4d} local environment) rather than $[Eu(H_2O)_6]^{3+}$ species (D_{4h} local environment).

The luminescence decay curves for **Eu_1.6** and **Eu_2.4** samples are shown in Fig. S8 in ESI, which are monitored within the $^5D_0 \rightarrow {}^7F_4$ (697 nm) transition under direct intra $4f^6$ excitation (394 nm, $^7F_0 \rightarrow {}^5L_6$). As can be seen, the $^5D_0 \rightarrow {}^7F_4$ transition decays exponentially, and the data can be best fitted using a biexponential function as $I(t) = A_1\exp(-t/\tau_1) + A_2\exp(-t/\tau_2)$, where $I(t)$ is the luminescence intensity, t is the time after excitation, A_1 and A_2 are constants, and τ_1 and τ_2 are the decay times for the exponential components. As shown in

Table 1, both values of τ_1 and τ_2 components slightly increase with an increase of Eu(III)-content in solid phase. τ_1 increases from 0.16 to 0.26 ms and τ_2 increases from 0.51 to 0.65 ms. This reveals that the luminescence decay can be associated with two different ways of radiative decay. In this case, Eu(III) cations absorbed on the surface of the α-TiPPr nanosheets could be the main contributor of the fast component as the surface is rich with disordered Eu(III) cations due to the surface defects compared to the inner core (intercalated) Eu(III) species that could be the source of the slow component [44].

4. Conclusions

We have shown that α-TiPPr nanosheets could be easily obtained by exfoliating the hexagonal-shaped α-TiPPr particles *via* a simple approach based on overnight stirring in aqueous medium. The europium(III)-functionalization of the obtained α-TiPPr nanosheets, by a solid-liquid reaction in aqueous solutions of europium(III) nitrate, leads to two distinguishable morphologies: The large stacked sheets and aggregated nanosheets. This can be explained by the fact that the Eu(III)-retention takes place by two different pathways: *i)* ion-exchange process involving propylammonium cations and Eu(III) species and, *ii)* absorption of Eu(III) species on the surface of single α-TiPPr nanosheets, and these two pathways are in turn attributed to the degree of exfoliation of α-TiPPr. We believe that the methodology presented here can serve as a simple and efficient route for the synthesis of luminescent layered ultra-nanoparticles of tetravalent metal phosphates. In addition, it implies the possibility of combining other tetravalent metal phosphate nanosheets and cationic species to further explore the plausible novel functionalities.

Acknowledgments

Financial support from Spanish *Ministerio de Economía y Competitividad* (MAT2013-40950-R and MAT2016-78155-C2-1-R) and *Gobierno del Principado de Asturias* (GRUPIN14-060), and FEDER funding are acknowledged.

Appendix A. Supplementary data

Supplementary data associated with this article can be found online at http://

References

1. K.A. Kraus, H.O. Phillips, Adsorption on inorganic materials. 1. Cation exchange properties of zirconium phosphate, J. Am. Chem. Soc. 78 (1956) 694.
2. A. Clearfield, J.A. Stynes, The preparation of crystalline zirconium phosphate and some observations on its ion exchange behavior, J. Inorg. Nucl. Chem. 26 (1964) 117-129.
3. J.M. Troup, A. Clearfield, Mechanism of ion-exchange in zirconium phosphates. 20. Refinement of crystal structure of α-zirconium phosphate, Inorg. Chem. 16 (1977) 3311-3314.
4. L. Kullberg, A. Clearfield, Mechanism of ion-exchange in zirconium phosphates. 32. Thermodynamics of alkali-metal ion-exchange on crystalline α-ZrP, J. Phys. Chem. 85 (1981) 1585-1589.
5. A. Clearfield, R.H. Blessing, J.A. Stynes, New crystalline phases of zirconium phosphate possessing ion-exchange properties, J. Inorg. Nucl. Chem. 14 (1968) 2249-2258.
6. M.A. Salvadó, P. Pertierra, S. García-Granda, J.R. García, J. Rodríguez, M.T. Fernández-Díaz, Neutron powder diffraction study of α-$Ti(HPO_4)_2 \cdot H_2O$ and α-$Hf(HPO_4)_2 \cdot H_2O$; H-atom positions, Acta Cryst. B52 (1996) 896-898.
7. S. García-Granda, S.A. Khainakov, A. Espina, J.R. García, G.R. Castro, J. Rocha, L. Mafra, Revisiting the thermal decomposition of layered γ-titanium phosphate and structural elucidation of its intermediate phases, Inorg. Chem. 49 (2010) 2630-2638.
8. A. Menéndez, M. Bárcena, E. Jaimez, J.R. García, J. Rodríguez, Intercalation of *n*-alkylamines by γ-titanium phosphate. Synthesis of new materials by thermal treatment of the intercalation compounds, Chem. Mater. 5 (1993) 1078-1084.
9. A. Espina, J.R. García, J.M. Guil, E. Jaimez, J.B. Parra, J. Rodríguez, Calorimetric study of amine adsorption on α- and γ-titanium phosphate, J. Phys. Chem. B 102 (1998) 1713-1716.
10. A. Espina, E. Jaimez, S.A. Khainakov, C. Trobajo, J.R. García, J. Rodríguez, Synthesis of new *n*-alkyldiamines intercalation compounds into α-titanium phosphate. Process selectivity and structural and morphological characterization, Chem. Mater. 10 (1998) 2490-2496.
11. A. Espina, C. Trobajo, S.A. Khainakov, J.R. García, A.I. Bortun, Intercalation of *n*-alkylamines into layered materials: A method for the recognition of isomorphism in semicrystalline compounds, J. Chem. Soc., Dalton Trans. (2001) 753-757.

12. L. Mafra, F.A.A. Paz, J. Rocha, A. Espina, S.A. Khainakov, J.R. García, C. Fernández, Structural characterization of layered γ-titanium phosphate $(C_6H_{13}NH_3)[Ti(HPO_4)(PO_4)]\cdot H_2O$, Chem. Mater. 17 (2005) 6287-6294.
13. L. Mafra, J. Rocha, C. Fernández, G.R. Castro, S. García-Granda, A. Espina, S.A. Khainakov, J.R. García, Characterization of layered γ-titanium phosphate $(C_2H_5NH_3)[Ti(H_{1.5}PO_4)(PO_4)]_2\cdot H_2O$ intercalate: A combined NMR, synchrotron XRD, and DFT calculations study, Chem. Mater. 20 (2008) 3944-3953.
14. E. Brunet, Usual molecules in unusual environments displaying unusual properties, Aust. J. Chem. 63 (2010) 1679-1685.
15. M. Osada, T. Sasaki, Two-dimensional dielectric nanosheets: Novel nanoelectronics from nanocrystal building blocks, Adv. Mater. 24 (2012) 210-228.
16. J.K. Wassei, R.B. Kaner, Oh, the places you'll go with graphene, Acc. Chem. Res. 46 (2013) 2244-2253.
17. K. Parvez, Z.S. Wu, R. Li, X. Liu, R. Graf, X. Feng, K. Mullen, Exfoliation of graphite into graphene in aqueous solutions of inorganic salts, J. Am. Chem. Soc. 136 (2014) 6083-6091.
18. Z.Y. Xia, S. Pezzini, E. Treossi, G. Giambastiani, F. Corticelli, V. Morandi, A. Zanelli, V. Bellani, V. Palermo, The exfoliation of graphene in liquids by electrochemical, chemical, and sonication-assisted techniques: A nanoscale study, Adv. Funct. Mater. 23 (2013) 4684-4693.
19. J.N. Coleman, M. Lotya, A. O'Neill, S.D. Bergin, P.J. King, U. Khan, K. Young, A. Gaucher, S. De, R.J. Smith, I.V. Shvets, S.K. Arora, G. Stanton, H.Y. Kim, K. Lee, G.T. Kim, G.S. Duesberg, T. Hallam, J.J. Boland, J.J. Wang, J.F. Donegan, J.C. Grunlan, G. Moriarty, A. Shmeliov, R.J. Nicholls, J.M. Perkins, E.M. Grieveson, K. Theuwissen, D.W. McComb, P.D. Nellist, V. Nicolosi, Two-dimensional nanosheets produced by liquid exfoliation of layered materials, Science 331 (2011) 568-571.
20. A. O'Neill, U. Khan, J.N. Coleman, Preparation of high concentration dispersions of exfoliated MoS_2 with increased flake size, Chem. Mater. 24 (2012) 2414-2421.
21. Z.P. Liu, R.Z. Ma, Y. Ebina, N. Iyi, K. Takada, T. Sasaki, General synthesis and delamination of highly crystalline transition-metal-bearing layered double hydroxides, Langmuir 23 (2007) 861-867.
22. Z.P. Liu, R.Z. Ma, M. Osada, N. Iyi, Y. Ebina, K. Takada, T. Sasaki, Synthesis, anion exchange, and delamination of Co-Al layered double hydroxide: Assembly of the exfoliated nanosheet/polyanion composite films and magneto-optical studies, J. Am. Chem. Soc. 128 (2007) 4872-4880.
23. T. Oshima, D.L. Lu, O. Ishitani, K. Maeda, Intercalation of highly dispersed metal nanoclusters into a layered metal oxide for photocatalytic overall water splitting, Angew. Chem. Int. Ed. 54 (2015) 2698-2702.
24. A.A. Jeffery, A. Pradeep, M. Rajamathi, Preparation of titanate nanosheets and nanoribbons by exfoliation of amine intercalated titanates, Phys. Chem. Chem. Phys. 18 (2016) 12604-12609.
25. L.Z. Wang, Y. Ebina, K. Takada, K. Kurashima, T. Sasaki, A new mesoporous manganese oxide pillared with double layers of alumina, Adv. Mater. 16 (2004) 1412-1416.
26. G. Alberti, S. Cavalaglio, C. Dionigi, F. Marmottini, Formation of aqueous colloidal dispersions of exfoliated γ-zirconium phosphate by intercalation of short alkylamines, Langmuir 16 (2000) 7663-7668.

27. T. Takei, Y. Kobayashi, H. Hata, Y. Yonesaki, N. Kumada, N. Kinomura, T.E. Mallouk, Anodic electrodeposition of highly oriented zirconium phosphate and polyaniline-intercalated zirconium phosphate films, J. Am. Chem. Soc. 128 (2006) 16634-16640.
28. H. Tanaka, K. Ishida, T. Okumiya, M. Murakami, Preparation and exfoliation of layered titanium butyl phosphates, Colloid Polym. Sci. 288 (2010) 1427-1433.
29. L.Y. Sun, W.J. Boo, D.Z. Sun, A. Clearfield, H.J. Sue, Preparation of exfoliated epoxy/α-zirconium phosphate nanocomposites containing high aspect ratio nanoplatelets, Chem. Mater. 19 (2007) 1749-1754.
30. C.V. Kumar, A. Chaudhari, Proteins immobilized at the galleries of layered α-zirconium phosphate: Structure and activity studies, J. Am. Chem. Soc. 122 (2000) 830-837.
31. A. Chaudhari, C.V. Kumar, Intercalation of proteins into α-zirconium phosphonates: Tuning the binding affinities with phosphonate functions, Micropor. Mesopor. Mater. 77 (2005) 175-187.
32. H.N. Kim, S.W. Keller, T.E. Mallouk, J. Schmitt, G. Decher, Characterization of zirconium phosphate/polycation thin films grown by sequential adsorption reactions, Chem. Mater. 9 (1997) 1414-1421.
33. H.B. Ortiz-Oliveros, R.M. Flores-Espinosa, E. Ordóñez-Regil, S.M. Fernández-Valverde, Synthesis of α-$Ti(HPO_4)_2 \cdot H_2O$ and sorption of Eu(III), Chem. Eng. J. 236 (2014) 398-405.
34. J. García-Glez, C. Trobajo, S.A. Khainakov, Z. Amghouz, α-Titanium phosphate intercalated with propylamine: An alternative pathway for efficient europium(III) uptake into layered tetravalent metal phosphates, Arab. J. Chem. 10 (2016) 885-894.
35. F. Menéndez, A. Espina, C. Trobajo, J. Rodríguez, Intercalation of *n*-alkylamines by lamellar materials of the α-zirconium phosphate type, Mater. Res. Bull. 25 (1990) 1531-1539.
36. V.V. Atuchin, A.S. Aleksandrovsky, O.D. Chimitova, T.A. Gavrilova, A.S. Krylov, M.S. Molokeev, A.S. Oreshonkov, B.G. Bazarov, J.G. Bazarova, Synthesis and Spectroscopic Properties of Monoclinic α-$Eu2(MoO_4)_3$, J. Phys. Chem. C 118 (2014) 15404-15411.
37. P. Shi, Z. Xia, M.S. Molokeev, V.V. Atuchin, Crystal chemistry and luminescence properties of red-emitting $CsGd_{1-x}Eu_x(MoO_4)_2$ solid-solution phosphors, Dalton Trans. 43 (2014) 9669-9676.
38. H. Ji, Z. Huang, Z. Xia, M.S. Molokeev, X. Jiang, Z. Lin, V.V. Atuchin, Comparative investigations of the crystal structure and photoluminescence property of eulytite-type $Ba_3Eu(PO_4)_3$ and $Sr_3Eu(PO_4)_3$, Dalton Trans. 44 (2015) 7679-7686.
39. Z Amghouz, S García-Granda, J.R García, A. Clearfield, R. Valiente, Organic-inorganic hybrids assembled from lanthanide and 1, 4-phenylenebis (phosphonate), Cryst. Growth Des. 11 (2011) 5289-5297.
40. Z Amghouz, S García-Granda, J.R. García, R.A.S. Ferreira, L. Mafra, L. D. Carlos, J. Rocha, Series of metal organic frameworks assembled from Ln (III), Na (I), and Chiral flexible-achiral rigid dicarboxylates exhibiting tunable UV–vis–IR light emission, Inorg. Chem. 51 (2012) 1703-1716.
41. M.S.M. Abdelbaky, Z. Amghouz, S. García-Granda, J.R. García, Synthesis, Structures and Luminescence Properties of Metal-Organic Frameworks Based on Lithium-Lanthanide and Terephthalate, Polymers 8 (2016) 86.
42. R.A.S. Ferreira, S.S. Nobre, C.M. Granadeiro, H.I.S. Nogueira, L.D. Carlos, O.L. Malta, A theoretical interpretation of the abnormal $^5D_0$-$^7F^4$ intensity based on the Eu^{3+} local coordination in the$Na_9[EuW_{10}O_{36}] \cdot 14H_2O$ polyoxometalate, J. Lumin. 121 (2006) 561-567.

43. K. Binnemans, Interpretation of europium(III) spectra, Coord. Chem. Reviews 295 (2015)1-45.
44. T. Ninjbadgar, G. Garnweitner, A Borger, L.M. Goldenberg, O.V. Sakhno, J. Stumpe, Synthesis of luminescent ZrO_2:Eu^{3+} nanoparticles and their holographic sub-micrometer patterning in polymer composites, Adv. Funct. Mater. 9 (2009) 1819-1825.

Table 1. Fitting parameters of the biexponential temporal dependence for the luminescence decay curves of **Eu_1.6** and **Eu_2.4** monitored at 697 nm and excited at 394 nm.

	τ (ms)		$ji^{\wedge 2}$
Sample	τ_1	τ_2	
Eu_1.6	0.16	0.51	1.295
Eu_2.4	0.26	0.65	1.262

Figure captions

Figure 1. Powder XRD patterns for **Eu_*x*** samples.

Figure 2. SEM images of **Eu_0** (a), **Eu_0.8** (b), **Eu_1.6** (c) and **Eu_2.4** (d).

Figure 3. TEM images of **Eu_0** (a-c), **Eu_0.8** (d-f), **Eu_1.6** (g-i) and **Eu_2.4** (j-l).

Figure 4. STEM-EDS elemental mapping for **Eu_0** (a-f), **Eu_0.8** (g-l), **Eu_1.6** (m-r) and **Eu_2.4** (s-x) samples; Ti (red), P (yellow), O (blue), C (cyan) and Eu (green) elemental maps.

Figure 5. AFM images of **Eu_0** and their thickness profiles.

Figure 6. Emission spectra of **Eu_0** (violet), **Eu_0.8** (green), **Eu_1.6** (blue) and **Eu_2.4** (red) samples obtained upon excitation at 394 nm.

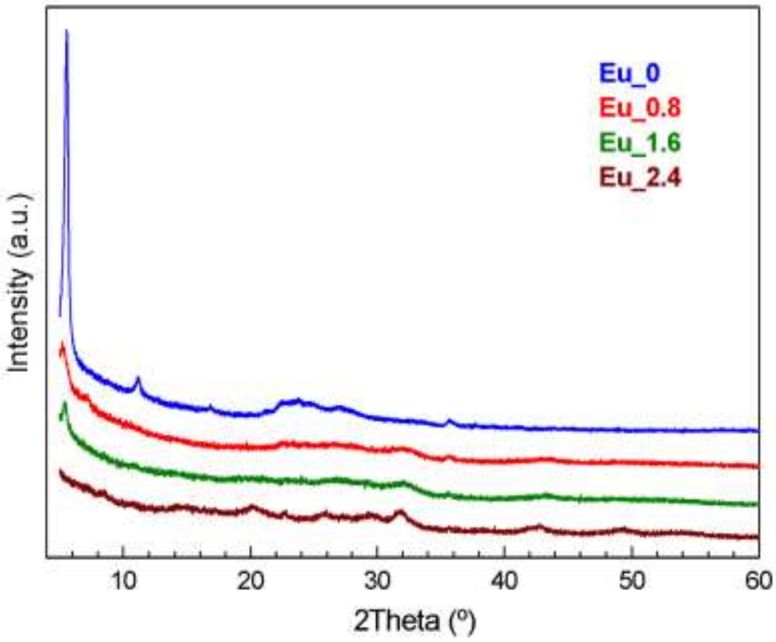

Figure 1

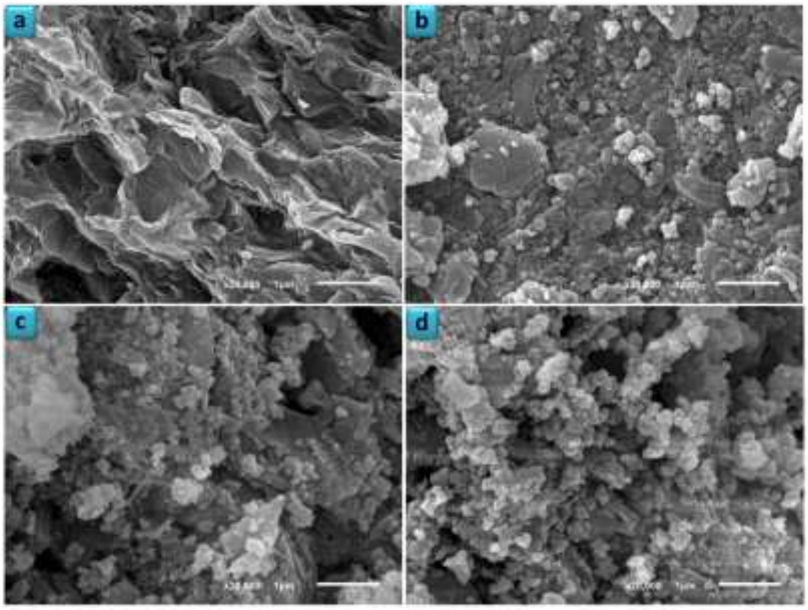

Figure 2

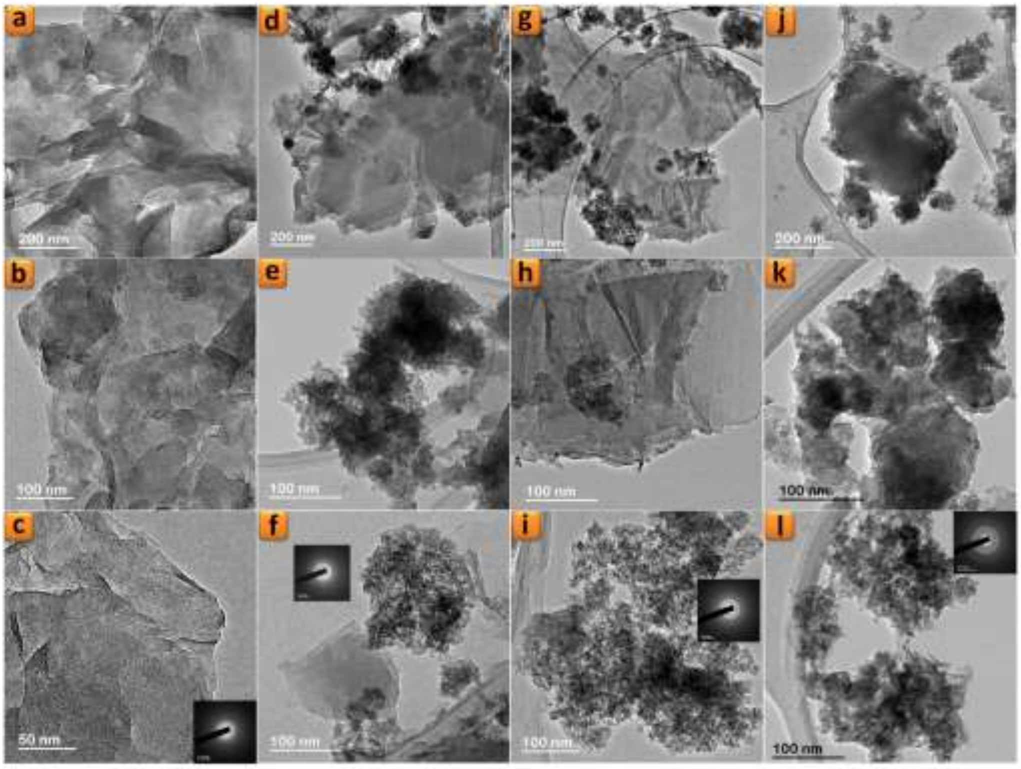
a
200 nm
b
100 nm
c
50 nm
d
200 nm
e
100 nm
f
100 nm
g
200 nm
h
100 nm
i
100 nm
j
200 nm
k
100 nm
l
100 nm

Figure 3

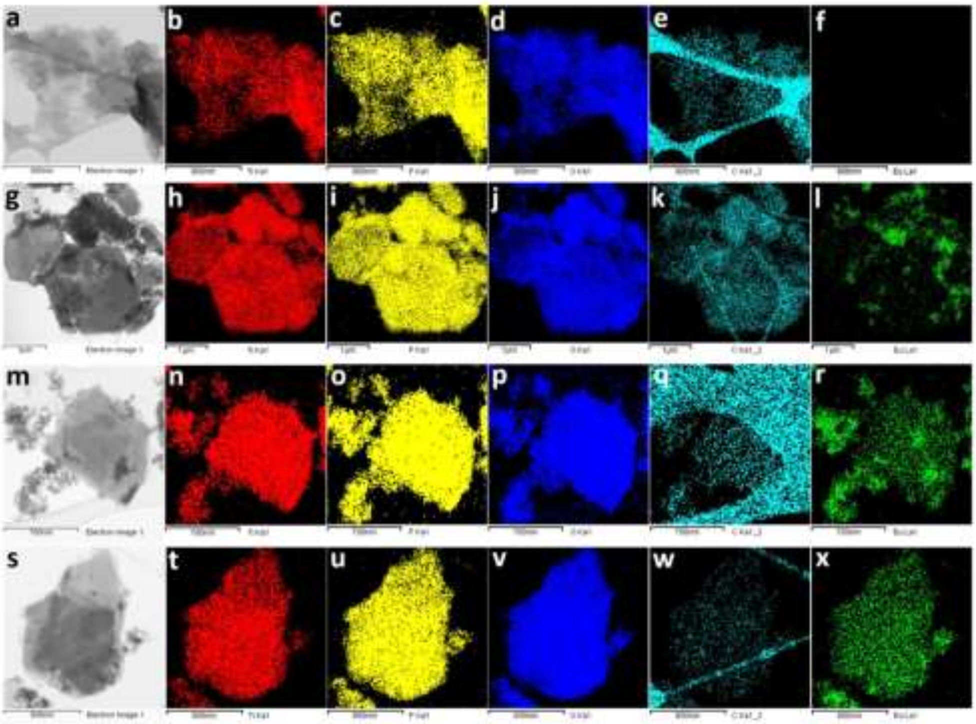

Figure 4

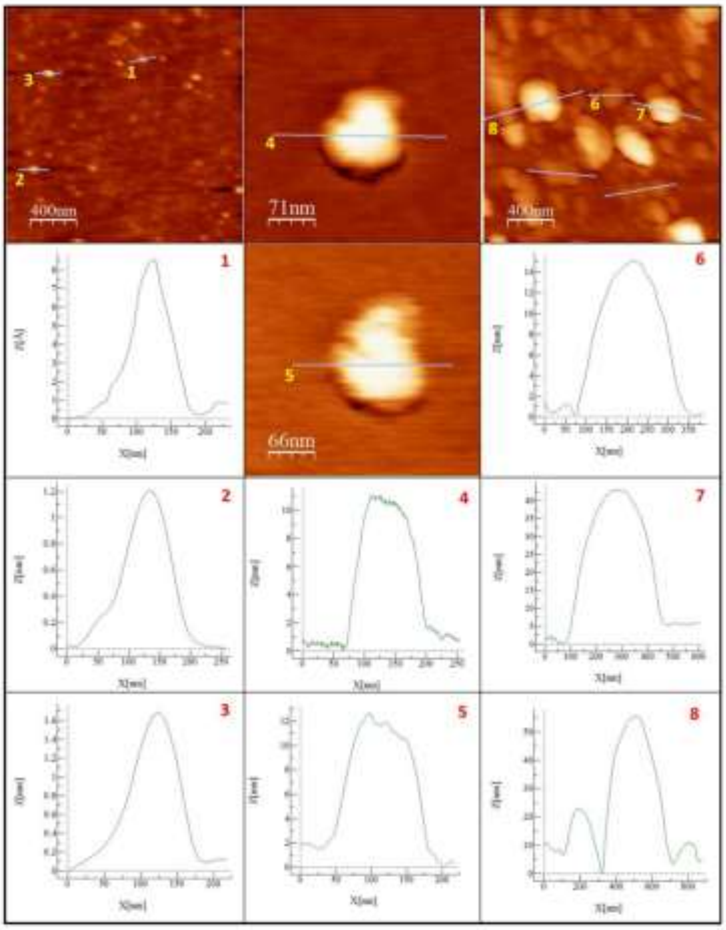

Figure 5

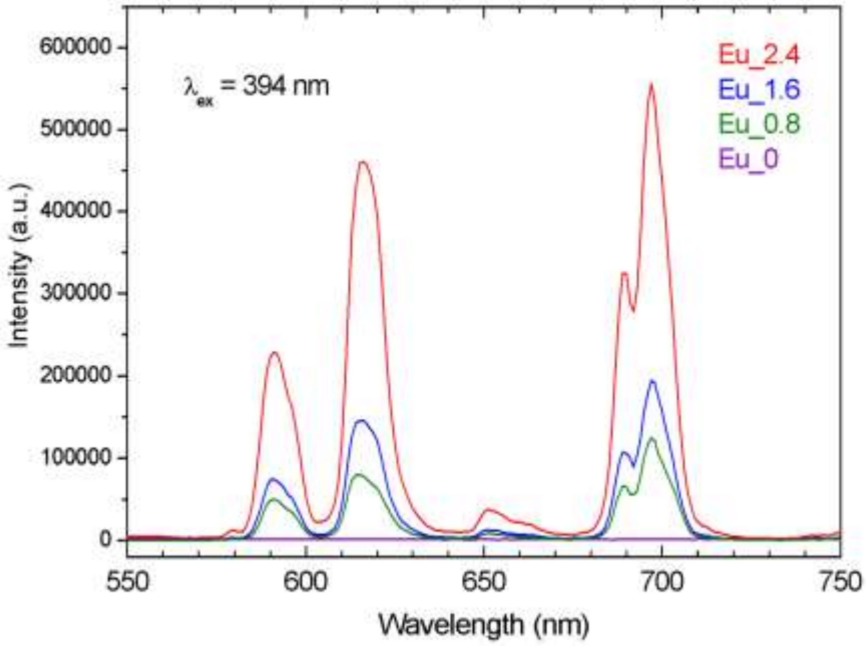
λ_ex = 394 nm
Eu_2.4
Eu_1.6
Eu_0.8
Eu_0
Intensity (a.u.)
600000
500000
400000
300000
200000
100000
0
550
600
650
700
750
Wavelength (nm)

Figure 6

Artículo S2

“Thermal behaviour of layered α-titanium phosphates: From the titanium(IV) bis(hydrogenphosphate) monohydrate to an europium(III)-phase *via* propylamine intercalation”

Journal of Thermal Analysis and Calorimetry

En trámite de publicación

Índice de Impacto: 1.953

Journal of Thermal Analysis and Calorimetry

Thermal behaviour of layered α-titanium phosphates: From the titanium(IV) bis(hydrogenphosphate) monohydrate to an europium(III)-phase via propylamine intercalation

--Manuscript Draft--

Manuscript Number:		
Full Title:	Thermal behaviour of layered α-titanium phosphates: From the titanium(IV) bis(hydrogenphosphate) monohydrate to an europium(III)-phase via propylamine intercalation	
Article Type:	S.I. : CEEC-TAC4	
Corresponding Author:	Zakriae Amghouz, PhD, Professor Universidad de Oviedo SPAIN	
Corresponding Author Secondary Information:		
Corresponding Author's Institution:	Universidad de Oviedo	
Corresponding Author's Secondary Institution:		
First Author:	Jorge García-Glez, PhD student	
First Author Secondary Information:		
Order of Authors:	Jorge García-Glez, PhD student	
	Olena Khainakova	
	Isabel Iglesias, Professor	
	Belén F. Alfonso, PhD, Professor	
	José A. Huidobro, PhD, Professor	
	Zakriae Amghouz, PhD, Professor	
	Aránzazu Espina, PhD	
	Camino Trobajo, PhD, Professor	
Order of Authors Secondary Information:		
Funding Information:	Ministerio de Economía y Competitividad (MAT2016-78155-C2-1-R)	Not applicable
	Ministerio de Economía y Competitividad (MAT2013-40950-R)	Not applicable
	Ministerio de Economía y Competitividad (MAT2011-27573-C04-02)	Not applicable
	Gobierno del Principado de Asturias (GRUPIN14-060)	Not applicable
	FEDER	Not applicable
Abstract:	Polycrystalline layered α-titanum phosphate, α-Ti(HPO4)2·H2O, has been obtained under H3PO4(aq) reflux conditions, and its intercalation compound with propylamine, α-Ti(HPO4)2·2C3H7NH2·H2O, was used for trapping luminescent Eu-centers in two-dimensional confined space. All materials were characterized by powder X-ray diffraction (PXRD), scanning electron microscopy (SEM), solid-state nuclear magnetic resonance (SS-NMR, 31P MAS and 13C CPMAS) and thermal analysis (TG-MS). Moreover, the activation energy of thermal decomposition has been calculated as a function of the extent of conversion, applying both a modified Friedman method developed in our Lab and the advanced nonlinear method proposed by Vyazovkin.	
Suggested Reviewers:	Abraham Clearfield, PhD	

Thermal behaviour of layered α-titanium phosphates: From the titanium(IV) bis(hydrogenphosphate) monohydrate to an europium(III)-phase *via* propylamine intercalation

Jorge García-Glez[1], Olena Khainakova[1], Isabel Iglesias[2], Belén F. Alfonso[2], José A. Huidobro[3], Zakariae Amghouz[4], Aránzazu Espina[5], Camino Trobajo[1]

[1]Departamento de Química Orgánica e Inorgánica, Universidad de Oviedo-CINN, 33006 Oviedo, Spain.
Departamentos de [2]Física, [3]Matemáticas, y [4]Ciencia de los Materiales e Ingeniería Metalúrgica, Escuela Politécnica de Ingeniería, Universidad de Oviedo, 33204 Gijón, Spain.
[5]Servicios Científico-Técnicos, Universidad de Oviedo, 33006 Oviedo, Spain.

Zakariae Amghouz amghouz.uo@uniovi.es

Abstract

Polycrystalline layered α-titanum phosphate, α-$Ti(HPO_4)_2\cdot H_2O$, has been obtained under H_3PO_4(aq) reflux conditions, and its intercalation compound with propylamine, α-$Ti(HPO_4)_2\cdot 2C_3H_7NH_2\cdot H_2O$, was used for trapping luminescent Eu-centers in two-dimensional confined space. All materials were characterized by powder X-ray diffraction (PXRD), scanning electron microscopy (SEM), solid-state nuclear magnetic resonance (SS-NMR, ^{31}P MAS and ^{13}C CPMAS) and thermal analysis (TG-MS). Moreover, the activation energy of thermal decomposition has been calculated as a function of the extent of conversion, applying both a modified Friedman method developed in our Lab and the advanced nonlinear method proposed by Vyazovkin.

Keywords Titanium phosphate · Propylamine · Europium · Thermal decomposition · Kinetic analysis

1. **Introduction**

α-$Ti(HPO_4)_2 \cdot H_2O$ (α-TiP) was the subject of continuous study over the past fifty years. The pioneering studies on this material were conducted by Alberti in its Lab at the University of Perugia (Italy) [1,2] and emerged in the wake of the work of the Clearfield Lab (USA) on zirconium phosphates [3]. The contributions of the Soviet school, particularly the Chernukov Lab in Nizhni Nóvgorod (Russia) have also to be mentioned [4]. In this context, our group at the University of Oviedo (Spain), published its first articles on this topic at the beginning of the 1980s [5-7].

According to the excellent review of Clearfield and Díaz [8], the first report of a crystalline form of zirconium phosphate was in 1964. Up to that time, only an amorphous white fine powder was known. The transformation from the amorphous to crystalline form is a slow process. It is therefore possible to control the size of the particles from very small, approximately 50 nm, up to micro-size and even to large crystals. These particles are layered and exhibit the ability to exchange positively charged species for protons, to undergo intercalation behaviour and exfoliation of the layers. In addition, it has been shown that the surface of the particles may be functionalized by bonding to silanes, isocyanates and epoxides, and this bonding may even be extended to phosphates and phosphonic acids after replacing the surface protons by Zr^{4+} or Sn^{4+}. Attachment of a functional group to the surface bonding ligands including phosphates or phosphonic acids, allows using this large class of functionalized materials for a variety of applications. Because of the extraordinary properties of this compound, a great variety of potential and realized uses have been invoked. As a result, from 1964 to the present, more than 10,000 scientific papers have been published describing the chemistry and applications of this remarkable compound. This phenomenon continues as every year a few hundred new papers appear in the chemical literature.

In our Lab, both α-TiP [9,10] and its propylamine intercalation product, α-$Ti(HPO_4)_2 \cdot 2C_3H_7NH_2 \cdot H_2O$ (α-TiPPr) [11-13], have been previously synthesized and characterized. On the other hand, the treatment of α-TiPPr with europium(III) nitrate solutions, involving an ion-exchange process between propylammonium cations, $C_3H_7NH_3^+$, and hexahydrate europium(III) species, $[Eu(H_2O)_6]^{3+}$, has led to a new luminescent material (α-EuTiPPr) [14].

Despite the large volume of information obtained in recent decades concerning to layered titanium phosphates, the kinetic studies on its thermal decomposition processes are relatively scarce [15-18]. This contribution reports the kinetic features of thermo-oxidative decomposition processes of the three aforementioned materials: α-TiP, α-TiPPr, and α-EuTiPPr.

2. Experimental procedures

Sample preparation and analytical procedures. All chemicals used were of reagent grade. MilliQ water was used throughout the experiments. α-TiP was obtained by the method described by Alberti *et al.* [1] using 10 M H_3PO_4 and heated under reflux for 50 h. Propylamine intercalation compound, α-TiPPr, was obtained by placing α-TiP in an atmosphere saturated with propylamine vapor during 6 days at room temperature [11]. α-EuTiPPr was prepared by equilibrating α-TiPPr with 0.1 M europium nitrate solution ($T = 25.0 \pm 0.1$ °C, t = 72 h, solution/solid ratio = 20 mL/g) [14].

The phosphorus and titanium contents of the solids were determined by inductively coupled plasma mass spectrometry (ICP-MS) analysis (Finnigan, Element model) after dissolving a weighed amount in HF(aq). Microanalytical data (C and N) were determined by an Elementar Model Vario MACRO elemental analyser. Elemental analysis (wt%) for α-TiP: P 23.9, Ti 18.6 (calculated for $Ti(HPO_4)_2 \cdot H_2O$: P 24.03, Ti 18.56), α-TiPPr: P 16.7, Ti 12.8, C 18.8, N 7.3 (calculated for $Ti(HPO_4)_2 \cdot 2C_3H_7NH_2 \cdot H_2O$: P 16.47, Ti 12.73, C 19.16, N 7.45), and α-EuTiPPr: P 13.7, Ti 10.8, Eu 24.0, C 2.5, N 0.9 (calculated for $[Eu(H_2O)_6]_{2/3}Ti(PO_4)_2 \cdot [(H_2O)_6]_{1/3}$: P 14.85, Ti 11.47, Eu 24.28).

Powder diffraction studies. Room temperature powder X-ray diffraction (PXRD) patterns were collected on an X'Pert PRO MPD X-ray diffractometer with PIXcel detector, operating in the Bragg-Brentano (θ/2θ) geometry and using CuK_α radiation ($\lambda = 1.5418$ Å).

Electron microscopy studies. SEM images were obtained by using JEOL 6610VL scanning electron microscope operating at 20 kV and equipped with an X-Max Silicon Drift Detector for EDX analysis.

Solid-state nuclear magnetic resonance studies. Room temperature SS-NMR spectra were collected on a Bruker AVANCE III 400 equipped with a 4-mm wide-bore MAS probe, operating at ^{31}P resonating frequency of 161.97 MHz and ^{13}C resonating frequency of 100.64 MHz. Samples were packed in zirconia rotor with Kel-F tape. ^{31}P MAS NMR spectra were acquired at 8 kHz spin rate. The relaxation delays were 20 s and number of scans of 100. All the spectra were referred to $NH_4H_2PO_4$ ($\delta = 0.9$ ppm) as external standard for chemical shift calibration. ^{13}C CPMAS NMR spectra were acquired at 5 kHz spin rate. The relaxation delays for all spectra were 5 s and number of scans 100. Chemical shift was externally referenced to the 43.5 ppm resonance of glycine.

Thermal analysis. A Mettler-Toledo TGA/SDTA851^e was used for the thermal analyses in dynamic oxygen atmosphere (50 mL min^{-1}) at a heating rate of 10 K min^{-1}. In all cases, *ca.* 15 mg of powder sample was thermally treated, and blank runs were performed. A Pfeiffer Vacuum ThermoStar^{TM} GSD301T mass spectrometer was used to determine the evacuated vapours. The masses 18 (H_2O), 44 (CO_2) and 59 ($C_3H_7NH_2$) were tested by using a detector C-SEM, operating at 1200 V, with a time constant of 1 s.

Determination of kinetic parameters. The kinetics of many solid-state reactions involving a change of mass can be described by the basic equation

$$\frac{\mathrm{d}\alpha}{\mathrm{d}t} = A\exp\left(-\frac{E}{RT}\right) f(\alpha) \tag{1}$$

where α is the extent of conversion, t is the time, T is the temperature, A is the Arrhenius factor, E is the activation energy, R is the universal gas constant and $f(\alpha)$ is the reaction model. Although the mechanisms in solid state reactions are usually very complex and tend to involve several steps, Eq (1) represents a simple kinetic model which can be used to describe an approximation of the kinetics of the process [19-21].

Many methods have been developed in order to estimate the kinetic parameters and nowadays, one can say that the most reliable results are provided by isoconversional methods. These methods are based on the isoconversional principle that states that the reaction rate depends only on the temperature for a given value of the extent of conversion. Several runs with different heating programmes, usually with constant heating rates $T = T_0 + \beta_i t$, are carried out and then the values of the activation energy are computed from experimental data.

The differential method of Friedman comes from of Eq. (1) by taking logarithms

$$\ln\left(\left(\frac{\mathrm{d}\alpha}{\mathrm{d}t}\right)_{\alpha,i}\right) = \ln(Af(\alpha)) - \frac{E_\alpha}{RT_{\alpha,i}} \tag{2}$$

where $T_{\alpha,i}$ denotes the temperature at which α is reached for the i-th heating program. Then, by plotting $\ln\left(\left(\frac{\mathrm{d}\alpha}{\mathrm{d}t}\right)_{\alpha,i}\right)$ against $1/T_{\alpha,i}$, the value of E_α can be estimated. As is well-known, a drawback of this procedure is its sensitivity to noise, in particular, when it is applied to data coming from thermogravimetric analysis (TG).

In order to decrease the effects of noise, a modified procedure (MFR) was proposed by Huidobro *et al.* [22]. Given a fixed value of α, set $\alpha_j = \alpha$, $\alpha_{j-2} = \alpha - 2\Delta\alpha$, $\alpha_{j-1} = \alpha - \Delta\alpha$, $\alpha_{j+1} = \alpha + \Delta\alpha$, $\alpha_{j+2} = \alpha + 2\Delta\alpha$. For each $= j-2, j-1, j, j+1, j+2$ and for n heating programmes, Eq. (2) leads to

$$\ln\left(\frac{\mathrm{d}\alpha(t_{k,j})}{\mathrm{d}t}\right) = \ln(A\, f(\alpha_k)) - \frac{E}{\mathrm{R}T_{k,j}} \quad (3)$$

Assuming that the variations of the activation energy over the interval $[\alpha_{j-2}, \alpha_{j+2}]$ are neglected, for each k, Eq. (3) involves five different straight lines with the same slope $m = -E/R$. Thus, we can find the slope by fitting to the experimental data for all these points simultaneously rather than only for α. This method can be applied to a different number of points.

Integral isoconversional methods are based on an integral of Eq. (1)

$$g(\alpha) = \int_{t_0}^{t_\alpha} \exp\left(-\frac{E}{RT}\right) \mathrm{d}t \quad (4)$$

where $g(\alpha) = \int_0^\alpha [1/(Af(\alpha))]\, \mathrm{d}\alpha$. The integral on the right-hand side of Eq. (4) is known as temperature integral and does not have an analytical solution and, for this reason, several approximations have been proposed giving rise to different methods. Although some of them are very popular [23], they have been criticized because of the inconsistency of their formulation, particularly when the activation energy changes with the extent of conversion [24,25].

The non-linear advanced method proposed by Vyazovkin [24,26] is one the most accurate procedures for kinetic analysis. For a small increment of conversion $\Delta\alpha$ and assuming that A is constant over the interval $[\alpha - \Delta\alpha, \alpha]$, integration of Eq. (1) with respect to t gives

$$\int_{\alpha-\Delta\alpha}^{\alpha} \frac{1}{Af(\alpha)} \mathrm{d}\alpha = J(E_\alpha) \quad (5)$$

where $J(E_\alpha) = \int_{t_{\alpha-\Delta\alpha}}^{t_\alpha} \exp(-E_\alpha/RT)\ dt$. Then, for a given value of α and several runs $i = 1, \ldots n$, the $J_{\alpha,i}$'s should be equal. To obtain E_α Vyazovkin proposed the minimization of the function

$$\Phi(E_\alpha) = \sum_{i=1}^{n} \sum_{j\neq i}^{n} \frac{J_i(E_\alpha)}{J_j(E_\alpha)} \quad (6)$$

Numerical integration has been used to evaluate $J(E_\alpha)$.

3. Results and discussion

PXRD analysis shows that α-TiP is highly crystalline (Fig. 1a) with the first characteristic peak at 2θ = 11.65° (d_{002} = 7.58 Å) corresponding to its interlayer distance. In α-TiPPr, the basal spacing increases up to 16.9 Å (Fig. 1b) as a consequence of the propylamine intercalation as a bimolecular film [11] in which the terminal amino groups are protonated by the POH groups and the carbon chains are roughly inclined by 59° to the titanium phosphate layers, showing a similar packing to that reported for γ-titanium phosphate intercalation compounds [27,28]. α-EuTiPPr presents a structural order in the direction perpendicular to the plane of the sheet with a diffraction peak at $2\theta = 7.33°$ corresponding to *d*-spacing of 12.0 Å (Fig. 1c). This new peak was attributed to the formation of an Eu-phase with the idealized formula $[Eu(H_2O)_6]_{2/3}Ti(PO_4)_2{\cdot}[(H_2O)_6]_{1/3}$, where $[Eu(H_2O)_6]^{3+}$ occupying 2/3 of the pseudo-zeolitic cavities so as to counteract the negatively charged titanium phosphate layer, while the rest of the pseudo-zeolitic cavities (1/3 of the total) are supposed to be occupied by water molecules [14].

SEM images (Fig. 2) show that all three samples present a platelet-like pseudo-hexagonal morphologies typical of the layered metal phosphates [29], indicating that in this case the both intercalation and ion-exchange processes preserve the sheets integrity of the α-titanium phosphate.

The ^{31}P MAS NMR spectrum of α-TiP (Fig. 3a, Table 1) shows two partially resolved peaks that according to the crystal data, correspond to two inequivalent HPO_4 groups in titanium phosphate layers [10]. After treatment with propylamine, the ^{31}P MAS NMR spectrum became substantially different for α-TiPPr. The former two signals transformed into a dozen peaks (Fig. 3b, Table 1), indicating a high disorder of the propylamine molecules in the interlayer space. The ^{13}C CPMAS NMR spectrum of α-TiPPr (Fig. 4a) displays three resonances at *ca.* 41.3, 21.8 and 11.6 ppm, which correspond to three different carbon types (α, β and γ) in the propylamine, indicating that the intercalated propylamine is protonated [30]. The titanium phosphate sample containing europium (α-EuTiPPr) does not present any relevant signal in the ^{13}C CPMAS NMR experiment (Fig. 4b). The carbon content in the sample is below the sensitivity of the NMR experiment used in the measurements of ^{13}C. The ^{31}P MAS NMR spectrum of α-EuTiPPr shows fairly broad peaks in the range between 0 ppm and -40 ppm (Fig. 3c, Table 1) and provides very little information, probably as a result of two adjuvant effects: the disorder in the interlayered space occupied by one layer of cationic species and the local magnetic field in the environment of the europium(III) cations.

Figure 5 displays the TG-DTG data for the three studied materials. The DTG curve of α-TiP (Fig. 5a) shows two minima, the first corresponds to the loss of hydration water at *ca.* 495 K and the second is due to the elimination of condensation water at 795 K, with a total mass loss of 14.5% (calculated for $Ti(HPO_4)_2{\cdot}H_2O$: 13.95%). The TG-DTG curves of α-TiPPr (Fig. 5b) show a complex decomposition behavior from the beginning of the process up to obtain the final titanium diphosphate phase (TiP_2O_7) with a total mass loss of 39.5% (calculated: 40.96%), and the probable formation of several α-

$Ti(HPO_4)_2 \cdot xC_3H_7NH_2$ (x = 2.0, 1.7, 1.3, 1.0, and 0.5) intermediate phases [31]. The first DTG peak at 353 K is associated with the loss of the hydration water, while the signals in the 400-1000 K range are related to the loss of both propylamine and condensation water (see MS-data, in Fig. 6a). Finally, the last peak (at 1173 K) corresponds to the combustion of organic matter occluded in the compound (see CO_2-signal, in Fig. 6a), as previously reported for other amine-metal phosphates [32].

The TG-DTG curves of α-EuTiPPr (Fig. 5c) show that the material decomposes in several overlapping steps with water evacuation from room temperature up to 1000 K (see MS-data, in Fig. 6b). In addition to the loss of water, at 500-600 K, the loss of propylamine is also observed according to the elemental composition data (see Table 1 in Ref. [14] where the residual amounts of organic matter in α-EuTiPPr are reported). Again, the combustion of small amounts of organic matter trapped on the collapsed solid is also observed at high temperatures (*ca.* 1200 K).

The kinetic study for the thermo-oxidative decomposition of the three materials (α-TiP, α-TiPPr, and α-EuTiPPr) was performed using thermogravimetric data obtained in air atmosphere at several constant heating rates. The kinetic evaluation was carried out by using the modified method of Friedman (MFR) [22] and the advanced nonlinear method proposed by Vyazovkin (Vyaz) [24,26]. The apparent activation energy as a function of the extent of conversion was calculated considering an increment $\Delta\alpha = 0.01$. In all cases, the E values obtained by applying both the MFR and Vyaz methods are very close to each other.

For α-TiP sample, Figure 7 shows two distinguished zones for the activation energy corresponding to the loss of water. The first zone, for the conversion range $0.15 \le \alpha \le 0.50$, is associated to the evacuation of hydration water with an average activation energy of 70 kJ mol^{-1}. The second conversion range, $0.60 \le \alpha \le 0.90$, corresponds to the loss of condensation water and the activation energy is relatively higher, about 205 kJ mol^{-1}. These results show a good agreement with the experimental TG-DTG curves (Fig. 5a).

The $E - \alpha$ curves for the other two materials, α-TiPPr in Figure 8a and α-EuTiPPr in Figure 8b, have a more irregular shape due to the overlapping mass loss processes. For a better understanding of this behavior, we have plotted both the apparent activation energy and the mass spectrometry signals (*m/z* 18 H_2O, *m/z* 44 CO_2, and *m/z* 59 $C_3H_7NH_2$) versus the extent of conversion for these two compounds. In the case of α-TiPPr, Figure 8a, a part of the hydration water is lost for $\alpha < 0.2$, and then, over the extent of conversion range $0.2 \le \alpha \le 0.5$, a part of the propylamine is lost and the value obtained for the apparent activation energy is *ca.* 95 kJ mol^{-1}. The first loss of water takes place in two overlapping steps, which are difficult to distinguish by thermogravimetric analysis, and the intercalated propylamine is lost in several overlapping steps [31]. When $\alpha = 0.65$ (see Fig. 8a), E reaches a maximum value of 300 kJ mol^{-1} that can be associated with the loss of the remaining hydration water and propylamine. For α ranging approximately between 0.65 and 0.85, the apparent activation energy is about 160 kJ mol^{-1} and attributed to the loss of the condensation water. These experimental results match with the theoretically calculated extent of conversion: α between 0.12 and 0.69 for the loss of hydration water and propylamine, and α = 0.88 for the loss of condensation water.

For α-EuTiPPr, the $E - \alpha$ and $m/z - \alpha$ curves are shown in Figure 8b. In the first stage, for α between *ca.* 0.1 and 0.4, the apparent activation energy is practically constant (*ca.* 50 kJ mol^{-1}). It corresponds to the largest loss of the hydration water. In the second stage, for α between *ca.* 0.45 and 0.65, the loss of hydration water is finished and the loss of propylamine is detected. Finally, when $\alpha >$ 0.65, the $m/z - \alpha$ curves show the loss of both condensation water and propylamine.

Figure 9 shows the reconstructed conversion curves and the experimental ones obtained in the laboratory for the three compounds at a heating rate β = 10 K min^{-1}. The excellent agreement of both MFR and Vyaz methods with the experimental data, in the whole temperature range and for several heating rates, is illustrated by the values of the correlation factor R^2 summarized in Table 2.

Conclusions

We have shown that the chemical modifications of the parent α-TiP compound could be successfully performed by taking advantage of its intercalation and ion-exchange properties. The morphology of the particles for the intercalated and ion-exchange forms (α-TiPPr, and α-EuTiPPr) is apparently similar to the parent α-TiP compound. However, solid-state NMR and thermal analysis were able to detect structural differences between these three compounds. In addition, the apparent activation energy was estimated for the thermo-oxidative decomposition stages observed in TG experiments for all the studied materials. An excellent agreement between the both applied MFR and Vyaz methods and the experimental data was obtained.

Acknowledgements

This work is supported by "Ministerio de Economía y Competitividad" (MAT2016-78155-C2-1-R, MAT2013-40950-R, MAT2011-27573-C04-02), "Gobierno del Principado de Asturias" (GRUPIN14-060), and FEDER.

References

[1] Alberti G, Cardini-Galli P, Costantino U, Torracca E. Crystalline insoluble salts of polybasic metals. 1. Ion-exchange properties of crystalline titanium phosphate. J Inorg Nucl Chem. 1967;29:571-8. **doi:** 10.1016/0022-1902(67)80063-0

[2] Alberti G, Torracca E. Crystalline insoluble salts of polybasic metals. 2. Synthesis of crystalline zirconium or titanium phosphate by direct precipitation. J Inorg Nucl Chem. 1968;30:317-8. **doi:** 10.1016/0022-1902(68)80096-X

[3] Clearfield A, Stynes JA. The preparation of crystalline zirconium phosphate and some observations on its ion exchange behavior. J Inorg Nucl Chem. 1964;26:117-29. **doi:** 10.1016/0022-1902(64)80238-4

[4] Chernorukov NG, Moskvich EP, Zhuk MI. Crystallographic characteristics of phosphates and arsenates of tetravalent elements. Kristallograf. 1974;19:1084-5.

[5] Suárez M, García JR, Rodríguez J. Calorimetric determination of H^+/Na^+ ion-exchange on α-titanium phosphate. J Phys Chem. 1984;88:157-9. **doi:** 10.1021/j150645a035

[6] Suárez M, García JR, Rodríguez J. Thermodynamic treatment of H^+/Na^+ ion-exchange on α-titanium phosphate. J Phys Chem. 1984;88:159-62. **doi:** 10.1021/j150645a036

[7] García JR, Suárez M, Guarido CG, Rodríguez J. X-Ray diffraction spectrometry for the analysis of crystalline solid phases. Anal Chem. 1984;56:193-6. **doi:** 10.1021/ac00266a016

[8] Clearfield A, Díaz A. Zirconium phosphate nanoparticles and their extraordinary properties. In Tailored organic-inorganic materials (Brunet E, Colón JL, Clearfield A, Eds.). John Wiley & Sons, Inc., Hoboken, New Jersey. 2014. Pp 1-44.

[9] Llavona R, Suárez M, García JR, Rodríguez J. Lamellar inorganic ion exchangers. Alkali metal ion exchange on α- and γ-titanium phosphate. Inorg Chem. 1989;28:2863-8. **doi:** 10.1021/ic00313a033

[10] Salvadó MA, Pertierra P, García-Granda S, García JR, Rodríguez J, Fernández-Díaz MT. Neutron powder diffraction study of $\alpha\text{-Ti}(HPO_4)_2\cdot H_2O$ and $\alpha\text{-Hf}(HPO_4)_2\cdot H_2O$; H-atom positions. Acta Cryst B. 1996;52:896-8. **doi:** 10.1107/S0108768196006702

[11] Menéndez F, Espina, A, Trobajo C, Rodríguez J. Intercalation of *n*-alkylamines by lamellar materials of the α-zirconium phosphate type. Mater Res Bull. 1990;25:1531-9. **doi:** 10.1016/0025-5408(90)90130-T

[12] Espina A, Jaimez E, Khainakov SA, Trobajo C, García JR, Rodríguez, J. Synthesis of new *n*-alkylamines

intercalation compounds with α-titanium phosphate. Process selectivity and structural and morphological characterization. Chem Mater. 1998;10:2490-6. **doi:** 10.1021/cm9802090

[13] Espina A, García JR, Guil JM, Jaimez E, Parra JB, Rodríguez J. Calorimetric study of amine adsorption on α- and γ-titanium phosphate. J Phys Chem. 1998;102:1713-6. **doi:** 10.1021/jp972410o

[14] García-Glez J, Trobajo C, Khainakov SA, Amghouz Z. α-Titanium phosphate intercalated with propylamine: An alternative pathway for efficient europium(III) uptake into layered tetravalent metal phosphates. Arab J Chem. 2017;10:885-94. **doi:** 10.1016/j.arabjc.2016.07.013

[15] Vecchio S, Di Rocco R, Ferragina C, Materazzi S. Thermal and kinetic study of dehydration and decomposition processes for copper intercalated γ-zirconium and γ-titanium phosphates. Thermochim Acta 2005;435:181-7. **doi:** 10.1016/j.tca.2005.04.029

[16] Vecchio S, Di Rocco R, Ferragina C. Kinetic analysis of the oxidative decomposition in γ-zirconium and γ-titanium phosphate intercalation compounds. The case of 2,2'-bipyridyl and its copper complex formed in situ. Thermochim Acta 2007;467:1-10. **doi:** 10.1016/j.tca.2007.10.015

[17] García-Granda S, Khainakov SA, Espina A, García JR, Castro GR, Rocha J, Mafra L. Revisiting the thermal decomposition of layered γ-titanium phosphate and structural elucidation of its intermediate phases. Inorg Chem. 2010;49:2630-8. **doi:** 10.1021/ic901254j

[18] García-Glez J, Amghouz Z, Khainakov SA, Espina A, Alfonso BF, Trobajo C. Ammonium-exchanged phase of γ-titanium phosphate. Hydrothermal synthesis, crystal structure, and thermal behavior. J Therm Anal Calorim. 2014;118:783-91. **doi:** 10.1007/s10973-014-3923-z

[19] Vyazovkin S, Burnham AK, Criado JM, Pérez-Maqueda LA, Popescu C, Sbirrazzuoli N. ICTAC Kinetic Committee recommendations for performing kinetic computations on thermal analysis data, Thermochim Acta. 2011;520:1-19. **doi:** 10.1016/j.tca.2011.03.034

[20] Simon P, Thomas PS, Okuliar J, Ray AS. An incremental integral isoconversional method. Determination of activation parameters. J Therm Anal Calorim. 2003;72: 867-74. **doi:** 10.1023_BJTAN.0000027811.80036.6c

[21] Sbirrazzuoli N, Vincent L, Mija A, Guigo N. Integral, differential and advanced isoconversional methods. Complex mechanisms and isothermal predicted conversion–time curves. Chemometr Intell Lab. 2009;96:219–26. **doi:** 10.1016/j.chemolab.2009.02.002

[22] Huidobro JA, Iglesias I, Alfonso BF, Espina A, Trobajo C, García JR. Reducing the effects of noise in the calculation of activation energy by the Friedman method. Chemometr Intell Lab.

2016;151:146-52. **doi:** 10.1016/j.chemolab.2015.12.012

[23] Ma Z, Chen D, Gu J, Bao B, Zhang Q. Determination of pyrolysis characteristics and kinetics of palm kernel shell using TGA-FTIR and model-free integral methods. Energ Convers Manage. 2015;89:251-9. **doi:** 10.1016/j.enconman.2014.09.074

[24] Vyazovkin S. Modification of the integral isoconversional method to account for variation in the activation energy. J Comput Chem. 2001;22:178-83. **doi:** 10.1002/1096-987X(20010130)22:2<178::AID-JCC5>3.0.CO;2-#

[25] Simon P, Thomas P, Dubaj T, Cibulkova Z, Peller A, Veverka M. The mathematical incorrectness of the integral isoconversional methods in case of variable activation energy and the consequences. J Therm Anal Calorim. 2014;115:853-9. **doi:** 10.1007/s10973-013-3459-7

[26] Vyazovkin S. Evaluation of activation energy of thermally stimulated solid-state reactions under arbitrary variation of temperature. J Comput Chem. 1997;18: 393-402. **doi:** 10.1002/(SICI)1096-987X(199702)18:3<393::AID-JCC9>3.0.CO;2-P

[27] Mafra L, Paz FAA, Rocha J, Espina A, Khainakov SA, Garcia JR, Fernández C. Structural characterization of layered γ-titanium phosphate $(C_6H_{13}NH_3)[Ti(HPO_4)(PO_4)]\cdot H_2O$. Chem Mater. 2005;17:6287-94. **doi:** 10.1021/cm051447f

[28] Mafra L, Rocha J, Fernández C, Castro GR, García-Granda S, Espina A, Khainakov SA, García JR. Characterization of layered γ-titanium phosphate $(C_2H_5NH_3)[Ti(H_{1.5}PO_4)(PO_4)]_2\cdot H_2O$ intercalate: A combined NMR, synchrotron XRD, and DFT calculations study. Chem Mater. 2008;20:3944-53. **doi:** 10.1021/cm800165p

[29] Manickam M, Minato K, Takata M. Synthesis and electrochemical properties of $TiNb(PO_4)_3$ cathode materials for lithium secondary batteries. J Electroanal Chem. 2004;562:1-7. **doi:** 10.1016/j.jelechem.2003.08.005

[30] MacLachlan DJ, Morgan KR. Solid-state NMR-studies of the structure of amine-intercalated α-zirconium phosphate. Reaction of α-zirconium phosphate with excess amine. J Phys Chem. 1990;19:7656-61. **doi:** 10.1021/j100382a062

[31] Espina A, Jaimez E, Suárez M, García JR, Rodríguez J. Thermal behavior of α-titanium phosphate/*n*-alkylamine intercalation compounds. Thermochim Acta 1992;210:263-72. **doi:** 10.1016/0040-6031(92)80296-9

[32] Fernández L, Espina A, Khainakov SA, Amghouz Z, Garcia JR, Garcia-Granda S. Novel ethylenediamine-gallium phosphate containing 6-fold coordinated gallium atoms with unusual four equatorial Ga–N bonds. J Solid State Chem. 2014;215:143-51. **doi:** 10.1016/j.jssc.2014.03.024

Table 1. ^{31}P MAS NMR chemical shifts

α-TiP	α-TiPPr	α-EuTiPPr
-18.4	1.5	-11.4
-18.7	-12.4	-15.0
	-14.3	-19.6
	-14.8	-23.6
	-15.2	
	-16.9	
	-17.5	
	-18.4	
	-19.7	
	-20.9	
	-22.5	

Table 2. Correlation factor in the fitting of the conversion obtained for the MFR and Vyaz methods, as a function of the heating rate (β, in K min^{-1})

Sample	Method	$\beta = 2.5$	$\beta = 5$	$\beta = 10$	$\beta = 20$	$\beta = 40$
α-TiP	MFR	0.98564	0.95813	0.96282	0.96941	0.99771
	Vyaz	0.99251	0.96500	0.96589	0.96760	0.99475
α-TiPPr	MFR	0.99897	0.99886	0.99930	0.99909	---
	Vyaz	0.99820	0.99886	0.99924	0.99879	---
α-EuTiPPr	MFR	0.99833	0.97167	0.99662	0.99935	---
	Vyaz	0.99694	0.96757	0.99518	0.99904	---

FIGURE CAPTIONS

Fig. 1 PXRD patterns for α-TiP (a), α-TiPPr (b) and α-EuTiPPr (c).

Fig. 2 SEM images for α-TiP (a), α-TiPPr (b) and α-EuTiPPr (c).

Fig. 3 ^{31}P MAS NMR spectra for α-TiP (a), α-TiPPr (b) and α-EuTiPPr (c).

Fig. 4 ^{13}C CPMAS NMR spectra for α-TiPPr (a) and α-EuTiPPr (b).

Fig. 5 TG (—) and DTG (—) curves for α-TiP (a), α-TiPPr (b) and α-EuTiPPr (c) obtained at 10 K min^{-1} heating rate in O_2-atmosphere.

Fig. 6 MS-signals of evacuated vapours on the TG-experiment [*m/z* 18 for H_2O, *m/z* 44 for CO_2, and *m/z* 59 for $C_3H_7NH_2$] for α-TiPPr (a) and α-EuTiPPr (b).

Fig. 7 Dependence of the apparent activation energy on the extent of conversion for α-TiP.

Fig. 8 Apparent activation energy and MS-signals of evacuated vapours [*m/z* 18 for H_2O, *m/z* 44 for CO_2, and *m/z* 59 for $C_3H_7NH_2$] *versus* extent of conversion for α-TiPPr (a) and α-EuTiPPr (b).

Fig. 9 Experimental and reconstructed $\alpha - T$ curves at 10 K min^{-1} heating rate for α-TiP (a), α-TiPPr (b) and α-EuTiPPr (c).

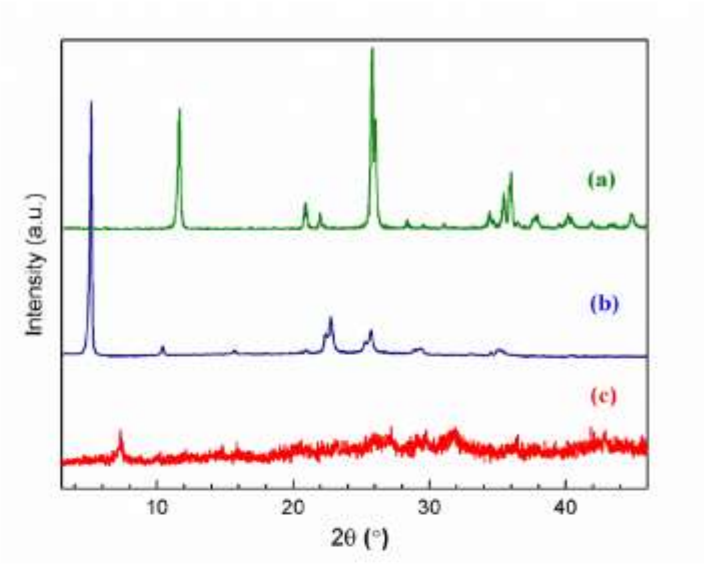

Figure 1

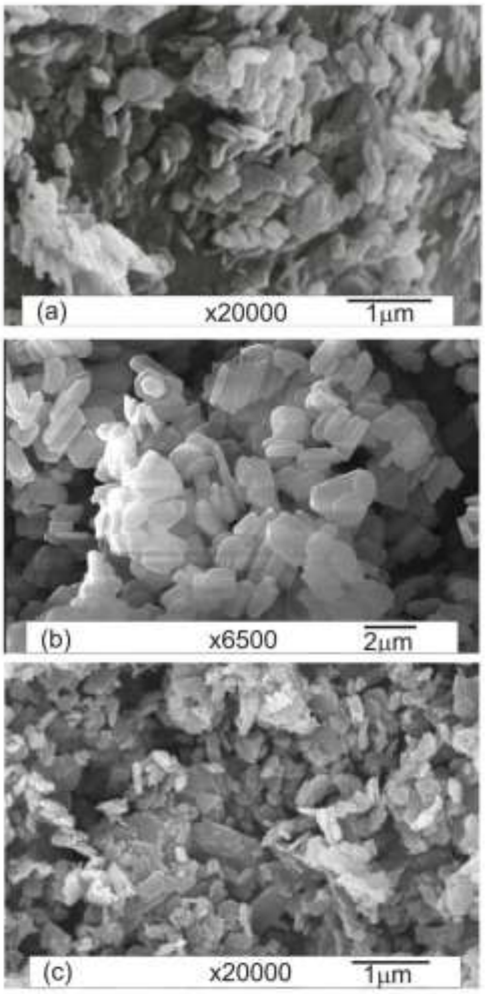

Figure 2

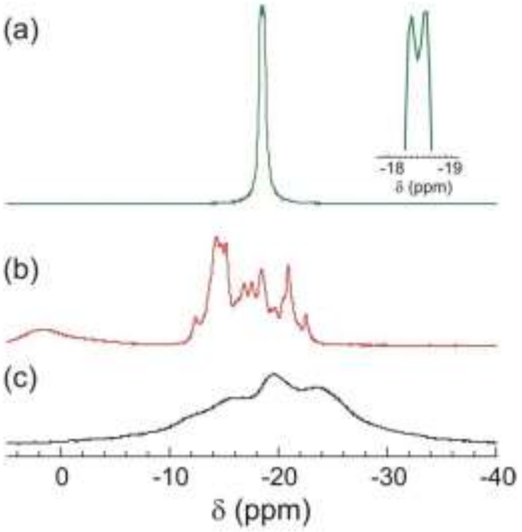

Figure 3

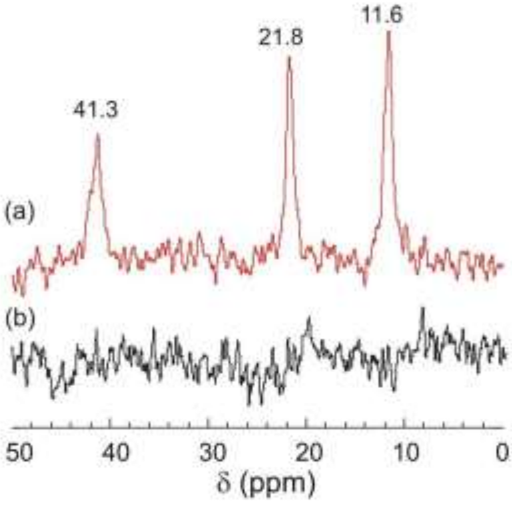

Figure 4

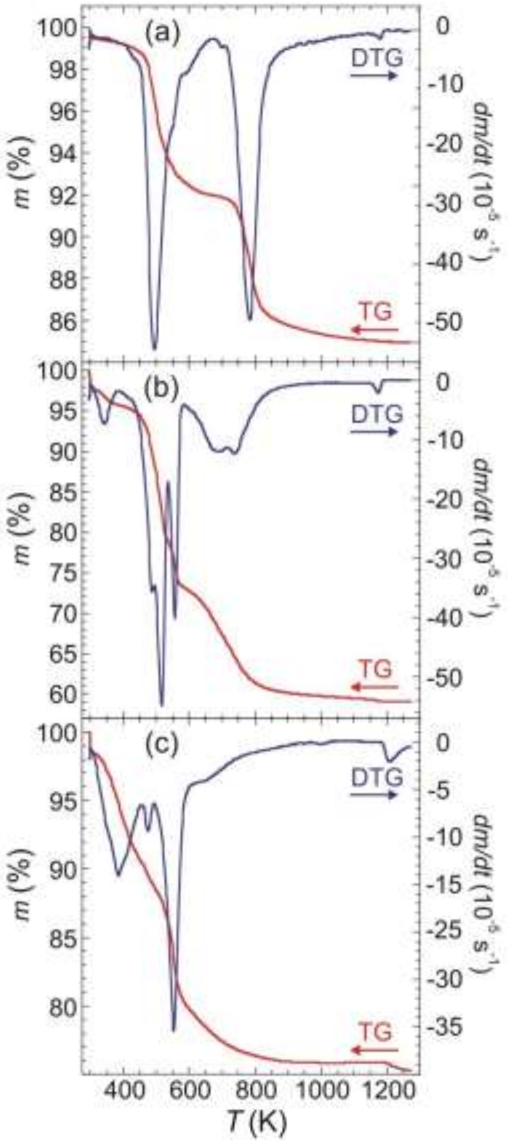
(a)
DTG
TG
m (%)
100
98
96
94
92
90
88
86
dm/dt (10^-5 s^-1)
0
-10
-20
-30
-40
-50
(b)
DTG
TG
m (%)
100
95
90
85
80
75
70
65
60
dm/dt (10^-5 s^-1)
0
-10
-20
-30
-40
-50
(c)
DTG
TG
m (%)
100
95
90
85
80
dm/dt (10^-5 s^-1)
0
-5
-10
-15
-25
-30
-35
400
600
800
1000
1200
T (K)

Figure 5

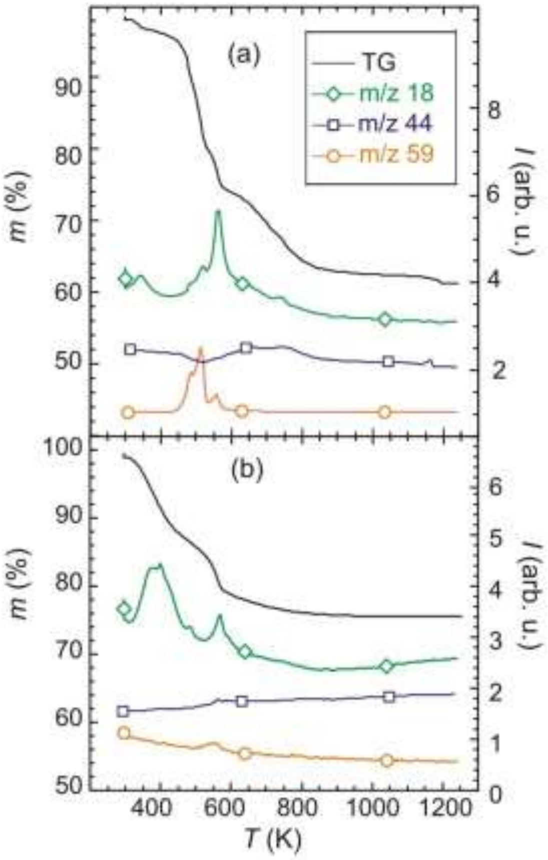
(a)
TG
m/z 18
m/z 44
m/z 59
m (%)
I (arb. u.)
90
80
70
60
50
8
6
4
2
(b)
100
90
80
70
60
50
6
5
4
3
2
1
0
400
600
800
1000
1200
T (K)

Figure 6

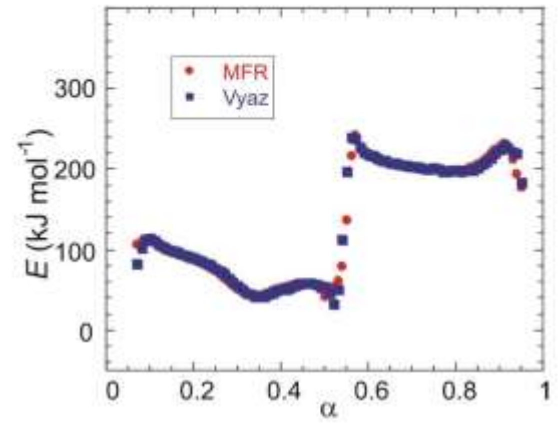

Figure 7

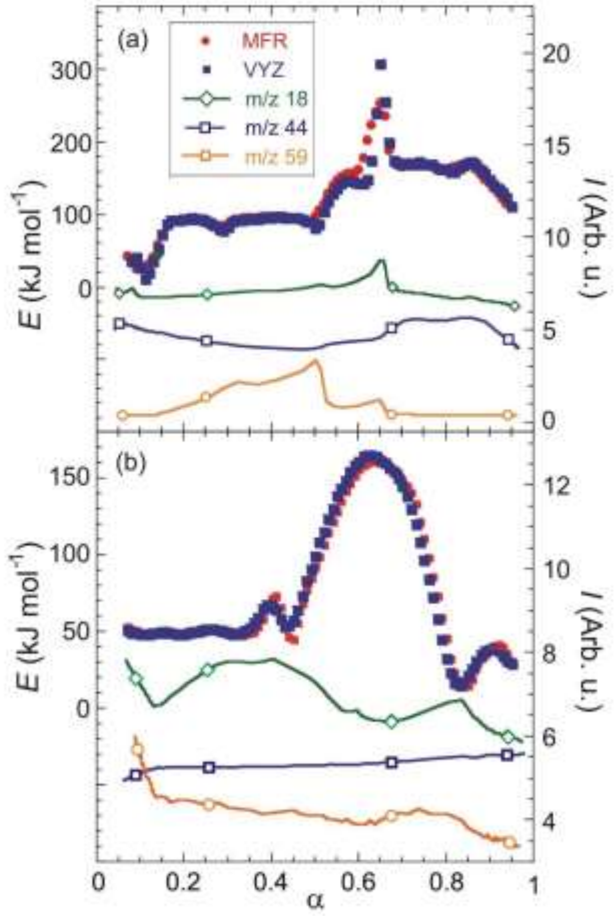

Figure 8

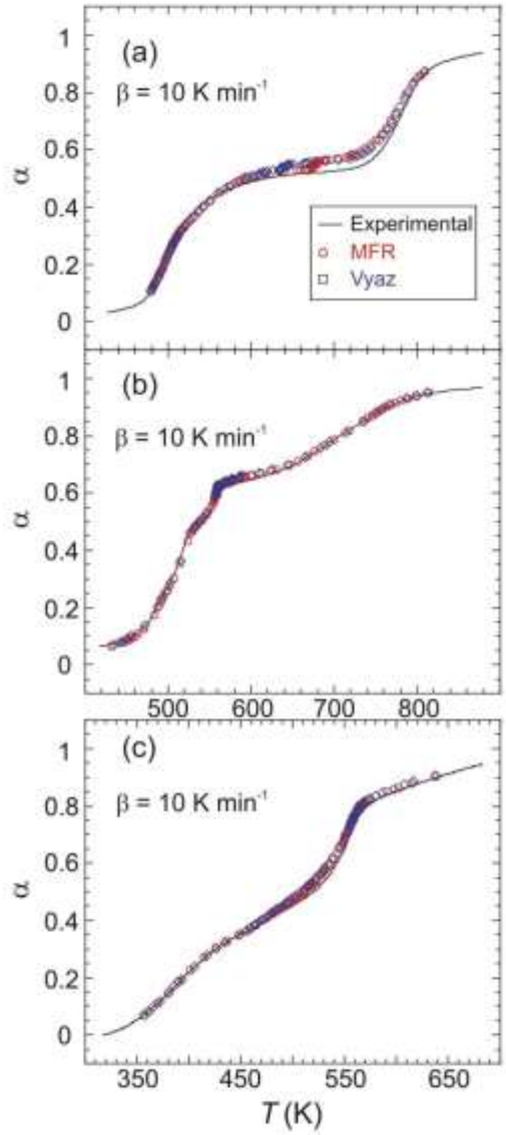
(a)
β = 10 K min⁻¹
Experimental
MFR
Vyaz
(b)
β = 10 K min⁻¹
500
600
700
800
(c)
β = 10 K min⁻¹
α
0
0.2
0.4
0.6
0.8
1
350
450
550
650
T (K)

Figure 9

Artículo S3

“Ammonium-exchanged phase of γ-titanium phosphate: Hydrothermal synthesis, crystal structure, and thermal behavior”

Journal of Thermal Analysis and Calorimetry

Vol. 118

Pág. 783–791

Año 2014

DOI: 10.1007/s10973-014-3923-z

Índice de Impacto: 2.042

J Therm Anal Calorim (2014) 118:783–791
DOI 10.1007/s10973-014-3923-z

Ammonium-exchanged phase of γ-titanium phosphate

Hydrothermal synthesis, crystal structure, and thermal behavior

**Jorge García-Glez · Zakariae Amghouz ·
Sergei A. Khainakov · Aránzazu Espina ·
Belén F. Alfonso · Camino Trobajo**

Received: 30 October 2013 / Accepted: 4 June 2014

Abstract The monoammonium salt of γ-titanium phosphate has been prepared by hydrothermal treatment of π-$Ti_2O(PO_4)_2 \cdot 2H_2O$ in the presence of urea and phosphoric acid, and its crystal structure was obtained by Rietveld analysis using powder X-ray diffraction data. γ-$Ti(PO_4)(NH_4HPO_4)$ crystallizes in the monoclinic space group $P2_1/m$ with $a = 5.0725(3)$ Å, $b = 6.3101(3)$ Å, $c = 11.2435(5)$ Å, $\beta = 97.980(3)°$ $(Z = 2)$. The structure consists of 2D titanium phosphate layers in the *ab*-plane. The titanium atoms and one of the phosphate groups are located nearly in the *ab*-plane of the layer. All the oxygen atoms of this phosphate group are involved in titanium coordination sphere. The other phosphate group located in the layers edges links two neighboring titanium atoms in the *a*-direction through two of its oxygen atoms. The remaining two oxygens are pointed toward the interlayer space being involved in hydrogen bond interactions with the ammonium ions. Each ammonium ion is shared by four oxygens belonging to four different phosphate hydroxyl groups. γ-$Ti(PO_4)(NH_4HPO_4)$ is stable until 453 K, while above this temperature, it transforms to γ'-$Ti(PO_4)(NH_4HPO_4)$ high temperature polymorph stable until 573 K. Thermal decomposition of this material leads to cubic TiP_2O_7 structure, with previous formation of two intermediate pseudo-layered compounds: $Ti(PO_4)(NH_4HP_2O_7)_{0.5}$ and $Ti(PO_4)(H_2P_2O_7)_{0.5}$. The activation energy of thermal decomposition has been calculated as a function of the extent of conversion applying the Kissinger–Akahira–Sunose (KAS) isoconversional method to the thermogravimetric data.

Keywords Ammonium-titanium phosphate-hydrogenphosphate · Crystal structure · Thermal decomposition · Kinetic parameters

Introduction

Metal salts of phosphoric acid have been known for over a century. However, research into layered tetravalent metal phosphates and their derivatives only began in the late 1950's due to the recognition of the application of some of these salts as cation exchangers in radioactive waste streams [1]. Because of their low solubility, tetravalent metal phosphates were only available as amorphous gels. In 1964, the first crystalline compound, α-$Zr(HPO_4)_2 \cdot H_2O$ (α-ZrP), was prepared by Clearfield and Stynes [2], which made its layered structure [3, 4] and chemical reactivity to being clearly understood [5]. Since then, the possibility of relating the properties of these metal acid salts to their crystalline structures and the many potential applications in the fields of ion exchange, intercalation, catalysis, and ionic conductivity prompted the comprehensive study into this class of compounds [6–9].

The existence of γ-layered compound, γ-$Zr(PO_4)(H_2PO_4) \cdot 2H_2O$ (γ-ZrP), was also reported by Clearfield et al. [10]. The originally given formula was γ-$Zr(HPO_4)_2 \cdot 2H_2O$. However, ^{31}P MAS-NMR studies performed by Clayden [11] showed that γ-ZrP contains tertiary phosphate groups and dihydrogen phosphate groups in equal amounts. In 1990,

---

J. García-Glez · C. Trobajo (✉)
Departamento de Química Orgánica e Inorgánica y Física,
Universidad de Oviedo-CINN, 33006 Oviedo, Spain
e-mail: ctf@uniovi.es

Z. Amghouz · S. A. Khainakov · A. Espina
Servicios Científico-Técnicos, Universidad de Oviedo,
33006 Oviedo, Spain

B. F. Alfonso
Departamento de Física, Universidad de Oviedo, 33006 Oviedo,
Spain

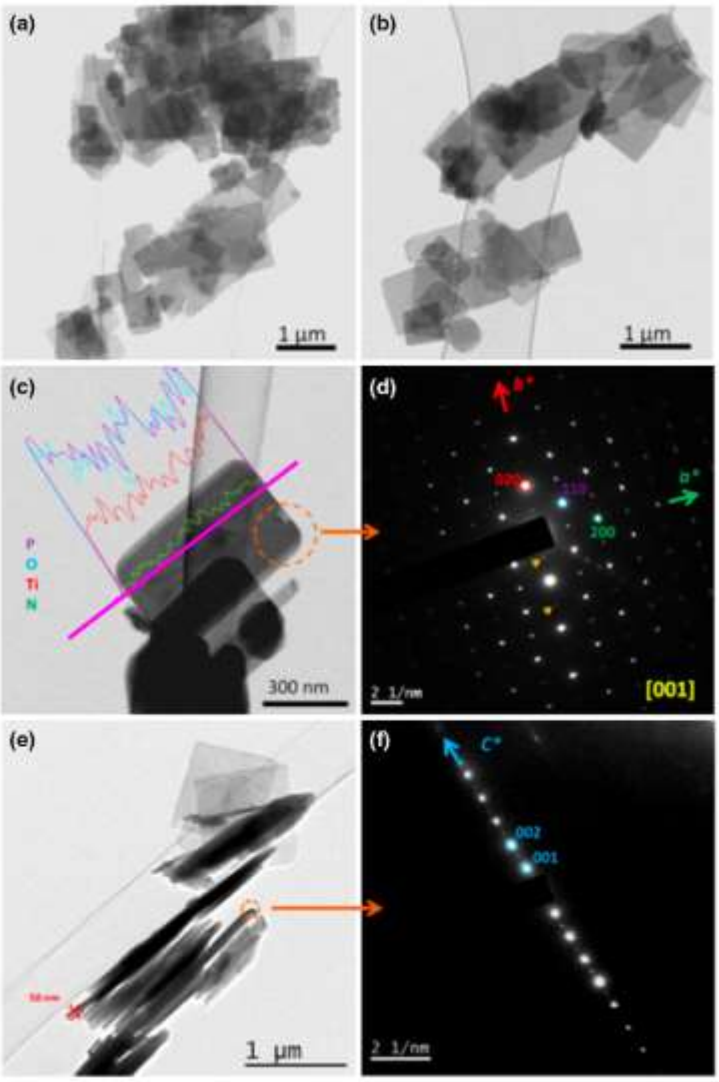

Fig. 1 (Color online). (**a**), (**b**) TEM images of γ-Ti(PO$_4$)(NH$_4$HPO$_4$). (**c**) BF-STEM image with EDX line profiles of elements P (*purple*), O (*cyan*), Ti (*red*), and N (*green*) along one plate of γ-Ti(PO$_4$)(NH$_4$HPO$_4$), the position where line scans were acquired is indicated by the *solid pink line*. (**d**) Selected area electron diffraction (SAED) pattern along [001] zone axis corresponding to the *orange area* in the image (**c**), *orange arrows* indicate the systematic absence of the type 0*k*0 ($k = 2n + 1$). (**e**) TEM image showing thickness of the plates. (**f**) SAED corresponding to the *orange area* in (**e**) shows the reflections corresponding to the interlayer spacing

Christensen et al. [12] proposed a structure for the titanium parent compound, γ-Ti(PO$_4$)(H$_2$PO$_4$)·2H$_2$O, from powder X-ray diffraction data that were in accordance with the results obtained by Clayden. However, the positions of the water molecules were not found and there was uncertainty about the space group. In 1995, the structure of γ-ZrP was solved from powder X-ray diffraction data by Poojary et al. [13], and the results confirmed the model reported by Christensen.

In previous contributions [14, 15], we have described the behavior of the γ-TiP as ion-exchanger. This material has very high affinity to both cesium [16] and ammonium cations [17], with the highest potential for use in the decontamination of radioactive metal wastes and renal dialysis treatment. Surprisingly, the crystal structure of γ-TiP ion-exchanged phases is unknown, and only the anhydrous monoammonium salt of γ-ZrP was solved up to now [18]. This contribution reports the hydrothermal synthesis and crystal structure of the first ammonium-exchanged γ-TiP phase, γ-Ti(PO$_4$)(NH$_4$HPO$_4$), and its thermal decomposition data.

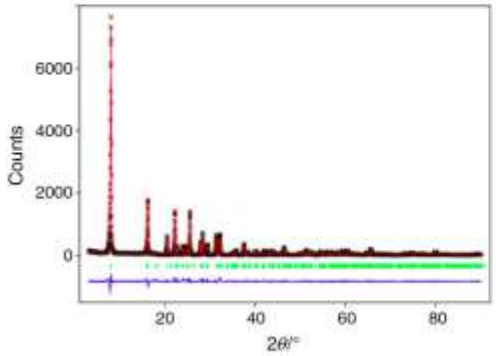

Fig. 2 (Color online). X-ray powder diffraction pattern for the γ-Ti(PO$_4$)(NH$_4$HPO$_4$) collected at room temperature. Observed (+) and calculated (*solid line*) patterns. Positions of the Bragg reflections are represented by *vertical bars*. The observed-calculated difference is depicted at the bottom of the Figure

Table 1 Crystal data and structure refinement

Molecular formula	$TiP_2O_8NH_5$
Formula mass/g mol^{-1}	251.85
Wavelength/Å	1.5418 Å
Radiation Type	X-ray
Radiation source	Cu tube
Crystal system	Monoclinic
Space group	$P2_1/m$
a/Å	5.0725(3)
b/Å	6.3101(3)
c/Å	11.2435(5)
β	97.980(3)
Z	2
Calculated density/g cm^{-3}	2.68
Volume/Å^3	356.40(3)
2θ range/deg	3°–90°
Step	0.02
Parameters	57
R_p/%	11.62
R_{wp}/%	15.98
R_{F2}/%	9.01

Table 2 Fractional coordinates for the γ-Ti(PO$_4$)(NH$_4$HPO$_4$)

Atom	x	y	z	U$_{iso}$, Å^2
Ti	0.7811(10)	0.25	0.1335(3)	0.006(1)
P1	0.2110(13)	0.25	0.9405(5)	0.012(2)
P2	0.3567(13)	0.25	0.3396(5)	0.003(2)
O1	0.9596(21)	0.25	−0.0036(8)	0.005(1)
O2	0.2195(34)	0.0577(11)	0.8639(7)	0.009(3)
O3	0.4379(15)	0.25	0.0455(8)	0.006(1)
O4	0.1133(20)	0.25	0.2485(10)	0.034(6)
O5	0.6200(18)	0.25	0.2951(7)	0.005(1)
O6	0.3174(30)	0.0455(18)	0.4133(7)	0.064(5)
N1	0.9012(31)	0.75	0.3715(11)	0.007(1)

Experimental

Sample preparation and analytical procedures

In a first step, π-Ti$_2$O(PO$_4$)$_2$·2H$_2$O (π-TiP) was prepared according to a previously reported method [19]. 2 M aqueous solutions of TiCl$_4$ and H$_3$PO$_4$ were used as the initial sources of titanium and phosphorus, respectively. The synthetic procedure included the mixing of TiCl$_4$ and H$_3$PO$_4$ solutions with a P:Ti molar ratio of 5:1 in a 100 mL stainless steel Teflon-lined vessel. Then, the reaction mixture (total volume 60 mL) was sealed and heated at 460 K for 5 days. The product (π-TiP) was filtered, thoroughly washed with deionized water, and dried in air at 330 K. After, 0.0024 mol of π-TiP was mixed with 20 mL of H$_3$PO$_4$ (85 mass%, Merck) and 0.075 mol of urea in a 100 mL stainless steel Teflon-lined vessel. The reaction mixture was sealed and heated at 450 K for 7 days. The product was then filtered off, thoroughly washed with an excess of deionized until neutral pH, and dried in air at room temperature. The titanium and phosphorus contents were determined by inductively coupled plasma mass spectrometry (ICP-MS) analysis (Finnigan, Element model) after dissolving a weighed amount of the sample in HF(aq). Elemental analysis (mass%): Ti: 18.1; P: 23.9; N: 5.8; H: 2.0. Calculated for γ-Ti(PO$_4$)(NH$_4$HPO$_4$): Ti: 18.65; P: 24.43; N: 5.45; H: 1.95.

Powder X-ray diffraction studies

Step-scanned X-ray powder data for the finely ground sample of γ-Ti(PO$_4$)(NH$_4$HPO$_4$) were collected by means of a X'Pert PRO X-ray diffractometer, operating in the Bragg–Brentano (θ/2θ) geometry, CuK$_\alpha$ radiation ($\lambda = 1.5418$ Å). Data were collected between 3° and 89° in 2θ with a step size of 0.02° and count time of 10 s per step. Powder pattern was indexed by TREOR [20] and Dicvol04 [21] on the basis of the first 20 observed lines. The best solutions indicated a monoclinic unit cell with the following lattice parameters: $a = 11.232$ Å, $b = 6.305$ Å, $c = 5.068$ Å, $\beta = 98.020°$ (by TREOR), or $a = 11.231$ Å, $b = 6.293$ Å, $c = 5.067$ Å, $\beta = 98.038°$ (by Dicvol04), related to the previously reported for γ-Zr(PO$_4$)(NH$_4$HPO$_4$) ($a = 5.3284(4)$ Å, $b = 6.6217(2)$ Å, $c = 11.326(1)$ Å,

Table 3 Selected bond lengths (Å) and angles (deg) for the γ-Ti(PO$_4$)(NH$_4$HPO$_4$)

Ti–O1	1.894(7)	O1–Ti–O2	90.8(5)
Ti–O2	1.942(7)x2	O1–Ti–O3	94.8(4)
Ti–O3	1.879(6)	O1–Ti–O4	94.1(5)
Ti–O4	1.976(8)	O1–Ti–O5	174.5(5)
Ti–O5	2.092(8)	O2–Ti–O2	178.3(5)
		O2–Ti–O3	90.3(4)
		O2–Ti–O4	89.6(5)
		O2–Ti–O5	89.2(4)
		O3–Ti–O4	171.1(5)
		O3–Ti–O5	90.7(4)
		O4–Ti–O5	80.4(4)
P1–O1	1.498(8)	O1–P1–O2	109.7(7)
P1–O2	1.492(5)x2	O1–P1–O3	105.5(6)
P1–O3	1.530(6)	O2–P1–O2	108.8(7)
		O2–P1–O3	111.5(6)
P2–O4	1.491(4)	O4–P2–O5	117.7(7)
P2–O5	1.490(6)	O4–P2–O6	102.1(7)
P2–O6	1.561(10)x2	O5–P2–O6	111.1(4)
		O6–P2–O6	111.5(7)
Ti–O1–P1	150.8(7)	N1–O6	3.08(2)
Ti–O2–P1	143.6(7)	N1–O6	2.81(2)
Ti–O3–P1	161.6(6)	N1–O2	2.89(1)
Ti–O4–P2	177.5(8)	O6–O6	2.56(2)
Ti–O5–P2	140.2(6)		

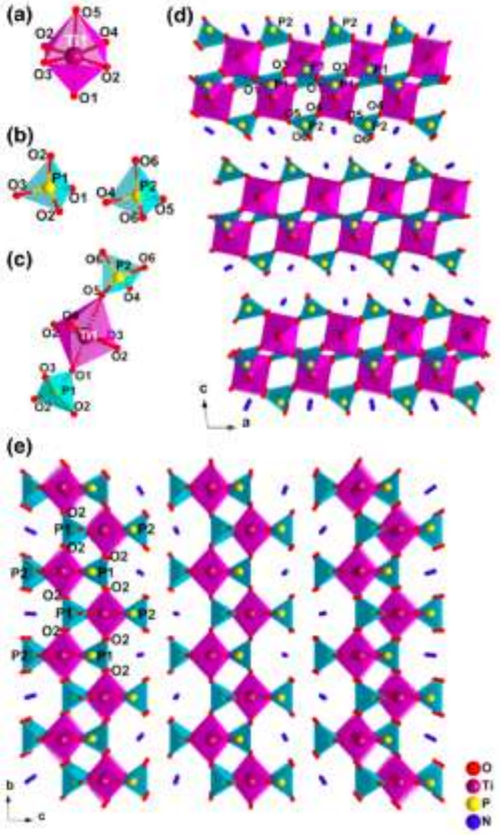

Fig. 3 (Color online). Perspective view of the coordination environment of Ti (**a**) and P (**b**). Perspective view of the SBU (**c**). Projection of the structure along the *a*-axis (**d**) and *b*-axis (**e**), respectively

$\beta = 96.63(1)^\circ$) [18] that crystallizes in the monoclinic space group $P2_1/m$.

Powder X-ray thermo-diffraction studies

These measurements were performed in air; the sample was placed in an Anton Paar HTK 1200N oven-chamber on a PANalyticalXPERT-PRO diffractometer, using CuK$_\alpha$ radiation, equipped with a PIXcel linear detector with 255 channels. Each powder pattern was recorded in the 5°–50° range (2θ) at interval of 10 K, from 303 up to 1,273 K, with a step of 0.013° and a counting time of 0.484 s. The temperature ramp between two consecutive temperatures was 10 K min^{-1}.

Transmission electron microscopy studies

TEM and BF-STEM images, selected area electron diffraction (SAED) patterns, and energy dispersive X-ray (EDX) microanalysis (line scans analysis) were collected on a JEOL JEM-2100F field-emission transmission electron microscope operated at an accelerating voltage of 200 kV and equipped with an ultra-high resolution pole-piece that provided a point-resolution better than 0.19 nm. It is also equipped with STEM control unit (Gatan), EDX detector (Oxford Instruments, INCA Energy TEM 250), CCD camera (14-bit Gatan Orius SC600), and bright-field (BF) and high-angle annular dark-field (HAADF) detectors (JEOL). Fine powder of the sample was dispersed in ethanol, sonified and sprayed on a carbon coated copper grid, and then allowed to air dry. Finally, SOLARUS 950 Advanced Plasma Cleaning System was used to clean samples before loading in the microscope.

Nuclear magnetic resonance spectroscopy studies

^{31}P single-pulse experiment (SPE) MAS NMR spectra were recorded at 161.9 MHz on a Bruker Avance III 400 (9.4 T) wide-bore spectrometer using a 4 mm MAS probe. The MAS rate was 14 kHz and the Fourier transform was done on the free induction decay (FID) signals obtained

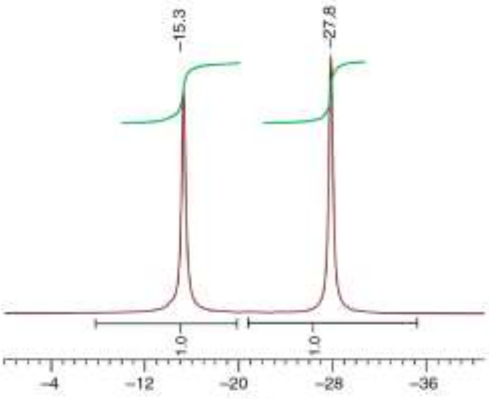

Fig. 4 (Color online). ^{31}P MAS-NMR spectrum of γ-Ti(PO$_4$)(NH$_4$HPO$_4$)

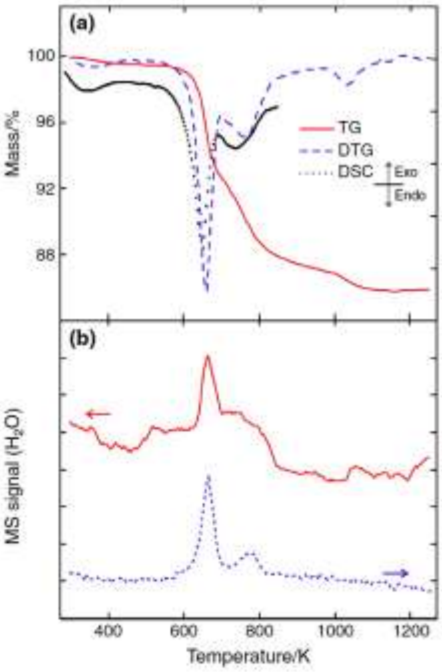

Fig. 5 (Color online). (a) TG, DTG, and DSC curves of γ-Ti(PO$_4$)(NH$_4$HPO$_4$) obtained at 10 K min^{-1} heating rate. (b) MS signals of evacuated vapors on the TG-experiment: m/z 15, NH$_3$ and m/z 18, H$_2$O

after 24 accumulations, with a recycle time of 120 s in a typical measurement. ^{31}P chemical shifts are depicted (in ppm) with respect to NH$_4$H$_2$PO$_4$ ($\delta = 0.9$ ppm).

Table 4 Selected temperatures data and mass loss from TG–DTG curves at 10 K min^{-1} heating rate for thermal decomposition of γ-Ti(PO$_4$)(NH$_4$HPO$_4$)

Stage	T_i/K	T_m/K	T_f/K	Δm/%
I	565.9	657.9	703.4	7.18
II	703.4	770.2	935.4	5.12
III	935.4	1,027.8	1,128.3	1.74

T_i, T_f Temperatures at the beginning and the end of each reaction step according to DTG curve

T_m Temperature corresponding at the "minima" (maxima rate of mass loss) in DTG curve

Δm Total mass loss corresponding to each step

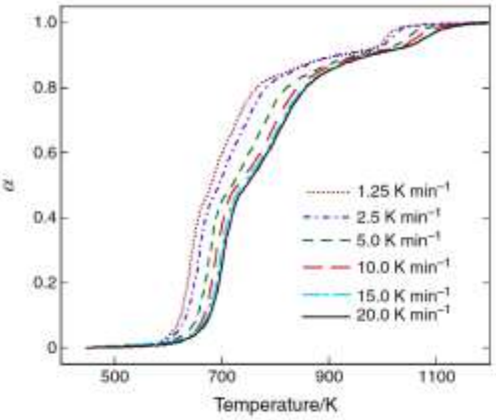

Fig. 6 (Color online). Thermal decomposition of γ-Ti(PO$_4$)(NH$_4$HPO$_4$): extent of conversion curves as a function of temperature at different heating rates

Thermal analysis procedure

A Mettler-Toledo TGA/SDTA851^e and a DSC822^e were used for the thermal analyses in nitrogen dynamic atmosphere (50 mL min^{-1}) at a heating rate of 10 K min^{-1}. In TG test, a Pfeiffer Vacuum ThermoStar™ GSD301T mass spectrometer was used to determine the evacuated vapors. The masses were tested by using a detector C-SEM, operating at 1,200 V, with a time constant of 0.5 s. In all cases, ca. 15 mg of compound was thermally treated.

Determination of kinetic parameters

The kinetics of conversion in solids are usually described by equation (1), where $f(\alpha)$ is the reaction model, α is the extent of conversion, which is determined experimentally as a fraction of the total mass loss in the process, $k(T)$ is the Arrhenius rate constant, T is the temperature, and t is the time. Then, the rate of a solid-state reaction can be generally described by equation (2), where A is the pre-exponential factor, E the activation energy, and R the gas constant. The above rate expression can be considered as a function of temperature as given in equation (3), where β is the heating rate.

$$\frac{d\alpha}{dt} = k(T)f(\alpha) \tag{1}$$

$$\frac{d\alpha}{dt} = A\exp(-E/RT)f(\alpha) \tag{2}$$

$$\frac{d\alpha}{dT} = \frac{A}{\beta}\exp(-E/RT)f(\alpha) \tag{3}$$

It is well known that the ambiguity of the kinetic triplet (E, A, $f(\alpha)$) creates difficulties for predicting the behavior of compounds over the range of experimental temperatures. This ambiguity can be overcomed by using model-free isoconversional methods which allow estimating the activation energy as a function of α, without the need to specify neither the reaction model nor the pre-exponential factor. The basic assumption of these methods is that the reaction rate for a constant extent of conversion, α, depends only on temperature [22–25]. Constant E values can be expected in the case of single state decomposition, while in a multistep process E varies with α due to changes in the relative contributions of each single step to the overall reaction rate.

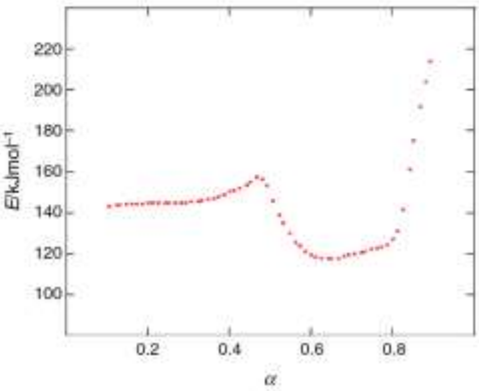

Fig. 7 (Color online). Thermal decomposition of γ-Ti(PO$_4$)(NH$_4$HPO$_4$): activation energy versus extent of conversion

The KAS method [26, 27] uses Coats–Redfern [28] approximation of the temperature integral that leads to

$$\ln\frac{\beta}{T^2} = \ln\left(\frac{AR}{Eg(\alpha)}\right) - \frac{E}{RT} \tag{4}$$

The integral form of the reaction model $f(\alpha)$ is given by $g(\alpha)$. Thus, for $\alpha = \text{const.}$, a plot of $\ln(\beta/T^2)$ *versus* $1/T$, obtained from thermal curves recorded at several heating rates, is a straight line whose slope allows evaluation of the activation energy [29]. In this study, six different heating rates were performed ($\beta = 1.25$, 2.5, 5, 10, 15, and 20 K min^{-1}) for the thermal treatment of a certain amount (ca. 15 mg) of title compound in a nitrogen dynamic atmosphere (50 mL min^{-1}).

Results and discussion

A representative low-magnification TEM and BF-STEM images (Fig. 1a–c) show the presence of both square and rectangular shapes of the plates in the hydrothermally product, with a thickness of ca. 50 nm (Fig. 1e) characterized by 90° or circle corners. According to EDX analysis, both these morphologies are phase-pure γ-Ti(PO$_4$)(NH$_4$HPO$_4$) particles, probably possessing a different growth magnitude along *a* and *b*-directions. EDX line scan profiles in the individual particles (e.g., Fig. 1b) confirm that the average molar ratio of P to Ti elements (P:Ti) is ca. 2:1, consistent with the chemical analysis and the proposed formula from powder X-ray diffraction data.

Table 5 Isoconversional data at selected extent of conversion (α) for the γ-Ti(PO$_4$)(NH$_4$HPO$_4$): Temperature as a function of the heating rate (T_β) ($\beta = 1.25$, 2.5, 5, 10, 15, and 20 K min^{-1}), and activation energy (E) and correlation coefficient (r^2) according to KAS calculation method

α	$T_{1.25}$/K	$T_{2.5}$/K	T_5/K	T_{10}/K	T_{15}/K	T_{20}/K	E/kJ mol^{-1}	r^2
0.1	595.2	608.2	626.7	639.7	647.1	650.8	144.70	0.9951
0.2	608.1	623.0	641.5	654.5	661.9	667.4	144.08	0.9928
0.3	617.4	630.4	650.8	665.6	673.0	678.6	142.14	0.996
0.4	628.6	641.5	663.7	674.9	684.1	689.7	148.32	0.9939
0.5	652.6	667.4	691.5	701.8	711.9	717.4	151.19	0.9915
0.6	674.9	691.5	724.9	752.6	752.6	758.2	121.11	0.9879
0.7	700.8	719.3	754.5	774.9	786.0	789.7	121.32	0.9876
0.8	735.9	754.5	793.4	811.9	824.9	828.6	127.83	0.9855
0.85	797.1	804.5	845.2	854.5	865.6	871.1	177.98	0.9703

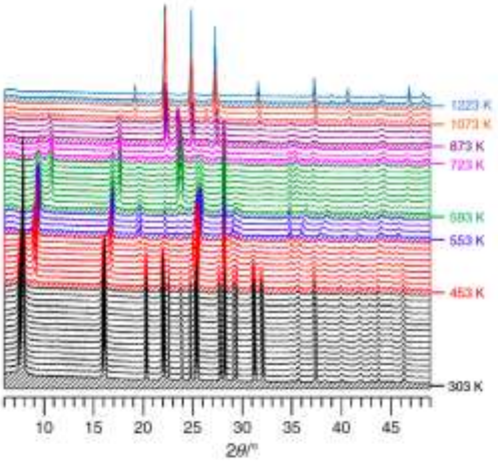

Fig. 8 (Color online). Powder X-ray thermo-diffraction patterns of γ-Ti(PO$_4$)(NH$_4$HPO$_4$) recorded in air heating up from 303 to 1,273 K. Color code corresponding to the structural change, *black* γ-Ti(PO$_4$)(NH$_4$HPO$_4$), *red* transformation of γ-Ti(PO$_4$)(NH$_4$HPO$_4$) to γ'-Ti(PO$_4$)(NH$_4$HPO$_4$), *blue* γ'-Ti(PO$_4$)(NH$_4$HPO$_4$), *green* transformation of γ'-Ti(PO$_4$)(NH$_4$HPO$_4$) to Ti(PO$_4$)(NH$_4$HP$_2$O$_7$)$_{0.5}$, *pink* transformation of Ti(PO$_4$)(NH$_4$HP$_2$O$_7$)$_{0.5}$ to Ti(PO$_4$)(H$_2$P$_2$O$_7$)$_{0.5}$, *purple* Ti(PO$_4$)(H$_2$P$_2$O$_7$)$_{0.5}$, *orange* transformation of Ti(PO$_4$)(H$_2$P$_2$O$_7$)$_{0.5}$ to TiP$_2$O$_7$, *cyan* TiP$_2$O$_7$

The indexed reflections of powder XRD pattern showed the systematic absences of the type $0k0$, $k = 2n + 1$, indicating that the space group is either $P2_1$ or $P2_1/m$. The unit cell parameters determined from electron diffraction data ($a = 5.17$ Å, $b = 6.48$ Å, $c = 11.05$ Å) confirm those obtained from powder X-ray diffraction studies. The presence of the reflections type $h00$ ($h = 2n + 1$) and $00l$ ($l = 2n + 1$), and the systematic absences (weak reflections) of the type $0k0$ ($k = 2n + 1$) in SAED patterns in Fig. 1d, f indicate that the possible space groups are $P2_1$ or $P2_1/m$, in agreement with those found from powder XRD studies. The initial selection of the centric space group was found to be correct from the successful refinement of the structure. Rietveld refinement was performed by GSAS [30] using as starting model the structure of their analogous zirconium compound, γ-Zr(PO$_4$)(NH$_4$HPO$_4$). At the beginning, background, zero point, lattice parameters, and atomic positions with restraints which define the expected geometries of the metal atoms and the phosphate groups within some allowable error limits were refined. In the next step, preferred orientations and thermal parameters were refined with reducing step-by-step weight factors for restraints. The final Rietveld plot from powder X-ray diffraction data is shown in Fig. 2. Crystallographic data and Rietveld refinement summary are given in Table 1. Fractional atomic coordinates and isotropic thermal parameters are reported in Table 2. Table 3 lists the selected bond lengths and bond angles.

The structure of γ-Ti(PO$_4$)(NH$_4$HPO$_4$) is a layered one extending along the *ab*-plane, with templating ammonium ions inserted between the layers and held in via hydrogen bonds. The core of each layer consists of titanium-oxygen octahedra (Fig. 3a) and phosphate tetrahedra (Fig. 3b). The layer can be described as the arrangement of the secondary building unit (SBU), based on one titanium-oxygen octahedra and two phosphate tetrahedra (Fig. 3c), leading to infinite anionic chains running along the *a*-direction which in turn are connected in successive switch manner along the *b*-direction to give rise to the γ-Ti(PO$_4$)(HPO$_4$) anionic layer. All four oxygens of orthophosphate group (P1) bridge across titanium atoms, one set of bridges (O1 and O3) running parallel to the *a*-axis (Fig. 3d), and another one consisting of two equivalent oxygens (O2) is parallel to the *b*-axis (Fig. 3e). The P2 phosphate group is located on the outer periphery of the layer involving two of its oxygens (O4 and O5) to bridge across titanium atoms in the *a*-direction, and the other two equivalent oxygens (O6) extend into the interlamellar space (Fig. 3d) and are bonding to a proton and NH$_4^+$ groups. The nitrogen atoms of NH$_4^+$ ions are located between two oxygen atoms (O6) of the neighboring P2 phosphate groups (Fig. 3d) arranged in the form of a chain. The titanium atom occupied one crystallographic site is a 6-fold coordinated and forms TiO$_6$ octahedra. The Ti–O bond lengths are within the 1.88–2.09 Å range. Two different sites are evidenced for P atoms (P1 and P2). The P1 corresponds to the inner tetrahedral phosphate groups with P1–O bond lengths within the 1.49–1.53 Å, while the P2 atoms form outer periphery tetrahedra with P2–O bonds from 1.49 to 1.56 Å.

In order to complete the structural information of titanium phosphate, ^{31}P nuclei were investigated by solid-state nuclear magnetic resonance spectroscopy. The spectrum of γ-Ti(PO$_4$)(NH$_4$HPO$_4$) (Fig. 4) shows two resonances with intensity relationship 1:1. A rather large difference in chemical shift of 12.5 ppm is observed for these two resonances which suggest two chemically distinct types of phosphate group rather than two similar but with crystallographically inequivalent phosphorus atoms. The signal at −27.8 ppm should be assigned to the PO$_4$ group (P2), while the signal at −15.3 ppm should be attributed to the HPO$_4$ group (P1) [11, 18, 31]. In addition, the presence of two peaks of equal integrated intensity confirms the $P2_1/m$ space group used in the refinement of diffraction data.

The TG/DTG curves of γ-Ti(PO$_4$)(NH$_4$HPO$_4$) depicted in Fig. 5a show three stages with the total mass loss of 14.0 % (cal. 13.62 %) up to 1,273 K. For each step, initial and final temperatures, temperature for the maximum rate of mass loss, and mass loss, are reported in Table 4. The DTG curve shows three minimum at ca. 660, 760, and 1,030 K indicating several decomposition processes with endothermic character (see DSC curve in Fig. 5a). The associated mass spectrometric analysis shown in Fig. 5b is in good agreement with the TG/DTG curves. The mass spectrometry signals (m/z 15, NH_3; m/z 18, H_2O) have their maxima at ca. 665 K (NH_3 and H_2O), 775 K for NH_3, and 1,045 K for H_2O which indicates a complex process of decomposition. In the interval 300–570 K, the compound is stable; then the first evacuation process appears in the range of 570–690 K with the loss of ca. the half of NH_3 and H_2O; later, in the interval 720–820 K takes place the evacuation of the rest of NH_3, and finally, the H_2O remaining leaves the compound at very high temperature (ca. 1,030–1,070 K). Fig. 6 shows the conversion curves for the thermal decomposition of γ-$Ti(PO_4)(NH_4HPO_4)$ at six different heating rates as a function of temperature. As it can be observed, the heating rate does not affect the mass loss, although it has an effect on the shape of the conversion curves, which move to higher temperatures as the heating rate increases. Application of KAS method to these curves leads to the calculation of the variation in activation energy (E) as a function of the extent of conversion (α) (Fig. 7; Table 5). E increases slightly (from ca. 140 to 150 kJ mol^{-1}) until the conversion is ca. 0.5. In this stage, desorption of approximately 50 % of NH_3 and H_2O takes place. Later, E diminishes from ca. 150 to 120 kJ mol^{-1} (0.6 of conversion). However, when the extent of conversion increases slightly to ca. 0.8, an abrupt increase takes place. In this stage, the evacuation of residual NH_3 takes place first, followed by the residual H_2O trapped in the material.

The thermal transformation from γ-$Ti(PO_4)(NH_4HPO_4)$ to TiP_2O_7 [32] was monitored by powder X-ray thermo-diffraction from 303 K to 1,273 K (Fig. 8). γ-$Ti(PO_4)(NH_4HPO_4)$ is stable until 453 K. Between 453 and 553 K (appreciable mass loss is not detected), the starting phase transforms slowly to a new polymorph (γ'-$Ti(PO_4)(NH_4HPO_4)$) that was apparently observed as unique phase in a narrow interval of temperatures (553–573 K). Later, between 593 and 723 K, the simultaneous loss of ammonia and water provokes the evolution of γ'-$Ti(PO_4)(NH_4HPO_4)$ to a new polycrystalline phase, probably $Ti(PO_4)(NH_4P_2O_7)_{0.5}$. This compound (has not been isolated) transforms to $Ti(PO_4)(H_2P_2O_7)_{0.5}$ between 723 and 873 K. The well-known $Ti(PO_4)(H_2P_2O_7)_{0.5}$ pseudo-layered compound [31] is stable until 1,073 K, and transforms to TiP_2O_7 at higher temperatures.

Conclusions

The ammonium-titanium(IV) phosphate-hydrogenphosphate, γ-$Ti(PO_4)(NH_4HPO_4)$, was hydrothermally synthesized. Its structure is a layered one consisting of zirconium–oxygen octahedra and phosphate tetrahedra extending along the *ab*-plane, with templating ammonium ions inserted between the layers and held in via hydrogen bonds. Thermal transformation from γ-$Ti(PO_4)(NH_4HPO_4)$ to TiP_2O_7 was monitored by TG-DSC-MS analysis (including activation energy data) and powder X-ray thermo-diffraction. The complete characterization of two new phases, layered γ'-$Ti(PO_4)(NH_4HPO_4)$ and pseudo-layered $Ti(PO_4)(NH_4HP_2O_7)_{0.5}$, is the tasks that should be carried out in the future.

Acknowledgements We thank financial support from Spanish MINECO (MAT2010-15094, MAT2011-27573-C04, *Factoría de Cristalización – Consolider Ingenio* 2010, *Técnicos de Infraestructuras Científico-Tecnológicas* Grant PTA2011-4903-I to ZA, and PTA2011-4950-I to SAK) and FEDER.

References

1. Kraus KA, Phillips HO. Adsorption on inorganic materials. I. Cation exchange properties of zirconium phosphate. J Am Chem Soc. 1956;78:694.
2. Clearfield A, Stynes JA. The preparation of crystalline zirconium phosphate and some observations on its ion exchange behaviour. J Inorg Nucl Chem. 1964;26:117–29.
3. Clearfield A, Smith GD. The crystallography and structure of a-zirconium bis (monohydrogen orthophosphate) monohydrate. Inorg Chem. 1969;8:431–6.
4. Troup JM, Clearfield A. On the mechanism of ion exchange in zirconium phosphates. 20. Refinement of the crystal structure of α-zirconium phosphate. Inorg Chem. 1977;16:3311–4.
5. Kullberg L, Clearfield A. Mechanism of ion exchange in zirconium phosphates. 31. Thermodynamics of alkali metal ion exchange on amorphous ZrP. J Phys Chem. 1981;85:1578–84.
6. Clearfield A, editor. Inorganic Ion Exchange Materials. Boca Raton: CRC Press; 1982.
7. Alberti G, Costantino U. In Intercalation Chemistry. In: Whitinghan MS, Jacobson AJ, editors. New York: Academic Press; 1982.
8. Alberti G. In Recent Developments in Ion Exchange. In: Williams PA, Hudson MJ, editors. London: Elsevier Applied Science; 1987.
9. Clearfield A. In Design of New Materials. In: Cocke DL, Clearfield A, editors. New York: Plenum; 1986.
10. Clearfield A, Blessing RH, Stynes JA. New crystalline phases of zirconium phosphate possessing ion-exchange properties. J Inorg Nucl Chem. 1968;30:2249–58.
11. Clayden NJ. Solid-state nuclear magnetic resonance spectroscopic study of γ-zirconium phosphate. J Chem Soc Dalton Trans. 1987;1877–81.
12. Christensen AN, Andersen EK, Andersen IGK, Alberti G, Nielsen M, Lehmann MS. X-ray powder diffraction study of layered compounds. The crystal structure of α-Ti(HPO4)2 2H2O and a proposed structure for γ-Ti(H2PO4)(PO4) 2H2O. Acta Chem Scand. 1990;44:865–72.
13. Poojary DM, Shpeizer B, Clearfield A. X-Ray powder structure and Rietveld refinement of γ-zirconium phosphate, $Zr(PO_4)(H_2PO_4)\cdot 2H_2O$. J Chem Soc Dalton Trans. 1995;111–3.
14. Àlvarez C, Llavona R, García JR, Suárez M, Rodríguez. Lamellar inorganic ion exchangers. H^+/Ca^{2+} ion exchange in γ-titanium phosphate. J. Inorg Chem. 1987;1045–49.
15. Llavona R, Suárez M, García JR, Rodríguez J. Lamellar inorganic ion exchangers. Alkali metal ion exchange on α and γ- titanium phosphate. Inorg Chem. 1989;28:2863–8.

16. González E, Llavona R, García JR, Rodríguez J. Lamellar inorganic ion exchangers. H^+/Cs^+ ion exchange in γ-titanium phosphate. J Chem Soc Dalton Trans. 1989;1825–29.
17. Alberti G, Bernasconi MG, Casciola M, Costantino U. Crystalline insoluble acid salts of tetravalent metals—XXXIV. Hydrogen-ammonium ion exchange on γ-titanium phosphate. J Inorg Nucl Chem. 1980;42:1637–40.
18. Poojary DM, Zhang B, Dong Y, Peng G, Clearfield A. X-ray powder structure of monoammonium-exchanged phase of γ-zirconium phosphate, $Zr(PO_4)(NH_4HPO_4)$. J Phys Chem. 1994;98:13616–20.
19. Bortun AI, Khainakov S, Bortun LN, Poojary DM, Rodríguez J, García JR, Clearfield A. Synthesis and characterization of two novel fibrous titanium phosphates $Ti2O(PO_4)_2$ 2H2O. Chem Mater. 1997;9:1805–11.
20. Werner PE, Eriksson L, Westdahl M. TREOR, a semi-exhaustive trial-and-error powder indexing program for all symmetries. J Appl Cryst. 1985;18:367–70.
21. Boultif A, Louer D. Powder pattern indexing with the dichotomy method. J Appl Cryst. 2004;37:724–31.
22. Vyazovkin S, Dollimore D. Linear and nonlinear procedures in isoconversional computations of the activation energy of non-isothermal reactions in solids. J Chem Inf Comput Sci. 1996;36:42–5.
23. Vyazovkin S. A unified approach to kinetic processing of non-isothermal data. Int J Chem Kinet. 1996;28:95–101.
24. Majchrzak-Kuceba I, Nowak W. Application of model-free kinetics to the study of dehydration of fly ash-based zeolite. Thermochim Acta. 2004;413:23–9.
25. Polli H, Pontes LAM, Araujo AS. Application of model-free kinetics to the study of thermal degradation of polycarbonate. J Therm Anal Calorim. 2005;79:383–7.
26. Kissinger HE. Reaction kinetics in differential thermal analysis. Anal Chem. 1957;29:1702–6.
27. Akahira T, Sunose T. Joint convention of four electrical institutes. Res Rep Chiba Inst Technol. 1971;16:22–31.
28. Coats AW, Redfern JP. Kinetic parameters from thermogravimetric data. Nature. 1964;201:68–9.
29. Svoboda R, Málek J. Is the original Kissinger equation obsolete today? J Therm Anal Calorim. 2013;115:1961–7.
30. Larson AC, Von Dreele RB. General Structure Analysis System (GSAS). Los Alamos National Laboratory Report LAUR. 2000;86:748.
31. García-Granda S, Khainakov SA, Espina A, García JR, Castro GR, Rocha J, Mafra L. Revisiting the thermal decomposition of layered γ-titanium phosphate and structural elucidation of its intermediate phases. Inorg Chem. 2010;49:2630–8.
32. Sanz J, Iglesias JE, Soria J, Losilla ER, Aranda MAG, Bruque S. Structural disorder in the cubic 3 × 3 × 3 superstructure of TiP_2O_7 XRD and NMR study. Chem Mater. 1997;9:996–1003.

Artículo S4

“Thermal behaviour of a fibrous titanium oxophosphate with ability for nitrogen adsorption above room temperature”

Thermochimica Acta

En trámite de publicación

Índice de Impacto: 2.236

Manuscript Details

Manuscript number	TCA_2018_120
Title	Thermal behaviour of a fibrous titanium oxophosphate with ability for nitrogen-adsorption above room temperature
Article type	Full length article

Abstract

A fibrous titanium oxophosphate, ro-Ti2O(PO4)2·2H2O (ro-TiP), with a three-dimensional network has been obtained under hydrothermal conditions. Both the fresh ro-TiP sample and the thermally treated ones at 673 K (24 h) and stored for 1 day, 2 months and 1 year (in Lab atmosphere at room temperature), were characterized by powder X-ray diffraction (PXRD), solid-state nuclear magnetic resonance (31P MAS NMR), thermal analysis (TG-MS) and scanning electron microscopy (SEM). Moreover, the activation energy has been calculated as a function of the extent of conversion for the thermal decomposition process of the fresh ro-TiP sample, applying both the modified Friedman method (developed by our group) and the advanced nonlinear method proposed by Vyazovkin. The quantification of the apparent mass gain and the total mass loss as a function of the storage time for the thermally activated ro-TiP at 673 K was also performed.

Keywords	Titanium phosphate; Nitrogen fixation; Thermal decomposition; Kinetic analysis
Manuscript category	Nonisothermal kinetics
Corresponding Author	Zakariae Amghouz
Corresponding Author's Institution	University of Oviedo
Order of Authors	Jorge García-Glez, Olena Khainakova, Isabel Iglesias, Belen Alfonso, Jose Angel Huidobro, Zakariae Amghouz, Aránzazu Espina, Camino Trobajo
Suggested reviewers	Sergey Vyazovkin, Weixuan Wu, Luis PErez-MAqueda

Submission Files Included in this PDF

File Name [File Type]

Cover Letter.doc [Cover Letter]

Manuscript ro-TiP_TCA_GarciaGlez.docx [Manuscript File]

To view all the submission files, including those not included in the PDF, click on the manuscript title on your EVISE Homepage, then click 'Download zip file'.

Thermal behaviour of a fibrous titanium oxophosphate with ability for nitrogen-adsorption above room temperature

Jorge Garcia-Glez[1], Olena Khainakova[1], Isabel Iglesias[2], Belén F. Alfonso[2], José A. Huidobro[3], Zakariae Amghouz[4], Aránzazu Espina[5], Camino Trobajo[1]

[1]Departamento de Química Orgánica e Inorgánica, Universidad de Oviedo-CINN, 33006 Oviedo, Spain.
Departamentos de [2]Física, [3]Matemáticas, y [4]Ciencia de los Materiales e Ingeniería Metalúrgica, Escuela Politécnica de Ingeniería, Universidad de Oviedo, 33204 Gijón, Spain.
[5]Servicios Científico-Técnicos, Universidad de Oviedo, 33006 Oviedo, Spain.

Zakariae Amghouz *amghouzzakariae@uniovi.es*

Abstract

A fibrous titanium oxophosphate, ρ-$Ti_2O(PO_4)_2 \cdot 2H_2O$ (ρ-TiP), with a three-dimensional network has been obtained under hydrothermal conditions. Both the fresh ρ-TiP sample and the thermally treated ones at 673 K (24 h) and stored for 1 day, 2 months and 1 year (in Lab atmosphere at room temperature), were characterized by powder X-ray diffraction (PXRD), solid-state nuclear magnetic resonance (^{31}P MAS NMR), thermal analysis (TG-MS) and scanning electron microscopy (SEM). Moreover, the activation energy has been calculated as a function of the extent of conversion for the thermal decomposition process of the fresh ρ-TiP sample, applying both the modified Friedman method (developed by our group) and the advanced nonlinear method proposed by Vyazovkin. The quantification of the apparent mass gain and the total mass loss as a function of the storage time for the thermally activated ρ-TiP at 673 K was also performed.

Keywords: Titanium phosphate; Nitrogen fixation; Thermal decomposition; Kinetic analysis

1. Introduction

In the last decades, a great variety of metal phosphates has been synthesized and characterized. These compounds exhibit a multitude of fascinating structures and the dimensionality of their inorganic framework encompasses one-dimensional chain or ladder structures, two-dimensional layers and three-dimensional structures possessing channels of different sizes [1]. By the end of the last century, two $Ti_2O(PO_4)_2 \cdot 2H_2O$ polymorphs (ρ-TiP and π-TiP), among other open-framework inorganic materials, were prepared hydrothermally and the crystal structure of ρ-polymorph was solved *ab initio* from both neutron and synchrotron X-ray powder diffraction data [2,3]. The topology of the fibrous ρ-TiP consists of a Ti/P/O framework enclosing two different linear channels parallel to the direction of the growth of the fibers, both containing water molecules coordinated to only one of the two octahedral-coordinated independent titanium atoms. Recently, we have described the structural features in the thermal transformation of ρ-TiP to its anhydrous phase, where the hydrated titanium coordination changes from octahedral to distorted tetrahedral [4]. Since the synthesis of ρ-TiP, and although this compound has been the subject of much attention and studies [5-12], our renewed interest in this material broke out as a result of its measurable thermally activated nitrogen-adsorption. This behavior constitutes the first example of nitrogen-fixation by an inorganic material at above ambient temperature [4].

Although it has been described that the thermal dehydration of ρ-TiP occurs in two partially overlapping steps, giving ρ-$Ti_2O(PO_4)_2$ as the final product, the kinetic parameters for this process are unknown so far. In addition, ρ-$Ti_2O(PO_4)_2$ is revealed as a no-inert material in the Lab atmosphere. This contribution reports the thermal features of ρ-$Ti_2O(PO_4)_2 \cdot 2H_2O$ in two different situations: freshly prepared and thermally activated.

2. Experimental procedures

Sample preparation and analytical procedures. All chemicals of reagent grade were used without further purification. The hydrothermal synthesis of ρ-TiP was carried out under autogenous pressure. 2 M aqueous solution of $TiCl_4$ was used as the initial source of titanium. 4 M H_3PO_4 solution was used as a source of phosphorus. The synthetic procedure included mixing of $TiCl_4$ and H_3PO_4 solutions, with a molar ratio P:Ti = 10:1, in a 100 mL stainless steel Teflon-lined vessel. Then the reaction mixture (total volume 60 mL) was sealed and heated at 463 K for 8 days. The product obtained was filtered, thoroughly washed with deionized water, and dried and stored in the Lab at room temperature. The phosphorus and titanium contents of the solids were determined by inductively coupled plasma mass spectrometry (ICP-MS) analysis (Finnigan, Element model) after dissolving a weighed amount in HF(aq). Elemental analysis (wt%): P 18.1, Ti 28.2 (calculated for $Ti_2O(PO_4)_2 \cdot 2H_2O$: P 18.34, Ti 28.40).

Electron microscopy studies. SEM images were obtained by using JEOL 6610VL scanning electron microscope operating at 20 kV and equipped with an X-Max Silicon Drift Detector for EDX analysis.

Powder diffraction studies. Room temperature powder X-ray diffraction (PXRD) patterns were collected on an X'Pert PRO MPD X-ray diffractometer with PIXcel detector, operating in the Bragg-Brentano (θ/2θ) geometry and using CuK_α radiation (λ = 1.5418 Å).

Solid-state nuclear magnetic resonance studies. SS-NMR spectra were acquired using a Bruker AVANCE III 400 equipped with a 4-mm wide-bore MAS probe and operating at ^{31}P resonating frequency of 161.97 MHz. The samples were packed in zirconia rotor with Kel-F tape. The ^{31}P MAS NMR spectra were acquired at 8 kHz spin rate. The relaxation delays were 10 s and number of scans 100. The spectra were referred to $NH_4H_2PO_4$ (δ = 0.9 ppm) as external standard for chemical shift calibration.

Thermal analysis. A Mettler-Toledo TGA/SDTA851^e was used for the thermal analyses in dynamic nitrogen atmosphere (50 mL min^{-1}) at a heating rate of 10 K min^{-1}. In all cases, *ca.* 15 mg of powder sample was thermally treated, and blank runs were performed.

Determination of kinetic parameters. Kinetics of solid state reactions are usually described by the equation

$$\frac{d\alpha}{dt} = k(T)f(\alpha) = A\exp(-\frac{E}{RT})f(\alpha) \tag{1}$$

where $f(\alpha)$ is the reaction model, α the extent of the conversion, $k(T)$ the Arrhenius rate constant, t the time, T the temperature, R the universal gas constant, A the pre-exponential factor and E the activation energy [13,14]. For a linear heating rate program with $\beta = dT(t)/dt = \text{const}$, Eq. (1) leads to

$$\beta\frac{d\alpha}{dT} = Af(\alpha)\exp\left(-\frac{E}{RT}\right) \tag{2}$$

The determination of the three components, A, $f(\alpha)$ and E would allow for adequate description of the process. Model-free isoconversional methods factor are considered the most reliable procedures [15] because they provide values of effective activation energy as a function of extent of conversion without the need of knowing the reaction model or the pre-exponential. Many isoconversional methods have been proposed to obtain the kinetic parameters. In general, they can be split in two types: differential and integral methods, but not all of them lead to the same values [16,17]. So, it seems necessary to check the computed kinetic parameters. The way to test them is by building a model able to reproduce the experimental $\alpha - T$ curves that have been used to obtain these parameters [14].

The Friedman differential method [18] is derived by taking logarithms in the general kinetic equation (2). For several runs with different heating rates β_i, $i = 1, \ldots, n$ and for a given value of the extent of conversion the equation (3) is obtained

$$\ln\left(\beta_i\left(\frac{\mathrm{d}\alpha}{\mathrm{d}T}\right)_{\alpha,i}\right) = \ln(Af(\alpha)) - \frac{E_\alpha}{RT_{\alpha,i}} \tag{3}$$

then, E_α and $\ln(Af(\alpha))$ are computed by fitting to the experimental data. The advantage of the Friedman method is that it is free of approximations. This method can be applied to integral data, as TG data, but the necessary numerical differentiation may introduce errors in the computations. As is well known, a drawback of the Friedman method is its sensitivity to noise (numerical or experimental).

Recently, a new procedure based on a modification of the Friedman method was proposed by Huidobro *et al.* (MFR) to decrease the sensitivity to noise [19]. Given a fixed value of α, set $\alpha_j = \alpha, \alpha_{j-2} = \alpha - 2\Delta\alpha$, $\alpha_{j-1} = \alpha - \Delta\alpha$, $\alpha_{j+1} = \alpha + \Delta\alpha$, $\alpha_{j+2} = \alpha + 2\Delta\alpha$. For each $= j-2, j-1, j, j+1, j+2$ and for n heating programmes of temperature, Eq. (3) leads to

$$\ln\left(\beta_i \frac{\mathrm{d}\alpha(T_{k,i})}{\mathrm{d}T}\right) = \ln(A\,f(\alpha_k)) - \frac{E}{\mathrm{R}T_{k,i}} \tag{4}$$

Assuming that the activation energy has neglected variations over the interval $[\alpha_{j-2}, \alpha_{j+2}]$, for each k, Eq. (4) involves five different straight lines with the same slope $m = -E/R$. Thus, we can find this slope by fitting to the experimental data for all these points simultaneously instead of only for α. This method can easily be applied to a different number of points.

Integral isoconversional methods are based on an integral from equation (2)

$$\int_0^\alpha \frac{\mathrm{d}\alpha}{f(\alpha)} \equiv g(\alpha) = \frac{A}{\beta}\int_{T_0}^{T_\alpha} \exp\left(-\frac{E}{RT}\right)\mathrm{d}T \tag{4}$$

where $g(\alpha)$ is the integral form of the reaction model. The temperature integral does not have analytical solution and numerical approximations are necessary for computations, for example, the Doyle [20] or Coats and Redfern [21] approximations. To avoid inaccuracies with approximations of the temperature integral, Vyazovkin proposed a non-linear integral isoconversional method [22,13]. For a given value of α and a series of runs carried out at different heating rates, the activation energy can be determined by minimizing the function

$$\Phi(E_\alpha) = \sum_{i=1}^{n}\sum_{j\neq i}^{n}\frac{I(E_\alpha,T_{\alpha,i})\beta_j}{I(E_\alpha,T_{\alpha,j})\beta_i} \tag{5}$$

where the $I(E_\alpha,T_\alpha) = \int_{T_{\alpha-\Delta\alpha}}^{T_\alpha}\exp\left(-\frac{E}{RT}\right)\mathrm{d}T$ is determined numerically

3. Results and discussion

The elemental chemical analysis (see Experimental Section), PXRD pattern (Fig. 1a) and ^{31}P MAS NMR data (Fig. 2a), confirm that the synthesized material is the previously reported ρ-TiP [2]. In addition, Fig. 3 shows the SEM images of the fresh ρ-TiP sample and the thermally treated one at 673 K (24 h). These two materials have a similar fibrous morphology, although the diameter of the fibers seems to be greater in the thermally treated material, whereas others form aggregates, resulting in a less uniform morphology as a consequence of the thermal treatment.

The ρ-TiP structure consists of three-dimensional network of TiO_6 octaedra linked by vertex sharing to PO_4 tetrahedra, where the two independent titanium atoms are connected by an oxo-bridge and the two independent water molecules are linked to one type of Ti-atoms [3]. The PO_4 groups and TiO_6 octahedron for Ti1 are almost regular, whereas the octahedron around Ti2 shows a significant distortion due to the presence of the water molecules as ligands. All the hydrogen atoms participate in weak hydrogen bonds, but no hydrogen bonding occurs between the two coordinated water molecules. Additionally, in our previous paper [4], the thermal dehydration of ρ-TiP (in vacuum) was monitored by high-temperature powder X-ray diffraction, showing that the starting phase (ρ-$Ti_2O(PO_4)_2\cdot 2H_2O$) is stable up to *ca.* 450 K; above this temperature the phase transition into ρ-$Ti_2O(PO_4)_2$ takes place and it is almost complete at *ca.* 500 K, as there is only a slight intensity contribution from the starting phase. At *ca.* 550 K no trace of ρ-$Ti_2O(PO_4)_2\cdot 2H_2O$ phase is found and no other phase transition is seen up to 700 K.

In our previous paper on ρ-TiP [2], it was reported that this compound (dried in air at 333 K) practically does not lose weight below 423 K, indicating that little or no physisorbed water is present in this compound; however, in the sample characterized in this work, stabilized at room temperature in the Lab environment, a significant amount of imbibition water has been now detected.

The TG/DTG curves of ρ-TiP (Fig. 4) shows a total mass loss of 11.8 wt% at 1273 K (calculated for $Ti_2O(PO_4)_2 \cdot 2H_2O$: 10.66 wt%), with the first stage related to the evacuation of water imbibition (*ca.* 0.9 wt%, DTG minimum at *ca.* 340 K). At *ca.* 400 K, the loss of water molecules coordinated to the titanium atoms takes place, with a DTG-minimum at *ca.* 600 K and minor signals in the left branch of the DTG curve at *ca.* 430 K (shoulder), 480 K and 550 K (shoulder).

The activation energy was obtained by using the MFR and Vyaz methods, showing an excellent agreement for both calculation procedures (Fig. 5). The experimental data were obtained from thermogravimetric analysis for $\beta = 2.5$, 5, 10 and 20 K min^{-1}. The model of the thermal decomposition has been obtained by using the kinetic parameters and the method proposed by Huidobro *et al.* [19]. By applying this model, $\alpha - T$ curves were reconstructed and compared with the experimental ones measured in the laboratory, and in all cases, the agreement was very good. Fig. 6 shows these $\alpha - T$ curves for $\beta = 5$ and 20 K min^{-1}.

The experimental data, disclosed by both TG/DTG (Fig. 4) and $E - \alpha$ (Fig. 5) curves, are unexpected for a dehydration process that should takes place in a single stage between two crystalline compounds, ρ-$Ti_2O(PO_4)_2 \cdot 2H_2O$ and ρ-$Ti_2O(PO_4)_2$, without detection of new partially hydrated crystalline phases (see Fig. S1 in Ref. [4], that shows the X-ray thermodiffractograms for ρ-TiP recorded in vacuum and heating up from RT to 673 K), where a single DTG band and a quasi-constant value for the apparent activation energy in all conversion range are expected.

Our surprise increases when looking at the TG-curve of ρ-TiP sample immediately after having been treated (in air) at 673 K (Fig. 7, 0 days). Although the total mass loss reaches a value of 1.6% indicating a rapid adsorption of water on the surface of the material, between 400 K and 550 K there is an appreciable gain of mass, which reaches a maximum (*ca.* 0.2 wt%) at *ca.* 500 K. After 24 hours of storage in air at room temperature (Fig. 7, 1 day), the thermal behaviour of the material is not altered (see Fig. 8 for the quantification of both the maximum mass gain and the total mass loss at 1150 K as a function of the storage time). After several weeks of storage, the material shows a higher mass gain (maximums of 0.6 wt%) while the total mass loss increases. After 2 months of storage, the total mass loss is 8.4 wt% and the mass gain is hardly observed (< 0.05 wt%). Finally, after 1 year the total mass loss reaches 10.3 wt% and the TG-curve is the one expected for ρ-TiP free from physisorbed water (calculated for $Ti_2O(PO_4)_2 \cdot 2H_2O$: 10.66%). Under our experimental conditions, the only possible explanation for this gain of mass observed in temperature range 400-550 K should be attributed to the ability of this material to retain nitrogen above room temperature, as we have reported previously [4].

Fig. 1 shows the PXRD patterns for some selected samples. After one year of storage, the pattern correspond to ρ-$Ti_2O(PO_4)_2 \cdot 2H_2O$ as the only crystalline phase detected (see Figs. 1a,d), while during intermediate periods, both the di-hydrated and anhydrous phase coexist (see Figs. 1b,c). Table 1 shows the ^{31}P MAS NMR chemical shifts for these materials (Fig. 2). Two peaks of equal intensity, at -13.2 ppm and -26.9 ppm, are observed for both the starting material and the solid after the thermal activation and one year of storage (Figs. 2a,d), in accord to the previously reported data [2]. Moreover, in the fresh material, the two additional peaks of low intensity, at -12.0 ppm and -25.3 ppm, are to be assigned to the surface phosphate groups, affected by the presence of physisorbed water (absent in the thermally activated material). When the two crystalline phases coexists, ρ-$Ti_2O(PO_4)_2 \cdot 2H_2O$ and ρ-$Ti_2O(PO_4)_2$, the two new peaks (at -11.3 ppm and -29.9 ppm) should be associated to the anhydrous phase (Figs. 2b,c, Table 1).

In the light of these new data, the apparent anomalies observed in the DTG-curve of ρ-TiP (Fig. 4) can be explained by the fact that all the minor peaks observed in the left branch of the DTG curve are found in the temperature range 400-550 K where the nitrogen uptake is feasible. In this temperature range, which corresponds with a conversion range of *ca.* $0.1 < \alpha < 0.4$, the adsorption/desorption processes are probably overlapped and the apparent activation energy fluctuates between 25 and 95 kJ mol^{-1}. Subsequently, it increases to 120 kJ mol^{-1} and then it lies below 100 kJ mol^{-1}.

Conclusions

The unexpected results have shown that thermal decomposition of a certain material could be a very complex process when it is simultaneously accompanied with adsorption processes above room temperature. In this work, we describe a simultaneous desorption (water)/ adsorption (N_2) processes at temperatures of 400-550 K that explains the anomalies observed in the kinetic parameters of a simple dehydration process. To our knowledge, this is the first study of a kinetic process with these characteristics when the "inert" entrainment gas (N_2) interacts with the sample causing an apparent delay in the dehydration process. Moreover, the activation energy was obtained as a function of the extent of conversion for the thermal decomposition of the fresh ρ-TiP sample by using the MFR and Vyaz methods. Both methods provide similar results and an excellent agreement between the reconstructed and the experimental $\alpha - T$ curves was achieved, in spite of been a very complex process.

Acknowledgements

This work is supported by "Ministerio de Economía y Competitividad" (MAT2016-78155-C2-1-R, MAT2013-40950-R, MAT2011-27573-C04-02), "Gobierno del Principado de Asturias" (GRUPIN14-060), and FEDER.

References

[1] Z. Amghouz, B. Ramajo, S.A. Khainakov, I. da Silva, G.R. Castro, J.R. García, S. García-Granda, Dimensionality changes in the solid phase at room temperature: 2D→1D→3D evolution induced by ammonia sorption–desorption on zinc phosphates, Chem. Commun. 50 (2014) 6729-6732 (and references therein).

[2] A.I. Bortun, S.A. Khainakov, L.N. Bortun, D.M. Poojary, J. Rodríguez, J.R. García, A. Clearfield, Synthesis and characterization of two novel fibrous titanium phosphates $Ti_2O(PO_4)_2{\cdot}2H_2O$, Chem. Mater. 9 (1997) 1805-1811.

[3] M.A. Salvadó, P. Pertierra, S. García-Granda, J.R. García, M.T. Fernández-Diaz, E. Dooryhee, Crystal structure, including H-atom positions of $Ti_2O(PO_4)_2{\cdot}2H_2O$ determined from synchrotron X-ray and neutron powder data, Eur J Solid State Inorg. Chem. 34 (1997) 1237-1247.

[4] J. García-Glez, Z. Amghouz, I. da Silva, C.O. Ania, J.B. Parra, C. Trobajo, S. García-Granda. The ability of a fibrous titanium oxophosphate for nitrogen-adsorption above room temperature, Chem. Commun. 53 (2017) 2249-2251.

[5] A.K. Cheetham, G. Férey, T. Loiseau, Open-framework materials, Angew. Chem. Int. Ed. 38(1999) 3268-3292.

[6] D.J. Jones, G. Aptel, M. Brandhorst, M. Jacquin, J. Jiménez-Jiménez, A. Jiménez-López, P. Maireles-Torres, I. Piwonski, E. Rodríguez-Castellón, J. Zajac, J. Rozière, High surface area mesoporous titanium phosphate: Synthesis and surface acidity determination, J. Mater. Chem. 10 (2000) 1957-1963.

[7] Y.H. Guo, Z. Shi, J.H. Yu, J.D. Wang, Y.L. Liu, N. Bai, W.Q. Pang, Solvothermal synthesis and characterization of a new titanium phosphate with a one-dimensional chiral chain, Chem. Mater. 13 (2001) 203-207.

[8] C. Serre, M. Hervieu, C. Magnier, F. Taulelle, G. Férey, Synthesis and characterization of mesostructured titanium(IV) fluorophosphates with a semicrystalline inorganic framework, Chem. Mater. 14(2002) 180-188.

[9] C. Pan, S. Yuan, W.X. Zhang, A neutral templating route to mesoporous titanium phosphate molecular sieves with enhanced thermal stability, Appl. Catal. A-Gen. 312 (2006)186-193.

[10] Wang, L., Yan, Z., Qiao S., Lu G.Q.M., Huang Y., Structural and morphological transformations of mesostructured titanium phosphate through hydrothermal treatment, J. Colloid Interf. Sci. 316 (2007) 954-961.

[11] S.Y. Guo, S. Han, B. Chi, J. Pu, J. Li, Synthesis of shape-controlled mesoporous titanium phosphate nanocrystals: The hexagonal titanium phosphate with enhanced hydrogen generation from water splitting, Int. J. Hydrog. Energy. 39 (2014) 2446-2453.

[12] M. Yada, Y. Inoue, A. Sakamoto, T. Torikai, T. Watari, Synthesis and controllable wettability of micro- and nanostructured titanium phosphate thin films formed on titanium plates, ACS Appl. Mater. Inter. 6 (2014) 7695-7704.

[13] A.K. Galwey, M.E. Brown, A theoretical justification for the application of the Arrhenius equation to kinetics of solid state reactions (mainly ionic crystals), Proc. R. Soc. Lond. A. 450 (1995) 501-512.

[14] S. Vyazovkin, A.K. Burnham, J.M. Criado, L.A. Pérez-Maqueda, C. Popescu, N. Sbirrazzuoli, ICTAC Kinetic Committee recommendations for performing kinetic computations on thermal analysis data, Thermochim. Acta 520(2011) 1-19.

[15] S. Vyazovkin, Model-free kinetics: Staying free of multiplying entities without necessity, J. Therm. Anal. Calorim. 83 (2006) 45-51.

[16] T. Vlase, G. Vlase, N. Birta, N. Doca, Comparative results of kinetic data obtained with different methods for complex decomposition steps, J. Therm. Anal. Cal. 88 (2007) 631-635.

[17] N. Sbirrazzuoli, L. Vincent, A. Mija, N. Guigo, Integral, differential and advanced isoconversional methods: Complex mechanisms and isothermal predicted conversion-time curves, Chemometr. Intell. Lab. Syst. 96 (2009) 219-226.

[18] H.L. Friedman, Kinetics of thermal degradation of char-forming plastics from thermogravimetry. Application to a phenolic plastic, J. Polym. Sci, Part C: Polym. Symp. 6 (1964) 183-195.

[19] J.A. Huidobro, I. Iglesias, B.F. Alfonso, A. Espina, C. Trobajo, J.R. Garcia, Reducing the effects of noise in the calculation of activation energy by the Friedman method. Chemometr. Intell. Lab. Syst. 151(2016) 146-152.

[20] C.D. Doyle, Estimating isothermal life from thermogravimetric data, J. Appl. Polym. Sci. 6 (1962) 639-642.

[21] AW. Coats, J.P. Redfern, Kinetic parameters from thermogravimetric data. Nature. 201(1964) 68-69.

[22] S. Vyazovkin, Modification of the integral isoconversional method to account for variation in the activation energy, J. Comput. Chem. 22 (2001) 178-183.

Table 1. ^{31}P MAS NMR chemical shifts for both ρ-TiP freshly prepared (a) and thermally treated at 673 K (24 h) and subsequently stored at RT for one day (b), two months (c) and one year (d).

Fresh (a)	1 day (b)	2 months (c)	1 year (d)
	-11.3	-11.3 (weak)	
-12.0 (weak)			
-13.2	-13.2	-13.2	-13.2
-25.3 (weak)			
-26.9	-26.9	-26.9	-26.9
	-29.9	-29.9 (weak)	

FIGURE CAPTIONS

Fig. 1 PXRD data for: ρ-TiP (a) and ρ-TiP (previously treated at 673 K) as a function of the storage time (in Lab atmosphere at room temperature): 1 day (b), two months (c), and 1 year (d).

Fig. 2 ^{31}P MAS NMR spectra for: ρ-TiP (a) and ρ-TiP (previously treated at 673 K) as a function of the storage time (Lab atmosphere and room temperature): 1 day (b), two months (c), and 1 year (d).

Fig. 3 SEM images of ρ-TiP at room temperature (a) and treated at 673 K (b).

Fig. 4 TG and DTG curves of thermal decomposition of ρ-TiP at heating rate $\beta = 10$ K min^{-1}.

Fig. 5 Dependencies of E on α for ρ-TiP calculated by MFR (red circles) and Vyaz (blue squares) isoconversional methods.

Fig. 6 Comparison of the experimental (solid lines) and reconstructed (points) $\alpha - T$ curves for ρ-TiP at β = 5 K min^{-1} (a) and β = 20 Kmin^{-1} (b).

Fig. 7 TG curves for ρ-TiP, previously treated at 673 K, as a function of the storage time (Lab atmosphere and room temperature).

Fig. 8 Quantification of both the apparent mass gain and the total mass loss using TG data of ρ-TiP, previously treated at 673 K, as a function of the storage time (Lab atmosphere and room temperature).

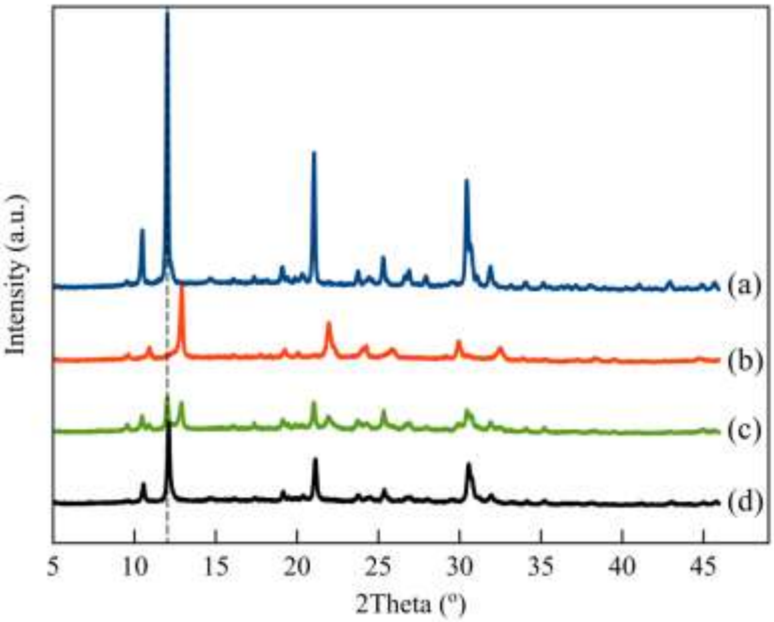

Figure 1

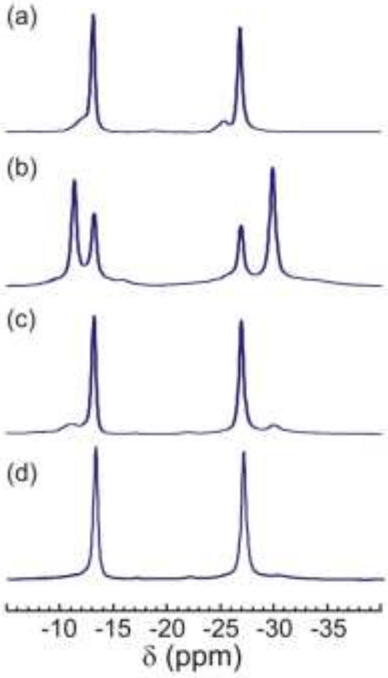

Figure 2

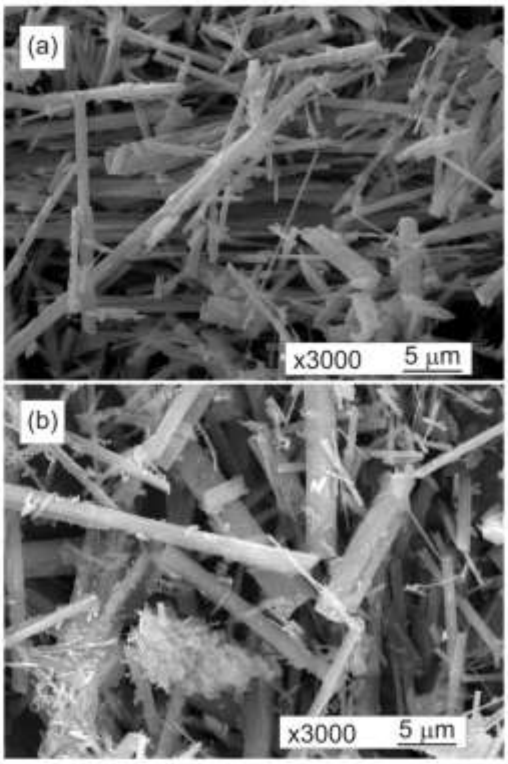

Figure 3

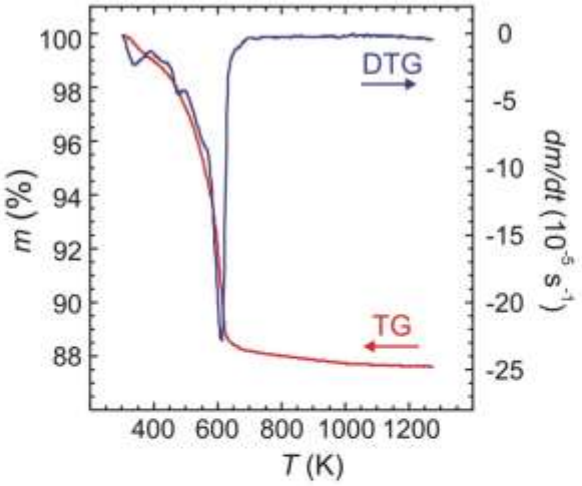

Figure 4

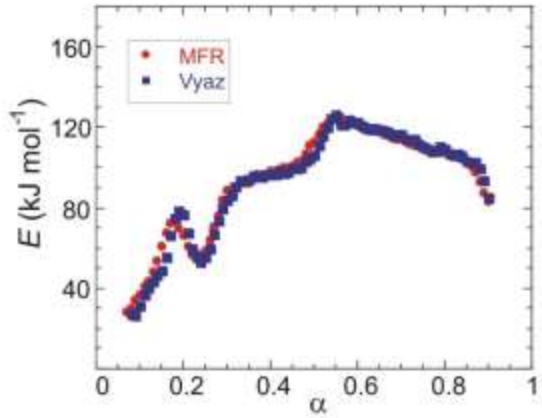

Figure 5

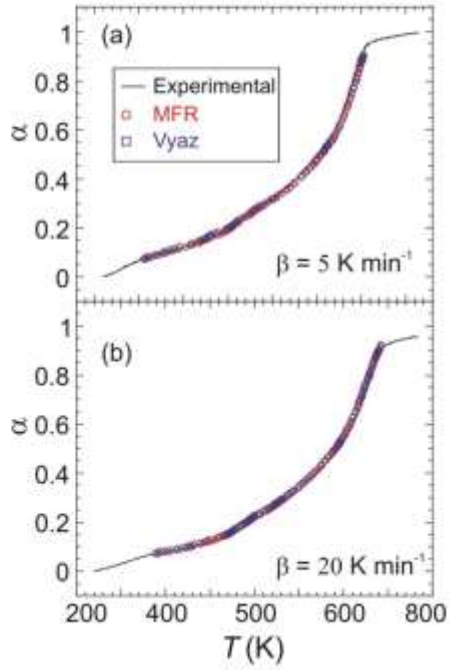
(a)
Experimental
MFR
Vyaz
α
T (K)
β = 5 K min⁻¹
(b)
β = 20 K min⁻¹
0
0.2
0.4
0.6
0.8
1
200
400
500
600
800

Figure 6

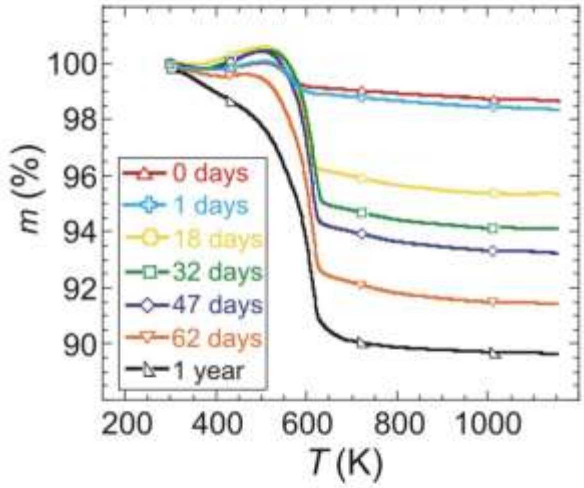

Figure 7

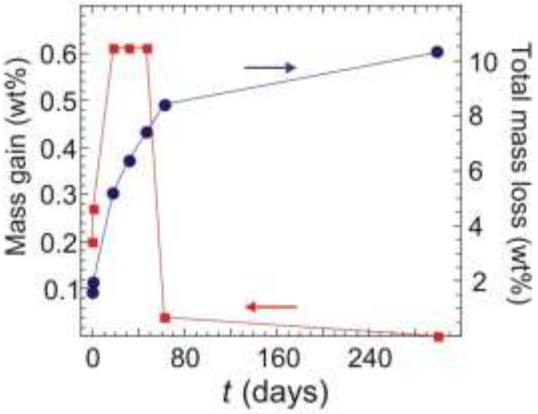

Figure 8